AXISYMMETRIC AND THREE-DIMENSIONAL LATTICE BOLTZMANN MODELS AND THEIR APPLICATIONS IN FLUID FLOWS

HUANG HAIBO
(*B.Eng., University of Science and Technology of China,*
M. Eng., Chinese Academy of Sciences, Beijing,China)

A THESIS SUBMITTED

FOR THE DEGREE OF DOCTOR OF PHILOSOPHY

DEPARTMENT OF MECHANICAL ENGINEERING

NATIONAL UNIVERSITY OF SINGAPORE

2006

ACKNOWLEDGEMENTS

I would like to express my sincere gratitude to my supervisors, Associate Professor T. S. Lee and Professor C. Shu for their support, encouragement and guidance on my research and thesis work.

Many people who are important in my life have stood behind me throughout this work. I am deeply grateful to my wife, Chaoling and every member of my family, my parents and my sisters, for their love and their confidence in me. Also I thank my friends Dr. Xing Xiuqing, Dr. Tang Gongyue for their encouragement and help in these years.

In addition, I will give my thanks to Dr. Peng Yan, Dr. Liao Wei, Cheng Yongpan, Zheng JianGuo, Xia Huanming, Wang Xiaoyong, Xu Zhifeng and other colleagues in Fluid Mechanics who helped me a lot during the period of my research.

Finally, I am grateful to the National University of Singapore for granting me research scholarship and precious opportunity to pursue a Doctor of Philosophy degree.

TABLE OF CONTENTS

SUMMARY

The lattice Boltzmann Method (LBM) has attracted significant interest in the CFD community. Uniform grids in Cartesian coordinates are usually adopted in the standard LBM. The axisymmetric flows which are described by two-dimensional (2D) Navier-Stokes equations in cylindrical coordinates can be solved by three-dimensional (3D) standard LBM but they are not able to be solved by 2D standard LBM directly. To simulate the axisymmetric flows by using 2D LBM, we suggest a general method to derive axisymmetric lattice Boltzmann D2Q9 models in 2D coordinates.

Using the general method, three different axisymmetric lattice Boltzmann D2Q9 model A, B and C were derived through inserting different source terms into the 2D lattice Boltzmann equation (LBE). Through fully considering the lattice effects in our derivation, all these models can mimic the 2D Navier-Stokes equation in the cylindrical coordinates at microscopic level. In addition, to avoid the singularity problem in simulations of Halliday et al. (2001), axisymmetric boundary conditions were proposed.

The LBM results of steady flow and 3D Womersley flow in circular tubes agree well with the FVM solutions and exact analytical solutions, which validated our models. It is observed that the present models reduce the compressibility effect shown in the study of Halliday et al. (2001) and is much more efficient than the direct 3D LBM simulations.

Using the axisymmetric model and the multi-block strategy, the steady and unsteady blood flows through constricted tubes and elastic vascular tubes were simulated. Our 3D multi-block LBM solver which has second-order accuracy in space was also used to study the blood flow through an asymmetric tube.

Besides the above application, an incompressible axisymmetric D2Q9 model considering the swirling effect and buoyancy force was proposed to simulate the benchmark problems for melt flows in Czochralski crystal growth. This is a hybrid scheme with LBM for the axial and radial velocities and finite difference method for the azimuthal velocity and the temperature. It is found the hybrid scheme can give very accurate results. Compared with the previous model (Peng et al. 2003), the present axisymmetric model seems more stable and provides a significant advantage in the simulation of melt flow cases with high Reynolds number and high Grashof number.

A revised axisymmetric D2Q9 model was also applied to investigate gaseous slip flow with slight rarefaction through long microtubes. In the simulations of microtube flows with Kn_o in range (0.01, 0.1), our LBM results agree well with analytical and experimental results. Our LBM is also found to be more accurate and efficient than DSMC when the slip flow in microtube was simulated.

For the simulation of the heat and fluid flow with LBM, besides the above hybrid scheme, it can also be solved by a double-population thermal lattice Boltzmann equation (TLBE). A recent curved non-slip wall boundary treatment for isothermal LBE (Guo, et al., 2002) was successfully extended to handle the 2D and 3D thermal curved wall boundary for TLBE and proved to be of second-order accuracy.

LIST OF TABLES

LIST OF FIGURES

NOMENCLATURE

Roman letters

A	function of body force in NS equation
B_α	function of body force in NS equation
$C_{\alpha\beta}$	function of body force in NS equation
c	velocity δ_x/δ_t
c_s	the speed of sound
$\mathbf{e}_i$	the particle velocity vector along direction i
E	some additional source terms in NS equation
f_i	the particle distribution function
f_i^+	distribution function after collision
F_α	body force in NS equation, α can represent x or r
g_i	the thermal energy density distribution function
g, g_0	gravitational acceleration
Gr	Grashof number
Kn	Knudsen number
M	Mach number
$M_{\max}$	$U_{\max}/c_s$
N_r	number of lattice nodes in radius
Nu	Nusselt number
p	pressure
p^*	the maximum amplitude of the oscillatory pressure gradient
Pr	Prandtl number (except Chapter 7)
Pr	ratio of inlet and outlet pressure (Chapter 7)
Re	Reynolds number
r	radius or radial coordinate
R	the radius of the circular pipe
St	Strouhal number of Womersley flow
S_i	source term added into lattice Boltzmann equation
t	time
T	temperature
T	sampling period in unsteady periodic flow (Chapter 4)
$U_{\max}$	the maximum velocity appear in tube axis during a sampling period
U_c	the characteristic velocity, which is equal to ($\alpha \to 0$) or much larger than ($\alpha \gg 1$) U_{max} (Chapter 4)
$\mathbf{u}$	fluid velocity vector
u_x	x component of the velocity
u_r	r component of the velocity
u_α	α component of the velocity, α can represent x or r
$\mathbf{x}$	spatial position vector

Greek letters

α	Womersley number (Chapter 4)
β_0	the thermal expansion coefficient
$\delta_{\alpha\beta}$	Kronecker symbol

δ_x	lattice space size
δ_t or δt	time step
θ	velocity error
$<\theta>$	overall θ averaged over a sampling period
λ	the mean free path of gas
ν	the kinetic viscosity of fluid
ξ	velocity error
$<\xi>$	overall ξ averaged over a sampling period
ρ_0	approximately constant density of incompressible fluid
ρ	fluid density
σ	shear stress
τ	the dimensionless relaxation time constant
Δ	the mean density fluctuation (Chapter 4)
ψ	stream function
ω	angular frequency of Womersley flow
ω_i	weight coefficients for the equilibrium distribution function
Ω	angular velocity
∂_t	partial time derivative
∂_α	partial space derivative, α can represent x or r

Superscripts

eq	local equilibrium, zeroth order
ne	non-equilibrium part
n	*n*th order of Chapman-Enskog series expansion
+	post-collision status
f	fine grid
c	coarse grid

Subscripts

i	the component in direction $\mathbf{e}_i$
α, β	axial coordinate x or radial coordinate r
x	axial coordinate *x*
r	radial coordinate *r*
o	parameter at outlet (Chapter 7)

Abbreviations

BGK	Bhatnagar-Gross-Krook
CFL	Courant-Friedrichs-Lewy
FD	finite difference
FVM	finite volume method
LBE	lattice Boltzmann equation
LBM	lattice Boltzmann method
LBGK	lattice BGK
NS	Navier-Stokes
TLBE	Thermal lattice Boltzmann equation

Chapter 1 Introduction & Literature Review

1.1 Background

Fluid flow phenomena are very common in our everyday life. The flow of water in rivers, movement of air in the atmosphere, the ocean currents and the blood flow in animal cardiovascular system are all the common fluid flow phenomena. The systematical studies on fluid dynamics have been conducted since the 18^{th} century. The fluid dynamics theory such as Navier-Stokes (NS) equation has been established to describe the fluid flow since the middle of the 19^{th} century. However, the NS equation cannot be solved theoretically without simplifications because till today the analytical solutions of the NS equation is only applicable to several ideal cases. When modern computers appeared in the 1940's, using the computers to solve the equation system and study the fluid dynamics became possible. From the 1940's to today, popular computational fluid dynamics (CFD) methods such as finite difference method (FDM) and finite volume method (FVM) have been developed to solve the Navier-Stokes equation numerically. These CFD methods solve the NS equations directly and the macro variables such as velocity and pressure can be obtained. It is also noticed that the above NS equation is based on the continuity assumption at macroscopic level, which means the macro variables are well defined in a infinite small point and vary continuously from one point to another.

On the other hand, the fluid system can also be viewed at microscopic level since fluid is composed of a huge number of atoms and molecules. Through modeling the motion of individual molecule and interactions between molecules, the behavior of fluid can also be simulated since the macroscopic variables (e.g.,

pressure and temperature) can be obtained through statistical sampling. Sometimes, the molecular dynamics simulation is very necessary, for example, when the molecular mean free path is comparable to the flow characteristic length (e.g., in study of rarefied gas dynamics), the continuum assumption breaks down and the common CFD method at macroscopic level is not available. However, this microscopic computation needs much more computational time than the common CFD method at macroscopic level since it has to simulate the motions of a huge number of molecules. That is the main disadvantage of this method.

Besides viewing the flow system at the above macroscopic scale and microscopic scale, one may also interested to view the system at an intermediate scale: the mesoscopic scale. At this scale, the lattice gas cellular automata (LGCA) was proposed to simulate fluid flows and other physical problems by Hardy, Pomeau and de Pazzis in 1973. This model considered a much smaller number of fluid 'particles' than molecular dynamics method because a fluid 'particle' is a large group of molecules. On the other hand, the fluid 'particle' is still considerably smaller than the smallest length scale of the simulation.

The LGCA model proposed by Hardy et al. (1973) conserves mass and momentum but it does not yield the desired Navier-Stokes equation at the macroscopic level. Later it is found that through a multiple-scale expansion, a LGCA over a lattice with higher symmetry than that of Hardy et al. (1973) can simulate the Navier-Stokes equation at the macroscopic level (Frisch et al., 1986). Hence, the LGCA can also be viewed a non-direct solver for the Navier-Stokes equation. However, the LGCA method suffers from some drawbacks such as statistical noise and lack of Galilean invariance (Qian et al., 1992). To get rid of above drawbacks, McNamara et al. (1988) proposed to model lattice gas with

Boltzmann equation. Hence, the LGCA method was further improved and developed into lattice Boltzmann method (LBM) (McNamara et al. 1988, Higuera et al. 1989, Qian, et al, 1992).

Unlike traditional CFD methods (e.g., FDM and FVM), LBM is based on the microscopic kinetic equation for the particle distribution function and from the function, the macroscopic quantities can be obtained. The kinetic nature provides LBM some merits. Firstly, it is easy to program. Since the simple collision step and streaming step can recover the non-linear macroscopic advection terms, basically, only a loop of the two simple steps is implemented in LBM programs. Secondly, in LBM, the pressure satisfies a simple equation of state when simulate the incompressible flow. Hence, it is not necessary to solve the Poission equation by the iteration or relaxation methods as common CFD method when simulate the incompressible flow. The explicit and non-iterative nature of LBM makes the numerical method easy to parallelize (Chen *et al.* 1996).

Over the past two decades, the LBM has achieved great progress in fluid dynamics studies (Chen and Doolen, 1998). The LBM can simulate the incompressible flow (Succi et al., 1991, Hou and Zou, 1995) and compressible flows (Alexander, 1992). The LBM has also been successfully applied to the multi-phase flow (Grunau et al., 1993), immiscible fluids (Gunstensen et al., 1991), flows through porous media (Chen et al., 1991) and turbulence flow (Benzi and Succi, 1990, Teixeira, 1998).

1.2 Axisymmetric LBM

As we know, the lattice Boltzmann method simulates the fluid flows through streaming and collision steps. In the streaming step, the post-collision distribution

function would stream to the nearby lattice nodes according to a certain lattice velocity model. Since all lattice velocity models are regular and defined in the Cartesian coordinates, the standard LBM is based on the Cartesian coordinate system and essentially requires uniform lattice grid.

Hence, to simulate the axisymmetric flows which are two-dimensional or quasi-three-dimensional problems in cylindrical coordinates, we may have to carry out 3D simulation in 3D cubic lattices if we use the standard LBM. However, 3D simulations mean a large grid size. It is not so efficient to simulate an axisymmetric swirling flow problem in that way.

To simulate the axisymmetric flow more efficiently, Halliday et al. (2001) proposed an axisymmetric D2Q9 model for the steady axisymmetric flow problems and it seems successful for simulation steady flow in straight tube with low Reynolds number (*i.e.*, $Re<100$). The main idea of the D2Q9 model is inserting several spatial and velocity-dependent source terms into the adjusted evaluation equation for the lattice fluid's momentum distribution. That is very similar to the idea of inserting source terms to Navier-Stokes equation to simulate some kind of flow problems in the conventional CFD methods (e.g., when simulate multiphase flow, the surface tension effect is usually incorporated into the NS equation).

However, Halliday et al. (2001) did not fully consider the lattice effects in their derivation and some important terms are not considered in their derivation. Hence, the model cannot recover the NS equation at macroscopic level correctly and it can only give poor simulation results for fluid flows in constricted or expended tubes. The problem would be addressed in Chapter 3 in detail.

In addition, Halliday et al. (2001) did not provide the LBM treatment for the

axisymmetric boundary condition. As a result, they have to study the whole computational domain bounded by upper and lower straight walls. They try to avoid the singularity by placing the axis in the center of the computational grid within the computational domain.

To further improve the computational efficiency and stability, as the other common CFD methods, axisymmetric flow problems should be simulated in an axisymmetric plane, which is a half computational domain of the above one. Thus, it is necessary to propose treatments for axisymmetric boundary.

Later, Peng et al. (2003) also proposed an axisymmetric D2Q9 model which including more source terms, to simulate the axisymmetric flow with swirl or rotation. However, it was found that the axisymmetric model (Peng et al. 2003) is unstable when simulate the axisymmetric flows with high Reynolds number (e.g., Re=10^4) and high Grashof number (e.g., Gr=10^6) even with fine grid such as 200 $\times$200.

Hence, to obtain an accurate, efficient and more stable axisymmetric model is very necessary for study of the axisymmetric flows by LBM.

1.3 Axisymmetric and Three-dimensional LBM Applications

1.3.1 Study of Blood Flow

Blood flow is a very complex phenomenon. The blood transports particles such as red and white blood cells through a sophisticated network of elastic branching tubes. The study of the arterial blood flow is of great interest to the cardiovascular doctors and fluid dynamicists because the majority of deaths in

developed countries result from cardiovascular diseases (Ku, 1997). Many cardiovascular diseases are due to abnormal blood flow in arteries. For example, in the disease of atherosclerosis, arterial stenoses are formed due to plaque growth. When the stenoses block more than about 70% (by area) of the artery, it is a significant health risk for the patient. On the other hand, very high shear stresses near the throat of the stenosis can activate platelets and thereby induce thrombosis (Ku, 1997). The blood clots in the arteries can totally block blood flow to the heart or brain. To further understand the hemodynamics in stenosed artery, it is necessary to carry out experimental or numerical studies.

Actually, much of our knowledge about blood flow comes from the experimental studies. Experimental studies for the steady and unsteady flows through rigid stenosed tubes with different constriction ratios were carried out by Young and Tsai (1973a, 1973b). However, these experimental studies mainly focused on the velocity measurement. In blood flow studies, to measure the near-wall shear stress is also very important. Shear stress may be determined through measured velocity which is very close to the wall. For steady flow, Ahmed and Giddens (1983) estimated the wall shear stress in stenosed tubes through the velocity measured by laser Doppler anemometry. However, for pulsatile flow, accurate measurements of distance from the wall and the shape of the velocity profile are technically difficult. A shear stress sensor is also not applicable for unsteady flow. Moreover, shear stress measurement also depends on the near-wall blood viscosity which is usually not precisely known. Thus arterial wall shear stress measurements are estimated and may have errors of 20–50% (Ku, 1997). Besides the above drawback, experimental studies are usually expensive to carry out and in many cases *in vivo* measurements are

extremely difficult.

Using numerical methods to study blood flow can overcome the above difficulties since the wall shear stress can be obtained accurately through CFD technology and it is very cheap to perform the blood flow simulation in computers. Using models of elastic tubes, CFD technology can also simulate the *in vivo* blood flow. Since the lattice Boltzmann method (LBM) has advantages such as ease of implementation, ease of parallelization and simple boundary treatments, the LBM may be very suitable for application in the blood flow simulation.

In the following part we would have a review on topics about simulation blood flow using lattice Boltzmann method.

Some studies have examined the fluid flows through different two-dimensional (2D) geometries to mimic the blood flow in circulation (Artoli, et al. 2002a, Cosgrove et al., 2003). Artoli et al. (2002a) studied the accuracy of 2D Womersley flow using 2D 9-velocity (D2Q9) LBM model. They observed a time shift between the analytical solutions and the simulations. That can be attributed to the compressibility effect of D2Q9 model. Cosgrove et al. (2003) also studied the 2D Womersley flow and showed that the results of LBM incorporating the halfway bounce-back boundary condition are second order in spatial accuracy. For the steady blood flow in a symmetric bifurcation, Artoli, et al. (2004) obtained some preliminary results. However, the above studies only addressed simple 2D geometries. Actually, the 2D cases cannot represent the 3D vascular tubes and 3D real arterial bifurcation.

The LBM was also applied to simulate the fluid flow through 3D straight circular tubes. The Poiseuille flow in 3D circular tube was studied by Maier et al. (1996). They found that using the simple bounce-back wall boundary treatment to

handle the curved surface may seriously decrease the computational accuracy or efficiency. To solve this problem, accurate 3D curved boundary treatments were proposed by Mei et al. (2000) and Bouzidi et al. (2001). Artoli et al. (2002b) used the above curved boundary treatments to study the pulsatile flow in a straight 3D circular pipe. They reported that compared with the analytical solutions, the error of velocity profiles can be reduced from 15% with the bounce back scheme to 7% with the accurate curved boundary condition (Bouzidi et al., 2001). Artoli et al. (2003) also studied the pulsatile flow in a 3D bifurcation model of the human abdominal aorta and gave preliminary results which were not confirmed by comparison with other numerical or experimental results.

The above 3D blood flow simulations carried out by Artoli et al. (2002b) are too simple because the study only reported the flow in straight tubes. The study did not consider the 3D blood flow in stenosed tubes which are usually found in atherosclerosis cases. The study of the pulsatile flow in a 3D bifurcation model by Artoli et al. (2003) is only a preliminary study. It can be seen from the above review that studies on blood flow using LBM are still limited. The studies of 3D blood flow in tubes with different 3D constrictions and arterial bifurcation are necessary to carry out.

Another problem is that the direct 3D simulations of flow in circular tubes (Artoli et al. 2002b) are very time-consuming for such an axisymmetric geometry. It is necessary to develop our accurate axisymmetric D2Q9 model to simulate the axisymmetric flow more efficiently.

The above studies of blood flow through 2D and 3D rigid vascular tubes are relatively simple compared with the blood flow through the models of the elastic vascular tubes. In the models of elastic tube, the wall is compliant and distensible

which can mimic the blood flow in actual large arteries. Studies of blood flow through compliant tube using LBM have also been carried out. Fang et al. (1998) studied the pulsatile blood flow in a simple 2D elastic channel. In the study, an elastic and movable boundary condition was proposed by introducing the virtual distribution function at the boundary and some good results were obtained. With further development of non-slip wall boundary condition (Guo et al., 2002), the unsteady moving boundary condition was proposed as the second-order extrapolation of all the possible directions in the study of Fang et al. (2002). Their results of pulsatile flow in 2D elastic channel are somewhat consistent with the experimental data in 3D elastic tubes. The study of Fang et al. (2002) demonstrated the potential of LBM application in study of blood flow through compliant wall boundary. Hoekstra et al. (2004) studied the unsteady flows in a 2D channel.

However, the Reynolds number in the above studies are very low and the geometry of study is only 2D which is different from the 3D actual elastic artery. Due to the compressibility of LBM, the results of unsteady cases (Hoekstra et al. 2004) are all inaccurate. Because the second-order extrapolation used to treat the compliant wall (Fang et al. 2002) is usually unstable in numerical method, numerical instability may be encountered for high Reynolds number cases. To further explore the LBM application in study of blood flow, it is necessary to propose or test other more robust moving boundary condition and apply our incompressible axisymmetric D2Q9 model.

1.3.2 Taylor-Couette Flow and Melt Flow in Czochralski Crystal Growth

Many important engineering flows involve swirl or rotation, for example, the flows in combustion, turbomachinery and mixing tanks. In this part we focus on the axisymmetric flows with swirl and rotation which are more complex than the axisymmetric flows without rotation. As we know, an axisymmetric swirling flow is a quasi-three-dimensional problem for conventional Navier-Stokes solvers in the cylindrical coordinate system because the gradient for any variable in the azimuthal direction is zero. In our study, two typical axisymmetric swirling and rotating flows would be studied.

One is Taylor-Couette flow between two concentric cylinders. At low rotational speed of the inner cylinder, the flow is steady and the vortices are planar. Three-dimensional vortices would begin to appear when the speed of rotation exceeds a critical value which depends on the radius ratio of two cylinders. Previously, there are some studies on Taylor-Couette flow using the conventional Navier-Stokes solvers (Liu, 1998).

The other typical axisymmetric swirling flow is the melt flow in Czochralski (CZ) crystal growth. CZ crystal growth is one of the major prototypical systems for melt-crystal growth. It has received the most attention because it can provide large single crystals. In typical CZ crystal growth systems, the high Reynolds number and Grashof number of the melt make numerical simulation difficult. The conventional CFD methods such as finite volume and finite difference methods have been developed to simulate the CZ crystal growth flow problems (Buckle and Schafer, 1993, Xu et al., 1997, Raspo et al., 1996). The second-order central difference scheme is usually chosen to discretize the convection terms in NS

equations. However, for melt flows with high Reynolds number and Grashof number which are the requirement of growth of larger and perfect crystals, the convection terms in the NS equations become dominant and the second-order central difference scheme may be unsuitable due to enhanced numerical instability (Xu et al., 1997). If the low-order upwind scheme is used, accurate solutions can only be obtained by using very fine grid (Xu et al., 1997). Considering the discretization problem in conventional CFD method, lattice Boltzmann method (LBM) was proposed to simulate the melt flow in CZ crystal flow (Peng et al., 2003).

As we know, one main advantage is that the convection operator of LBM in phase space is linear which may overcome the above discretization difficulty in conventional CFD method.

Following the idea of Halliday et al. (2001), Peng et al. (2003) used LBM to study the melt flow in CZ crystal growth as a quasi-three-dimensional problem. They proposed an axisymmetric D2Q9 LBM to solve the axial and radial velocity in an axisymmetric plane and swirl velocity and temperature were solved by finite difference method. However, Peng et al. (2003) only simulated test cases of lower Reynolds number and Grashof number.

It was found that the axisymmetric model proposed by Peng et al. (2003) is unstable for simulations of melt flows with high Reynolds number (Re=10^4) and high Grashof number (Gr=10^6) even with very fine grid.

On the other hand, since the model proposed by Peng et al. (2003) is derived from the standard D2Q9 model, the compressible effect of standard D2Q9 model (Hou et al., 1995, He and Luo, 1997) may be involved into the simulation.

To improve the numerical stability and eliminate the compressibility effect of

standard LBM, It is necessary to obtain a more robust incompressible axisymmetric D2Q9 model.

1.3.3 Study of Gas Slip Flow in Microtubes

MEMS (Micro-Electro-Mechanical-Systems) devices with dimensions ranging from 100 microns to 1 micron have found many applications in engineering and scientific researches (Gad-el-Hak, 1999). The fast development of these devices motivated the study of the fluid flow in MEMS (Arkilic *et al.*, 1997). MEMS are often operated in gaseous environments where the molecular mean free path of the gas molecules could be the same order as the typical geometric dimension of the device. Hence the dynamics associated with MEMS can exhibit rarefied phenomena and compressibility effects (Arkilic *et al.*, 1997). Usually the Knudsen number *Kn* is used to identify the effects. *Kn* is the ratio of the mean free path λ to the characteristic length *L*. Generally speaking, the continuum assumption for Navier–Stokes (NS) equations may break down if $Kn>0.01$. For a flow case $0.01<Kn<0.1$, a slip velocity would appear in the wall boundary. The value of $0.1\leqslant Kn<10$ are associated with a transition flow regime. In the slip-flow regime, by introducing a slip velocity at the solid boundary the NS solver can still be used. In the transition regime the conventional flow solver based on the NS equations is no longer applicable because the rarefaction effect is critical (Lim *et al.*, 2002).

Many analytical studies of rarefied flow in microchannel have been carried out since the 1970's. An important analytical and experimental study for gaseous flow in two-dimensional (2D) microchannels was carried out by Arkilic *et al.* (1997). Through a formal perturbation expansion of the NS equations under an

assumption of 2D isothermal flow, the study demonstrates the relative significance of the contribution of compressibility and rarefied effects and good agreements between the analytical and experimental studies were observed.

There are also some analytical studies about rarefied flow in circular microtubes. Analytical studies of Prud'homme *et al*. (1986) and van den Berg *et al*. (1993) demonstrated nonconstant pressure gradients but their analysis did not incorporate rarefied behavior and the analysis is only one-dimensional (1-D) perturbation solution of the NS equations. Based on the assumption of isothermal flow, Weng *et al*. (1999) obtained the analytical solution for rarefied gas flow in long circular microtubes. Some experiments were also carried out to measure the friction constant $C=f*Re$ in microtubes, which is not equal to 64 as the theoretical prediction for fully developed incompressible flow (Chio *et al*., 1991; Yu *et al*., 1995).

In addition to the above analytical and experimental investigations, there are many numerical studies on rarefied gas behavior in microchannels. Through introducing a slip velocity at the solid boundary, Beskok and Karniadakis (1993) presented numerical solutions of the Navier–Stokes and energy equations for flows with slight rarefaction. For simulations of microflow, the direct simulation Monte Carlo method (DSMC) (Bird 1994) are more popular because the approach is valid for the full range of flow regimes (continuum through free molecular). However, very large computational effort is required in the DSMC simulations since the total number of simulated particles is directly related to the number of molecules.

Besides numerical solution of Navier–Stokes Equation and DSMC, the lattice Boltzmann method (LBM), which based on meso-scale level and has no

continuum assumption, was also applied to simulate the microflows (Lim *et al*., 2002; Nie *et al*., 2002).

Previous LBM study of microflow is only concentrated in microchannel. Here we would like to extend LBM to simulate axisymmetric flows in microtubes.

1.4 Objectives and Significance of the Study

The main aim of this study was to suggest a general method to derive D2Q9 axisymmetric lattice Boltzmann models and apply these models to study the axisymmetric fluid flows. Developing D3Q19 incompressible isothermal and thermal LBM to study the 3D flows with complex geometries is also one of our aims. The more specific aims were:

1) To suggest a general method to derivate D2Q9 models by inserting proper source terms into the lattice Boltzmann equation (LBE). An axisymmetric boundary condition is also proposed to simulate the axisymmetric flows more efficiently.

2) To apply our axisymmetric model and 3D incompressible model in study of blood flows through stenosed and elastic vascular tubes. The moving boundary condition for the flow through an elastic tube was tested. Blood flows through 3D asymmetric tube were also investigated.

3) To apply a new axisymmetric D2Q9 model considering the swirling effect and buoyancy force to investigate melt flows in Czochralski crystal growth.

4) To develop an axisymmetric D2Q9 model for simulation of gas slip flow in microtubes. The gas slip flows in long microtubes with the outlet Knudsen number $0.01<Kn<0.1$ were investigated in detail.

5) To propose a robust thermal curved wall boundary treatment to solve 2D

and 3D heat and fluid flow problems.

Theoretically, our axisymmetric D2Q9 model should further improve the accuracy and efficiency of LBM application in study of axisymmetric flows. Our numerical model could be applied to predict hemodynamic flows and axisymmetric flows in engineering.

However, the above flow phenomena are actually very complex, it is not possible to consider all the factors in the numerical studies. There are some assumptions made in our study.

Firstly, the Blood flow, Taylor-Couette flow and the melt flow in Czochralski crystal growth are all assumed incompressible flow since the Mach number in our studies are usually much less than 0.3.

Secondly, the blood is assumed Newtonian fluid since the blood usually behaves as a Newtonian fluid in large arteries, especially at moderate to high shear rates (Ku, 1997).

To provide the basis for our LBM study, we will present the basic knowledge about LBM in Chapter 2 and the general method to derivate axisymmetric D2Q9 models in detail in Chapter 3.

1.5 Outline of Thesis

In Chapter 2, the basic knowledge of lattice Boltzmann methods are introduced. The derivation and theory of the classical Boltzmann equation are discussed. A brief derivation from LBM to Navier-Stokes equation is also given.

In Chapter 3, a general method to derivate D2Q9 axisymmetric models was suggested and three different models were proposed to simulate axisymmetric flows. The theoretical difference between our model and the previous models was

analyzed. Axisymmetric boundary conditions were presented. An incompressible isothermal and thermal 3D LBM was also presented.

In Chapter 4, our axisymmetric D2Q9 models were evaluated. The spatial accuracies of the axisymmetric D2Q9 models with difference boundary conditions were compared in detail. The LBM's compressibility effect was investigated in detail. The effects of Reynolds number and Womersley number on pulsatile flows in straight tube were also investigated. Then the accuracy and efficiency of 3D multi-block LBM solver were tested.

In Chapter 5, the steady and unsteady blood flows through axisymmetric and 3D asymmetric stenosed vascular tubes were studied. The viscous flows in large distensible blood vessels were also investigated. The moving boundary conditions in flows through compliant tubes were tested.

In Chapter 6, the axisymmetric swirling flows would be solved by a hybrid scheme. The axial and radial velocities were solved by LBM and swirl velocity and temperature were solved by finite difference method. This hybrid scheme was firstly validated by simulation of Taylor-Couette flows between two concentric cylinders. Then the melt flows in Czochralski crystal growth were studied in detail.

In Chapter 7, a slightly compressible axisymmetric D2Q9 model was presented and applied to simulate the gas slip flow in microtubes. The gas slip flows in long microtubes with the outlet Knudsen number $0.01<Kn<0.1$ were investigated in detail. The efficiency of LBM was compared with the DSMC method with is more common in micro-flow simulations.

In Chapter 8, a recent curved non-slip wall boundary treatment for isothermal lattice Boltzmann equation (Guo et al. 2002a) is extended to handle the thermal

curved wall boundary. After the thermal boundary condition was validated, the natural convection in a square cavity, and the natural convection in a concentric annulus between an outer square cylinder and an inner circular cylinder were studied. 3D heat and fluid flows were also studied using this thermal curved wall boundary treatment.

Chapter 2 Lattice Boltzmann Method

In this chapter we focus our attention on the formulation of lattice Boltzmann equation (LBE) and the boundary conditions used in the present LBM simulations.

2.1 Introduction

The lattice Boltzmann method (LBM) is the successor of the lattice gas cellular automata (LGCA). Consequently, the LBM retains the advantages of LGCA (e.g., simplicity, locality and parallelism). On the other hand, LBM also get rid of the drawbacks such as statistical noise and lack of Galilean invariance (Qian et al., 1992) through modeling lattice gas with Boltzmann equation (Higuera et al., 1989, McNamara et al., 1988).

The LBM can be regarded as a discrete, fictitious molecular dynamics numerical method in mesoscopic scale. In LBM, fluid particles which be regarded as a large group of molecules occupy the nodes of a regular lattice. During each time step, they propagate to the neighboring lattice sites according to a certain regular lattice velocity model and then undergo a collision. The collision follows very simple kinetic rules. The streaming (i.e., propagation) and collision steps can conserve mass, momentum and energy.

The above two steps are illustrated in Figure 2.1. In the figure we can see that the density distribution function represented by vectors propagate along their directions of motion to the center lattice node “A”. Then in the collision step, the incoming distribution function value changes to a new outgoing value according to the relax collision rule.

2.2 Continuum Boltzmann Equation and Bhatnagar-Gross-Krook Approximation

Although the development of LBM for simulation of fluid dynamics was original from LGCA and independent of the continuum Boltzmann equation, later, it has been argued that the LBM can be derived from the continuum Boltzmann equation with a BGK collision model (He and Luo, 1997b, 1997c). To better understand LBM, the continuum Boltzmann equation would be introduced here briefly.

The Boltzmann equation is a useful mathematical model to describe a fluid at microscopic level. The classical Boltzmann equation is an integro-differential equation for the single particle distribution function $f(\mathbf{x},\mathbf{c},t)$, which may be written as

$$\frac{\partial f}{\partial t}+\mathbf{c}\frac{\partial f}{\partial \mathbf{r}}+\mathbf{F}\frac{\partial f}{\partial \mathbf{c}}=Q(f,f), \tag{2.1}$$

where **x** is position in space, **c** is particle velocity and **F** is the body force. $Q(f,f)$ is the collision integral describing the two-particle collision and can be written as

$$Q(f,f)=\int d^3\mathbf{c}_2\int d\Omega\sigma(\Omega)|\mathbf{c}_1-\mathbf{c}_2|[f(\mathbf{c}_1')f(\mathbf{c}_2')-f(\mathbf{c}_1)f(\mathbf{c}_2)]. \tag{2.2}$$

$\sigma(\Omega)$ is the differential collision cross section for the two particle collision which transforms the velocities from {$\mathbf{c}_1$,$\mathbf{c}_2$} (incoming) into { $\mathbf{c}_1$',$\mathbf{c}_2$'} (outgoing).

The notion of local equilibrium is important for recovering the hydrodynamic behavior from the continuum Boltzmann equation. Mathematically, this requires that the collision term is annihilated (i.e., $Q(f,f)=0$) . It can be further shown (see, for example, Cercignani, 1988) that positive functions f exist which give $Q(f,f)=0$.

These equilibrium distribution functions are all of the form

$$f^{eq}(\mathbf{c}) = \exp\left(A + \mathbf{B}\mathbf{c} + C\mathbf{c}^2/2\right), \tag{2.3}$$

where A, $\mathbf{B}$ and C are Lagrangian parameters carrying the functional dependence on the conjugate hydrodynamic fields ρ, $\mathbf{u}$, e (internal energy). The Maxwell distribution function can be written as

$$f^{eq}(\mathbf{x},\mathbf{c},t) = \rho(2\pi RT)^{-\frac{D}{2}} \exp\left[-\frac{(\mathbf{c}-\mathbf{u})^2}{2RT}\right]. \tag{2.4}$$

To solve the Boltzmann equation analytically or numerically, the complicated collision integral $Q(f,f)$ is often replaced by a simpler expression. The most widely known replacement is called the Bhatnagar-Gross-Krook (BGK) approximation (Bhatnagar, Gross and Krook, 1954)

$$Q_{BGK}(f,f) = -\frac{f - f^{eq}}{\lambda}, \tag{2.5}$$

where λ is a typical relaxation time associated with collision relaxation to the local equilibrium.

In principle, the relaxation time λ is a complicated function of the distribution function f. The BGK approximation is intended to lump the whole spectrum of relaxation scales into a single constant value.

2.3 Formulation of the Lattice Boltzmann Method

2.3.1 Lattice Boltzmann Equation

The LBE with BGK models can be written as

$$f_i(\mathbf{x} + \mathbf{e}_i\delta_t, t + \delta_t) = f_i(\mathbf{x},t) - \frac{1}{\tau}\left(f_i(\mathbf{x},t) - f_i^{eq}(\mathbf{x},t)\right) \quad (i=0,1,\ldots N), \tag{2.6}$$

where $f_i(\mathbf{x},t)$ is the density distribution function, which depend on the position $\mathbf{x}$

and time t. $f_i^{eq}(\mathbf{x},t)$ is the corresponding equilibrium state which is depend on the local density ρ and velocity $\mathbf{u}$. τ is the single dimensionless relation time constant which is related with the hydrodynamic viscosity by $\nu = c_s^2\delta_t(\tau - 0.5)$. δ_t is the time step and c_s is the sound speed. N is the number of discrete velocity.

The above LBE (2.2) can be implemented by two steps, namely, collision and streaming. In the collision step

$$f_i^{ne} = f_i(\mathbf{x},t) - f_i^{eq}(\mathbf{x},t), \tag{2.7}$$

$$f_i^{+}(\mathbf{x},t) = f_i^{eq}(\mathbf{x},t) + (1-\frac{1}{\tau})f_i^{ne}, \tag{2.8}$$

where f_i^{ne} is the non-equilibrium distribution function and $f_i^{+}(\mathbf{x},t)$ is the post-collision distribution function.

In the streaming step, the post-collision distribution function would propagate to the neighbouring lattice nodes as illustrated by Eq. (2.9)

$$f_i(\mathbf{x} + \mathbf{e}_i\delta_t, t + \delta_t) = f_i^{+}(\mathbf{x},t). \tag{2.9}$$

The macroscopic density ρ and momentum density ρu_α are defined as momentum of distribution function f_i

$$\rho = \sum_{i=0}^{N} f_i \quad , \qquad \rho u_\alpha = \sum_{i=0}^{N} e_{i\alpha} f_i \quad . \tag{2.10}$$

The equation of state is defined as

$$p = \rho c_s^2, \tag{2.11}$$

where p is the pressure.

2.3.2 From the Continuum Boltzmann Equation to LBE

Although the above LBE originated from the LGCA independently of the Boltzmann equation, we next show how the LBE can be derived from the

continuum Boltzmann equation with a BGK collision model (He and Luo, 1997b, 1997c).

The Boltzmann equation (2.1) with BGK approximation (2.5) can be written as

$$\frac{\partial f(\mathbf{x},\mathbf{c},t)}{\partial t}+\mathbf{c}\frac{\partial f(\mathbf{x},\mathbf{c},t)}{\partial \mathbf{r}}=-\frac{1}{\lambda}\left(f(\mathbf{x},\mathbf{c},t)-f^{eq}(\mathbf{x},\mathbf{c},t)\right). \tag{2.12}$$

The velocity space of $\mathbf{c}$ can be discretized by introducing a finite set of velocities $\mathbf{e}_i$. In the discrete velocity space, the Boltzmann equation becomes

$$\frac{\partial f_i(\mathbf{x},t)}{\partial t}+\mathbf{e}_i\frac{\partial f_i(\mathbf{x},t)}{\partial \mathbf{r}}=-\frac{1}{\lambda}\left(f_i(\mathbf{x},t)-f_i^{eq}(\mathbf{x},t)\right),\quad (i=0,1,\ldots N), \tag{2.13}$$

where i indicate the different velocity direction and N is number of different velocities in the model. Integrating Eq. (2.13) from t to $t+\delta t$, with the second order of accuracy gives

$$f_i(\mathbf{x}+\mathbf{e}_i\delta_t,t+\delta_t)=f_i(\mathbf{x},t)-\frac{\delta_t}{\lambda}\left(f_i(\mathbf{x},t)-f_i^{eq}(\mathbf{x},t)\right). \tag{2.14}$$

With $\tau=\lambda/\delta_t$, Eq. (2.14) is identical with Eq. (2.6).

2.3.3 Equilibrium Distribution

The equilibrium distribution function $f_i^{eq}(\mathbf{x},t)$ in the LBE Eq. (2.6) or (2.14) is obtained by expanding the Maxwell-Boltzmann distribution function (i.e., Eq. (2.4)) in Taylor series of $\mathbf{u}$ up to second-order.

$$\begin{aligned} f^{eq}(\mathbf{x},\mathbf{c},t)&=\rho(2\pi RT)^{-\frac{D}{2}}\exp\left[-\frac{(\mathbf{c}-\mathbf{u})^2}{2RT}\right]\\ &=\rho(2\pi RT)^{-\frac{D}{2}}\exp\left[-\frac{\mathbf{c}^2}{2RT}\right]\exp\left[\frac{2\mathbf{c}\cdot\mathbf{u}-\mathbf{u}^2}{2RT}\right]\\ &=\rho(2\pi RT)^{-\frac{D}{2}}\exp\left[-\frac{\mathbf{c}^2}{2RT}\right]\left(1+\frac{\mathbf{c}\cdot\mathbf{u}}{RT}+\frac{(\mathbf{c}\cdot\mathbf{u})^2}{2(RT)^2}-\frac{\mathbf{u}^2}{2RT}\right)+O(\mathbf{u}^3) \end{aligned} \tag{2.15}$$

Rewriting Eq. (2.15) in velocity space $\{\mathbf{e}_i\}$ and noting that $c_s^2=RT$ from Eq. (2.11), we can obtain $f_i^{eq}(\mathbf{x},\mathbf{e}_i, t)$ in the LBE as

$$f_i^{eq}(\mathbf{x},\mathbf{e}_i,t)=E_i(\rho,\mathbf{u})=\omega_i\rho\left[1+\frac{\mathbf{e}_i\cdot\mathbf{u}}{c_s^2}+\frac{(\mathbf{e}_i\cdot\mathbf{u})^2}{2c_s^4}-\frac{\mathbf{u}^2}{2c_s^2}\right] \quad (i=0,1,\ldots N), \tag{2.16}$$

where $\omega_i=(2\pi RT)^{-\frac{D}{2}}\exp\left[-\frac{\mathbf{e}_i^2}{2RT}\right]$ is a weighting factor.

2.3.4 Discrete Velocity Models

The discrete velocity model is usually written as D*n*Q*m*, where *n* is the space dimension and *m* is the number of velocities. The popular 2D and 3D discrete velocity models are D2Q9, D2Q7, D3Q19 and D3Q15, which are shown in Figure 2.2.

Then we would like to go back to the weighting factors ω_i. They are chosen so as to ensure the mass and momentum conservation as well as the isotropy of lattice tensor (i.e., lattice tensor is invariant with respect to arbitrary orthogonal transformations) (Wolf-Gladrow, 2000). A lattice tensor of rank *n* is defined as

$$L_{\alpha_1\alpha_1\ldots\alpha_n}=\sum_i e_{i\alpha_1}e_{i\alpha_2}\ldots e_{i\alpha_n}\ . \tag{2.17}$$

Jeffreys (1965) has proved that the isotropic tensor of rank 2 should be proportional to $\delta_{\alpha\beta}$ and an isotropic tensor of rank 3 should be proportional to $\delta_{\alpha\beta\gamma}$. The lattice tensors with odd rank vanish due to the symmetry of the lattice. If the lattice tensor of rank *n* is non-isotropic, weights ω_i should be chosen to make the generalized lattice tensor (i.e., Eq. (2.18)) isotropic.

$$G_{\alpha_1\alpha_1\ldots\alpha_n}=\sum_i \omega_i e_{i\alpha_1}e_{i\alpha_2}\ldots e_{i\alpha_n}\ . \tag{2.18}$$

Here we give an example of how to determine the weighting factors ω_i for

D2Q9 model. The D2Q9 velocity model can also be written as Eq. (2.19).

$$\mathbf{e}_i = \begin{cases} (0,0) & i = 0 \\ (\cos[(i-1)\pi/2], \sin[(i-1)\pi/2])c & i = 1,2,3,4 \\ \sqrt{2}(\cos[(i-5)\pi/2+\pi/4], \sin[(i-5)\pi/2+\pi/4])c & i = 5,6,7,8 \end{cases}, \quad (2.19)$$

where $c \equiv \delta_x/\delta_t$ is the unit speed, and δ_x and δ_t are the lattice constant and time step, respectively.

Due to symmetry, the ω_i for directions with identical speeds are equal. Consequently, for D2Q9 model, there are only 3 weighting factor to be determined (i.e., W_0, W_1 and W_2).

$$\omega_i = \begin{cases} W_0 & i = 0 \\ W_1 & i = 1,2,3,4 \\ W_2 & i = 5,6,7,8 \end{cases}. \quad (2.20)$$

Due to the non-isotropy of lattice tensor of rank 4 in D2Q9 model, W_2 is chosen as $4W_1$ to make the generalized lattice tensor isotropic. (Wolf-Gladrow, 2000). When determining the weighting factor, besides the requirement of isotropy of lattice tensor, the weighting factor should ensure the mass and momentum conservation. That is

$$\rho = \sum_{i=0}^{8} f_i^{eq} \quad , \quad \rho u_\alpha = \sum_{i=0}^{8} e_{i\alpha} f_i^{eq} \, . \quad (2.21)$$

Substituting the Eq. (2.16) into the Eq. (2.21), it gives

$$\sum_{i=0}^{8} \omega_i = 1 \quad \text{and} \quad \sum_{i=0}^{8} \omega_i e_{i\alpha} e_{i\beta} = c_s^2 \delta_{\alpha\beta} \, . \quad (2.22)$$

Hence,

$$W_0 + 4W_1 + 4W_2 = 1 \quad \text{and} \quad 2W_1 + 4W_2 = c_s^2/c^2 \, . \quad (2.23)$$

With $W_1 = 4W_2$ and $c_s^2 = c^2/3$ (Wolf-Gladrow, 2000), the weighting factors for D2Q9 model are obtained as $W_0 = 4/9$, $W_1 = 1/9$ and $W_2 = 1/36$.

The main parameters of popular 2D and 3D velocity models are listed in Table 2.1.

2.4 From LBE to the Navier-Stokes Equation

To show that the standard LBE can be used to describe fluids, here the 2D Navier-Stokes equations are derived by Chapman-Enskog expansion which is a multi-scale analysis developed by Chapman and Enskog between 1910 and 1920. The Chapman-Enskog expansion here relies on the Knudsen number *Kn*, which is the ratio of the molecular mean free path λ to the characteristic macroscopic length *L*. To treat the fluid as a continuous system, the Knudsen number should be much less than one.

Theoretically, the LBE simulates the compressible NS equation rather than the incompressible one since the spatial density variation is not zero in simulations. Only with the Mach number $M<<1$, can the LBE recover the incompressible NS equation.

For incompressible flow, the continuity equation and NS momentum equations in the Cartesian coordinates (x,y) can be written as (White, 1991)

$$\partial_\beta u_\beta = 0, \tag{2.24}$$

$$\partial_t u_\alpha + \partial_\beta \left(u_\beta u_\alpha\right) + \frac{1}{\rho}\partial_\alpha p - \nu\partial_\beta\left(\partial_\alpha u_\beta + \partial_\beta u_\alpha\right) = 0. \tag{2.25}$$

It is noticed that the Einstein summation convention is used here. u_α, u_β are the velocity u_x or u_y and α, β means x or y. ν in Eq.(2.25) is the kinematic viscosity related to the dynamic viscosity by $\nu=\mu/\rho$.

In the following, we would show how Eq. (2.24) and (2.25) can be recoved from LBE using multi-scale analysis. In the derivation, the D2Q9 model is used

with c=1.

Initially, we adopt the following expansions (He and Luo, 1997a),

$$f_i(x+e_{ix}, y+e_{iy}, t+1) = \sum_{n=0}^{\infty} \frac{\varepsilon^n}{n!} D^n f_i(x, y, t), \tag{2.26}$$

$$\begin{cases} f_i = f_i^{(0)} + \varepsilon f_i^{(1)} + \varepsilon^2 f_i^{(2)} + \ldots \\ \partial_t = \varepsilon \partial_{1t} + \varepsilon^2 \partial_{2t} + \ldots \\ \partial_\beta = \varepsilon \partial_{1\beta} \end{cases}, \tag{2.27}$$

where $\varepsilon=\delta_t$ and $D \equiv \left(\partial_t + \mathbf{e}_\beta \cdot \partial_\beta\right)$, β=x,y.

Retaining terms up to $O(\varepsilon^2)$ in Eqs. (2.26) and (2.27) and substituting into LBE Eq. (2.6) results in the following equations:

$$O(\varepsilon^0): \ \left(f_i^{(0)} - f_i^{eq}\right)/\tau = 0, \tag{2.28}$$

$$O(\varepsilon^1): \ \left(\partial_{1t} + e_{i\beta}\partial_{1\beta}\right) f_i^{(0)} + f_i^{(1)}/\tau = 0, \tag{2.29}$$

$$O(\varepsilon^2): \ \partial_{2t} f_i^{(0)} + \left(1 - \frac{1}{2\tau}\right)\left(\partial_{1t} + e_{i\beta}\partial_{1\beta}\right) f_i^{(1)} + \frac{1}{\tau} f_i^{(2)} = 0. \tag{2.30}$$

The distribution function f_i is constrained by the following relationships:

$$\sum_{i=0}^{8} f_i^{(0)} = \rho \quad , \quad \sum_{i=0}^{8} e_{i\alpha} f_i^{(0)} = \rho u_\alpha, \tag{2.31}$$

$$\sum_{i=0}^{8} f_i^{(m)} = 0 \quad , \quad \sum_{i=0}^{8} \mathbf{e}_i f_i^{(m)} = 0 \qquad \text{for } m>0. \tag{2.32}$$

Note that the general lattice tensors $G^{(n)}$ (Eq. (2.18)) for D2Q9 model are

$$G_{\alpha\beta} = \sum_{i=0}^{8} \omega_i e_{i\alpha} e_{i\beta} = c_s^2 \delta_{\alpha\beta}, \tag{2.33}$$

$$G_{\alpha\beta\gamma\zeta} = \sum_{i=0}^{8} \omega_i e_{i\alpha} e_{i\beta} e_{i\gamma} e_{i\zeta} = c_s^4 \Delta_{\alpha\beta\gamma\zeta}, \tag{2.34}$$

where $\delta_{\alpha\beta}$ is the Kronecker tensors, and

$$\Delta_{\alpha\beta\gamma\zeta} = \delta_{\alpha\beta}\delta_{\gamma\zeta} + \delta_{\alpha\gamma}\delta_{\beta\zeta} + \delta_{\alpha\zeta}\delta_{\beta\gamma} \ . \tag{2.35}$$

All the general lattice tensors with odd rank vanish due to the symmetry of the lattice.

With the above properties of the tensor $G^{(n)}$, we have

$$\sum_{i=0}^{8} e_{i\alpha}e_{i\beta}f_i^{(0)} = \rho u_\alpha u_\beta + c_s^2\rho\delta_{\alpha\beta}, \tag{2.36}$$

$$\sum_{i=0}^{8} e_{i\alpha}e_{i\beta}e_{ik}f_i^{(0)} = \rho c_s^2\left(\delta_{jk}\delta_{\beta\alpha} + \delta_{j\alpha}\delta_{\beta k} + \delta_{j\beta}\delta_{\alpha k}\right)u_j. \tag{2.37}$$

2.4.1 Mass Conservation

Summing on i in Eq. (2.29), we obtain at $O(\varepsilon)$

$$\partial_{1t}\rho + \partial_\beta\left(\rho u_\beta\right) = 0. \tag{2.38}$$

Then we proceed to $O(\varepsilon^2)$ now. Summing on i in Eq. (2.30) gives

$$\partial_{2t}\rho = 0. \tag{2.39}$$

Combining Eq. (2.38) and Eq. (2.39) lead to the continuum equation

$$\partial_t\rho + \partial_\beta\left(\rho u_\beta\right) = 0. \tag{2.40}$$

2.4.2 Momentum Conservation

Multiplying Eq. (2.29) by $e_{i\alpha}$ and summing on i, gives

$$\partial_{1t}\rho u_\alpha + \partial_{1\beta}\Pi^0_{\alpha\beta} = 0, \tag{2.41}$$

where, $\Pi^0_{\alpha\beta} = \sum_{i=0}^{8} e_{i\alpha}e_{i\beta}f_i^{(0)}$ is the zeroth-order momentum flux tensor. With $\Pi^0_{\alpha\beta}$ given by Eq. (2.36), Eq. (2.41) gives

$$\partial_{1t}\rho u_\alpha + \partial_{1\beta}\left(c_s^2\rho\delta_{\alpha\beta} + \rho u_\beta u_\alpha\right) = 0. \tag{2.42}$$

Multiplying Eq. (2.30) with $e_{i\alpha}$ and summing over i gives,

$$\partial_{2t}\rho u_\alpha + \left(1-\frac{1}{2\tau}\right)\partial_{1\beta}\Pi^{(1)}_{\alpha\beta} = 0\,, \tag{2.43}$$

where, $\Pi^{(1)}_{\alpha\beta} = \sum_i e_{i\alpha}e_{i\beta}f_i^{(1)}$ is the first-order momentum flux tensor. With the aid of Eqs. (2.29) and (2.37), we have

$$\begin{aligned}
\Pi^{(1)}_{\alpha\beta} &= \sum_i e_{i\alpha}e_{i\beta}f_i^{(1)} = -\tau\sum_i e_{i\alpha}e_{i\beta}D_{1t}f_i^{(0)} \\
&= -\tau\left[\partial_{1t}\Pi^{(0)}_{\alpha\beta} + \partial_k\left(\sum_i e_{i\alpha}e_{i\beta}e_{ik}f_i^{(0)}\right)\right] \\
&= -\tau\left[\partial_{1t}\Pi^{(0)}_{\alpha\beta} + c_s^2\left(\delta_{\alpha\beta}\partial_j\rho u_j + \partial_\beta\rho u_\alpha + \partial_\alpha\rho u_\beta\right)\right]
\end{aligned}. \tag{2.44}$$

For the term $\partial_{1t}\Pi^{(0)}_{\alpha\beta}$ in Eq. (2.44), using Eqs. (2.38) and (2.42), it can be written as

$$\begin{aligned}
\partial_{1t}\Pi^{(0)}_{\alpha\beta} &= c_s^2\delta_{\alpha\beta}\partial_{1t}\rho + u_\alpha\partial_{1t}\left(\rho u_\beta\right) + u_\beta\partial_{1t}\left(\rho u_\alpha\right) - u_\alpha u_\beta\partial_{1t}\rho \\
&= c_s^2\delta_{\alpha\beta}\partial_{1t}\rho - u_\alpha\left[c_s^2\partial_\beta\rho + \partial_\gamma\left(\rho u_\beta u_\gamma\right)\right] - u_\beta\left[c_s^2\partial_\alpha\rho + \partial_\gamma\left(\rho u_\alpha u_\gamma\right)\right] - u_\alpha u_\beta\partial_{1t}\rho\,. \\
&= c_s^2\delta_{\alpha\beta}\left(-\partial_\gamma\rho u_\gamma\right) - c_s^2\left(u_\alpha\partial_\beta\rho + u_\beta\partial_\alpha\rho\right) + O\left(u^3\right)
\end{aligned} \tag{2.45}$$

The terms of $O(u^3)$ can be neglected. The term $c_s^2\left(\delta_{\alpha\beta}\partial_j\rho u_j + \partial_\beta\rho u_\alpha + \partial_\alpha\rho u_\beta\right)$ in Eq. (2.44) can also be written as

$$\begin{aligned}
&c_s^2\left(\delta_{\alpha\beta}\partial_j\rho u_j + \partial_\beta\rho u_\alpha + \partial_\alpha\rho u_\beta\right) \\
&= c_s^2\delta_{\alpha\beta}\left(\partial_j\rho u_j\right) + c_s^2\left(u_\alpha\partial_\beta\rho + u_\beta\partial_\alpha\rho\right) + \rho c_s^2\left(\partial_\beta u_\alpha + \partial_\alpha u_\beta\right)
\end{aligned}. \tag{2.46}$$

With Eqs. (2.45) and (2.46), the Eq. (2.43) can be written as

$$\partial_{2t}\rho u_\alpha + \left(1-\frac{1}{2\tau}\right)\partial_{1\beta}\left[\rho c_s^2\left(\partial_\beta u_\alpha + \partial_\alpha u_\beta\right)\right] = 0\,. \tag{2.47}$$

With kinematic viscosity $\nu = c_s^2(\tau - 0.5)$ and Eqs. (2.42) and (2.47), the NS momentum equation can be recovered as

$$\partial_t\rho u_\alpha + \partial_\beta\left(\rho u_\beta u_\alpha\right) + \partial_\alpha p - \nu\partial_\beta\left[\rho\left(\partial_\alpha u_\beta + \partial_\beta u_\alpha\right)\right] = 0\,. \tag{2.48}$$

The density variation can be neglected in the flow with small Mach number. Consequently, the Eqs. (2.40) and (2.48) can recover the incompressible NS

equation (2.24) and (2.25).

2.5 Incompressible LBM

As illustrated in above section, if the density fluctuation can be neglected, the incompressible Navier-Stokes equation can be recovered from a LBE through the Chapman-Enskog procedure. However, in LBM, the density may fluctuate to a great extent in flows with large pressure gradient because the pressure and density variations satisfy the equation of states of an isothermal gas given by $\Delta p=c_s^2\Delta\rho$, where c_s^2 is a constant. In many previous studies (Hou et al., 1995, Artoli et al., 2002), the compressibility effect of standard lattice BGK (LBGK) model has been highlighted.

Some incompressible models were proposed to eliminate the compressibility effect of the standard LBGK model (He and Luo, 1997a, Guo et al. 2000). One of the most successful incompressible LBGK model was proposed by He and Luo in 1997. The incompressible LBGK model was validated by steady plane Poiseuille flow and the unsteady 2D womersley flow. In their model, the compressibility effect of the order $o(M^2)$ is explicitly eliminated (He and Luo, 1997a).

It is noticed that the main difference between the incompressible LBM and the standard LBM is the form of equilibrium distribution function (He and Luo, 1997a). Through substituting $\rho = \rho_0+\delta\rho$ into the equilibrium distribution function (i.e., Eq. (2.16)) and neglecting the terms proportional to $\delta\rho(\mathbf{u}/c)$, *and* $\delta\rho(\mathbf{u}/c)^2$, a new equilibrium distribution function is proposed as (He and Luo, 1997a)

$$f_i^{eq}(\mathbf{x},\mathbf{e}_i,t)=\omega_i\left\{\rho+\rho_0\left[\frac{\mathbf{e}_i\cdot\mathbf{u}}{c_s^2}+\frac{(\mathbf{e}_i\cdot\mathbf{u})^2}{2c_s^4}-\frac{\mathbf{u}^2}{2c_s^2}\right]\right\} \qquad (i=0,1,2\ldots,N). \quad (2.49)$$

In the incompressible model, besides the limit of $M<<1$, for unsteady flow, an

additional condition $T>>L/c$ must be satisfied, where T is the time scale of temporal variation and L is the characteristic length.

2.6 Thermal LBE

After obtaining the athermal LBE, we would like to obtain the thermal LBE models which can be used to simulate heat transfer phenomena. In general, the present thermal lattice Boltzmann models can be classified into three categories: the multispeed approach (McNamara et al., 1993), the passive-scalar approach, and the double-population approach. In the multispeed approach (McNamara et al., 1993), the internal energy term is incorporated with a density distribution function so that only the density distribution function is needed, however, these multi-speed models suffer severe numerical instability, and the temperature variation is limited to a narrow range (He et al., 1998). To enhance numerical stability, a separate distribution function which is independent of the density distribution is proposed in the passive-scalar thermal LBE model (Shan, 1997). However, the viscous heat dissipation and compression work done by the pressure cannot be taken into account (He et al., 1998). In the third approach (He et al., 1998), the temperature field is obtained through an independent internal energy density distribution function. The model has better numerical stability and the viscous heat dissipation and compression work done by the pressure can be solved fundamentally.

In our study, the double-population TLBE derived by He *et al.*(1998) is used. The two discrete evolution equations in the TLBE are illustrated as following

$$\begin{aligned}&\overline{f_i}(\mathbf{x}+\mathbf{e}_i\delta_t,t+\delta_t)-\overline{f_i}(\mathbf{x},t)\\&=-\frac{\delta_t}{\tau_f+0.5\delta_t}\left[\overline{f_i}(\mathbf{x},t)-f_i^{eq}(\mathbf{x},t)\right]+\frac{\tau_f\delta_t}{\tau_f+0.5\delta_t}F_i,\end{aligned}\tag{2.50}$$

$$\begin{aligned}&\overline{g_i}(\mathbf{x}+\mathbf{e}_i\delta_t,t+\delta_t)-\overline{g_i}(\mathbf{x},t)\\&=-\frac{\delta_t}{\tau_g+0.5\delta_t}\left[\overline{g_i}(\mathbf{x},t)-g_i^{eq}(\mathbf{x},t)\right]-\frac{\tau_g\delta_t}{\tau_g+0.5\delta_t}f_i(\mathbf{x},t)q_i,\end{aligned}\tag{2.51}$$

where, the new variables $\overline{f}$ and $\overline{g}$ are defined as

$$\overline{f_i}=f_i+\frac{0.5\delta_t}{\tau_f}\left(f_i-f_i^{eq}\right)-\frac{\delta_t}{2}F_i\quad,\tag{2.52}$$

$$\overline{g_i}=g_i+\frac{0.5\delta_t}{\tau_g}\left(g_i-g_i^{eq}\right)+\frac{\delta_t}{2}f_iq_i,\tag{2.53}$$

$$F_i=\frac{\mathbf{G}(\mathbf{e}_i-\mathbf{u})}{RT}f_i^{eq},\tag{2.54}$$

$$q_i=(\mathbf{e}_i-\mathbf{u})[\partial\mathbf{u}/\partial t+(\mathbf{e}_i\cdot\nabla)\mathbf{u}].\tag{2.55}$$

$f(\mathbf{x},t)$ and $g(\mathbf{x},t)$ are the density distribution function and the thermal energy density distribution function in position $\mathbf{x}$ at time t respectively. τ_f and τ_g are the momentum and internal energy relax time, respectively. In Eq. (2.54), $\mathbf{G}$ are the external forces acting on unit mass. $\mathbf{e}_i$ is the lattice velocity and i denotes the velocity direction. δ_x, δ_t and are the lattice spacing and time step size. Eq. (2.55) represents the effect of viscous heating and it can be expressed as (D'Orazio et al. 2003)

$$q_i=(\mathbf{e}_i-\mathbf{u})[\mathbf{u}(\mathbf{x}+\mathbf{e}_i\delta t,t+\delta t)-\mathbf{u}(\mathbf{x},t)]/\delta_t\ .\tag{2.56}$$

For the D2Q9 model, the 9 discrete velocities are illustrated in Eq.(2.19). In above expression, $c=\delta_x/\delta_t=\sqrt{3RT_0}$, T_0 is the average temperature.

In Eqs. (2.50) to (2.55), f_i^{eq}, g_i^{eq} are the equilibrium density distribution functions and equilibrium internal energy distribution functions respectively. They are defined as (He et al. 1998),

$$f_i^{eq}(\mathbf{x},t)=\omega_i\rho\left[1+\frac{\mathbf{e}_i\cdot\mathbf{u}}{c_s^2}+\frac{(\mathbf{e}_i\cdot\mathbf{u})^2}{2c_s^4}-\frac{\mathbf{u}^2}{2c_s^2}\right]\quad i=0,1,2\ldots..,8,\tag{2.57}$$

$$g_0^{eq}(\mathbf{x},t) = \omega_i \rho e\left(-\frac{3\mathbf{u}^2}{2c^2}\right), \tag{2.58}$$

$$g_i^{eq}(\mathbf{x},t) = \omega_i \rho e\left[\frac{3}{2} + \frac{3(\mathbf{e}_i \cdot \mathbf{u})}{2c^2} + \frac{9(\mathbf{e}_i \cdot \mathbf{u})^2}{2c^4} - \frac{3\mathbf{u}^2}{2c^2}\right] \quad i=1,2,3,4, \tag{2.59}$$

$$g_i^{eq}(\mathbf{x},t) = \omega_i \rho e\left[3 + \frac{6(\mathbf{e}_i \cdot \mathbf{u})}{c^2} + \frac{9(\mathbf{e}_i \cdot \mathbf{u})^2}{2c^4} - \frac{3\mathbf{u}^2}{2c^2}\right] \quad i=5,6,7,8, \tag{2.60}$$

where $c_s = c/\sqrt{3}$, ω_0=4/9 , ω_i =1/9, (i=1,2,3,4) , ω_i =1/36, (i=5,6,7,8). The internal energy density is $\rho e = \rho RT$ for two-dimensional problems.

Finally, the macroscopic density ρ and momentum $\rho\mathbf{u}$, internal energy per unit mass e, heat flux $\mathbf{q}$, which is a vector different from q_i in Eq. (2.53) or (2.55), kinetic viscosity ν and thermal diffusivity α are obtained by (He et al., 1998; D'Orazio et al., 2003)

$$\rho = \sum_{i=0}^{8} \overline{f}_i , \qquad \rho\mathbf{u} = \sum_{i=0}^{8} \overline{f}_i \mathbf{e}_i + \frac{\rho \mathbf{G} \delta_t}{2}, \tag{2.61}$$

$$\rho e = \sum_{i=0}^{8} \overline{g}_i - \frac{\delta_t}{2} \sum_i f_i q_i , \tag{2.62}$$

$$\mathbf{q} = \left(\sum_{i=0}^{8} \mathbf{e}_i \overline{g}_i - \rho e \mathbf{u} - \frac{\delta t}{2} \sum_{i=0}^{8} \mathbf{e}_i f_i q_i \right) \frac{\tau_g}{\tau_g + 0.5\delta_t}, \tag{2.63}$$

where,

$$\nu = \tau_f RT_0 \quad \text{and} \quad \alpha = 2\tau_g RT_0 . \tag{2.64}$$

2.7 Boundary Conditions

Modelling of the boundary condition is very important for the LBM because it would affect the overall accuracy and stability of the method. (Ziegler, 1993; Zou and He, 1997; He and Zou, *et al.*, 1997).

2.7.1 Bounce-back Boundary Condition

The most commonly used non-slip boundary condition in LBM is the bounce back scheme, which originates from the LGCA. To describe the boundary condition, a wall $\partial\Omega$ is specified. For a point $\mathbf{x}$ ($\mathbf{x} \in \partial\Omega$), $\mathbf{n}$ is the inward unit normal vector of the wall. After the streaming step, the unknown distribution functions of $f_i(\mathbf{x},t)$, $\mathbf{e}_i \cdot \mathbf{n} > 0$ can be evaluated by

$$f_i(\mathbf{x},t) = f_j(\mathbf{x},t), \tag{2.65}$$

where $f_j(\mathbf{x},t)$ is the distribution function in $\mathbf{e}_j$ direction, where $\mathbf{e}_i - \mathbf{e}_j = 2\mathbf{e}_i$.

However, the original bounce-back scheme is only of first order in numerical accuracy. Ziegler (1993) noticed that if the wall boundary is placed in the half way between a boundary site and an adjacent non-boundary site, the bounce-back scheme is of second-order.

While for the free-slip boundary condition where no momentum is to be exchanged with the wall along the tangential component, specular reflection scheme can be applied. When use this scheme, after streaming step implemented, the unknown distribution functions of $f_i(\mathbf{x},t)$, $\mathbf{e}_i \cdot \mathbf{n} > 0$ can be evaluated by

$$f_i(\mathbf{x},t) = f_k(\mathbf{x},t), \tag{2.66}$$

and $f_k(\mathbf{x},t)$ is the distribution function in $\mathbf{e}_k$ direction, where $\mathbf{e}_i - \mathbf{e}_k = 2\mathbf{n}$.

The bounce-back, half-way bounce-back and specular reflection scheme are illustrated in Figure 2.3.

2.7.2 Curved Wall Non-slip Boundary Condition

Besides the bounce-back scheme, to handle the wall boundary, Skordos (1993) proposed to use the new equilibrium distribution function which includes velocity

gradients at the wall nodes. Chen et al. (1996) proposed a simple extrapolation scheme. Through the above schemes, the unknown distribution functions that come from the solid are well defined. However, all these boundary conditions are difficult to implement for general geometries because one has to distinguish the distribution functions according to the wall orientation and a special treatment is required for corner nodes.

To handle wall boundary for general geometry, in 1998, an accurate curved wall boundary treatment was proposed by Filippova and Hanel (1998) and later improved by Mei *et al.* (1999). And later Mei *et al.* (2000) extended the 2D curved wall boundary treatment to 3D cases. Guo *et al.* (2002a) also proposed a curved wall boundary treatment based on the idea of Zou and He (1997). However, the most successful one was the treatment proposed by Bouzidi *et al.* (2001). It combined the "bounce back" scheme and spatial second-order interpolation. Mei *et al.* (2002) and Lallemand and Luo (2003) also found that the boundary condition is a simple, robust, efficient and accurate scheme. Here this boundary condition is introduced in detail.

The concept of Bouzidi's curve boundary treatment is very simple. Here, we use a 2D problem to illustrate the idea. In Figure 2.4, q is defined as the fraction of the intersection link in the fluid region: $q=(|\mathbf{x}_f-\mathbf{x}_b|)/(|\mathbf{x}_f-\mathbf{x}_w|)$, where $\mathbf{x}_f$, $\mathbf{x}_b$ and $\mathbf{x}_w$ are positions of fluid node, boundary node and wall node respectively. Because the collision step is not applicable to the wall nodes, for the fluid node which is most near to the wall nodes, the distribution functions in some directions are actually unknown for the streaming step. For example, in Figure 2.4, for fluid node "j", distribution functions f_3, f_4, f_7, f_6 are unknown.

Bouzidi *et al.* (2001) used the scheme below to determine these unknowns.

Firstly the half way bounce-back boundary condition should be understood. In Figure 2.4, for case q =1/2, the actual position of the wall is located at "b_3", which is about one-half grid spacing beyond the last fluid node "j". The distribution function $f_3(\mathbf{x}_j,t+1)$ can be obtained from a formula $f_3(\mathbf{x}_j,t+1)= f_1^+(\mathbf{x}_j,t)$, which means the particle with the velocity $\mathbf{e}_1$, traveled one grid spacing for one time step.

With the picture for the simple bounce-back scheme in mind, it is easy to understand the situation depicted for other cases. For case q<1/2, at time t, the distribution function of the particle with velocity $\mathbf{e}_5$ at the point "c", which located at a distance $\sqrt{2}\,(1-2q)\delta x$ away from the grid point "j" would end up at the grid point "j" after bounce-back collision. That is indicated by the thick bent arrow in Figure 2.4. So, it is easy to obtain $f_7(\mathbf{x}_j,t+1)$ if we know $f_5^+(\mathbf{x}_c,t)$ because $f_7(\mathbf{x}_j,t+1)= f_5^+(\mathbf{x}_c,t)$. Although $\mathbf{x}_c$ is not a grid point, the value of $f_5^+(\mathbf{x}_c,t)$ at the point can be reconstructed by a quadratic interpolation involving values of $f_5^+(\mathbf{x}_j,t)$, $f_5^+(\mathbf{x}_d,t)$ and $f_5^+(\mathbf{x}_e,t)$. In a similar manner, for the case of q>1/2 depicted in Figure 2.4, we can construct $f_4(\mathbf{x}_j,t+1)$ by a quadratic interpolation involving $f_4(\mathbf{x}_a,t+1)$, $f_4(\mathbf{x}_f,t+1)$ and $f_4(\mathbf{x}_g,t+1)$, where $f_4(\mathbf{x}_a,t+1)= f_2^+(\mathbf{x}_j,t)$. In this way, extrapolations in the boundary conditions are avoided for the sake of numerical stability. This leads to the following quadratic interpolation formulas.

For the case of q<1/2:

$$\begin{aligned} &f_7(\mathrm{x}_j,t+1) \\ &= q(1+2q)f_5^+(\mathbf{x}_j,t)+(1-4q^2)f_5^+(\mathrm{x}_d,t)-q(1-2q)f_5^+(\mathrm{x}_e,t) \end{aligned}. \qquad (2.67)$$

For case q>1/2, to get $f_4(\mathbf{x}_j,t+1)$,

$$\begin{aligned} &f_4(\mathrm{x}_j,t+1) \\ &= \frac{1}{q(1+2q)}f_2^+(\mathbf{x}_j,t)+\frac{(2q-1)}{q}f_4(\mathrm{x}_f,t+1)-\frac{(2q-1)}{(2q+1)}f_4(\mathrm{x}_g,t+1) \end{aligned}. \qquad (2.68)$$

The study of Lallemand and Luo (2003) provides more general formulas for

moving and stationary boundaries.

For the curved wall boundary condition, the non-equilibrium distribution function extrapolation scheme (Guo et al. 2002a) illustrated in Figure 2.5 is also easy to implement. In the scheme, the velocity on wall nodes (lattice nodes outside and most near to physical boundary) is obtained from extrapolation (e.g., in Figure 2.5, to obtain the unknown $f_7^+(\mathbf{x}_w,t)$, velocity on "w" is extrapolated from velocity of "*f*" and "*ff*") and *p* value obtained from the nearest fluid node, hence the equilibrium distribution function for wall nodes can be obtained through Eq. (2.16). With the corresponding non-equilibrium distribution function extrapolated from the fluid nodes, the collision step on wall nodes can be fulfilled. This treatment is proved to be second order in space. (Guo et al. 2002a)

2.7.3 Inlet/Outlet Boundary Condition

For the pressure and velocity boundary conditions, Zou and He (1997) proposed a scheme based on the bounceback of the non-equilibrium distribution function. Guo *et al.* (2002c) proposed a scheme based on an extrapolation method for non-equilibrium distribution. For example, if a particular velocity profile is specified, since the corresponding pressure of the fluid can be extrapolated from the next inner nodes, the equilibrium distribution function can be determined through Eq. (2.16). The corresponding non-equilibrium distribution function can be extrapolated from the next inner nodes. So the collision step can be implemented. For the pressure boundary condition, the pressure is specified and corresponding velocity is extrapolated from the inner nodes. The equilibrium and non-equilibrium part of distribution functions can be determined in the same way as inlet boundary condition.

2.8 Multi-block Strategy

As we known, originally the numerical mesh for LBM is the uniform Cartesian grid which is identical as the "molecular" lattice. That makes LBM not so efficient (case of uniform fine grid) or accurate (case of uniform coarse grid) to achieve high resolution in regions involving large gradient of macro-dynamic variables. Later Nannelli and Succi (1992) proposed the finite volume lattice Boltzmann scheme to handle Cartesian non-uniform grids. Based on an interpolation strategy, some studies also extended the LBGK method to curvilinear grids (He and Doolen 1997a, 1997b). However, if the numerical mesh spacing is very different from the "molecular" lattice, the accuracy of the scheme may decrease in the regions of high gradients of macro-dynamic variables. (Filippova and Hanel, 2000)

To avoid decoupling the numerical mesh and "molecular" lattice, Filippova and Hanel (1998, 2000) employed locally refined patches for uniform Cartesian grid in their studies. That means some finer grids are superposed on the basic, coarser grid. The coarse and fine grids have different relax time constants τ. The calculation proceeds with a small τ accordingly to the coarse grid, while on the finer grids with large τ, several time steps are performed to advance to the same time level. In this way, the accuracy of the LBGK scheme can be conserved. The coupling of solutions on the different meshes was solved by Filippova and Hanel (1998) through rescaling of the non-equilibrium part of distribution functions and second-order spatial interpolation in transition between different grids.

Yu, et al. (2002) suggested a multi-block method for viscous flows slightly different from Fillippova and Hanel (1998). Yu, et al. (2002) decomposed the whole computational domain into several sub-domains. Some sub-domains adopt

fine meshes, the others adopt coarse meshes. The coupling of solutions on different meshes is identical to that of Fillippova and Hanel (1998) except the high order fitting for spatial and temporal interpolation is employed when transfer the information from coarse block to nearby fine grid.

Although Yu, et al. (2002) used cubic spline interpolation and Fillippova and Hanel, (1998) used second-order interpolation on the grid interfaces, according to the Fillippova and Hanel's (2000) analysis, the common error introduced in the solution on the interface between coarse and fine grids due to the linear interpolation of $f_i^{eq,c}$'s from the neighboring nodes of the coarse grid is consistent with the order of accuracy of the solution on the coarse grid. Hence, in our study, for 2D cases, the simplest linear interpolation method is employed at the grid interfaces. For 3D cases, when transfer the distribution function from coarse grid to fine grid, bilinear spatial interpolation was used. The temporal interpolation for interface on fine grids is also linear. A multi-block strategy for 3D cases is next described in detail.

In our study, the whole 3D computational domain was decomposed into several sub-domains with coarse or fine meshes. In this way, all parts of the flow can be solved with appropriate accuracy and memory and CPU time can be saved compared to a uniform fine grid. However, the transition of f_i^+ in the interface of different grids is needed and multiple time steps are necessary on fine grids according to the refinement ratio due to the explicit manner of the LBGK scheme (Fillippova and Hanel, 2000). A typical interface structure between two different spacing blocks is illustrated in Figure 2.6. In the figure, the ratio of lattice spacing is $n=\delta x_c/\delta x_f=2$. The fine block's boundary surface ABCD is embedded into the coarse block and the coarse block's boundary surface EFGH is also embedded

into the fine block.

To implement the multi-block strategy, the calculation procedure is almost the same as that of Yu et al. (2002) except for the spatial and temporal interpolation method. The procedure is briefly described below with $\delta x_c/\delta x_f=2$.

1) Initialize the flow field
2) Transfer $f_i^{+,f}(\mathbf{x}, n\delta t_c)$ to $f_i^{+,c}(\mathbf{x}, n\delta t_c)$ on the coarse block boundary interface (i.e., EFGH in Figure 2.6).
3) Streaming in coarse block.
4) Collision in coarse block, obtain $f_i^{+,c}(\mathbf{x}, (n+1)\delta t_c)$ in all coarse block lattices.
5) Transfer $f_i^{+,c}(\mathbf{x}, n\delta t_c)$ to $f_i^{+,f}(\mathbf{x}, n\delta t_c)$ for lattices represented by "●" on the fine block boundary interface (i.e., ABCD in Figure 2.6), to obtain $f_i^{+,f}(\mathbf{x}, n\delta t_c)$ for lattices represented by "o" and "□" , spatial interpolation is needed.
6) Streaming in fine block.
7) Collision in fine block, obtain $f_i^{+,f}(\mathbf{x}, (n+0.5)\delta t_c)$ for all fine block lattices.
8) Obtain $f_i^{+,f}(\mathbf{x}, (n+0.5)\delta t_c)$ from $f_i^{+,c}(\mathbf{x}, n\delta t_c)$ and $f_i^{+,c}(\mathbf{x}, (n+1)\delta t_c)$ on the fine block boundary interface (i.e., ABCD in Figure 2.6), Here spatial and temporal interpolations are needed.
9) Streaming in fine block.
10) Collision in fine block, obtain $f_i^{+,f}(\mathbf{x}, (n+1)\delta t_c)$ for all fine block lattices.

Steps of 2) – 10) are iterated till the converge criteria is achieved. The macroscopic pressure p and momentum $p_0\mathbf{u}$ were obtained just before each collision step. This was not indicated in above steps for simplicity. In above procedure, both the interpolation method and the transition of f_i^+ between difference grids are important. A consistent and accurate relationship for the distribution function transition for different grids has been developed by Filippova

and Hanel (1998) and applied in our study.

To get identical velocity on interface of coarse and fine meshes and make $Re_f=Re_c$, the kinetic viscosities on both grids should satisfy $v_f=v_c$, which lead to

$$\tau_f - 0.5 = n(\tau_c - 0.5), \tag{2.69}$$

where n is the ratio of time step or the lattice spacing $n=\delta x_c/\delta x_f=\delta t_c/\delta t_f$. To ensure the velocity and pressure continuously across the interface, we have

$$f_i^{eq,c} = f_i^{eq,f} . \tag{2.70}$$

The distribution function can be split into equilibrium and non-equilibrium component as

$$f_i = f_i^{eq} + f_i^{neq} . \tag{2.71}$$

Under the assumption of continuous physical space ($\mathbf{x}$,t) in the limit of small δt, the LBE can be expanded in Taylor series with respect to small δt as Eq. (2.72).

$$\delta t\left[\frac{\partial}{\partial t} + e_{i\alpha}\frac{\partial}{\partial x_\alpha}\right] f_i + \frac{\delta t^2}{2}\left[\frac{\partial}{\partial t} + e_{i\alpha}\frac{\partial}{\partial x_\alpha}\right]^2 f_i - \frac{1}{\tau}\left[f_i^{eq} - f_i\right] = O\left(\delta t^3\right). \tag{2.72}$$

Substituting Eq. (2.71) into Eq.(2.72) and sorting in order of δt, we obtain

$$f_i^{neq} = -\tau\delta t\left[\frac{\partial}{\partial t} + e_{i\alpha}\frac{\partial}{\partial x_\alpha}\right] f_i^{eq} + O\left(\delta t^2\right). \tag{2.73}$$

Since the time and space derivatives of f_i^{eq} are continuous across an interface between two different grids, omitting the term of $O(\delta t^2)$, from Eq. (2.73) one can obtain

$$f_i^{neq,c} = n\left(\tau_c / \tau_f\right) f_i^{neq,f} \quad . \tag{2.74}$$

Hence, through rescaling the non-equilibrium distribution function, the transition of the post distribution function from the fine grid to coarse grid can be written as Eq. (2.75).

$$f_i^{+,c} = f_i^{eq,c} + (1-\frac{1}{\tau_c}) f_i^{neq,c} = f_i^{eq,f} + \frac{(\tau_c - 1)n}{\tau_f} f_i^{neq,f} \tag{2.75}$$

Similarly, the transition of the post distribution function from the coarse grid to fine grid can be written as

$$f_i^{+,f} = f_i^{eq,c} + \frac{(\tau_f - 1)}{\tau_c n} f_i^{neq,c}. \tag{2.76}$$

According to Filippova and Hanel's (2000) analysis, the higher order terms appearing from expression of f_i^{neq} which are not rescaled correctly is approximately $\sim O(\delta t^3)$ and can be omitted.

From Figure 2.6, we can see that in the surface ABCD, for the lattices which represented by the filled circle, their post-collision distribution function $f_i^{+,f}$ which transited from coarse block is easy to obtain according to the above Eq. (2.76). However, getting $f_i^{+,f}$ for lattices which are represented by an open circle and open square cannot be done directly and an interpolation method is needed.

In the present study, the simple bilinear interpolation was applied to get $f_i^{+,f}$ for lattices which represented by open circle and open square in Figure 2.7. For example, in Figure 2.7, through transition procedure (i.e., Eq. (2.76)), in point A,B,C,D, $f_i^{+,f}(\mathbf{x}_A)$, $f_i^{+,f}(\mathbf{x}_B)$, $f_i^{+,f}(\mathbf{x}_C)$ and $f_i^{+,f}(\mathbf{x}_D)$ are known. E is a lattice in fine boundary. To get the unknown $f_i^{+,f}(\mathbf{x}_E)$, firstly two parameter t and u are defined to describe the position of point E,

$$t \equiv (x_E - x_A)/(x_D - x_A), \qquad u \equiv (y_E - y_A)/(y_B - y_A), \tag{2.77}$$

usually t and u each lie between 0 and 1, and $f_i^{+,f}(\mathbf{x}_E)$ can be obtain through below bilinear formula

$$f_i^{+,f}(\mathbf{x}_E) = (1-t)(1-u) f_i^{+,f}(\mathbf{x}_A) + (1-t)u f_i^{+,f}(\mathbf{x}_B) + tu f_i^{+,f}(\mathbf{x}_C) + t(1-u) f_i^{+,f}(\mathbf{x}_D). \tag{2.78}$$

Bilinear interpolation is the simplest interpolation in 2D surface. As the interpolating point wanders from grid square to grid square, the interpolated value

changes continuously. The circumstances of t, or $u \in [-0.5,0] \cup [1,1.5]$ may be encountered in some cases. It is noticed that even when t and u are in the range [-0.5, 1.5], an interpolation result can also be obtained.

Table 2.1 Main parameters of popular 2D and 3D discrete velocity models

Model	$\mathbf{e}_i$	ω_i	c_s^2
D2Q9	(0,0) $(\pm1,0)c$, $(0,\pm1)c$ $(\pm1, \pm1)c$	4/9 (i=0) 1/9 (i=1,2,3,4) 1/36 (i=5,6,7,8)	$c^2/3$
D2Q7	(0,0) $(\pm1,0)c$, $(\pm1/2, \pm\sqrt{3}/2)c$	1/2 (i=0) 1/12 (i=1,…6)	$c^2/4$
D3Q19	(0,0,0) $(\pm1,0,0)c$, $(0,\pm1,0)c$, $(0,0, \pm1)c$ $(\pm1, \pm1,0)c$, $(0, \pm1 , \pm1)c$, $(\pm1,0, \pm1)c$	1/3 (i=0) 1/18 (i=1,…6) 1/36 (i=7,…18)	$c^2/3$
D3Q15	(0,0,0) $(\pm1,0,0)c$, $(0,\pm1,0)c$, $(0,0, \pm1)c$ $(\pm1, \pm1, \pm1)c$	2/9 (i=0) 1/9 (i=1,…6) 1/72 (i=7,…14)	$c^2/3$

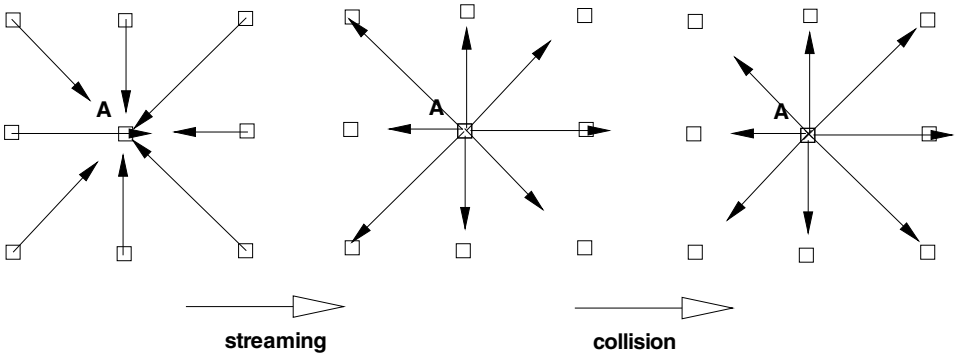

Figure 2.1 Streaming and collision steps in one time step

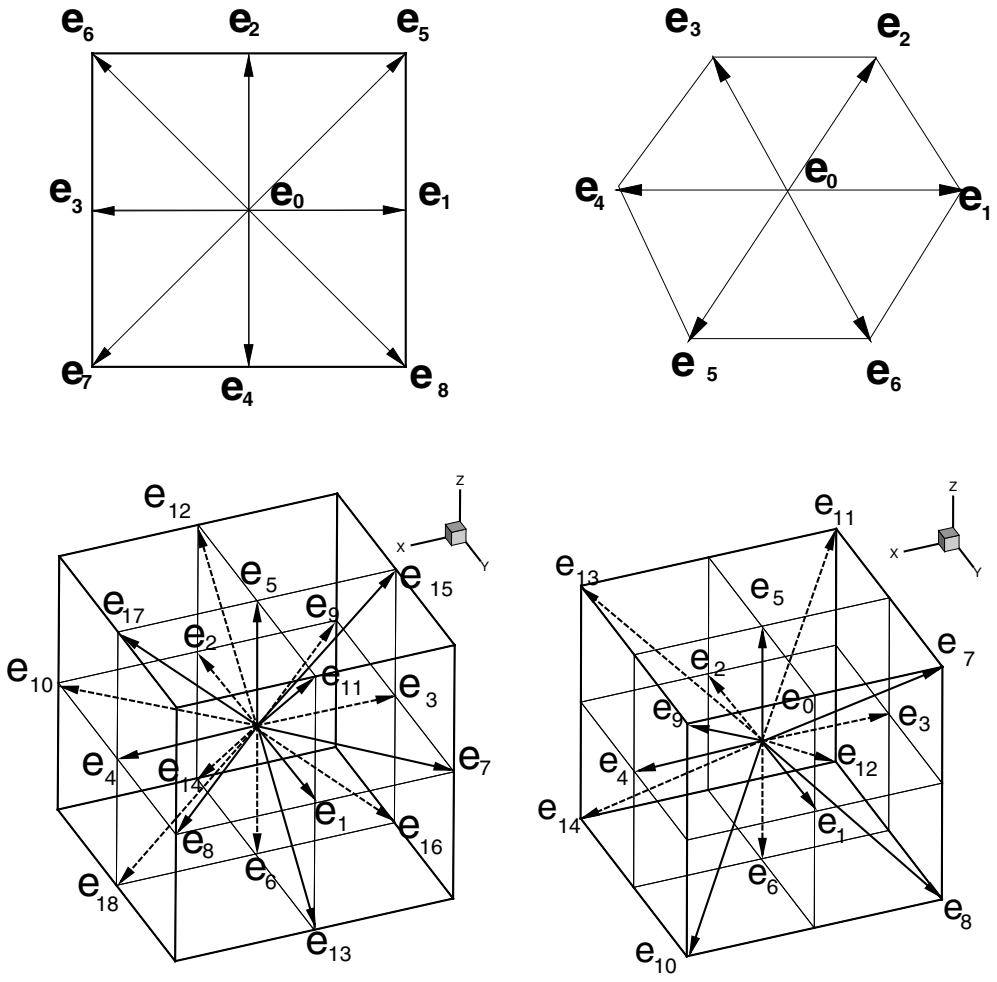

Figure 2.2 Discrete velocity sets $\{\mathbf{e}_i\}$ for D2Q9, D2Q7, D3Q19 and D3Q15 models

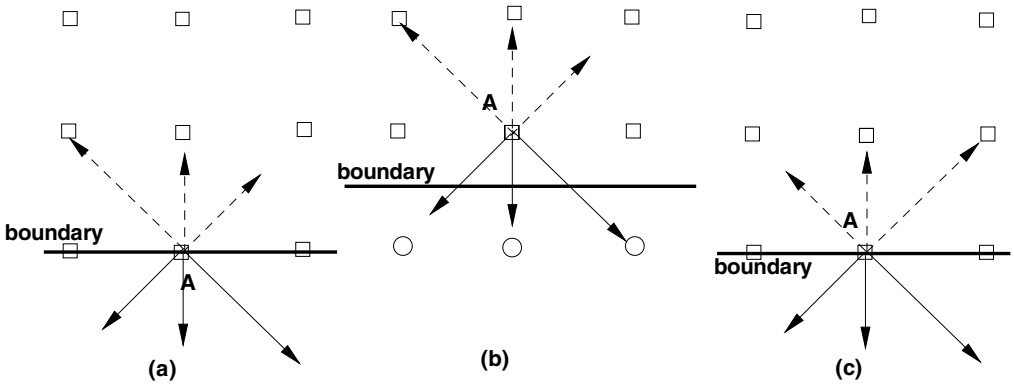

Figure 2.3 The bounce-back (a), half-way bounce-back (b) and specular reflection (c) schemes

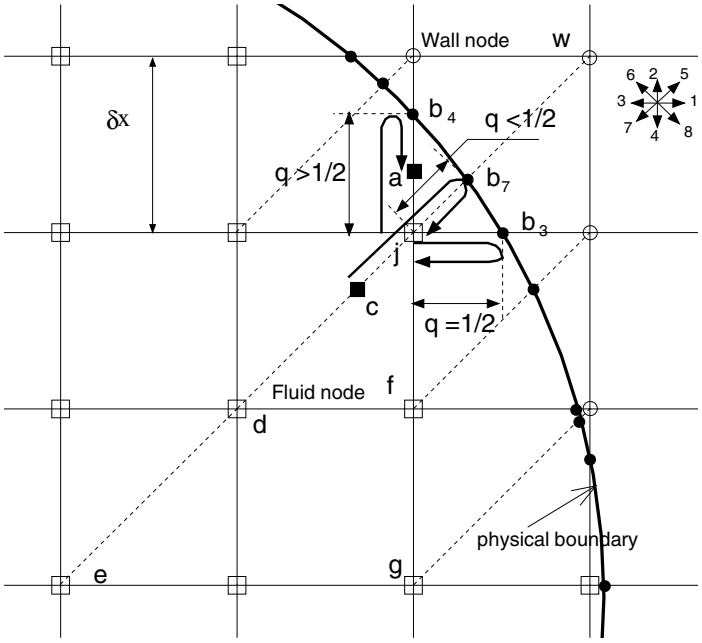

Figure 2.4 curved boundary geometry and lattice nodes. Open circles (○) are wall nodes and open squares (□) are the fluid nodes. The disks (●) are the nodes in physical boundary. Solid squares (■) are located in the fluid region but not on grid nodes. The thin solid lines are the grid lines. The thick arrows represent the trajectory of a particle interacting with the wall.

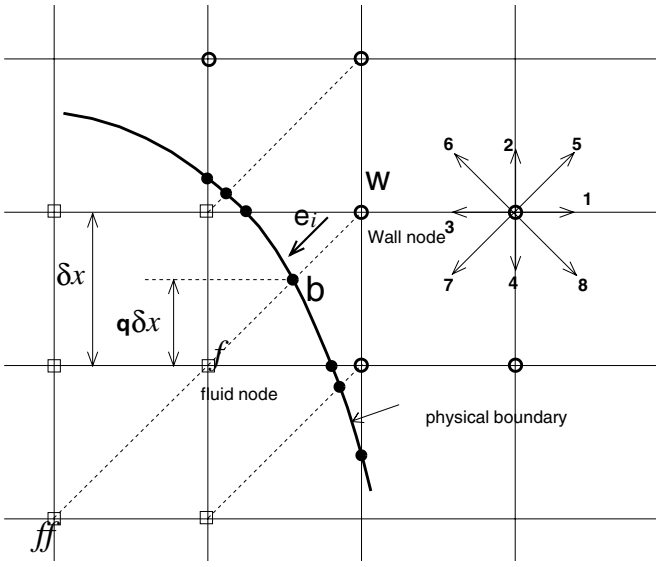

Figure 2.5 Curved wall boundary treatment of Guo et al. (2002a)

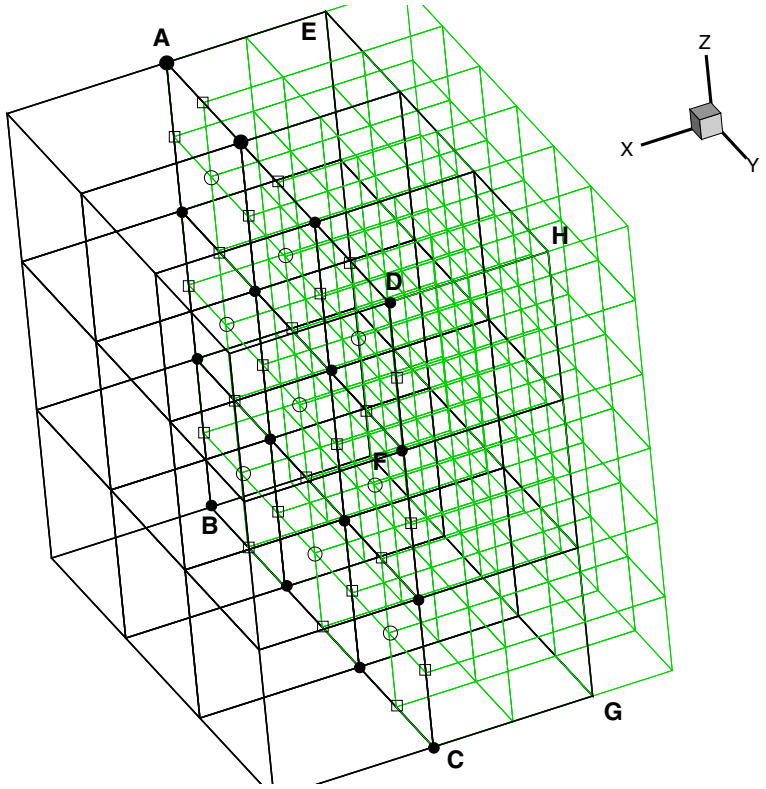

Figure 2.6 Interface structure between fine and coarse blocks

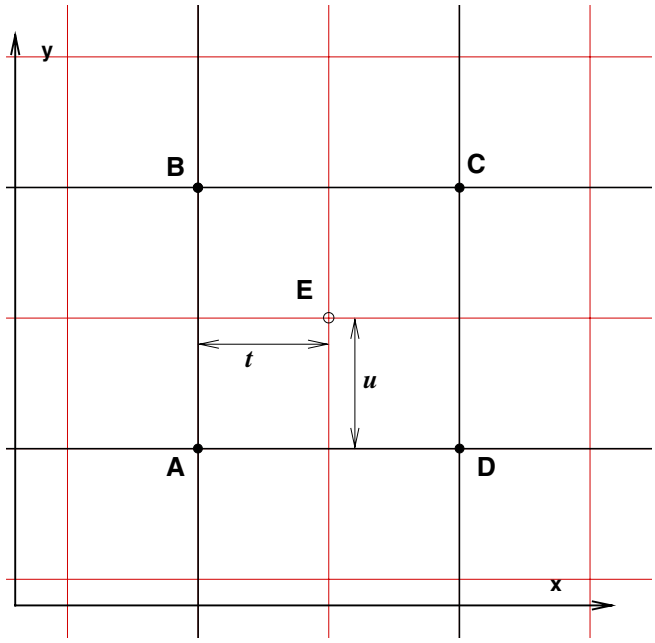

Figure 2.7 Bilinear spatial interpolation scheme

Chapter 3 Axisymmetric and 3D Lattice Boltzmann Models

In this Chapter[1], a general method to derive D2Q9 axisymmetric models was suggested and three different models were proposed to simulate axisymmetric flows. The theoretical difference between our model and the previous models was analyzed. Axisymmetric boundary conditions were presented. An incompressible 3D isothermal LBM and 3D Thermal LBM were also presented.

3.1 Source Term in LBE

In the continuum Boltzmann equation (i.e., Eq.(2.1)), there is a body force term $\mathbf{F}\partial f/\partial \mathbf{c}$. In the LBE, a similar term may also be added to incorporate a body force.

Buick et al. (2000) considered inserting the forcing term into the LBE to mimic the Navier-Stokes equation with the body force. The NS equation with body force can be written as

$$\partial_t \rho + \partial_\beta \rho u_\beta = 0, \tag{3.1}$$

$$\partial_t \rho u_\alpha + \partial_\beta \left(\rho u_\beta u_\alpha\right) = -\partial_\alpha p + \nu \partial_\beta \left[\rho\left(\partial_\beta u_\alpha + \partial_\beta u_\alpha\right)\right] + F_\alpha . \tag{3.2}$$

The first scheme to incorporate the gravity into the LBE is combining the gravity term and the pressure tensor. This method is valid only when the density variation produced by the body force is negligible (Buick et al. 2000). The second scheme is calculating the equilibrium distribution with an altered velocity, for

[1] Part of this work has been published as:
Lee, T.S., Huang, H., Shu, C., An axisymmetric incompressible Lattice-BGK model for simulation of the pulsatile flow in a circular pipe, *Int. J. Numer. Meth. Fluids*, 49(1), pp.99-116. (2005)
Lee, T.S., Huang, H., Shu, C., An axisymmetric incompressible lattice Boltzmann model for pipe flow, *Int. J. Mod. Phys. C.*, 17 (5), pp.645-661. (2006)

example, $f_i^{eq}(\mathbf{x},t) = E_i(\rho, u_\alpha^*)$ (refer to Eq. (2.16)), and $\rho u_\alpha^* = \rho u_\alpha + F_\alpha/2$, where $\rho u_\alpha = \sum e_{i\alpha} f_i$ and F_α is the body force (Shan and Doolen, 1995). The third scheme is adding an additional term to the LBE. However, it is found that only through combining the second and third schemes can the NS equation with body force be recovered from the modified LBE correctly. (Buick et al. 2000; Guo et al. 2002b)

Guo et al. (2002b) further analyzed the discrete lattice effects on forcing term in the LBM. In practical application, the method of adding $S_i = \omega_i e_{i\alpha} F_\alpha / c_s^2$ to LBE to mimic the NS equation with body force **F** (He and Zou et al. 1997) is usually used for flows exposed to a constant body force. According to the analysis of Guo et al. (2002b), this method is incorrect if the velocity gradient in flow field is not zero. To mimic the NS equation with body force **F**, Luo (1998, 2000) proposed adding the source term $S_i = \omega_i \left[\left(e_{i\alpha} - u_\beta \delta_{\alpha\beta} \right) / c_s^2 + \left(e_{i\beta} \cdot u_\beta \right) e_{i\alpha} / c_s^4 \right] F_\alpha$ into the LBE. However, the LBE still cannot recover the NS equation with the body force **F** correctly due to not taking into account the discrete lattice effect. The other schemes of adding a force term (e.g., Ladd et al. 2001, Buick et al. 2000) were also analyzed by Guo et al. (2002b). Due to the limitation of the above schemes, Guo et al. (2002b) proposed

$$S_i' = \omega_i (1 - 1/2\tau) \left[\left(e_{i\alpha} - u_\beta \delta_{\alpha\beta} \right) / c_s^2 + \left(e_{i\beta} u_\beta \right) e_{i\alpha} / c_s^4 \right] F_\alpha$$

as a forcing term in LBE to recover the NS equation with body force correctly.

3.2 Axisymmetric LBE

As we known, comparing with the NS equation in 2D Cartesian coordinates, there are extra terms in NS equation in cylindrical coordinates. These extra terms

would be regarded as the body force terms in 2D NS equation in Cartesian coordinates.

Through inserting forcing terms into the LBE, Halliday et al. (2001) proposed an axisymmetric D2Q9 model to simulate the axisymmetric flow in circular tube. However, in this model, the discrete lattice effects are not considered and the momentum and the equilibrium distribution function (EDF) are still defined as common standard D2Q9 model which do not include the effect of body force. Hence the NS equation in cylindrical coordinates may not be accurately recovered from the model.

Here through considering the discrete lattice effects and refining the momentum and EDF in D2Q9 model, our model can recover the NS equation in cylindrical coordinates accurately.

3.2.1 Incompressible NS Equation in Cylindrical Coordinates

Here, we consider the axisymmetric flows of an incompressible liquid with an axis in x direction. The continuity equation (3.3) and Navier-Stokes momentum equations (3.4) in the pseudo-Cartesian coordinates (x,r) are used to describe the flow in axial and radial directions.

$$\partial_\beta u_\beta = -\frac{u_r}{r}, \tag{3.3}$$

$$\partial_t u_\alpha + \partial_\beta \left(u_\beta u_\alpha\right) + \frac{1}{\rho_0}\partial_\alpha p - \nu\partial_\beta\left(\partial_\beta u_\alpha\right) = -\frac{u_\alpha u_r}{r} + \frac{\nu}{r}\left(\partial_r u_\alpha - \frac{u_r}{r}\delta_{\alpha r}\right) + E, \tag{3.4}$$

where u_β (β=x,r) is the two components of velocity. u_α is the velocity u_x or u_r. E is the additional source term which may appear in some flow problems. In

the above Equations we adopt the Einstein summation convention.

3.2.2 Source Terms for Axisymmetric D2Q9 Model

In the presence of a body force in the NS equation, to mimic the equation correctly, the LBE must be modified to account for the body force. Here we add a source term into the LBE as

$$f_i(\mathbf{x}+\mathbf{e}_i\delta_t, t+\delta_t) = f_i(\mathbf{x},t) - \frac{1}{\tau}\left(f_i(\mathbf{x},t) - f_i^{eq}(\mathbf{x},t)\right) + \delta_t S_i . \tag{3.5}$$

Our derivation would begin from the incompressible D2Q9 model (He and Luo, 1997a). Hence the EDF f_i^{eq} is defined as (He and Luo, 1997a)

$$f_i^{eq}(\mathbf{x},\mathbf{e}_i,t) = \omega_i\left\{\rho + \rho_0\left[\frac{e_{i\alpha}u_\alpha^*}{c_s^2} + \frac{u_\alpha^* u_\beta^*}{2c_s^2}\left(\frac{e_{i\alpha}e_{i\beta}}{c_s^2} - \delta_{\alpha\beta}\right)\right]\right\} \quad (i=0,1,2\ldots,8), \tag{3.6}$$

with

$$\rho u_\alpha^* = \sum_i e_{i\alpha} f_i + mF_\alpha\delta_t . \tag{3.7}$$

Here m is a constant to be determined. The source term S_i can be written in a power series in the particle velocity (Ladd, 2001)

$$S_i = \omega_i\left\{A + \frac{e_{i\alpha}B_\alpha}{c_s^2} + \frac{C_{\alpha\beta}}{2c_s^2}\left(\frac{e_{i\alpha}e_{i\beta}}{c_s^2} - \delta_{\alpha\beta}\right)\right\}, \tag{3.8}$$

where A, B_α and $C_{\alpha\beta}$ are functions of body force in NS equation F_α. The zeroth to second momentum of S_i are

$$\sum_i S_i = A, \quad \sum_i S_i e_{i\alpha} = B_\alpha, \quad \sum_i S_i e_{ij} e_{ik} = c_s^2 A\delta_{jk} + \left(C_{jk} + C_{kj}\right)/2 . \tag{3.9}$$

At the beginning of our derivation, we adopt the following expansions (Buick et al., 2000),

$$f_i(x + e_{ix}\delta_t, r + e_{ir}\delta_t, t+\delta_t) = \sum_{n=0}^{\infty}\frac{\varepsilon^n}{n!}D^n f_i(x,r,t), \tag{3.10}$$

$$\begin{cases} f_i = f_i^{(0)} + \varepsilon f_i^{(1)} + \varepsilon^2 f_i^{(2)} + \ldots \\ \partial_t = \varepsilon \partial_{1t} + \varepsilon^2 \partial_{2t} + \ldots \\ \partial_\beta = \varepsilon \partial_{1\beta} \\ S_i = \varepsilon S_i^{(1)} + \varepsilon^2 S_i^{(2)} + \ldots \\ F_\beta = \varepsilon F_\beta^{(1)} + \varepsilon^2 F_\beta^{(2)} \end{cases}, \tag{3.11}$$

where $\varepsilon=\delta_t$ and $D \equiv \left(\partial_t + \mathbf{e}_\beta \cdot \partial_\beta\right)$, $\beta=x,r$. It is noticed that in Eq. (3.11), there is no "equilibrium" S_i term. In the equations below, the Einstein summation convention is used. It should be noticed that since S_i is expanded to $O(\varepsilon^2)$, the coefficient A, B_α and $C_{\alpha\beta}$ in Eq. (3.9) should also be expanded to $O(\varepsilon^2)$ (e.g., $A=\varepsilon A^{(1)}+ \varepsilon^2 A^{(2)}$, $B_\alpha=\varepsilon B_\alpha^{(1)} + \varepsilon^2 B_\alpha^{(2)}$)

Retaining terms up to $O(\varepsilon^2)$ in Eqs. (3.10) and (3.11) and substituting them into Eq. (3.5) results in Eqs. (3.12), (3.13) and (3.14) as follows,

$$O(\varepsilon^0): \ \left(f_i^{(0)} - f_i^{eq}\right)/\tau = 0, \tag{3.12}$$

$$O(\varepsilon^1): \ \left(\partial_{1t} + e_{i\beta}\partial_{1\beta}\right) f_i^{(0)} + f_i^{(1)} / \left(\delta_t \tau\right) - S_i^{(1)} = 0, \tag{3.13}$$

$$O(\varepsilon^2): \begin{array}{l} \partial_{2t} f_i^{(0)} + \left(1 - \dfrac{1}{2\tau}\right)\left(\partial_{1t} + e_{i\beta}\partial_{1\beta}\right) f_i^{(1)} + \dfrac{\delta_t}{2}\left(\partial_{1t} + e_{i\beta}\partial_{1\beta}\right) S_i^{(1)} + \\ \dfrac{1}{\tau\delta_t} f_i^{(2)} - S_i^{(2)} = 0 \end{array}. \tag{3.14}$$

The distribution function f_i is constrained by the following relationships:

$$\sum_{i=0}^{8} f_i^{(0)} = \frac{p}{c_s^2} = \rho, \qquad \sum_{i=0}^{8} e_{i\alpha} f_i^{(0)} = \rho_0 u_\alpha^*, \tag{3.15}$$

$$\sum_{i=0}^{8} f_i^{(k)} = 0, \qquad \sum_{i=0}^{8} e_{i\alpha} f_i^{(k)} = -m F_\alpha^{(k)} \delta_t. \quad \text{(for } k>0\text{)} \tag{3.16}$$

with the properties of the general lattice tensors $G^{(n)}$ (Eqs. (2.33), (2.34), (2.35)), we have

$$\sum_{i=0}^{8} e_{i\alpha} e_{i\beta} f_i^{(0)} = \rho_0 u_\alpha^* u_\beta^* + p\delta_{\alpha\beta}, \tag{3.17}$$

$$\sum_{i=0}^{8} e_{i\alpha}e_{i\beta}e_{ik}f_i^{(0)} = \rho_0 c_s^2\left(\delta_{jk}\delta_{\beta\alpha} + \delta_{j\alpha}\delta_{\beta k} + \delta_{j\beta}\delta_{\alpha k}\right)u_j^* . \tag{3.18}$$

Summing on i in Eq. (3.13), we obtain at $O(\varepsilon)$

$$\partial_{1t}\left(p/c_s^2\right) + \partial_{1\beta}\rho_0 u_\beta^* = A^{(1)} . \tag{3.19}$$

Rewriting Eq. (3.19) in a dimensionless form, we can see that a condition of $L_x/(c_sT)<<1$ should be satisfied to neglect the first LHS term (He and Luo, 1997a), where L_x is the character length in the x direction, T is the characteristic time of unsteady flow. That is an additional limit of our derivation besides condition Mach number $M<<1$.

Multiplying Eq. (3.13) by $e_{i\alpha}$ and summing on i, gives

$$\rho_0\partial_{1t}u_\alpha^* + \partial_{1\beta}\Pi_{\alpha\beta}^0 = \left(n + m/\tau\right)F_\alpha^{(1)}, \tag{3.20}$$

where, $B_\beta^{(1)} = nF_\beta^{(1)}$ is assumed and n is a constant to be determined. $\Pi_{\alpha\beta}^0 = \sum_{i=0}^{8} e_{i\alpha}e_{i\beta}f_i^{(0)} = \rho_0 u_\alpha^* u_\beta^* + p\delta_{\alpha\beta}$ is the zeroth-order momentum flux tensor. To recover the Euler equation from Eq. (3.20), we can choose

$$A^{(1)} = -\rho_0 u_r^*/r , \quad n + m/\tau = 1 \text{ and } F_\alpha^{(1)} = -\rho_0 u_\alpha^* u_r^*/r . \tag{3.21}$$

Then we proceed to $O(\varepsilon^2)$ now. Summing on i in Eq. (3.14) gives

$$\begin{aligned} &\partial_{2t}\left(\frac{p}{c_s^2}\right) + \left(1 - \frac{1}{2\tau}\right)\partial_{1\beta}\left(-mF_\alpha^{(1)}\delta_t\right) + \frac{\delta_t}{2}\partial_{1t}A^{(1)} + \frac{\delta_t}{2}\partial_{1\beta}B_\alpha^{(1)} - A^{(2)} \\ &= \partial_{2t}\left(\frac{p}{c_s^2}\right) - \delta_t\left(m - \frac{1}{2}\right)\partial_{1\beta}F_\alpha^{(1)} + \frac{\delta_t}{2}\partial_{1t}A^{(1)} - A^{(2)} = 0 \end{aligned} . \tag{3.22}$$

Since $\partial_{2t}\left(p/c_s^2\right)$ is of order $O(M^3)$, it can be negligible (He and Luo, 1997a). Hence, we can obtain

$$A^{(2)} = \frac{\delta_t}{2}\partial_{1t}A^{(1)} - \delta_t\left(m - \frac{1}{2}\right)\partial_{1\beta}F_\alpha^{(1)} . \tag{3.23}$$

Multiplying Eq. (3.14) with $e_{i\alpha}$ and summing over i gives,

$$\begin{aligned}&\rho_0\partial_{2t}u_\alpha^*+\left(1-\frac{1}{2\tau}\right)\partial_{2t}\left(-mF_\alpha^{(1)}\delta_t\right)+\left(1-\frac{1}{2\tau}\right)\partial_{1\beta}\Pi_{\alpha\beta}^{(1)}=\\&-\frac{\delta_t}{2}\left\{\partial_{1t}B_\alpha^{(1)}+\partial_{1\beta}\left[c_s^2A^{(1)}\delta_{\alpha\beta}+\frac{1}{2}\left(C_{\alpha\beta}^{(1)}+C_{\beta\alpha}^{(1)}\right)\right]\right\}+\frac{mF_\alpha^{(2)}\delta_t}{\tau\delta_t}+B_\alpha^{(2)}\end{aligned}, \tag{3.24}$$

where $\Pi_{\alpha\beta}^{(1)}=\sum_i e_{i\alpha}e_{i\beta}f_i^{(1)}$ is the first-order momentum flux tensor. It can be written as

$$\begin{aligned}\Pi_{\alpha\beta}^{(1)}&=\sum_i e_{i\alpha}e_{i\beta}f_i^{(1)}=-\tau\delta_t\sum_i e_{i\alpha}e_{i\beta}D_{1t}f_i^{(0)}+\tau\delta_t\sum_i e_{i\alpha}e_{i\beta}S_i^{(1)}\\&=-\tau\delta_t\left[\partial_{1t}\Pi_{\alpha\beta}^{(0)}+\partial_k\left(\sum_i e_{i\alpha}e_{i\beta}e_{ik}f_i^{(0)}\right)\right]+\tau\delta_t\sum_i e_{i\alpha}e_{i\beta}S_i^{(1)}\end{aligned}. \tag{3.25}$$

For the first term in Eq. (3.25), with similar derivation procedure in Eq. (2.45) and Eq. (3.20), we can obtain

$$\partial_{1t}\Pi_{\alpha\beta}^{(0)}=c_s^2\rho_0\delta_{\alpha\beta}\left(-\partial_k u_k^*-u_r^*/r\right)+u_\alpha^*F_\beta^{(1)}+u_\beta^*F_\alpha^{(1)}+O\left(u^3\right). \tag{3.26}$$

The terms of order $O(u^3)$ or higher in Eq. (3.26) can be neglected.

For the second term in Eq. (3.25), with aid of Eq. (3.18), it can be written as

$$\partial_k\left(\sum_i e_{i\alpha}e_{i\beta}e_{ik}f_i^{(0)}\right)=\rho_0c_s^2\left(\delta_{\alpha\beta}\partial_j u_j^*+\partial_\beta u_\alpha^*+\partial_\alpha u_\beta^*\right). \tag{3.27}$$

With the results of Eq. (3.9), the third term can be written as

$$\tau\delta_t\sum_i e_{i\alpha}e_{i\beta}S_i^{(1)}=\tau\delta_t\left(c_s^2\delta_{\alpha\beta}A^{(1)}+C_{\alpha\beta}^{(1)}/2+C_{\beta\alpha}^{(1)}/2\right). \tag{3.28}$$

Noticing the assumptions of $B_\beta^{(1)}=nF_\beta^{(1)}$, $B_\beta^{(2)}=nF_\beta^{(2)}$ and using Eqs. (3.21), (3.25), (3.26), (3.27), (3.28), Eq. (3.24) can be simplified as

$$\rho_0\partial_{2t}u_\alpha^*=\delta_t\left(m-\frac{1}{2}\right)\partial_{2t}F_\alpha^{(1)}+\partial_{1\beta}\sigma_{\alpha\beta}+F_\alpha^{(2)}, \tag{3.29}$$

where the stress tensor $\sigma_{\alpha\beta}$ is given by

$$\begin{aligned}\sigma_{\alpha\beta} &= -\left(1-\frac{1}{2\tau}\right)\Pi^{(1)}_{\alpha\beta} - \frac{\delta_t}{2}\left[c_s^2 A^{(1)}\delta_{\alpha\beta} + \frac{1}{2}\left(C^{(1)}_{\alpha\beta} + C^{(1)}_{\beta\alpha}\right)\right] \\ &= (\tau-0.5)c_s^2\delta_t\rho_0\left(\partial_\beta u^*_\alpha + \partial_\alpha u^*_\beta - \delta_{\alpha\beta}u^*_r/r\right) + (\tau-0.5)\delta_t\left(u^*_\alpha F^{(1)}_\beta + u^*_\beta F^{(1)}_\alpha\right). \\ &\quad -\tau\delta_t\left(C^{(1)}_{\alpha\beta}/2 + C^{(1)}_{\beta\alpha}/2\right) - \tau\delta_t\left(c_s^2 A^{(1)}\delta_{\alpha\beta}\right)\end{aligned} \tag{3.30}$$

In Eq. (3.30), there are additional contributions to the viscous stress due to the discrete lattice effects and existence of body force. The artifact due to the lattice effect can be absorbed through redefine the viscosity as

$$\nu = c_s^2\delta_t(\tau-0.5). \tag{3.31}$$

The contribution of the stress due to force in Eq. (3.30) can be cancelled through choosing $C^{(1)}_{\alpha\beta}$ as

$$C^{(1)}_{\alpha\beta} = 2[1-1/(2\tau)]u^*_\alpha F^{(1)}_\beta \quad \text{or} \quad C^{(1)}_{\alpha\beta} = [1-1/(2\tau)]\left(u^*_\alpha F^{(1)}_\beta + u^*_\beta F^{(1)}_\alpha\right). \tag{3.32}$$

To eliminate the spatial and temporal derivation of $F^{(1)}_\alpha$ in Eqs. (3.22) and (3.29), we choose

$$m = 1/2 \quad \text{and hence} \quad \rho u^*_\alpha = \sum_i e_{i\alpha} f_i + F_\alpha\delta_t/2. \tag{3.33}$$

According to Eq. (3.21), we obtain

$$n = 1 - \frac{1}{2\tau}. \tag{3.34}$$

Substituting the Eq. (3.30) into the Eq. (3.29), with aid of Eq. (3.31), the Eq. (3.29) can be further simplified and rewritten as

$$\rho_0\partial_{2t}u^*_\alpha = \nu\rho_0\left(\partial^2_\beta u^*_\alpha + \partial_\alpha(\nabla\cdot\mathbf{u}^*)\right) - (\tau-1)\delta_t\partial_\alpha\left(c_s^2A^{(1)}\right) + F^{(2)}_\alpha. \tag{3.35}$$

In the axisymmetric case, $\nabla\cdot\mathbf{u}^* = \partial_\beta u^*_\beta + u^*_r/r$. To recover the NS equations correctly, $F^{(2)}_\alpha$ should be chosen as follows

$$F^{(2)}_\alpha = -\delta_t(\tau-1)c_s^2\partial_\alpha A^{(1)} + \frac{\rho_0\nu}{r}\left(\partial_r u^*_\alpha - \frac{u^*_r}{r}\delta_{\alpha r}\right) + \rho_0 E. \tag{3.36}$$

With *m*=1/2, Eq. (3.23) can be simplified and rewritten as

$$A^{(2)} = -\left(\delta_t \partial_{1t} \rho_0 u_r^*\right)/2r = \delta_t \partial_\beta \left(p\delta_{r\beta} + \rho_0 u_\beta^* u_r^*\right)/2r \,. \tag{3.37}$$

Since the term $C_{\alpha\beta}^{(2)}$ does not appear in our derivation, finally, the formula of S_i can be written as

$$S_i = \omega_i \left\{ A^{(1)} + \frac{e_{i\alpha} n F_\alpha^{(1)}}{c_s^2} + \frac{C_{\alpha\beta}^{(1)}}{2c_s^2}\left(\frac{e_{i\alpha} e_{i\beta}}{c_s^2} - \delta_{\alpha\beta} \right) \right\} + \omega_i \left\{ A^{(2)} + \frac{e_{i\alpha} n F_\alpha^{(2)}}{c_s^2} \right\} . \tag{3.38}$$

With above source terms $A^{(1)}$, $F_\alpha^{(1)}$ (i.e., Eq. (3.21)), $A^{(2)}$, $F_\alpha^{(2)}$ (i.e., Eq. (3.37) and Eq. (3.36)) and $C_{\alpha\beta}^{(1)}$ (i.e., Eq. (3.32)), the Eqs. (3.19), (3.22) can recover the continuity equation Eq. (3.3) and Eqs. (3.20), (3.29) can recover the incompressible NS equation (i.e., Eq.(3.4)).

3.2.3 Other Choices of the Source Terms for Axisymmetric D2Q9 Models

From the above derivation of Source terms, we can see that when we make appropriate choice in Eq. (3.21), in the order of $O(\varepsilon^1)$, the Euler equation can be recovered. However, if the macroscopic equations in the order of $O(\varepsilon^1)$ are not required to recover the Euler equation and we only intend to recover NS equation by combining the macroscopic equations of order $O(\varepsilon^1)$ and $O(\varepsilon^2)$ as a whole, the choice of the source terms can be different.

In the following, we refer the above model as **model A**.

If the macroscopic equations in the order of $O(\varepsilon^1)$ are not required to recover the Euler equation, for simplicity, we can make a choice as

$$A^{(1)} = -\rho_0 u_r^*/r \,, \quad n + m/\tau = 1 \text{, } m\text{=1/2 and } F_\alpha^{(1)} = 0 \,. \tag{3.39}$$

In this way, as a result, the expression of $C_{\alpha\beta}^{(1)}$ are highly simplified as $C_{\alpha\beta}^{(1)} = 0$ and $F_\alpha^{(2)}$ should becomes

$$F_\alpha^{(2)} = -\frac{\rho_0 u_\alpha^* u_r^*}{r} - \delta_t(\tau-1)c_s^2\partial_\alpha A^{(1)} + \frac{\rho_0\nu}{r}\left(\partial_r u_\alpha^* - \frac{u_r^*}{r}\delta_{\alpha r}\right) + \rho_0 E\,. \quad (3.40)$$

$A^{(2)}$ is the same as Eq. (3.37). Then, in this scheme, the final expression of the source term is

$$S_i = \omega_i\{A^{(1)}\} + \omega_i\left\{A^{(2)} + \frac{e_{i\alpha}nF_\alpha^{(2)}}{c_s^2}\right\}. \quad (3.41)$$

This model will be referred as **model B**.

Alternatively, we can put all of the force terms in $F_\alpha^{(2)}$ to $F_\alpha^{(1)}$ and make $F_\alpha^{(2)}$=0. Actually, we can make a choice as follows

$$A^{(1)} = -\rho_0 u_r^*/r\,, \quad n + m/\tau = 1\,,\ m=1/2, \quad (3.42)$$

and

$$F_\alpha^{(1)} = -\frac{\rho_0 u_\alpha^* u_r^*}{r} - \delta_t(\tau-1)c_s^2\partial_\alpha A^{(1)} + \frac{\rho_0\nu}{r}\left(\partial_r u_\alpha^* - \frac{u_r^*}{r}\delta_{\alpha r}\right) + \rho_0 E\,. \quad (3.43)$$

As a result, the $C_{\alpha\beta}^{(1)}$ should be

$$C_{\alpha\beta}^{(1)} = 2[1-1/(2\tau)]u_\alpha^* F_\beta^{(1)} \quad \text{or} \quad C_{\alpha\beta}^{(1)} = [1-1/(2\tau)]\left(u_\alpha^* F_\beta^{(1)} + u_\beta^* F_\alpha^{(1)}\right), \quad (3.44)$$

which is identical to Eq. (3.32) in scheme A.

In this scheme, $A^{(2)}$ is also the same as Eq. (3.37). Hence, for this model that will be referred as **model C**, the final expression of the source terms are

$$S_i = \omega_i\left\{A^{(1)} + \frac{e_{i\alpha}nF_\alpha^{(1)}}{c_s^2} + \frac{C_{\alpha\beta}^{(1)}}{2c_s^2}\left(\frac{e_{i\alpha}e_{i\beta}}{c_s^2} - \delta_{\alpha\beta}\right)\right\} + \omega_i\{A^{(2)}\}. \quad (3.45)$$

3.2.4 Theoretical Difference between Present and Previous Models

Through comparison, it is found that present axisymmetric D2Q9 models are theoretically different from the previous axisymmetric models of Halliday et al.

(2001) and Peng et al. (2003). It should be noticed that the model of Peng et al. (2003) is identical to that of Halliday et al. (2001) if the swirl velocity is not considered.

In the axisymmetric model of Halliday et al. (2001) and Peng et al. (2003), the velocity is not redefined as in the present schemes (i.e., Eq. (3.7)). It is just defined as common LBM (i.e., $\rho u_\alpha = \sum_i e_{i\alpha} f_i$) and the components of non-equilibrium distribution function at scale $O(\varepsilon^1)$ and $O(\varepsilon^2)$ satisfy the following equations as standard LBM which is different from the Eq. (3.16) in our schemes.

$$\sum_{i=0}^{8} f_i^{(k)} = 0, \qquad \sum_{i=0}^{8} e_{i\alpha} f_i^{(k)} = 0 \qquad (\text{for } k>0). \tag{3.46}$$

The source terms in their models are somewhat similar to those in our present model B. It seems their models are just for a specific case of model B with n=1, m=0, $A^{(1)} = -\rho u_r / r$, $F_\alpha^{(1)} = 0$ and $A^{(2)}$, $F_\alpha^{(2)}$ written as

$$A^{(2)} = \delta_t \partial_\beta \left(\rho c_s^2 \delta_{r\beta} + \rho u_\beta u_r \right) / 2r, \tag{3.47}$$

$$F_\alpha^{(2)} = \nu \partial_\alpha A^{(1)} + \frac{\nu}{r}\left(\partial_r \rho u_\alpha - \frac{\rho u_r}{r} \delta_{\alpha r} \right). \tag{3.48}$$

As a result, the macroscopic equations of their axisymmetric models (i.e., Halliday et al. (2001) and Peng et al. (2003)) are

$$\partial_\beta \rho u_\beta = -\frac{\rho u_r}{r}, \tag{3.49}$$

$$\begin{aligned} &\partial_t \rho u_\alpha + \partial_\beta \left(\rho u_\beta u_\alpha \right) + \partial_\alpha p \\ &= \nu \partial_\beta \left[\rho \left(\partial_\beta u_\alpha + \partial_\alpha u_\beta \right) \right] - (\tau - 1)\delta_t c_s^2 \partial_\alpha \left(\frac{\rho u_r}{r} \right) + \frac{\nu}{r}\left(\partial_r \rho u_\alpha - \frac{\rho u_r}{r} \delta_{\alpha r} \right) \end{aligned}. \tag{3.50}$$

From Eqs. (3.49) and (3.50), we can see that the previous models can recover the continuity equation. However, it is also found that there are extra terms such as $\nu \partial_\beta \left[\rho \left(\partial_\alpha u_\beta \right) \right]$ and $-(\tau - 1)\delta_t c_s^2 \partial_\alpha (\rho u_r / r)$, which cannot be canceled to recover

the correct NS equation (3.3). This failure is due to the fact that they did not fully consider the lattice effects in their derivation. It may also be noticed that besides the failure, the term of $-\rho u_\alpha u_r / r$ in Eq. (3.3) is not considered in the models of Halliday et al. (2001) and Peng et al. (2003). However, this term is important since $\rho u_\alpha u_r / r + \partial_\beta (\rho u_\beta u_\alpha) = u_\beta \partial_\beta (\rho u_\alpha)$.

After fully considering the lattice effects in our derivation and including the term $-\rho u_\alpha u_r / r$, the correct $A^{(2)}$, $F_\alpha^{(2)}$ for model of Halliday et al. (2001) should be the same as the choices of model B.

In conclusion, the previous models of Halliday et al. (2001) and Peng et al. (2003) are only specific cases of present model B.

3.2.5 Axisymmetric Boundary Condition

In the study by Halliday et al. (2001), treatment of the axisymmetric boundary condition is not given. As a result, they have to study the whole computational domain bounded by upper and lower straight walls. They try to avoid the singularity (e.g., Eq. (3.47) and (3.48)) by placing the axis in the center of the computational grid within the computational domain.

Using proper axisymmetric boundary conditions has many advantages. Firstly, with proper axisymmetric boundary conditions, the axisymmetric flow problem can be simulated in an axisymmetric plane, which is only a half the computational domain of the above. Hence, the computational efficiency can be further improved. Secondly, with the proper axisymmetric boundary conditions, the singularity problem may be solved.

Here we propose a new scheme to treat the axisymmetric boundary. The computational domain for axisymmetric flow simulation is illustrated in Figure

3.1. In the figure, the axis is represented by the thick straight line while the curved thick line is the geometry of a constricted tube. There is an extra lattice layer outside the axis. Due to axis-symmetry,

$$(u_x)_{i,j=1} = (u_x)_{i,j=3} \quad \text{and} \quad (u_r)_{i,j=1} = -(u_r)_{i,j=3}, \tag{3.51}$$

where *i,j* are lattice node index in the Cartesian coordinates. Since the f_k (k=2,5,6) is unknown after the streaming step, they have to be determined to fulfill the collision and streaming steps. If we simply impose the unknown distribution function as $f_k = f_k^{eq} = E_k(\rho, \mathbf{u}_{i,j=1})$ (k=2,5,6), the numerical instability is easy to appear in the simulation.

Here we propose a more stable treatment for the axisymmetric boundary condition. Firstly, from Eq. (3.25), the first-order momentum flux tensor can be written as

$$\begin{aligned}\Pi_{\alpha\beta}^{(1)} &= \sum_k e_{i\alpha} e_{i\beta} f_k^{(1)} = -\tau\delta_t\left[\rho_0 c_s^2\left(\partial_\beta u_\alpha + \partial_\alpha u_\beta\right)\right] - \delta_t/2\left(u_\alpha F_\beta^{(1)} + u_\beta F_\alpha^{(1)}\right) \\ &\approx -\tau\delta_t\left[\rho_0 c_s^2\left(\partial_\beta u_\alpha + \partial_\alpha u_\beta\right)\right]\end{aligned}. \tag{3.52}$$

In Eq. (3.52), comparing with the first term, the term of $\delta_t/2\left(u_\alpha F_\beta^{(1)} + u_\beta F_\alpha^{(1)}\right)$ is higher order term that can be neglected. Due to axis-symmetry, we have

$$\left(\partial_x u_y + \partial_y u_x\right)_{i,j=1} = -\left(\partial_x u_y + \partial_y u_x\right)_{i,j=3}. \tag{3.53}$$

Here the unknown distribution function at j=1 lattice nodes (i.e., lattice nodes in axisymmetric boundary) was proposed to calculate using the following equation

$$f_k = f_k^{eq} + f_k^{(1)} \quad \text{with} \quad f_k^{eq} = E_k(\rho, \mathbf{u}_{i,j=1}) \quad \text{and} \quad \left(f_k^{(1)}\right)_{i,j=1} = -\left(f_k^{(1)}\right)_{i,j=3}. \tag{3.54}$$

In this way, the Eq. (3.53) can be satisfied and this boundary condition treatment is expected to be more stable since not only the equilibrium distribution function but also the non-equilibrium distribution function are considered.

It is also noticed that the specular reflection scheme (see Chapter 2) for lattice

nodes in axis can also handle the axisymmetric boundary (Peng et al. 2003). Using this scheme, the extra layer lattice nodes are not needed. Hence, the computational domain in vertical direction is beginning from the layer j=2 in Figure 3.1.

3.3 Three-dimensional Incompressible LBE

To simulate 3D viscous flows, usually, three athermal 3D Lattice Boltzmann Equation (LBE) models (D3Q15, D3Q19, and D3Q27) are available. Because the D3Q19 model provides a balance between computational reliability and efficiency comparing with the D3Q15 model and the D3Q27 model (Mei et al. 2000), here the D3Q19 velocity model was adopted in our simulation. To diminish the compressibility effect of the standard D3Q19 model (Artoli et al., 2002), the incompressible D3Q19 model proposed by He and Luo (1997a) are employed.

As we known, the standard LBGK D2Q9 and D3Q19 models involve the compressibility effect (Hou *et al.*, 1995; Artoli *et al.*, 2002). To solve any problem, when using LBM, the pressure changes are described by density variance. In our present study of viscous flow through constricted vascular tubes, the non-dimensional pressure drop $\Delta p/(\rho U^2)$ is equal to $c_s^2\Delta\rho/(\rho U^2)$, where c_s^2=1/3 and U is the characteristic velocity (usually the maximum value of the inlet fully developed parabolic velocity profile). Hence, when using the standard D3Q19 model to simulate the flow that involves high non-dimensional pressure drop, only very small U can be used to diminish the compressibility effects (i.e., to make $\Delta\rho/\rho<<1$). However, for certain Reynolds number, reducing U would make τ value very close to 0.5, which may lead to numerical instability. To solve the problem, the technique of increasing the mesh size is commonly used (He *et al.*, 1996), which may result in a much larger mesh system than conventional CFD

methods such as FVM.

To eliminate the above difficulties, He and Luo (1997) proposed an incompressible D2Q9 model for steady and unsteady flows. Using the incompressible D2Q9 model, characteristic velocity U<0.15 is valid and not necessary to adopt very small value.

In the present study, we applied an incompressible D3Q19 model which is similar to the incompressible D2Q9 model proposed by He and Luo (1997). In LBGK method, $f_i(\mathbf{x},t)$ is the distribution function for particles with velocity $\mathbf{e}_i$ at position $\mathbf{x}=(x,y,z)$ and time t. $\mathbf{u}=(u,v,w)$, u,v,w are x, y and z component velocities respectively. The macroscopic density $\rho$and momentum $\rho_0\mathbf{u}$ are defined as

$$\sum_{i=0}^{18} f_i = \rho, \qquad \sum_{i=0}^{18} f_i \mathbf{e}_i = \rho_0 \mathbf{u}. \tag{3.55}$$

where ρ_0 is the average density. The 3D 19 velocity model can be written as

$$\begin{aligned}&[\mathbf{e}_0,\mathbf{e}_1,\mathbf{e}_2,\mathbf{e}_3,\mathbf{e}_4,\mathbf{e}_5,\mathbf{e}_6,\mathbf{e}_7,\mathbf{e}_8,\mathbf{e}_9,\mathbf{e}_{10},\mathbf{e}_{11},\mathbf{e}_{12},\mathbf{e}_{13},\mathbf{e}_{14},\mathbf{e}_{15}\mathbf{e}_{16},\mathbf{e}_{17},\mathbf{e}_{18}]\\ &=\begin{bmatrix} 0 & 1 & -1 & 0 & 0 & 0 & 0 & 1 & 1 & -1 & -1 & 1 & -1 & 1 & -1 & 0 & 0 & 0 & 0 \\ 0 & 0 & 0 & 1 & -1 & 0 & 0 & 1 & -1 & 1 & -1 & 0 & 0 & 0 & 0 & 1 & 1 & -1 & -1 \\ 0 & 0 & 0 & 0 & 0 & 1 & -1 & 0 & 0 & 0 & 0 & 1 & 1 & -1 & -1 & 1 & -1 & 1 & -1 \end{bmatrix}.\end{aligned} \tag{3.56}$$

For this incompressible D3Q19 model, the equilibrium function $f_i^{eq}(\mathbf{x},t)$ is defined as

$$f_i^{eq}(\mathbf{x},t) = \omega_i \rho + \omega_i \rho_0 \left[\frac{\mathbf{e}_i \cdot \mathbf{u}}{c_s^2} + \frac{(\mathbf{e}_i \cdot \mathbf{u})^2}{2c_s^4} - \frac{\mathbf{u}^2}{2c_s^2} \right], \tag{3.57}$$

where i=0,1,2…..,18 with ω_0=1/3 , ω_i=1/18, (i=1,2,….6) , ω_i =1/36, (i=7, 8,…18) c_s^2=1/3

3.4 Three-dimensional Incompressible Thermal LBE

In order to solve the 3D thermal problems for the engineering application, a 3D thermal model based on the double-population TLBE derived by He et

al.(1998) is used in our simulation. As 2D thermal lattice Boltzmann equations introduced in section 2.6, this 3D thermal model also uses two distribution functions to model the flow and thermal fields.

The discrete evolution equations for the density distribution function $f(\mathbf{x},t)$ and the thermal energy density distribution function $g(\mathbf{x},t)$ are illustrated as follows (He et al.,1998)

$$f_i(\mathbf{x}+\mathbf{e}_i\delta_t, t+\delta_t) - f_i(\mathbf{x},t) = -\frac{1}{\tau_f}\left[f_i(\mathbf{x},t) - f_i^{eq}(\mathbf{x},t)\right] + \delta_t F_i, \tag{3.58}$$

$$g_i(\mathbf{x}+\mathbf{e}_i\delta_t, t+\delta_t) - g_i(\mathbf{x},t) = -\frac{1}{\tau_g}\left[g_i(\mathbf{x},t) - g_i^{eq}(\mathbf{x},t)\right], \tag{3.59}$$

where,

$$F_i = \omega_i(1-0.5\tau)\left[(\mathbf{e}_i - \mathbf{u})/c_s^2 - (\mathbf{e}_i\cdot\mathbf{u})\mathbf{e}_i/c_s^4\right]\cdot\mathbf{G}, \tag{3.60}$$

τ_f and τ_g are the momentum and internal energy relax time, respectively. In Eq. (3.60), **G** are the external forces acting on unit mass. $\mathbf{e}_i$ is the lattice velocity and i denotes the velocity direction. δ_x, δ_t and are the lattice spacing and time step size.

For D3Q19 model, the 19 discrete velocities are illustrated in Eq.(3.56). In above Eqs. (3.58) and (3.59), f_i^{eq} are the equilibrium density distribution functions defiend by Eq.(3.57). g_i^{eq} are the equilibrium internal energy distribution functions defined as following (He et al. 1998),

$$g_0^{eq}(\mathbf{x},t) = \omega_0\rho e\left(-\frac{3\mathbf{u}^2}{2c^2}\right), \tag{3.61}$$

$$g_i^{eq}(\mathbf{x},t) = \omega_i\rho e\left[1 + \frac{(\mathbf{e}_i\cdot\mathbf{u})}{2c^2} + \frac{9(\mathbf{e}_i\cdot\mathbf{u})^2}{2c^4} - \frac{3\mathbf{u}^2}{2c^2}\right] \quad i=1,2,..6, \tag{3.62}$$

$$g_i^{eq}(\mathbf{x},t) = \omega_i\rho e\left[2 + \frac{4(\mathbf{e}_i\cdot\mathbf{u})}{c^2} + \frac{9(\mathbf{e}_i\cdot\mathbf{u})^2}{2c^4} - \frac{3\mathbf{u}^2}{2c^2}\right] \quad i=7,8,..18 \tag{3.63}$$

where $c_s = c/\sqrt{3}$, ω_0=1/3 , ω_i=1/18, (i=1,2,….6) , ω_i =1/36, (i=7, 8,…18). The internal energy density is $\rho e = 3\rho RT/2$ for three-dimensional problems.

The macroscopic density ρ and momentum $\rho\mathbf{u}$ can be obtained through Eq.(3.55). Internal energy per unit mass e are defined as (He et al., 1998)

$$\rho e = \sum_{i=0}^{18} g_i \,. \tag{3.64}$$

The kinetic viscosity ν and thermal diffusivity α are obtained by $\nu = \delta t(\tau_f - 0.5)c_s^2$ and $\alpha = 5(\tau_g - 0.5)/9$.

It should notice that compared with the 2D TLBM introduced in section 2.6, the compression work done by the pressure and the viscous heat dissipation $q_i = (\mathbf{e}_i - \mathbf{u})[\partial\mathbf{u}/\partial t + (\mathbf{e}_i \cdot \nabla)\mathbf{u}]$ are neglected here for the incompressible applications (Peng et al., 2003b).

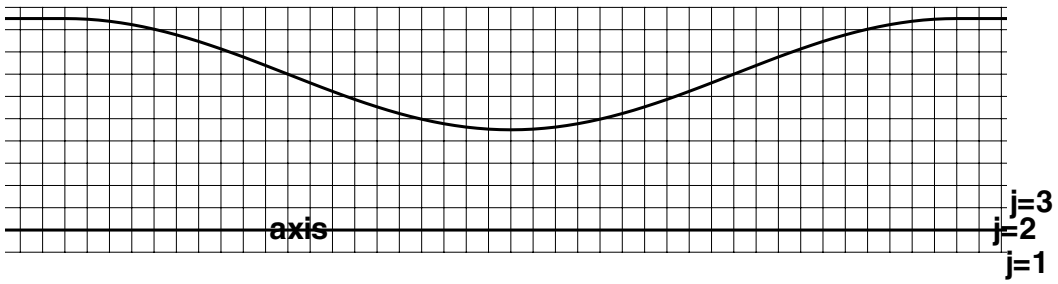

Figure 3.1 The computational domain for axisymmetric flow simulation

Chapter 4 Evaluation of Axisymmetric and 3D Lattice Boltzmann Models

In this Chapter[2], we would evaluate our axisymmetric D2Q9 models. The simulation results were compared with analytical solutions or those obtained by finite volume method. The spatial accuracies of the axisymmetric D2Q9 models incorporating difference boundary conditions were compared in detail. The 3D LBM solver would also be validated. The multi-block strategy used in simulations would also be tested.

4.1 Implementation of the Axisymmetric Models

In Chapter 3, three axisymmetric D2Q9 models through scheme A, B and C were derived. In these models, the source terms $F_\alpha^{(1)}$ (scheme C) or $F_\alpha^{(2)}$ (scheme A and B) contain the derivatives of velocities.

These velocity derivations can be computed from appropriate higher order momentums of non-equilibrium distribution function. The velocity derivatives $\partial_r u_x+\partial_x u_r$, $\partial_x u_x$ and $\partial_r u_r$ can all be obtained through Eq. (4.1) which is the same as Eq. (3.52) with $\alpha=x,\beta=r$; $\alpha=\beta=x$; $\alpha=\beta=r$ respectively

[2] Part of this work has been published as:
Lee, T.S., Huang, H., Shu, C., An axisymmetric incompressible Lattice-BGK model for simulation of the pulsatile flow in a circular pipe, *Int. J. Numer. Meth. Fluids*, 49(1), pp.99-116. (2005)
Lee, T.S., Huang, H., Shu, C., An axisymmetric incompressible lattice Boltzmann model for pipe flow, *Int. J. Mod. Phys. C.*, 17 (5), pp.645-661. (2006)
Huang, H., Lee, T.S., Shu, C., Lattice-BGK simulation of steady flow through vascular tubes with double constrictions, *Int. J. Numer. Methods Heat Fluid Flow*,16(2), pp. 185-203. (2006)
Huang, H., Lee, T.S., Shu, C., A multi-block Lattice-BGK method for 3D viscous fluid flows, Asian Joint Conference on Propulsion and Power 2006, Apr.20-23, Beijing, China

$$\begin{aligned}\rho_0 \nu\left(\partial_\beta u_\alpha + \partial_\alpha u_\beta\right) &= -\left(1-\frac{1}{2\tau}\right)\sum_{i=0}^{8} f_i^{(1)} e_{i\alpha} e_{i\beta} \\ &= -\left(1-\frac{1}{2\tau}\right)\sum_{i=0}^{8} f_i^{ne} e_{i\alpha} e_{i\beta} + o(\varepsilon^2)\end{aligned} . \tag{4.1}$$

For the term $\partial_r u_x$, it equal to $(\partial_r u_x+\partial_x u_r)$-$\partial_x u_r$. Since $(\partial_r u_x+\partial_x u_r)$ can be easily obtained by Eq. (4.1), only value of $\partial_x u_r$ is left unknown to determine $\partial_r u_x$. Here we recourse to finite difference method to obtain $\partial_x u_r$ at lattice node (i,j), which can be calculated by following equation

$$\left(\partial_x u_r\right)_{i,j} = \left(\left(u_r\right)_{i+1,j} - \left(u_r\right)_{i-1,j}\right)/\left(2\delta_x\right). \tag{4.2}$$

The values of $\partial_r u_x+\partial_x u_r$, $\partial_x u_x$, $\partial_r u_r$, $\partial_r u_x$ and $\partial_x u_r$ for the lattice nodes which just on the wall boundary can also be calculated from Eqs. (4.1) and (4.2). Obtaining these values for lattice nodes on the periodic boundary is also easy. These derivative values for the lattice nodes on the inlet/outlet pressure-specified boundary are extrapolated from those of the inner nodes.

After the above velocity derivatives are determined, the axisymmetric models can be implemented as common D2Q9 lattice Boltzmann models by adding the source terms into the post-collision distribution function and obtaining the macro variables by slightly revised formula $\rho u_\alpha^* = \sum_i e_{i\alpha} f_i + mF_\alpha \delta_t$ (i.e., Eq. (3.7)) if $m \neq 0$.

4.2 Steady Flow through Constricted Tubes

To validate our axisymmetric D2Q9 models, the steady flows through constricted tubes were simulated.

In our study, the geometry of the constrictions is described by Cosine curve. The geometry of the stenose is shown in Figure 4.1. If r_0 is the radius of the

nonstenotic part of the pipe, radius of the stenose $r(x)$ is given out as following

$$r(x) = r_0 - \beta r_0\{1+\cos[\pi x/ S_0]\}/2 \quad (-S_0< x <S_0) , \tag{4.3}$$

where $r_0=D/2$, β=50% is severity of stenose and the axial length of the stenose is $2S_0$. To make flow fully developed and save grid nodes, the upstream and downstream boundaries are at S_1=-3D and S_2=8D as illustrated in Figure 4.1.

In the simulations, the non-equilibrium distribution function extrapolation method (Guo et al. 2002a) was applied for curvature wall boundary. For the inlet/outlet boundary conditions, the pressure or velocity boundary condition treatments proposed by Guo, et al. (2002c) was adopted for its simplicity. At the inlet boundary, a fully developed parabolic velocity profile is specified. In the outlet boundary, the outlet pressure was specified and $\partial \mathbf{u}/\partial x = 0$ was also imposed.

It should notice that axisymmetric boundary conditions are very important in simulations. Without axisymmetric boundary conditions, we have to study the whole computational domain bounded by upper and lower straight walls and the axis should be placed in the center of the computational grid within the computational domain to avoid the singularity. Alternatively, if the axis is placed in the computational grid, source terms for lattice nodes in the axis should be interpolated from those of the upper and lower layer lattices (Lee, Huang and Shu, 2006).

Here we used axisymmetric boundary conditions. For the lattice nodes in the axis, the slip wall boundary condition introduced in Chapter 2 was used. The source terms on these lattice nodes are not necessary to be known. Hence, the singularity problem is avoided.

In our simulations, Reynolds number defined as $Re=U_0D/v$, where U_0 is

central value of the inlet parabolic velocity. The zero velocities are initialized everywhere. For defining steady state, our criterion is

$$\eta = \sum_{i,j} \frac{\left\| \mathbf{u}(x_i, r_j, t+\delta_t) - \mathbf{u}(x_i, r_j, t) \right\|}{\left\| \mathbf{u}(x_i, r_j, t+\delta_t) \right\|} < 10^{-6} \tag{4.4}$$

where the summation is over the entire system.

Firstly, we would like to compare the performance of the three axisymmetric models (model A, B and C) proposed in Chapter 3. The three models are used to simulate the same case with $S_0=D$, Re=50. In the simulation, a uniform grid with $N_x \times N_r$=441×22 (N_r is the lattice nodes in radial direction) was used. The nonstenotic radius is represented by 21 lattice nodes and N_r includes one extra layer beyond the wall boundary. After reach the criterion of Eq. (4.4), they are able to give the same accurate results illustrated in Figure 4.2. In the Figure, the velocity profiles in positions x=0, 0.5D, D and 2D are compared with that of Finite Volume method (FVM). The results obtained by FVM can be regard as accurate results since a fine grid (i.e., 881×41) is used in FVM simulations. In Figure 4.2, we can see that both the axial and radial velocity components agree well with that of FVM.

To run 15000 time steps in this simulation, the CPU time taken by the model A,B and C are 359s, 368s, 389s respectively. It seems that model C takes slightly more CPU time than those of model A and B. It is easy to understand since the $F_\alpha^{(1)}$ in model C is more complex than that of model A, slightly extra effort would be taken to calculate the term of $\omega_i n/2c_s^2 \left(e_{i\alpha}e_{i\beta}/c_s^2 - \delta_{\alpha\beta}\right)\left(u_\alpha^* F_\beta^{(1)} + u_\beta^* F_\alpha^{(1)}\right)$ in Eq. (3.45). Among these models, since model A, B and C are all able to give accurate results and the model B has the simplest form, this model B is subsequently used mainly in all our following applications.

The converge behavior (Relative error η is defined in Eq. (4.4)) of model A, B and C is almost identical which illustrated in Figure 4.3.

For steady flow problem, the case of $S_0=D$, $Re=100$ was also simulated. In the simulation, a uniform grid of $N_x \times N_r=441\times22$ was used. The results were given in Figure 4.4, Figure 4.5 and Figure 4.6. In the Figure 4.4, the velocity profiles in positions $x=0$, $0.5D$, D and $2D$ are compared with that of FVM. Both the axial and radial velocity components agree well with that of FVM. In the Figure 4.5, the streamlines were shown above the axis and the shear stress contours were shown below the axis. The flow is separated and a circulating eddy exists behind the stenose. In the Figure 4.6, the wall vorticity obtained by LBM is compared with that of FVM. It seems the wall vorticity of the LBM solution has small discrepancy with that of FVM solution. That may due to the facts that finite difference method were used to calculate the wall vorticity and the grid we used is not very fine. The scheme to obtain wall shear stress and wall vorticity is illustrated in Figure 4.7. In Figure 4.7, the open square and circle represents the lattice node outside and inside of the boundary respectively. The near-wall fluid lattices are represented by filled circles. Here the wall shear stress and vorticity were approximated by those on the near-wall fluid lattices. The shear stress on lattice node can be obtained through the first order momentum of non-equilibrium distribution function (i.e., Eq(4.1)). After obtaining $\partial_x u_r$ at these lattice nodes through Eq. (4.2), the vorticity can be obtained.

For comparison purpose, a result obtained by the model of Halliday et al. (2001) is also shown. Our analysis of the Halliday et al (2001) model (refer to the part 3.2.4) and present simulation show that the model does not give accurate results for flow through constricted tubes. Figure 4.8 demonstrates that problem.

In Figure 4.8, the velocity profiles obtained by the model of Halliday et al. are compared with those of FVM. It is observed neither the axial nor the radial velocity profiles agree well with those of FVM for case $S_0=D$, $Re=10$. The model of Halliday, et al. (2001) can only give poor results although very fine lattices $N_x \times N_D=881\times 83$ were used (Huang, Lee and Shu, 2004).

4.3 Pulsatile Flow in Tube (3D Womersley Flow)

After our models were validated by simulations of the steady axisymmetric flow problem, an unsteady axisymmetric flow problem was employed here to further validate our axisymmetric models. Since models A, B and C can all give accurate results and their performances of convergence are almost the same, in this section, only model B is used to do further validation.

The unsteady axisymmetric flow problem employed here is the 3D Womersley flow. The 3D Womersley Flow (pulsatile flow in aixsymmetric pipe) is driven by periodic pressure gradient at the inlet of the pipe which is defined as

$$\frac{\partial p}{\partial x} = -p^* e^{i\omega t}, \tag{4.5}$$

where p^* is the maximum amplitude of the sinusoidally varying pressure gradient.

In our study, R is defined as the radius of the circular pipe. ω is the angular frequency and v is the kinetic viscosity of fluid. The Reynolds number is defined as $Re=2U_cR/v$, where U_c is the characteristic velocity defined as

$$U_c = \frac{p^*\alpha^2}{4\omega\rho} = \frac{p^*R^2}{4\rho\nu}, \tag{4.6}$$

which is the velocity that would be observed in the axis of the tube if a constant forcing term p^* were applied in the limit of $\alpha\rightarrow 0$. The Womersley number is defined as $\alpha = R\sqrt{\omega/\nu}$. The Strouhal number is defined as $St=R/(U_cT)$, where T

is the sampling period.

The analytical solution for 3D Womersley flow (Artoli et al., 2002) is

$$u(r,t)=\mathrm{Re}\left\{\frac{p^*}{i\omega\rho_0}\left[1-\frac{J_0\left[\frac{1}{\sqrt{2}}(-\alpha+i\alpha)\frac{r}{R}\right]}{J_0\left[\frac{1}{\sqrt{2}}(-\alpha+i\alpha)\right]}\right]e^{i\omega t}\right\}, \tag{4.7}$$

where J_0 is the zeroth order Bessel function of the first type.

All the simulations in this part began with an initial condition of zero velocity every where, and an initial run of $10T$ steps.

It should be noticed that the maximum velocity U_{max} appear in tube axis during a sampling period would less than character velocity U_c for case α>0. For a case of α>>1, the maximum velocity U_{max} would be much less than U_c. That is illustrated in Figure 4.9, which shows the normalized maximum velocity in tube axis U_{max}/U_c, and the phase lag of the velocity field, ζ (normalized by π), as a function of α. In the figure, the numerical results agree well with the analytical solution. It seems when oscillatory pressure gradient changes very fast and it is impossible for velocity field to reach the fully developed velocity profile with maximum value U_c.

In the 3D Womersley flow simulations, to implement the uniform oscillatory pressure gradient, besides the scheme of both inlet and outlet pressures specified, the scheme of adding an equivalent oscillatory body force is also applicable (Cosgrove et al. 2003). When applying a uniform equivalent body force, the periodic boundary conditions should be imposed at the open ends of the pipe. After each collision step was implemented, the following oscillatory body force term (Guo et al. 2002b)

$$S_i'=\omega_i(1-1/2\tau)\left[\left(e_{i\alpha}-u_\beta\delta_{\alpha\beta}\right)/c_s^2+\left(e_{i\beta}u_\beta\right)e_{i\alpha}/c_s^4\right]F_\alpha \quad i=1,2\ldots..,8, \tag{4.8}$$

should be added into the post-collision distribution function f_i^+ as Eq. (4.9).

$$f_i^+(x,r,t) = f_i^+(x,r,t) + S_i' \qquad i=1,2\ldots..,8. \tag{4.9}$$

In above Eq. (4.8), **F**=($p^*\cos(\omega t)$, 0) is the body force. As the analysis of Guo et al. (2002b) shown, the present source term (i.e., Eq(4.8)) should be accurate. It is also noticed that in our previous work (Lee, Huang and Shu, 2005), the oscillatory body force term was $S_i' = \omega_i e_{i\alpha} F_\alpha / c_s^2$ (i=1,2…..,8) and is different from the present source term used. That is also valid since T in our previous work is very large (Guo et al. 2002b).

4.3.1 Convergence Criterion and Spatial Accuracy

To evaluate the error between the numerical and analytical solution, we introduce a velocity error formula which is illustrated in Eq. (4.10). At each time step the error can be defined as

$$\xi = \frac{\sum_i |u(r_i) - u_a(r_i)|}{\sum_i |u_a(r_i)|}, \tag{4.10}$$

where $u(r_i)$ is the numerical solution, $u_a(r_i)$ is the analytical velocity at r_i in middle pipe. The overall average error $<\xi>$ is averaged over the period T. For all the cases in this study, the convergence criterion was set as following

$$\frac{\sum_{\mathbf{x}} |u(\mathbf{x}, t+T) - u(\mathbf{x}, t)|}{\sum_{\mathbf{x}} |u(\mathbf{x}, t+T)|} \le 10^{-6}, \tag{4.11}$$

where t was usually chosen as t=1+nT in this study.

As we know, for the wall boundary condition, the extrapolation scheme (Guo et al. 2002a) or bounce-back scheme with interpolation (Bouzidi et al. 2001) can

be used. For the axisymmetric boundary condition, specular reflection scheme (i.e., slip wall boundary condition) or axisymmetric extrapolation scheme can be used. In this part, the overall spatial accuracy of the axisymmetric model B incorporating difference boundary conditions was evaluated. To eliminate the compressible effect and focus on the spatial accuracy evaluation, the equivalent oscillatory body force (Eq. (4.8)) was added into the post-collision distribution function and periodic boundary condition was used for two open ends of the pipe.

Here in all simulations, the pipe length was chosen as $4N_r$, where N_r is the number of lattice nodes in the radius (usually N_r excludes the extra layers outside the wall boundary). Two set parameters for our simulations of cases α=7.93 and α=3.17 when N_r =20 are listed in Figure 4.1. For a certain α, as N_r was increased α was kept constant by varying the period T accordingly within the range $T>10^3$. For cases of α=7.93 and α=3.17, the corresponding τ was kept constant at 0.6 and 1.0 respectively. For all cases, p^* was kept constant at 10^{-4}.

Firstly, the overall accuracy of the above two wall boundary conditions combining with specular reflection scheme was investigated. Figure 4.10 illustrates the global errors as a function of the pipe radius N_r. In Figure 4.10, the solid lines represent the linear fits and the slope of each line is labeled. It seems the LBM incorporating the extrapolation wall boundary condition and specular reflection scheme (i.e., 'Guo+slip' in graph), is around second-order in space since the slope of the lines are -1.89 (α=7.93) and -2.01 (α=3.17). While the Bouzidi's wall boundary condition slightly decrease the overall accuracy because the slope of the lines are -1.61 (α=7.93) and -1.83 (α=3.17).

The overall accuracy of Guo's wall boundary condition combining with axisymmetric extrapolation scheme for axisymmetric boundary was investigated.

Figure 4.11 shows the global errors as a function of the pipe radius N_r for α=7.93. It is found that this combination can only give first-order accuracy.

Hence, in the following simulations of this Chapter, the extrapolation wall boundary condition and specular reflection scheme for axisymmetric boundary are applied.

4.3.2 Validation by Cases with Different Womersley Number

In this part, the 3D Womersley flow results obtained by axisymmetric model B would be compared with the analytical solution. Here the scheme of adding oscillatory body force term was used to implement the uniform oscillatory pressure gradient.

As a typical Reynolds number in the Abdominal aorta is about 1250 and a typical Womersley number α=8 (Artoli et al., 2002), in our simulations, firstly the case of Re=1200, α=7.93, T=1200, τ=0.6 was performed with N_r=21 and the corresponding U_c=1.0. The numerically evaluated velocity profiles along the radius are compared with the exact analytical solutions of Eq. (4.7) in Figures 4.12. In the figure, the velocity is normalized by U_c and the r-axis is normalized by the radius of the tube. Although in this case U_c=1.0, the U_{max} observed in whole oscillatory period is only about 0.063, M=0.063$\sqrt{3}$≈0.109<<1, which satisfy the limit of LBM.

In the above study, parameters T=1200, τ=0.6, U_c=1.0 were chosen to avoid numerical stability and save CPU time. In the following, an example is given to illustrate this issue. If U_c=0.1 was assigned, to fix the parameter Re and α and use the same grid, the ν should be 1/300 and then τ is 0.51 with τ very close to 0.5,

numerical instability may appear. On the other hand, the corresponding T value would be 12000 and not just 1200. Hence much more CPU time is required. However, U_c=1.0 in this case is correct as in the whole period of the pulsatile flow M<<1.

The overall numerical average error of the above case is about 1.23%. While Artoli, et al. (2002) mentioned that the overall average error for almost the same 3D case is around 7% using standard D3Q19 model with the curve boundary condition proposed by Bouzidi, et al. (2001). Present better performance may be due to the incompressible D2Q9 model (He and Luo, 1997a) we used in our axisymmetric model derivation. The second order extrapolation wall boundary treatments may also account for the better performance.

In the following, two more cases of different Womersley number were simulated. Figure 4.13 and Figure 4.14 show the velocity evolution of an oscillation over a period for α=1.373 and 24.56, respectively. For the case illustrated in Figure 4.13, T=4000, Re=1.2, τ=1.5, U_c=0.01, N_r= 21, which is a viscous-dominated system (Cosgrove et al. 2003). For case illustrated in Figure 4.14, T=1000, Re=1920, τ=0.7, U_c=0.8, N_r=81, which is a momentum-dominated system in the laminar regime (Cosgrove et al. 2003).

As we know, the shear stress tensor computation is important (e.g., for the study of hemodynamics). In LBM simulations, the shear stress tensor σ_{xr} can be conveniently calculated from Eq. (4.1). This calculation is usually implemented during the collision process. Here an example with α=7.93, T=1200, τ=0.6, Re=1200, N_r=21 are shown in Figure 4.15. In the figure, the numerically evaluated shear stress were compared with analytical solutions along the radius at time t=nT/16 (n=1,…,16). The numerical results agree well with analytical solution.

4.3.3 Comparison of Schemes to Implement Pressure Gradient

All the above accurate results were achieved through adding force term into post collision step. Here, we would also like to make further investigation on the two schemes to implement pulsatile pressure gradient. In the Table 4.2, the performance of two schemes was compared. Here, in all of the cases considered, α=3.963, mesh size $N_x \times N_r$=41×21, T=4800 and the convergence criterion is Eq. (4.11).

For the scheme of specifying inlet/outlet pressure, from the derivation in Chapter 3, we notice that the value $L_x/(c_s T)$ should be small enough to neglect the compressibility effect due to the time variation of pressure field (He and Luo, 1997a). In these cases, T=4800>>L_x/c_s=40$\sqrt{3}$, which satisfy the limit. The physical meaning is that in the range of the distance L_x, the time, T, during which the flow field undergoes a macroscopic change must be greater than the time, L_x/c_s (He and Luo, 1997a).

From Table 4.2, we can see that for the scheme of specifying pressure on inlet/outlet boundary, the overall average error increase with Δp between two ends or Reynolds number, which is consistent with the conclusion for 2D Womersley flow (He and Luo, 1997a). For the scheme of adding forcing term, the overall average error decreases slightly with Δp. That also agrees with results of Artoli, et al. (2002). It seems that the scheme of applying additional forcing term has advantages than the scheme of specify pressure on inlet/outlet boundary for simulations of the 3D Womersley flow, which has uniform pressure gradient at any time.

4.3.4 Compressibility Effect and Comparison with Halliday's Model

In this section, the compressibility effect was investigated in detail. One quantity that may represent compressibility is the mean variation of density. It is defined as

$$\Delta = \frac{1}{\rho_0}\sqrt{\sum_{x,t}\left((\rho(x,t)-\rho_0)^2\right)/N}\,, \tag{4.12}$$

where the mean density is ρ_0 and N is the total number of nodes. For comparison, three cases of Re=1200, α=7.93 were simulated by our axisymmetric model and Halliday's model. In all simulations, $N_x \times N_r$ =41×21, the Re and α were kept constant through varying T , p^* and τ value. In the three cases, the maximum Mach number $M_{\max}$ in tube axis are 0.109, 0.055 and 0.022 respectively. The scheme of specifying inlet/outlet pressure was used to implement pressure gradient. The results of density fluctuation were listed in Table 4.3. The table shows that for both models of Halliday and present,

$$\Delta\,(M_{max}=0.055) \approx \frac{1}{4}\,\Delta\,(M_{max}=0.109),$$

and

$$\Delta\,(M_{max}=0.022) \approx \frac{1}{25}\,\Delta\,(M_{max}=0.109).$$

These results demonstrated that Δ is proportional to M^2. The Δ obtained by our model and Halliday's model are almost identical. In the following, another comparison was performed to show the advantage of our model more clearly.

As we know, the velocity field error can also be employed to investigate the compressibility effect (He and Luo, 1997a). In this comparison, four cases with α=3.963, $N_x \times N_r$ =41×21, T=4800 were simulated using both present model and the

Halliday's model. The scheme of specifying inlet/outlet pressure was chosen to implement pressure gradient. Table 4.4 shows the velocity field error measured by θ and $<\theta>$. θ at time t is defined as

$$\theta = \frac{\sum_i \left(u(r_i,t) - u_a(r_i,t)\right)^2}{\sum_i u_a{}^2(r_i,t)}, \tag{4.13}$$

where the summation is over the radius in middle pipe and the overall average error $<\theta>$ is averaged over the period T. The θ_{max} means the maximum value of θ in a sampling period. In Table 4.4, the $M_{\max}$ in tube axis for case 1 to 4 are 0.054, 0.108, 0.272 and 0.544, respectively.

Comparing the maximum particular velocity error and the overall numerical average errors of two models in Table 4.4, it is observed that as $M_{\max}$ in tube axis increase, the corresponding errors of Halliday's increases much faster than present incompressible model. The observation is consistent with conclusion got for the standard and incompressible D2Q9 models (He and Luo, 1997a). Hence, comparing with Halliday's model, present model can eliminate the compressibility effect.

4.3.5 Comparison with 3D LBM:

To show the performance of the proposed model, several cases were also simulated by the 3D incompressible LBGK model. The 3D simulation is based on the D3Q19 lattice velocity model. The mesh size used for the axisymmetric model is $N_x \times N_r$ =81×21, while in the 3D LBM simulation, the mesh size used is $N_x \times N_y \times N_z$= 81×41×41. Notice in 3D simulations the curvature wall boundary treatment (Guo et al., 2002a) was applied. In this comparison, two cases with parameters of α=7.93, T=1200, τ=0.6 were simulated. Table 4.5 listed the overall

numerical average error, period number to reach convergence criterion Eq. (4.11) and the CPU time required by our axisymmetric model B and 3D LBM.

All the computations were carried out on a super computer (Compaq ES40: total performance of 5300 Mflops) in the National University of Singapore. It can be observed from Table 4.5 that the periodic number of iteration required by 3D LBM is equal to that of the axisymmetric model. However, the 3D LBM simulation takes about 280 times more CPU time than present axisymmetric model to obtain solutions. Hence, our axisymmetric model is much more efficient for such an axisymmetric pulsatile flow problem. According to the overall average error, the axisymmetric LBM result is slightly better than the 3D LBM result. One possible reason is that the axisymmetric model did not involve the error in the circumferential direction.

4.4 Flow over an Axisymmetrical Sphere Placed in a 3D Circular Tube

To further demonstrate the validation of our axisymmetric D2Q9 model, the flow over an axisymmetrical sphere placed in a 3D circular tube is also studied here. If the flow field is assumed axisymmetric, our present axisymmetric D2Q9 model can be used to study this axisymmetric flow. The geometry of the ball and circular tube are illustrated in the Figure 4.16. The diameter of the ball is D and the diameter and length of tube are $2D$ and L, respectively. The Reynolds number is defined as $Re=U_0 D/\nu$, where U_0 is the maximum velocity in the inlet parabolic velocity profile. In all our LBM simulations, there are 30 lattice nodes in the radius of tube and uniform square grid is used.

Using LBM, the cases of Re=50, 100 and 150 were carried out. The

streamlines for these cases are illustrated on Figure 4.17. For Reynolds number 50 and 100, the flows are passing over the sphere without separation. For Re=150, there is a circulation zone immediately behind the sphere.

To validate our LBM results, the axial velocity profiles in different axial positions are compared with those obtained by FVM in Figure 4.18. It seems that the axial velocity profiles all agree very well with those given by FVM. The axial and radial velocity profiles in different axial position for Re=150 are also compared with those given by FVM in Figure 4.19. It is found that both the axial and radial velocity profiles given by our LBM simulation are highly consistent with those given by FVM.

4.5 Test of Multi-block Strategy by 2D Driven Cavity Flows

To validate our 2D multi-block LBM solver, in this part, benchmark problem of 2D driven cavity flow was simulated. In this problem, the top boundary moves from left to right with velocity U. In all of our simulations, the uniform top velocity was set as U=0.1 and character length L=256. The non-equilibrium distribution function extrapolation method (Guo et al. 2002c) was used for top moving boundary condition and the non-slip boundary condition (Guo et al. 2002a) was also used for the other three stationary wall boundary. In our simulations, Cartesian coordinates with the origin located at lower left corner were used. Initially, the velocities of all nodes except the top nodes are set to zero. For all the cases run in this section, steady state is reached when the difference between the maximum value of the stream function for successive 10,000 steps is less than 10^{-5}.

Our simulations were carried out for Re=400 using (i) a single block with a grid 67×67 (i.e., 64 lattice units in one side), and (ii) two block with a upper fine grid 133×37 and a lower coarse grid 67×50. For the coarse block, $\delta x_c=\delta t_c=4$ and $\tau_c=0.548$, for the fine block $\delta x_f=\delta t_f=2$ and $\tau_f=0.596$. Figure 4.20 shows the pressure contours of the single block case and multi-block case. Figure 4.21 shows the vorticity contours of the two cases. The vorcitity is normalized by $\mu U/L$. For the figures of the multi-block case, the interface between fine and coarse mesh is also plotted. It is observed that in the single-block case, since only 64×64 grid points with dx=4 cover the physical domain 256×256, oscillations exist for the pressure and vorticity contours in the upper corner regions. While for the results of multi-block case, the pressure and vorticity contours are smoother and resolution on upper corner region is improved significantly.

Figure 4.22 shows the stream function for above two cases. The ψ_{max} value for the primary vortex and the ψ_{min} values for the lower left and lower right vortices along with the x and y coordinates of the center are listed in Table 4.6. The maximum stream function value for single-block and multi-block case are 0.1108 and 0.1092 respectively. Compared with the result of Ghia et al. (1982), for stream function, the single-block case is slightly more accurate than the multi-block case. That may be due to the interpolation error introduced at the interface.

To investigate the spatial convergence rate, two relative velocity errors, the $L1$ and $L2$ error were calculated according to the following formula

$$E1=\frac{\sum_{x,y}|u_1-u_0|+|v_1-v_0|}{\sum_{x,y}|u_0|+|v_0|} \tag{4.14}$$

$$E2=\sqrt{\frac{\sum_{x,y}(u_1-u_0)^2+(v_1-v_0)^2}{\sum_{x,y}\left(u_0^2+v_0^2\right)}} \tag{4.15}$$

where *u, v* are the *x* and *y* components of the velocity at a lattice node, respectively. The subscript 0, 1 indicate the 259×259 case and two-block cases, respectively and the sums are taken over the entire lattice system. Figure 4.23 shows the overall spatial convergence rate of single-block cases and two-block cases. The lattice units of multi-block cases are based on the horizontal lattice units on the lower coarse grid. For single-block case and multi-block case with same lattice units, although the higher resolution obtained in upper corner region in multi-block case, the errors $E1$ and $E2$ of multi-block case are slightly larger than those of single-block case due to the interpolation error. However, it is found that the overall convergence rate of multi-block cases is approximately second-order in space. Hence, the linear interpolation accuracy is consistent with the second-order spatial accuracy of LBM. The above numerical experiments further proved that the common error introduced in the solution on the interface between coarse and fine grids due to the linear interpolation of $f_i^{eq,c}$'s from the neighboring nodes of the coarse grid is consistent with the order of accuracy of the solution on the coarse grid (Fillippova and Hanel, 2000).

4.6 3D Flow through Axisymmetric Constricted Tubes

In this part, our 3D LBM program would be validated by the cases of 3D flow through axisymmetric constricted tubes. Accuracy and efficiency of 3D LBM solver are compared with that of finite volume solver (i.e., FLUENT).

Geometry of the constrictions is described by a Cosine curve. The geometry of the stenosis is shown in Figure 4.24. If r_0 is the radius of the nonstenotic part of the tube, radius of the stenosis $r(x)$ is given by following formula

$$r(x) = r_0 - \beta r_0\{1+\cos[\pi x/D]\}/2 \quad (-S_0 < x < S_0) \tag{4.16}$$

where $D=2r_0$, $2S_0$ is the length of stenosis and β=50% is severity of the stenosis. In the cases studied here, $S_0=D$.

In our simulations, the 3D Cartesian coordinates with the origin located at center of the constriction were used. In Eq. (4.16), $r=\sqrt{y^2+z^2}$. To make flow fully developed and save grid nodes, the upstream and downstream boundaries are at S_1=-3D and S_2=8D as illustrated in Figure 4.24.

In our LBM simulations, the 3D uniform cubic lattices were used and for curved wall boundary condition, the bounce-back scheme (Bouzidi et al. 2001) was used. Initially the velocities of all lattices are set as zero and the criterion of steady state is defined as

$$\sum_{i,j}\frac{\sqrt{[u(i,j,t+1)-u(i,j,t)]^2+[v(i,j,t+1)-v(i,j,t)]^2}}{\sqrt{[u(i,j,t+1)]^2+[v(i,j,t+1)]^2}}<10^{-4} \tag{4.17}$$

where i, j are the lattice nodes in $z=0$ plane and $u(i,j,t)$, $v(i,j,t)$ are x,y component velocity at time t respectively.

Firstly, to investigate whether the flow is axis-symmetric is interesting for such 3D simulation. To measure the asymmetry, a variable of state, χ is defined as (Luo, 1997)

$$\chi=\sum_{\mathbf{x_{i,j}}\in\Omega}\left[u(\mathbf{x_{i,j}})-u(\overline{\mathbf{x_{i,j}}})\right]^2 \tag{4.18}$$

where Ω is one of eight planes illustrated in Figure 4.25. Plane i can be described in cylinder coordinate system by $\varphi=(i-1)\pi/4$, ($1\le i\le 8$). $\overline{\mathbf{x_{ij}}}$ is an axisymmetric node of $\mathbf{x_{i,j}}$. It is obvious that when the flow pattern is axisymmetric, χ=0. However, the value of χ, is not exactly zero when the system reaches its steady state, which depends on the system size in the simulation. To investigate value of χ, cases of Re=10, 50 and 150 were simulated. Through

observation made with two lattice system sizes, $N_x \times N_y \times N_z$ = 221×23×23 (i.e., 20 lattice units in a diameter) and 441×43×43 (i.e., 40 lattice units in a diameter), it is found that the values of χ at the steady state decays to zero as N_x^{-3}.

Then, the results of 3D LBM and FVM are presented and compared. Appling the two solvers, the case of *Re*=10, 100 are simulated. In the following figures of velocity comparison, due to axis-symmetry, only the data along a radius are shown for results obtained from FVM.

The case of *Re*=10 was simulated using a lattice size lattice system sizes $N_x \times N_y \times N_z$ = 331×33×33 (i.e., 30 lattice units in a diameter). In Figure 4.26, the normalized axial and radial velocity component *U*, *V* profiles in different *x* positions, wall vorticity and pressure drop along axis obtained by Lattice BGK method are compared with those of FVM. It is found that the results obtained by LBGK and FVM agree very well. The wall vorticity of the LBGK solution has small discrepancy with that of FVM. That is easy to explain since the finite difference method was involved in vorticity calculation and only 31 fluid lattice nodes in a nonstenotic diameter.

In Figure 4.27, for case of *Re*=100 and $N_x \times N_y \times N_z$ = 441×43×43 (i.e., 40 lattice units in a diameter), comparisons of the normalized axial and radial component velocity at different axial position are illustrated. The results of LBGK method agree well with that of FVM.

In the following part, the accuracy and efficiency of 3D LBM solver are investigated in detail. For comparison purpose, a pressure-based finite-volume Navier-Stokes solver, FLUENT (a commercial software), is used. When applying FLUENT, we used an implicit solver, which is relatively efficient in obtaining steady-state solutions. However, the LBM is a time-accurate explicit solver. We

should notice the difference when we compare their efficiency. Actually, some other studies (e.g., Noble *et al.*, 1996) have found that the LBM is as efficient as conventional methods when similar explicit time-marching schemes are used.

For comparison, three uniform meshes with $N_x \times N_y \times N_z$ = 111×13×13(*coarse*), 221×23×23(*medium*) and 441×43×43(*fine*) grid nodes are used for LBGK solver to simulate case of *Re*=10. Each finer mesh is obtained by doubling the number of cells of the coarser mesh in each direction. Unstructured linear brick element meshes with equivalent total grid nodes are generated for FVM solver.

The overall order of accuracy of a solution can be estimated using the following formula (Ferziger and Peric, 1999)

$$n \approx \frac{\lg\left(\sum|\phi_{2h} - \phi_{4h}|/N\right) - \lg\left(\sum|\phi_h - \phi_{2h}|/N\right)}{\lg 2} \tag{4.19}$$

where φ represents a dependent variable; N is the total number of points compared; and subscripts *h,2h,4h* stand for solutions on *fine*, *medium*, and *coarse* meshes with grid spacing doubled each time. Here, the accuracy is presented in terms of u-velocity component. With $\varphi=u$ in Eq. (4.19), the order of accuracy for LBGK solver estimated from the solutions with the three grids is 1.89. The average discretization error of a simulation on mesh h can be estimated via the Richardson extrapolation (Ferziger and Peric, 1999) as

$$\varepsilon = \frac{Error}{\sum|\phi_h|/N + Error} \quad \text{where} \quad Error \approx \frac{\sum|\phi_h - \phi_{2h}|/N}{2^n - 1}. \tag{4.20}$$

In the above, the denominator in the first equation is the estimated average "exact'' solution and n in the second equation is the order of accuracy of the solver obtained from Eq. (4.19) (Lai *et al.*, 2001). If Eq. (4.20) is used to estimate the average errors on the *medium* and *fine* meshes for u velocity, it is found that LBGK solutions have discretization errors of about *1.33%* and *0.40%* for the

medium and *fine* mesh, respectively.

The efficiency of each solver is evaluated by comparing the respective computing times required. This comparison is not straightforward. To minimize the influence of computers and convergence criterion, in this study, both the LBGK solver and FLUENT are executed on a super computer (Compaq ES40: total performance of 5300 Mflops) in the National University of Singapore. The initial conditions of the flow field are the same. The residual used to monitor the convergence is defined using the *u*-momentum equation for two solvers, and they are defined as (Lai *et al.*, 2001)

LBM: $\sum \left| \frac{u-u^0}{\delta t} vol \right|$ and

FLUENT: $\sum \left| \left(u\frac{\partial u}{\partial x} + v\frac{\partial u}{\partial y} + w\frac{\partial u}{\partial z} - \nu(\frac{\partial^2 u}{\partial x^2} + \frac{\partial^2 u}{\partial y^2} + \frac{\partial^2 u}{\partial z^2}) + \frac{\partial p}{\partial x} \right) vol \right|$

Note that all the computations are carried out on a single-CPU of the computer Compaq ES40, which does not take parallel advantage of the lattice Boltzmann method. In Table 4.7, it seems that the lattice BGK simulation takes about 6-10 times more CPU time to obtain the steady-state solutions when compared with FVM (FLUENT) implicit solver.

4.7 Three-dimensional Driven Cavity Flow

Flow structure in the 3D driven cavity is more complex than 2D driven cavity, as shown by Iwatsu et al. (1989). The presence of side-walls produces totally 3D vortex structure in cavity. Due to the corner singularity in 3D driven cavity flow, the macro-dynamic variables gradient near to the region of upper corner is very high. 3D simulations are very time-consuming and it is hard to obtain accurate results near the region with a uniform coarse grid for computation. Here the

multi-block strategy applied to the 3D driven cavity problem. The multi-blocks is constructed based on a single coarse block $N_x \times N_y \times N_z = 65 \times 65 \times 65$ as shown in Figure 4.28. The grid resolution near to the upper corner (block A and B) is increased by a factor of 2. In this multi-block case $\delta x_c=1$ and $\delta x_f=0.5$. The number of Lattices for block A,B,C,D and the range in *x,y,z* direction are listed in Table 4.8. For comparison purpose the simulation of cubic driven cavity flow with a uniform grid $N_x \times N_y \times N_z = 65 \times 65 \times 65$ is also performed.

There are two schemes to handle boundary conditions. For the first scheme, the side length of cubic cavity is $H=62\delta x_c$ with 63 coarse lattice nodes. The coarse block is located in Cartesian coordinates $-\delta x_c \le x \le 63\delta x_c$, $-\delta x_c \le y \le 63\delta x_c$, $-\delta x_c \le z \le 63\delta x_c$. All of the six most outside layer lattices are defined as "wall nodes" with $q=0$ (refer to Figure 2.4) to implement the curve boundary treatment. The other inner $63 \times 63 \times 63$ lattice nodes are defined as "fluid nodes". Initially, the velocity at all "fluid nodes", except the top layer "fluid nodes", is set to zero and uniform fluid pressure $p_0=1.0c_s^2$ is imposed initially. The non-equilibrium distribution function extrapolation method (Guo et al. 2002c) was used for top moving boundary condition. The upper corners are singularity points can be treated as part of lid or stationary wall, our test shown that there is little difference.

For the second scheme, the top moving lid can be located between two layers (e.g., $y=63\delta x_c$, $y=62\delta x_c$) with $q=0.5$ and other stationary walls are all located between two lattice layers (e.g., the bottom wall can be located between $y=-\delta x_c$ and $y=0$) with $q=0.5$ (refer to Figure 2.4). Hence, the side length of cubic cavity is $H=63\delta x_c$. Since the above two schemes give similar results, here only the result of first treatment is presented.

For the multi-block case, it is easy to understand that the boundary conditions

can be handled with the first scheme or combine of both schemes. Here we also only present the results with first treatment.

Next, the results of single-block case and multi-block case for Re=400 are presented. The Reynolds number defined as $Re=UH/v$. The top lid moves with velocity U=0.2 in x direction. For incompressible model, U=0.2 is still valid. For the multi-block case, the relaxation time parameter is τ_c =0.593 for the coarse grid block and τ_f =0.686 for the fine-grid block. Here, the Multi-block Navier-Stokes solution obtained by Salom (1999) used as the benchmark result.

The positions of the centers of the primary vortices in the plane $z=H/2$ are listed in Table 4.9. It seems the result of multi-block case is more accurate than the single-block case.

In Figure 4.29, the u_x profiles at $x/H=z/H$ =0.5 using multi blocks and a single block is compared with the benchmark solution (Salom, 1999) for Re=400. In Figure 4.30, u_y profiles at $y/H=z/H$ =0.5 using multi blocks and a single block is also compared. From Figure 4.29 and Figure 4.30, we can see that both single-block solution and multi-block solution agree well with the benchmark result. The solution of multi-block LBGK is better than that of single coarse block.

From the above comparison, we can see that although the single block method with 65×65×65 lattices can obtain satisfactory velocity field, the multi-block method can improve the numerical accuracy.

Figure 4.31 shows a pressure contour of $p=0.3318$ from the single-block case. In Figure 4.31, the pressure contour exhibits oscillations near the upper corner due to the insufficient resolution near the singularities. Figure 4.32 shows the same pressure contour obtained from the multi-block case. It is observed that except the

very small oscillation near the conjunction area of moving lid and stationary walls, the pressure contour becomes much smoother than that in Figure 4.31. In Figure 4.32, we also observed that the pressure contour is rather continuous across the interface of block B, C and interface of block B, D. Hence, the multi-block method can highly improve the accuracy of pressure field near the singularity corner area.

Finally, to validate the spatial and temporal interpolation of post-collision distribution functions, particle paths, pressure, mass flux and momentum flux near the block interfaces were examined in detail in the following. For the multi-block LBGK method, the interpolation is only applied to distribution function and other macro-dynamic variables are conserved automatically across the interfaces (Yu et al, 2002).

Figure 4.33 illuminates a picture of particle paths. The particle paths are all pass through in the secondary eddy area. For observation convenience, only part of the each particle path is shown. The particle paths are all continuous across the interfaces.

Figure 4.34 shows the pressure contours on the interface between the block B and C. The dashed curves represent the contours in fine grid B and the solid curves represent the contours in coarse grid C. The dashed curves and solid curves are match very well. It is also observed that the contours are very smooth except the conjunction area of moving lid and stationary wall. The area shown in Figure 4.34 and Figure 4.35 is $x=47\delta x_c$, $y\in[48\delta x_c, 61\delta x_c]$, $z\in[\delta x_c, 61\delta x_c]$. Figure 4.35 shows that mass and momentum fluxes on the interface between the block B and C, where $\rho = p/c_s^2$. The dashed contours all agree well with the solid contours. The mass ρu_x, ρu_y, and momentum ρu_x^2 cross the interface seems very continuous.

The 3D multi-block LBGK cases are simulated on a super computer (Compaq ES40: total performance of 5300 Mflops) in the National University of Singapore. The CPU time for this multi-block case is about *2,360* minutes. There are about 525,000 lattice nodes (280,000 fine lattice nodes and 245,000 coarse lattice nodes) in the computational domain. If a single fine block $N_x \times N_y \times N_z$ =127×127×127 was adopted, totally about 2,048,000 lattices, the CPU time and memory requirement may increase dramatically. Considering one time step in the coarse grid requires 2 time steps in fine grid block, for a single uniform fine block, the CPU time for the single fine block case can be estimated as

$$2{,}360 \times (2{,}048{,}000 \times 2)/(280{,}000 \times 2 + 245{,}000) \sim 12{,}000 \text{ min (7.3day)}$$

Hence, here the multi-block LBGK method can save more than 80% CPU time compared with uniform fine case while the multi-block method can still obtain accurate resolution in most regions.

4.8 Multi-Block for 3D Flow through Stenotic Vessels

Here, a 3D test case of fluid flow through constricted circular pipe is investigated. The geometry of the stenosed tube is the same as that illustrated in Figure 4.24 and Eq. (4.16) with $S_0=D/2$.

For this case, the curved boundary treatment is important. Figure 4.36 shows a 2D projection of the discretized domain at $x=3.0D$ and the boundary nodes (denoted by open circular) on the *yz* plane where tube diameter is 16 lattice units. Geometrically, the fraction of the intersected link $q \in [0,1)$ is not constant over the entire boundary for the simulation of the pipe flow.

A case of $Re=50$ with a single block $N_x \times N_y \times N_z$ =177×19×19 (i.e., 16 lattice units in a diameter) was simulated. The parameter are $U=0.1$ and $\tau=0.596$.

However, the calculation procedure is unsuccessful and results cannot be obtained due to numerical instability. Because there are only 8 lattice units for throat diameter, this single block seems too coarse to describe such a tube with complex geometry. Hence, we refined the grid resolution of region near the stenose increased by factor 2, the multi-block strategy illustrated in Figure 4.37. The front coarse block lattices is $N_x \times N_y \times N_z = 25 \times 19 \times 19$, $x \in [-3.0D, -1.5D]$, the rear coarse block $N_x \times N_y \times N_z = 105 \times 19 \times 19$, $x \in [1.5D, 8D]$, For the fine block involving the throat $N_x \times N_y \times N_z = 101 \times 37 \times 37$, (i.e., 32 lattice units in a diameter), $x \in [-1.5625D, 1.5625D]$.

The multi-block case for Re=50 is successful. The u,v velocity profiles at x=0.5D, D and 2D are illustrated in Figure 4.38. For comparison, the solution obtained from a pressure-based finite-volume Navier-Stokes solver (FLUENT, a commercial software) is used as a benchmark in this study. To get accurate result, the Navier-Stokes solution was obtained from very fine meshes. Both the u_x and u_y component velocity profiles at different x position agree very well with those of FLUENT solution. To demonstrate the velocity continuity across the interface, Figure 4.39 shows the exemplary particle paths in this case. We can see the velocities conserved continuity crossing the interface.

From this 3D multi-block case, we can see that adopting a fine grid in complex geometry regions can get high resolution in these regions and satisfy the LBM stability requirement. While on the other region, coarse mesh may be enough to obtain accurate resolution. Hence multi-block LBM can save CPU time as well as memory compared with the case with a single fine grid.

4.9 Summary

As we can see in section 4.1, with the implementating our axisymmetric model, most of the velocity derivations can be conveniently calculated from appropriate higher order momentums of non-equilibrium distribution function. Through using our axisymmetric boundary conditions, the singularity problem in simulations of Halliday et al. (2001) is avoided.

In simulations of flow through a constricted tube, compared with FVM solution, our axisymmetric model A, B and C can all give accurate results while the model of Halliday et al. (2001) can only give relatively poor result. Since the model B has the simplest form, this model is subsequently used mainly in all our applications.

The 3D Womersley flow simulations with different Reynolds number and Womersley number further validated our axisymmetric model B. The LBM incorporating the extrapolation wall boundary condition and specular reflection scheme (i.e., 'Guo+slip' in graph), is around second-order in space. While the spatial convergence ratio of Bouzidi's wall boundary condition is about 1.6.

It is found that applying additional forcing term can eliminate the overall average error in velocity field than the scheme of both pressures on inlet and outlet boundary specified for simulations of the 3D Womersley flow, which has uniform pressure gradient at any time.

It is observed that compared with Halliday's model, the present model can eliminate the compressibility effect. It is also observed that our axisymmetric model is much more efficient for such an axisymmetric pulsatile flow problem than direct 3D LBM simulation. The study of flows over an axisymmetrical sphere placed in a 3D circular tube further validates our models.

The multi-block strategy was tested here to solve flow problems efficiently and achieve higher resolution in regions involving large gradient of macro-dynamic variables, the whole computational domain was decomposed into several sub-domains. Some sub-domains adopted fine grids, the others adopted coarse meshes.

In our study, 2D driven cavity flows were simulated to test the accuracy of linear interpolation in interface of coarse mesh and fine mesh. Our numerical experiments further proved that the common error introduced in the solution on the interface between coarse and fine grids due to the linear interpolation in space and time is consistent with the order of accuracy of the solution on the coarse grid.

The accuracy and efficiency of 3D LBM solver are tested through simulations of steady flow through constricted tube. Our 3D LBM solver approximately has second-order accuracy in space (i.e., spatial convergence rate is 1.89). It seems that the 3D LBM simulation takes about 6-10 times more CPU time than 3D FVM (FLUENT) implicit solver to obtain the steady-state solutions.

Two 3D multi-block cases were simulated to validate the bilinear interpolation on the interface of coarse grid and fine grid. One is the 3D driven cavity flow and the other is the 3D steady fluid flow through axisymmetric constricted tubes. It seems the solution of the 3D multi-block LBGK is more accurate than that of a single block. The continuity of pressure, velocity, mass and momentum fluxes on interfaces were presented. For simulation of 3D flow through axisymmetric constricted tube, multi-block case improves numerical stability of single-block case and obtained accurate result.

Table 4.1 Parameters for simulations of cases α=7.93 and α=3.17 when N_r =20

	α=7.93	α=3.17
p*	0.0001	0.0001
T	1200	1500
τ	0.6	1.0

Table 4.2 The overall average error 〈ξ〉 comparison for two schemes to implement the pressure gradient

Scheme / Cases	Scheme of Addition Force term 〈ξ〉	Scheme of Specify pressure on inlet/outlet BC 〈ξ〉
Re=12, p*=10^{-5}	8.14e-3	9.01e-3
Re=120, p*=0.0001	6.88e-3	1.54e-2
Re=600, p*=0.0005	6.78e-3	6.62e-2

Table 4.3 Mean density fluctuation

Models / Cases	Halliday's model	Present model
	Δ (%)	Δ (%)
M_{max}= 0.109, τ=0.6 , p*=0.001 c_s^2, T=1200	1.657	1.659
M_{max}= 0.055, τ=0.55 , p*=0.00025 c_s^2, T=2400	0.4117	0.4118
M_{max}= 0.022, τ=0.52, p*=0.00004 c_s^2, T=6000	0.0658	0.0658

Table 4.4 The error of velocity field in 3D womersley flow

	Models / Cases	Halliday's model		Present model	
		θ_{max}	〈θ〉 (%)	θ_{max}	〈θ〉 (%)
1	Re=120, p*=0.0001	0.00670	0.0484	0.00661	0.0462
2	Re=240, p*=0.0002	0.0148	0.145	0.0154	0.135
3	Re=600, p*=0.0005	0.0736	0.781	0.0581	0.697
4	Re=1200, p*=0.001	0.385	2.93	0.191	2.44

Table 4.5 Comparison of CPU time and error between two lattice BGK model for 3D womersley flow

Cases	Models	To satisfy convergence criterion, Total iterate Period (T)	CPU (min)	$\langle\xi\rangle$
Re=1200	3D (D3Q19)	24	338	1.288e-002
	2D (present model)	24	1.20	1.145e-002
Re=120	3D (D3Q19)	24	281	1.193e-2
	2D (present model)	24	1.16	1.165e-2

Table 4.6 Vortex Centers, Stream function and Location for Multi-block scheme

		Primary vortex			Lower left vortex			Lower right vortex		
Re		ψ_{max}	x	y	ψ_{min}	x	y	ψ_{min}	x	y
400	A	0.1108	0.5569	0.6081	-5.03e-6	0.0460	0.0468	-5.17e-4	0.8905	0.1247
400	B	0.1092	0.5627	0.6108	-4.15e-6	0.0465	0.0466	-6.12e-4	0.8757	0.1254
400	C	0.1139	0.5547	0.6055	-1.42e-5	0.0508	0.0469	-6.42e-4	0.8906	0.1250

A present simulation with grid 67×67

B present simulation with two-block (a upper fine grid 133×37 and a lower coarse grid 67×50)

C Ghia et al., 1982

Table 4.7 Comparison of CPU times in minutes to get 3 order of residual reduction for steady flow through constricted tube (Re=10) (number in parentheses is the number of steps)

solver	*Coarse* mesh	*Medium* mesh	*Fine* mesh
LBGK simulation	4.3 (3,600)	80.8 (8,947)	2101 (21,240)
FVM(FLUENT)	0.5 (30)	6.2 (120)	323.2 (370)

Table 4.8 The number of Lattices for block A,B,C,D and range in *x,y,z* direction

BLOCK	3D Lattices $N_x \times N_y \times N_z$	*x*	*y*	*z*
A (fine)	33×33×129	$[-\delta x_c, 15\delta x_c]$	$[47\delta x_c, 63\delta x_c]$	$[-\delta x_c, 63\delta x_c]$
B (fine)	33×33×129	$[47\delta x_c, 63\delta x_c]$	$[47\delta x_c, 63\delta x_c]$	$[-\delta x_c, 63\delta x_c]$
C (coarse)	35×17×65	$[14\delta x_c, 48\delta x_c]$	$[47\delta x_c, 63\delta x_c]$	$[-\delta x_c, 63\delta x_c]$
D (coarse)	65×49×65	$[-\delta x_c, 63\delta x_c]$	$[-\delta x_c, 48\delta x_c]$	$[-\delta x_c, 63\delta x_c]$

Table 4.9 The position of the center of the primary vortices in plane *z=H/2*

Method	*x/H*	*y/H*
Multi-block LBGK	0.624	0.582
Single-block LBGK	0.623	0.574
NS solution (Iwatsu et al. 1989)	0.625	0.587

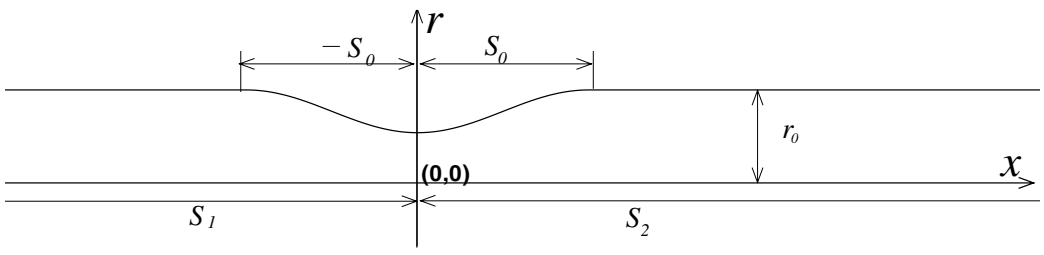

Figure 4.1 Geometry of constricted tubes

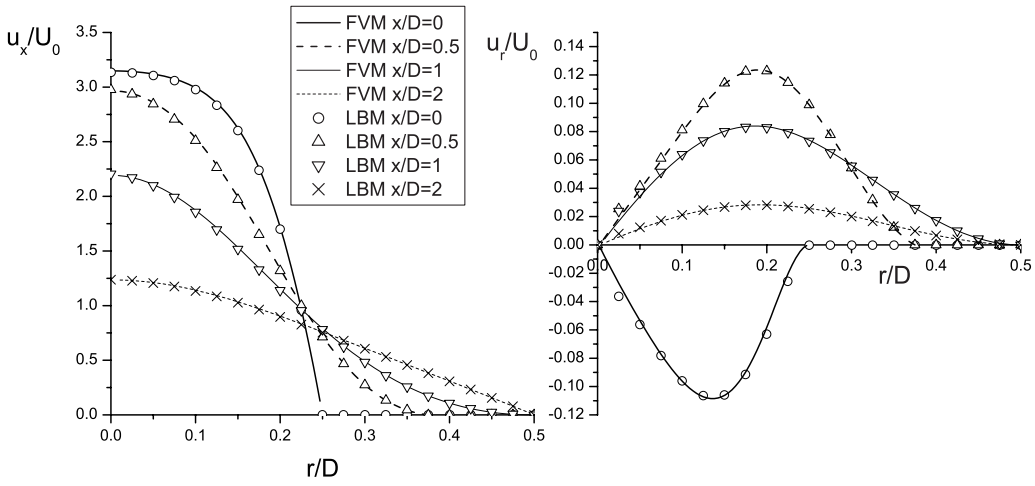

Figure 4.2 Velocity profiles in different position in case of $S_0=D$, Re=50

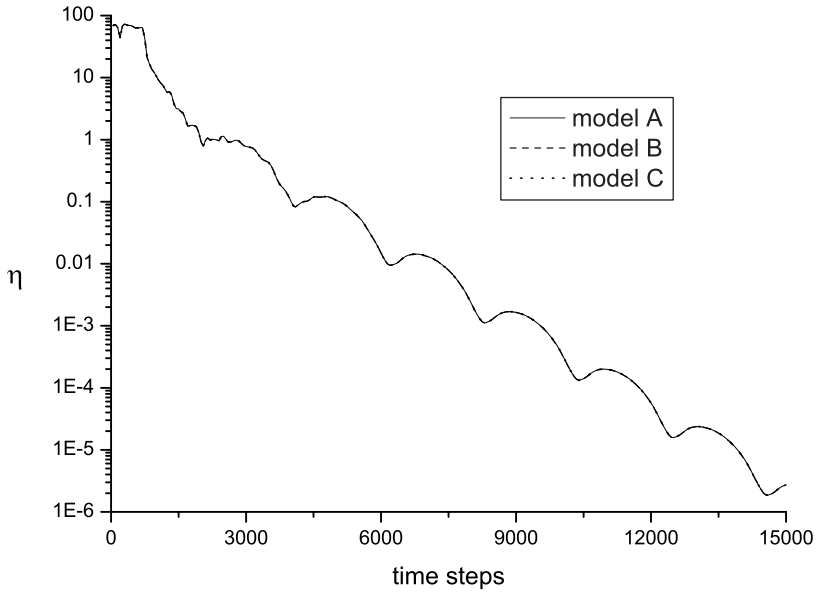

Figure 4.3 Relative error η in simulations with model A,B and C

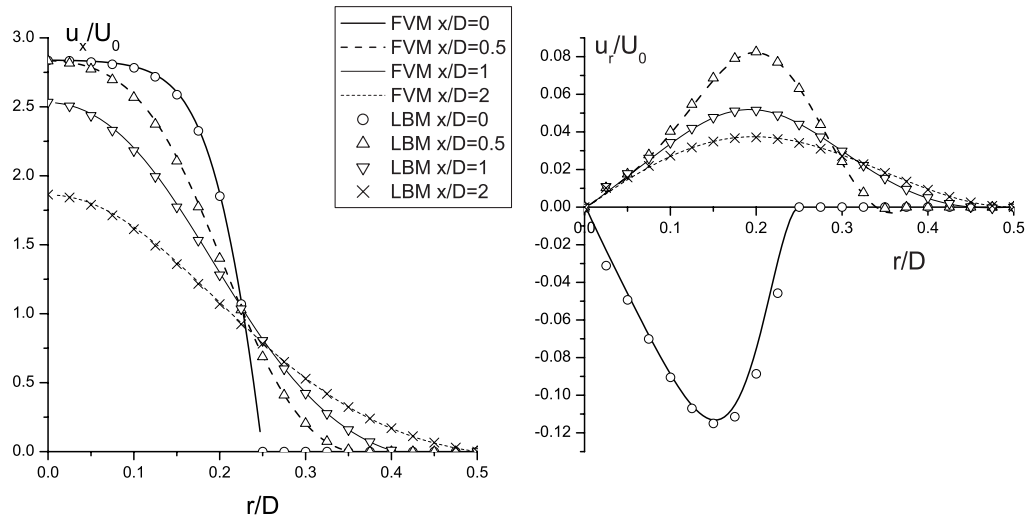

Figure 4.4 Velocity profiles in different position in case of S_0=D, Re=100

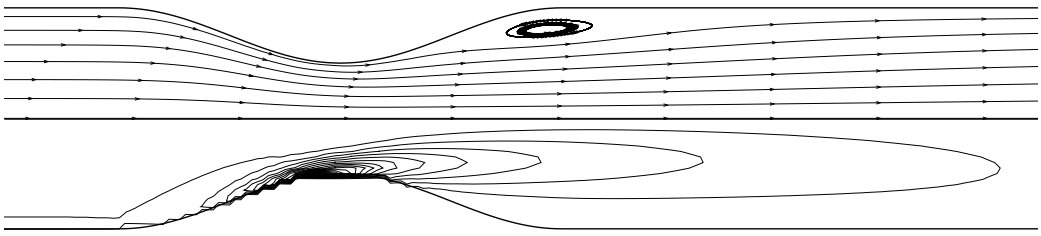

Figure 4.5 Streamlines and shear stress contours for case of S_0=D, Re=100

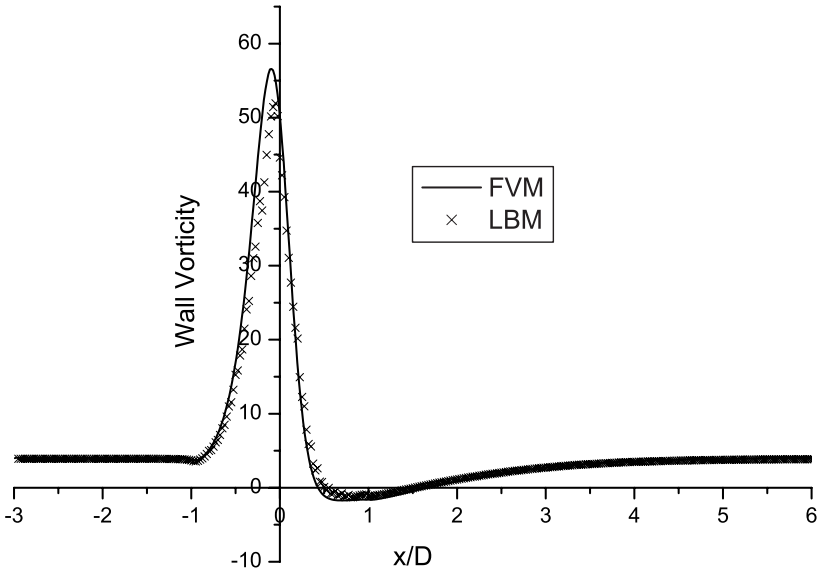

Figure 4.6 Wall vorticity for case of S_0=D, Re=100

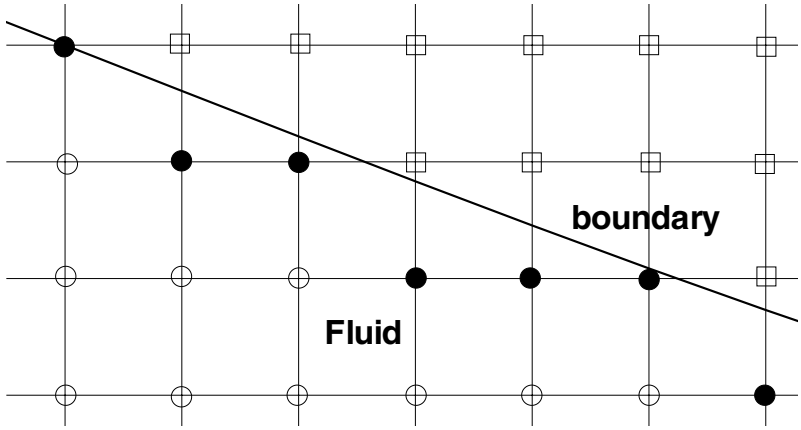

Figure 4.7 Scheme to obtain wall shear stress and wall vorticity, the open square and circle represents the lattice node outside and inside of the boundary respectively. The near-wall fluid lattices are represented by filled circle.

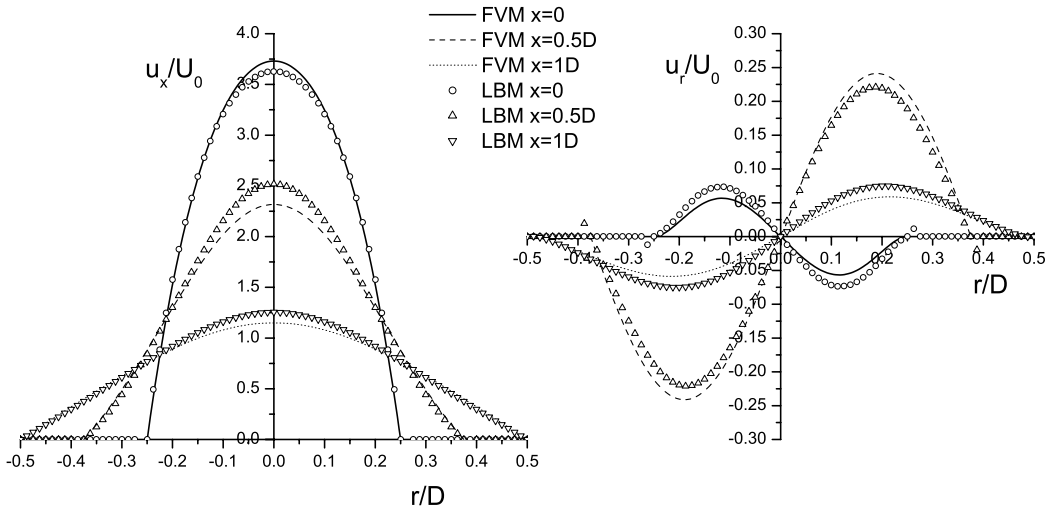

Figure 4.8 Results obtained from model of Halliday et al. for case of $S_0=D$, $Re=10$

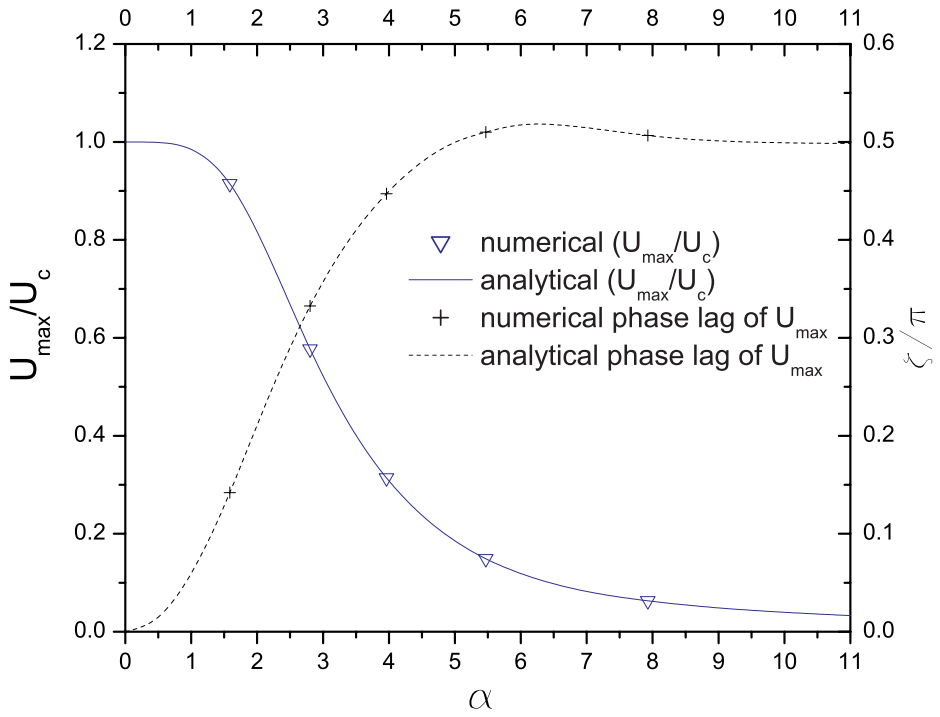

Figure 4.9 Maximum velocity in the axis of tube and the phase lag as a function of Womersley number

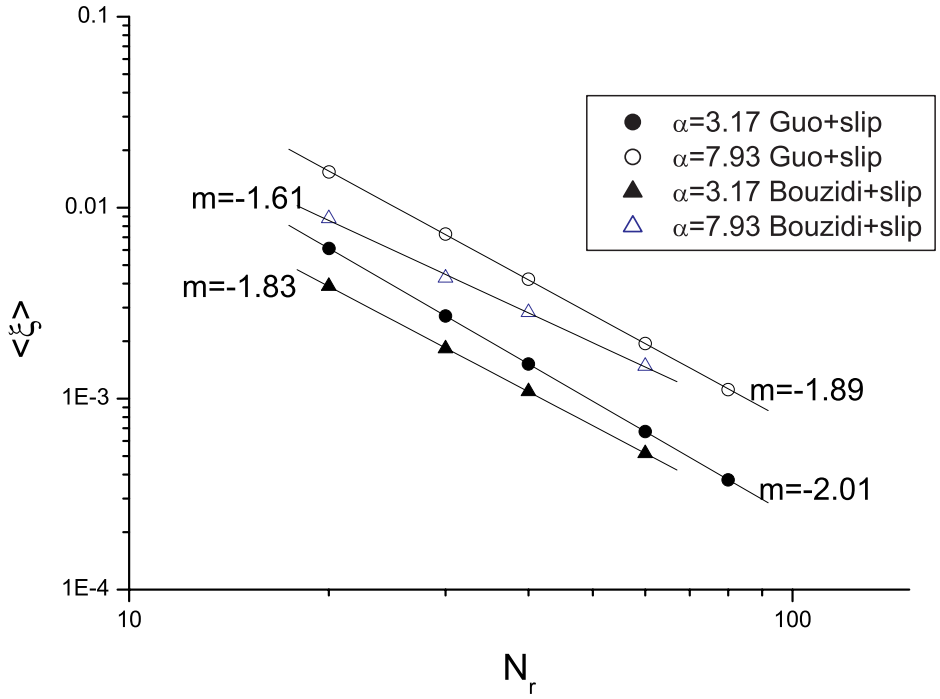

Figure 4.10 The global error <ξ> as a function of the pipe radius N_r for α=7.93 and α=3.17

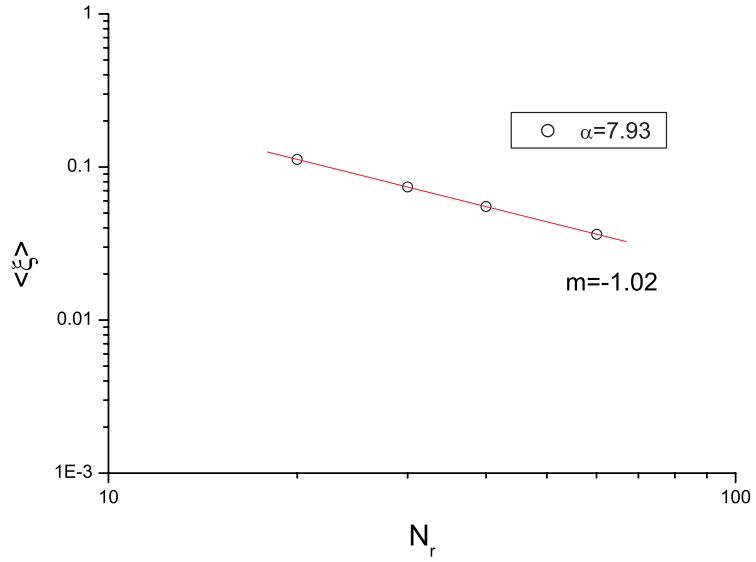

Figure 4.11 The overall accuracy of extrapolation wall boundary condition combining with axisymmetric extrapolation scheme

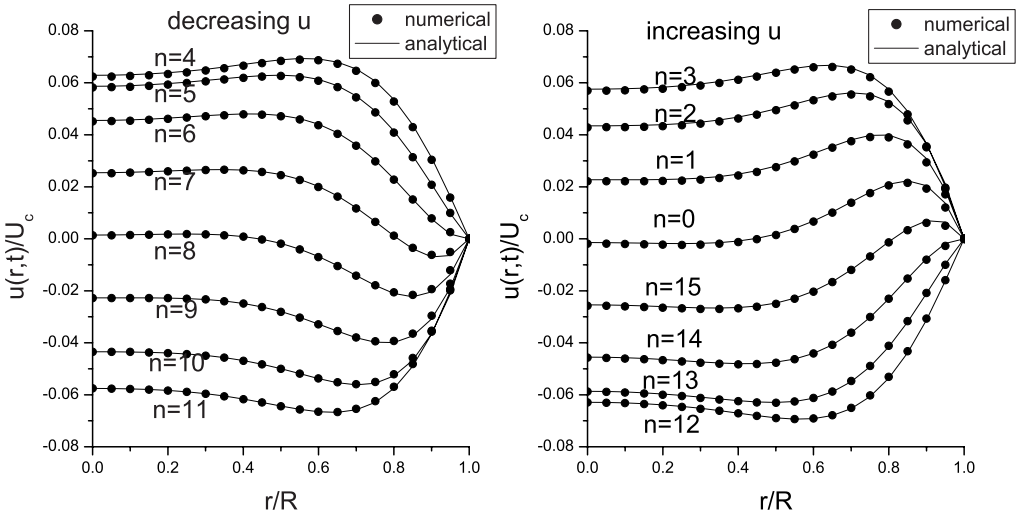

Figure 4.12 Profiles of decreasing and increasing velocities along the radius of a tube for α=7.93, T=1200, Re=1200, τ=0.6, at $t=nT/16$ (n=0,…,15) (U_c=1.0, actually U_{max}~0.07)

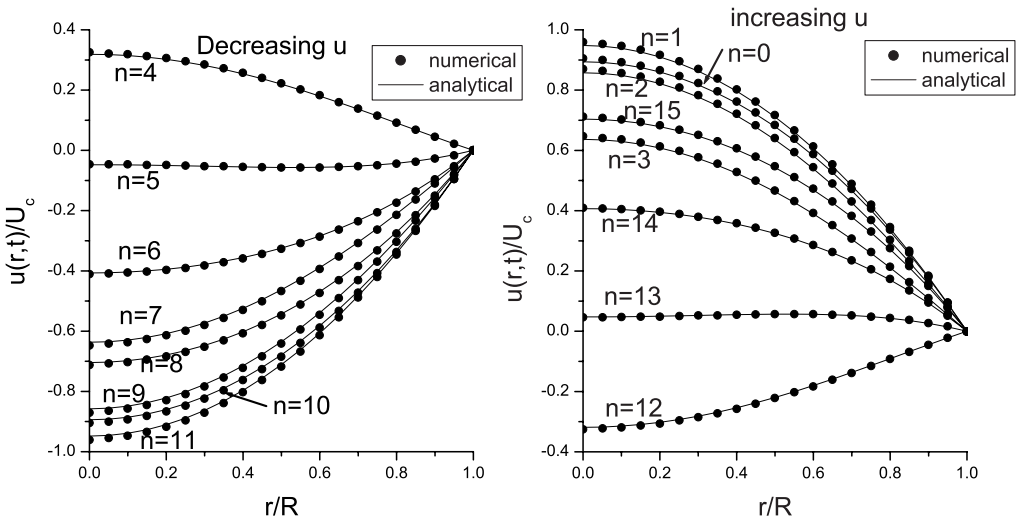

Figure 4.13 Profiles of velocities along the radius of a tube for α=1.37, T=4000, Re=1.2, τ=1.5, at $t=nT/16$ (n=0,…,15) (U_c=0.01)

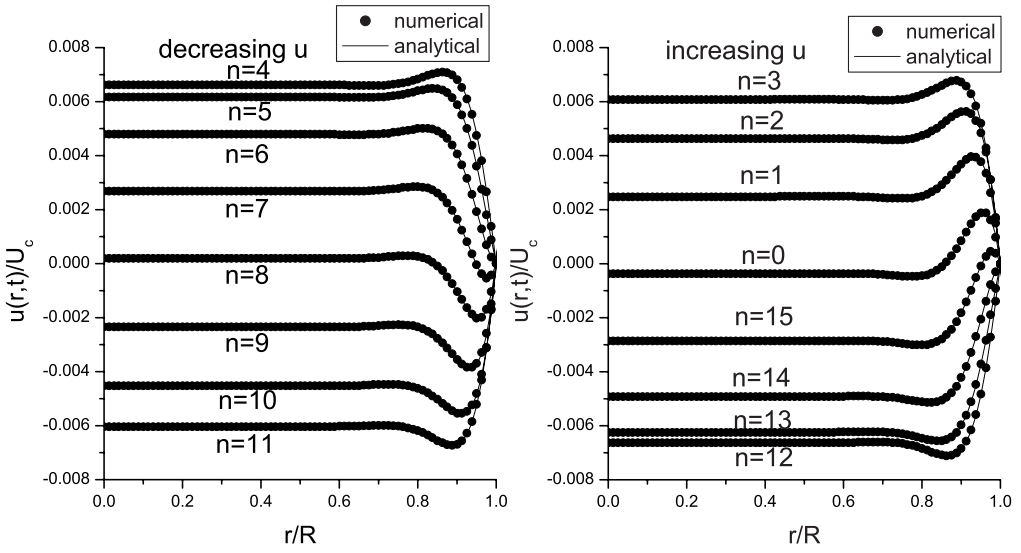

Figure 4.14 Profiles of velocities along the radius of a tube for α=24.56, T=1000, Re=1920, τ=0.7, at $t=nT/16$ (n=0,…,15) (U_c=0.8, actually U_{max}~0.0056)

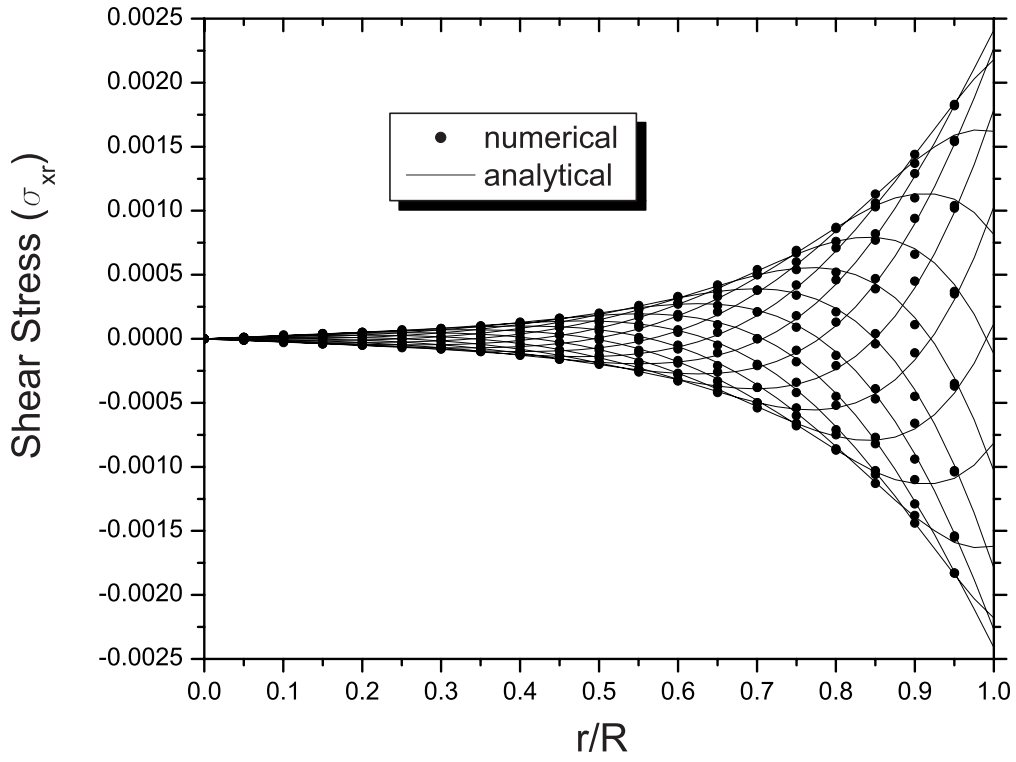

Figure 4.15 Shear stress in a oscillatory tube flow for case α=7.93, T=1200, Re=1200, τ=0.6, at t=nT/16 (n=0,…,15)

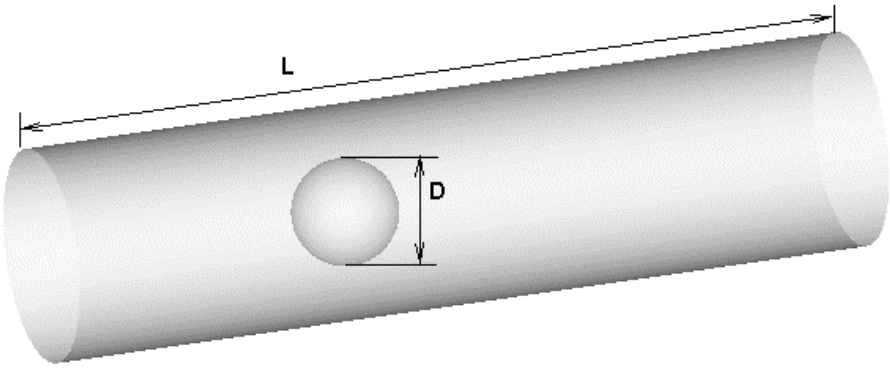

Figure 4.16 Geometry of flow over an axisymmetrical sphere placed in a 3D circular tube

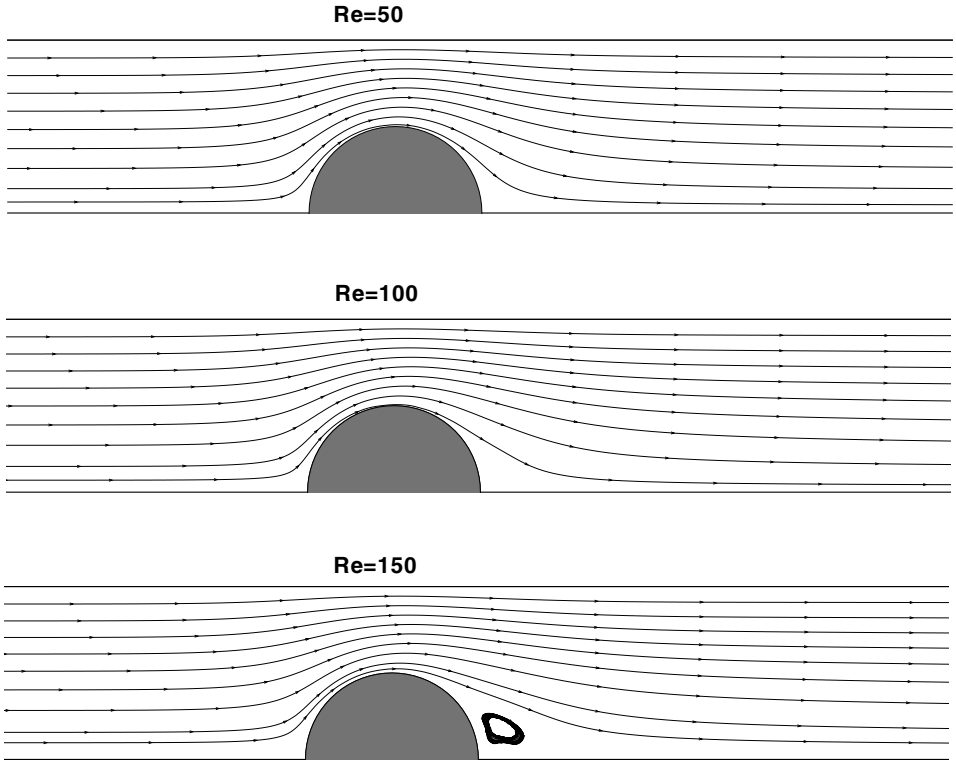

Figure 4.17 Streamlines for flows over an axisymmetrical sphere placed in a 3D circular tube at *Re*=50, 100 and 150

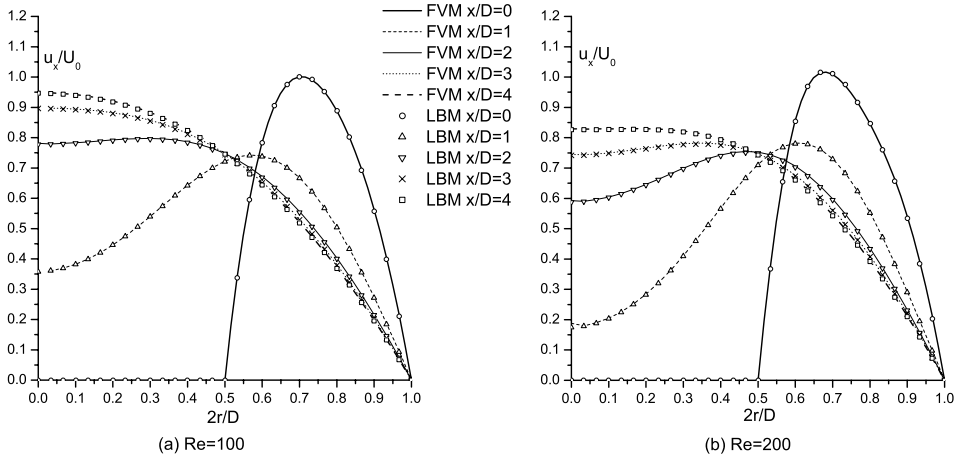

Figure 4.18 Velocity profiles in different position for flows over an axisymmetrical sphere placed in a 3D circular tube (a) *Re*=50, (b) *Re*=100

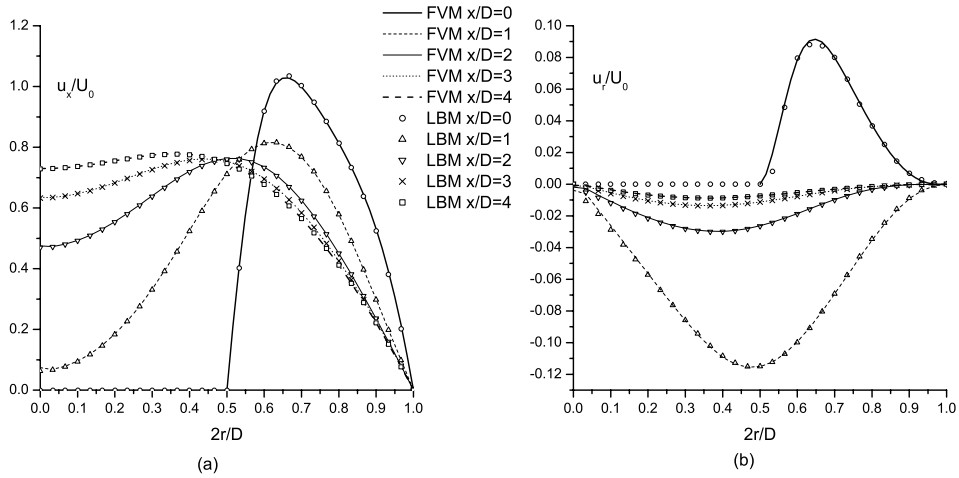

Figure 4.19 Velocity (a) u_x, (b) u_r profiles in different position for flow over an axisymmetrical sphere placed in a 3D circular tube *Re*=150

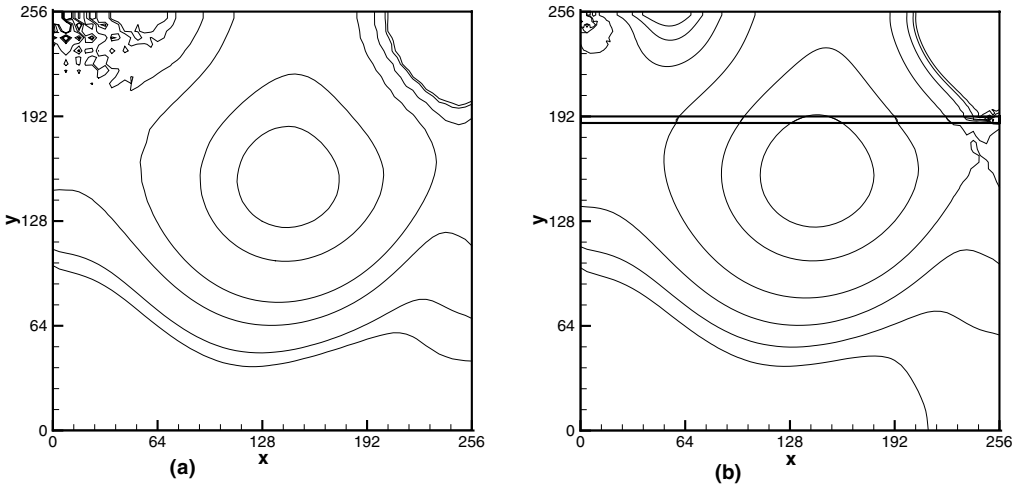

Figure 4.20 Pressure contours for *Re*=400 (a) single-block case with a grid 67×67 and (b) two-block case with a upper fine grid 133×37 and a lower coarse grid 67×50

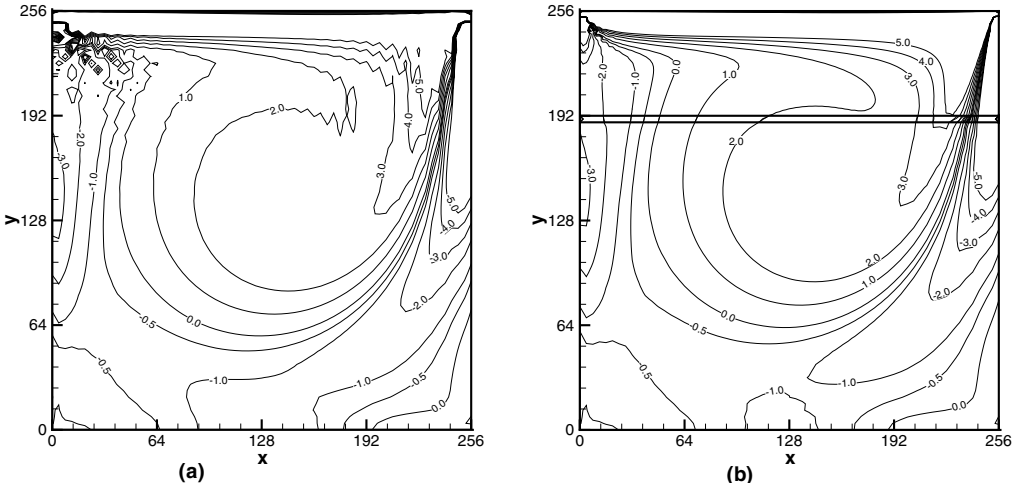

Figure 4.21 Vorticity contours for *Re*=400 (a) single-block (67×67) case and (b) two-block case (a upper fine grid 133×37 and a lower coarse grid grid 67×50)

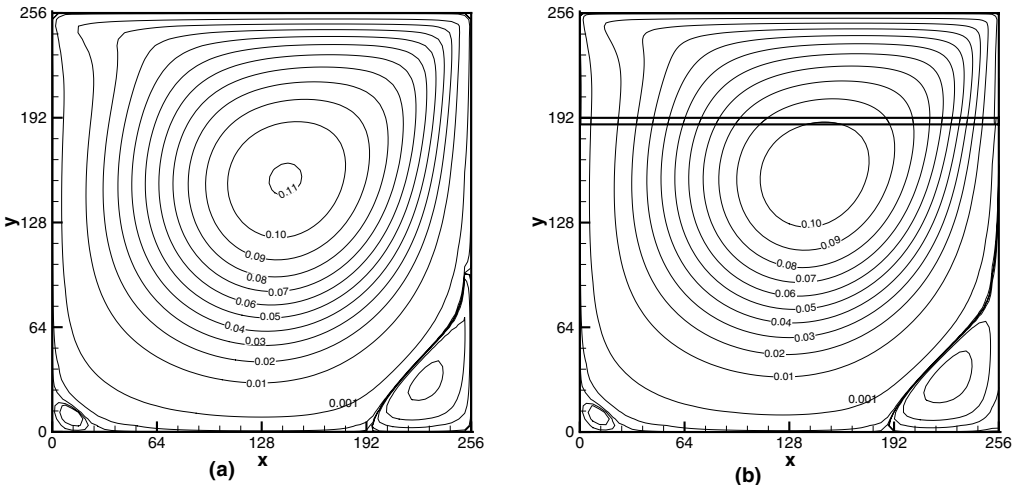

Figure 4.22 Stream function for *Re*=400 (a) single-block (67×67) case and (b) two-block case (a upper fine grid 133×37 and a lower coarse grid grid 67×50)

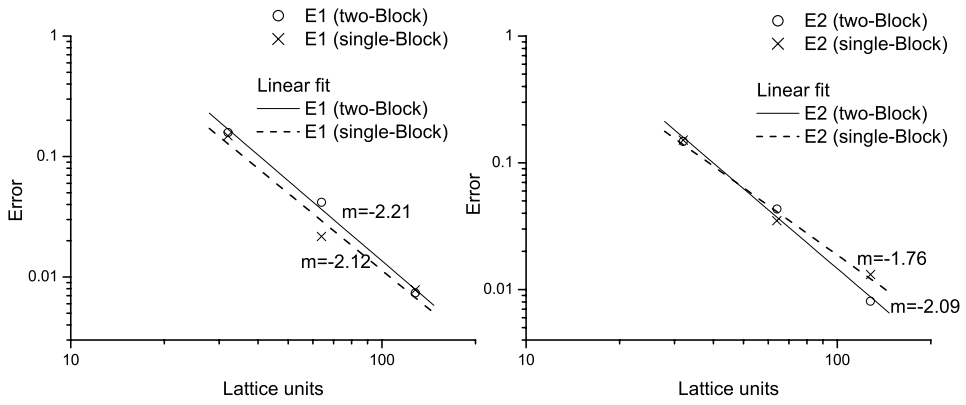

Figure 4.23 Spatial convergence rate for Re=400. The errors $E1$ and $E2$ are calculated relative to results obtained on a 259×259 grid. (a) Slope of linear fit of $E1$ (two-block case) is m=-2.21±0.16. Slope of linear fit of $E1$ (single-block case) is m=-2.12±0.38. (b) Slope of linear fit of $E2$ (two-block case) is m=-2.09±0.18. Slope of linear fit of $E2$ (single-block case) is m=-1.76±0.20.

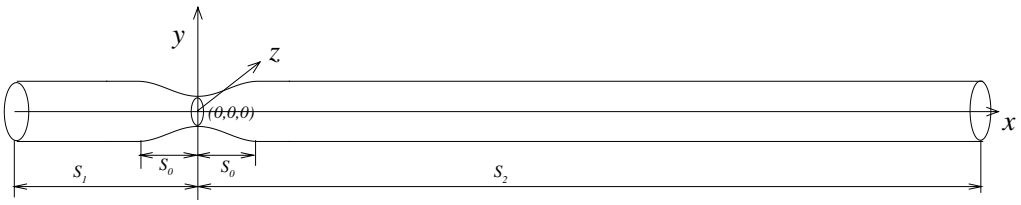

Figure 4.24 Three-dimensional geometry of the stenosis in 3D Cartesian coordinates

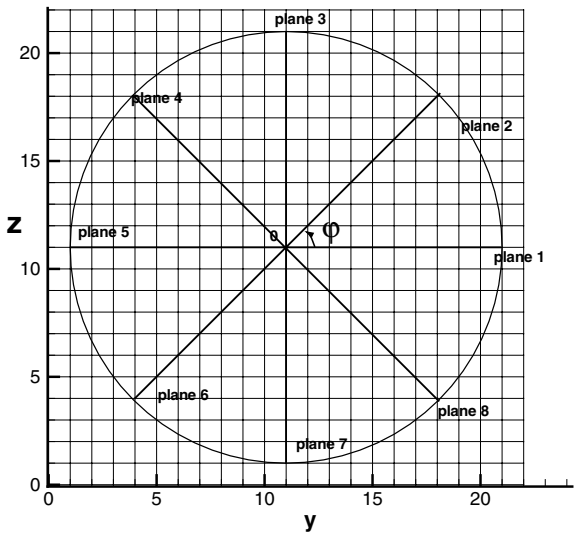

Figure 4.25 u velocities in the 8 planes were investigated for asymmetry

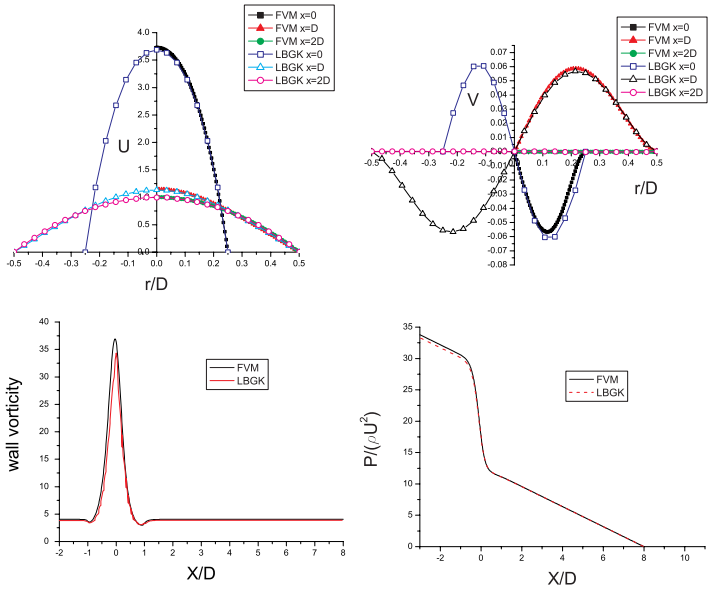

Figure 4.26 Solutions of 3D LBM and FVM (*Re*= 10)

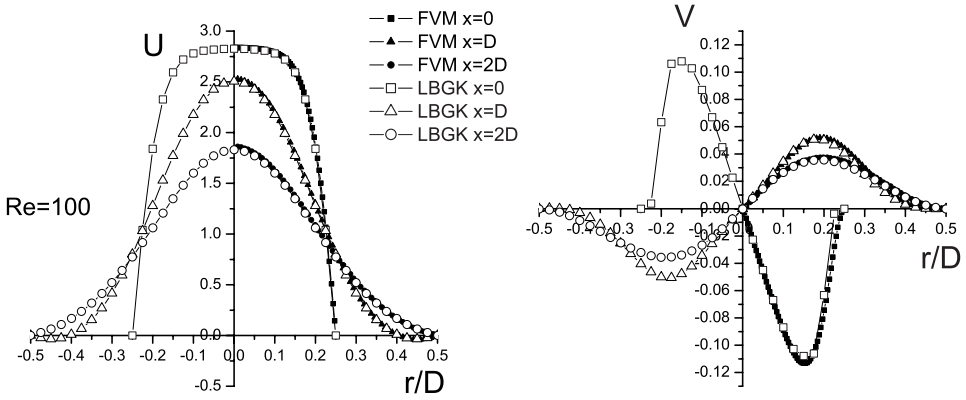

Figure 4.27 Axial and radial velocity profiles in a 3D constricted tube (*Re*=100)

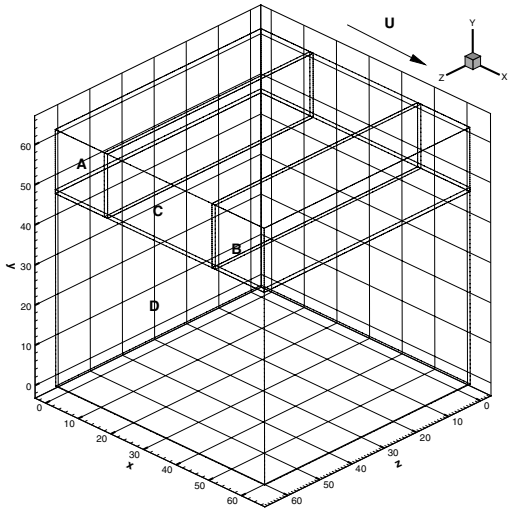

Figure 4.28 Geometry and multi-block strategy of 3D driven cavity flow

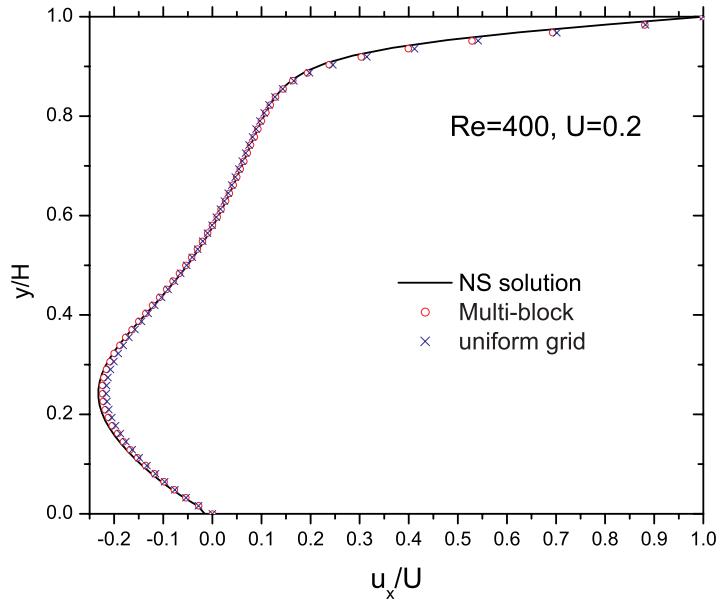

Figure 4.29 Comparison of u_x profiles of the LBM multi-block case and single-block case with a Navier–Stokes (NS) solution (Salom 1999) at $x/H = z/H = 0.5$ for Re=400 in a 3D lid-driven cavity flow.

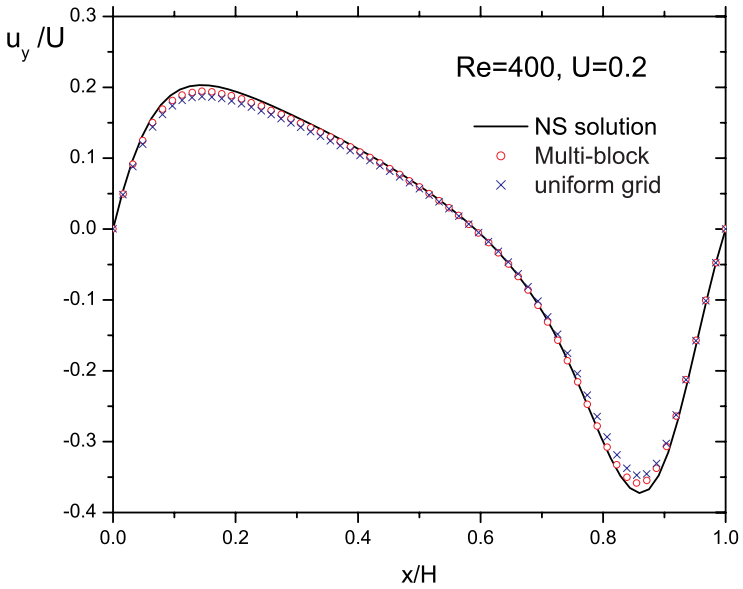

Figure 4.30 Comparison of u_y profiles of LBM multi-block case and single-block case with a NS solution (Salom 1999) at $y/H = z/H = 0.5$ for Re=400 in a 3D lid-driven cavity flow.

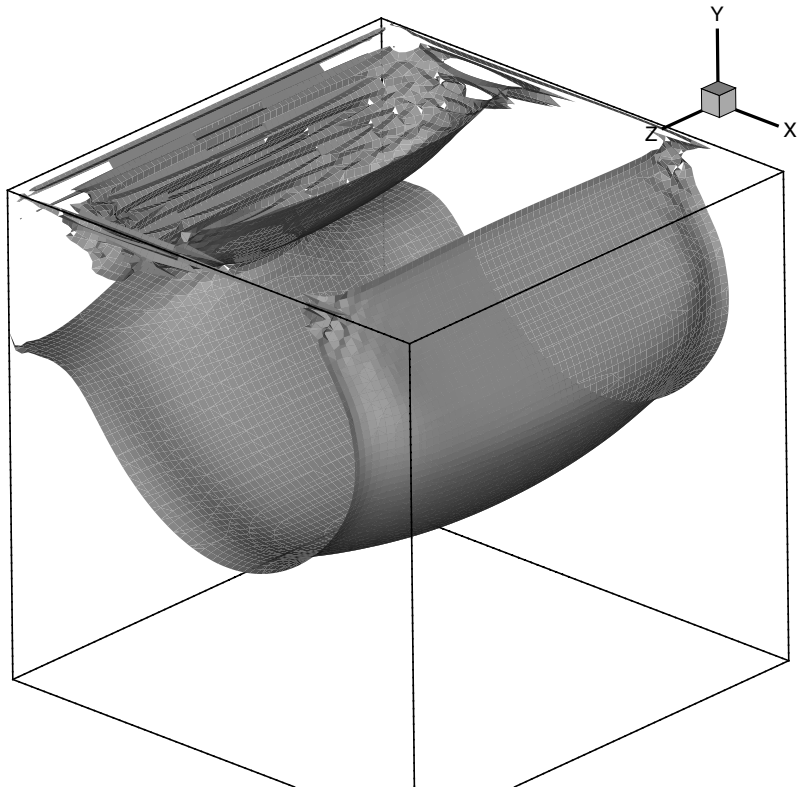

Figure 4.31 A pressure contour obtained from the single 65^3 block solution

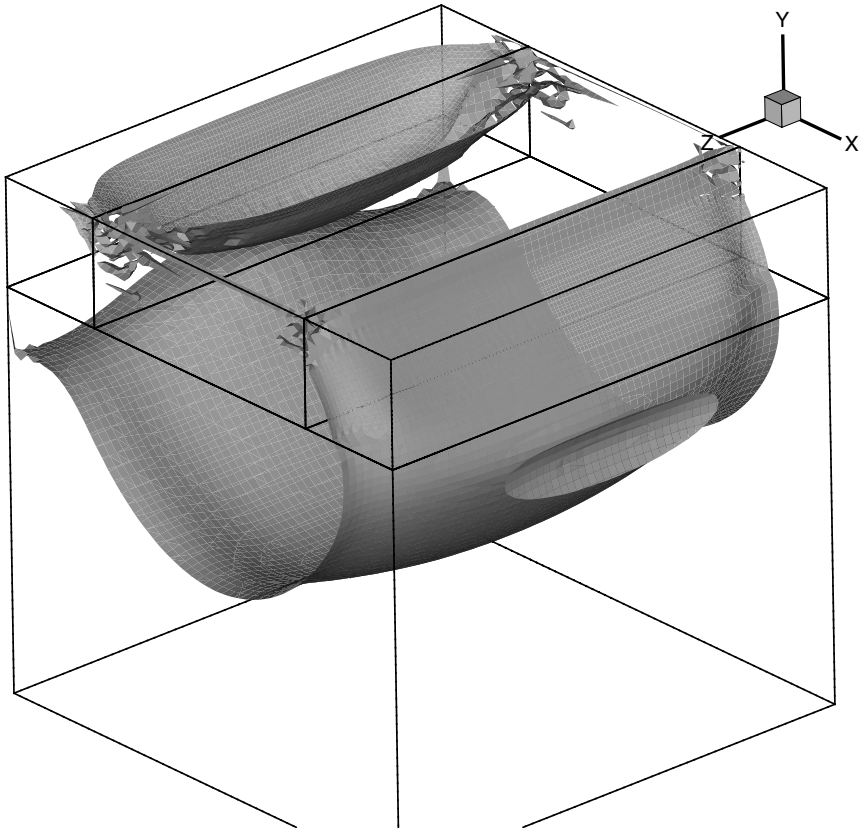

Figure 4.32 A pressure contour obtained from the multi-block solution

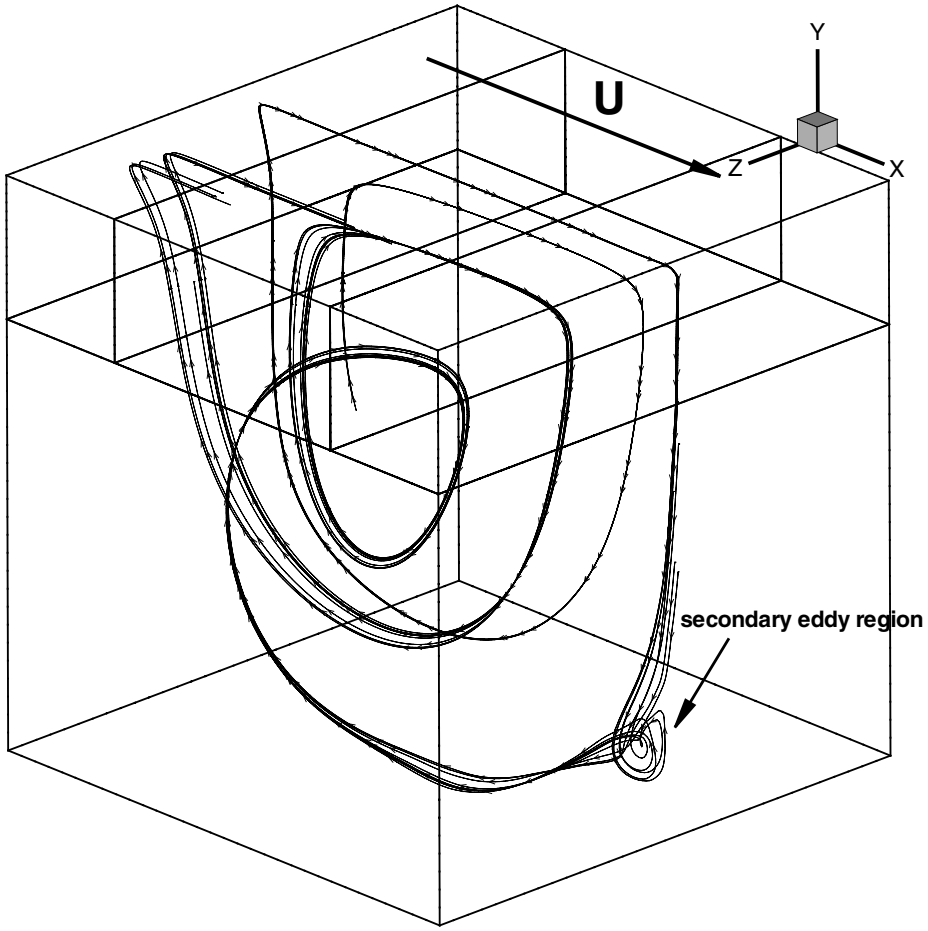

Figure 4.33 Exemplary particle paths of the steady solution at *Re* = 400. Particles pass through the downstream secondary eddy region.

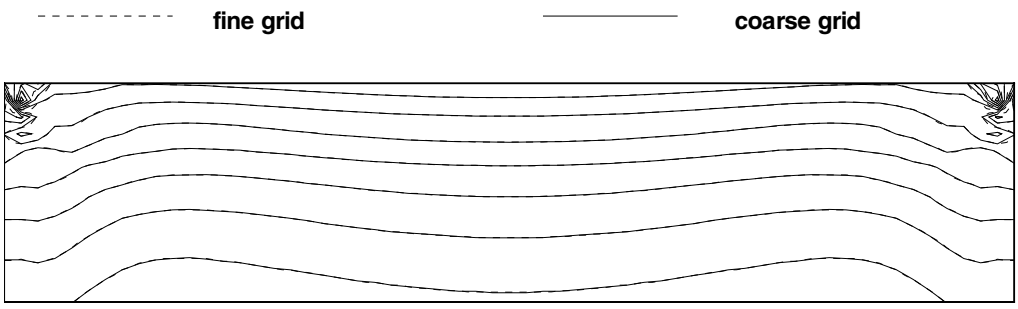

Figure 4.34 The pressure contours on the interface between block B and C

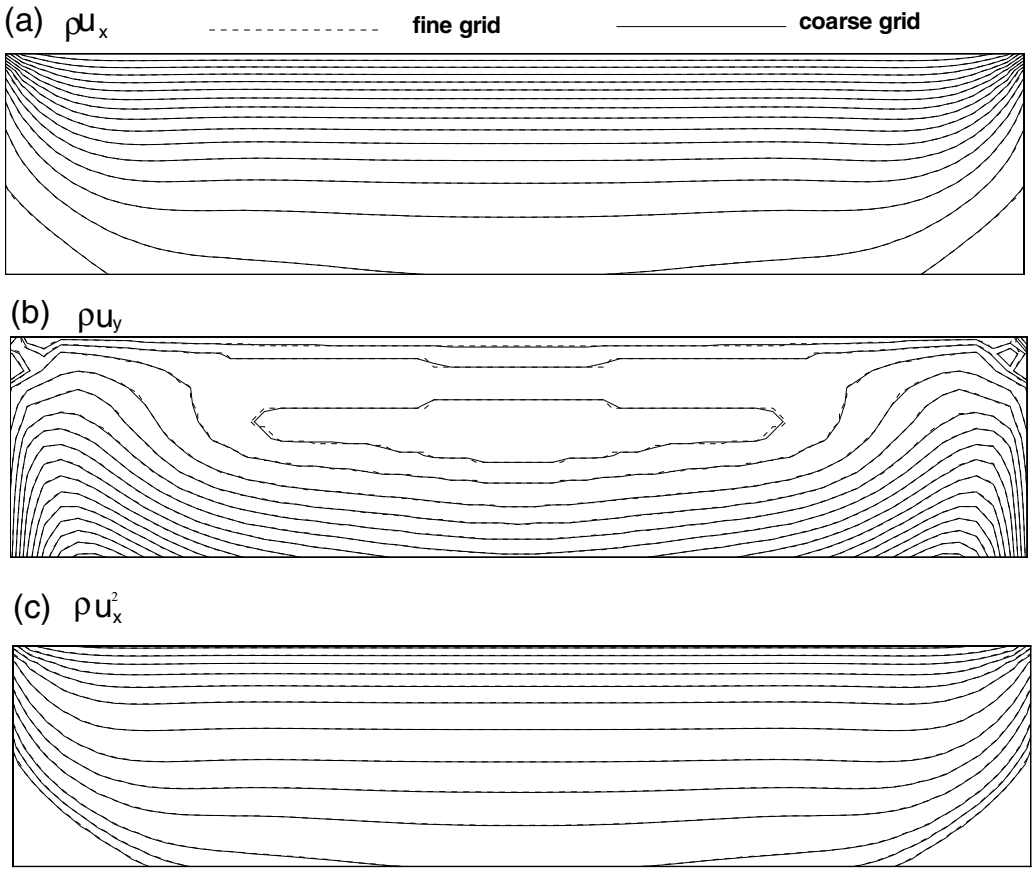

Figure 4.35 Mass and momentum fluxes contours on the interface between block B and C

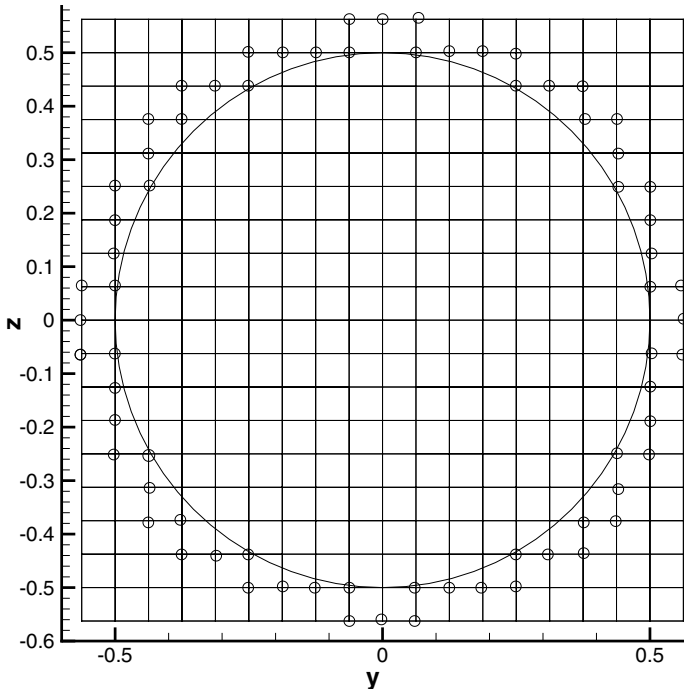

Figure 4.36 2D projection of the discretized domain and the boundary nodes (denoted by open circle) on the *yz* plane (D=16 coarse lattice units)

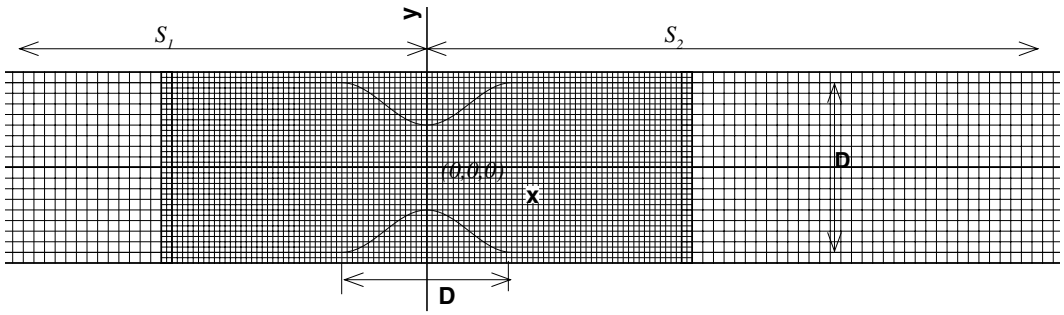

Figure 4.37 The multi-block strategy for a 3D constricted tube (*xy* plane)

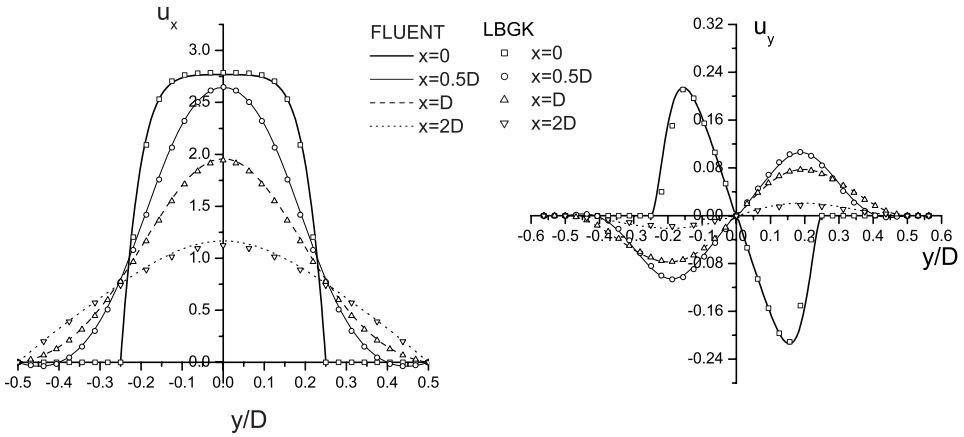

Figure 4.38 The velocity component u_x and u_y profile along a diameter in *xy* plane at x=0.5D, D and 2D

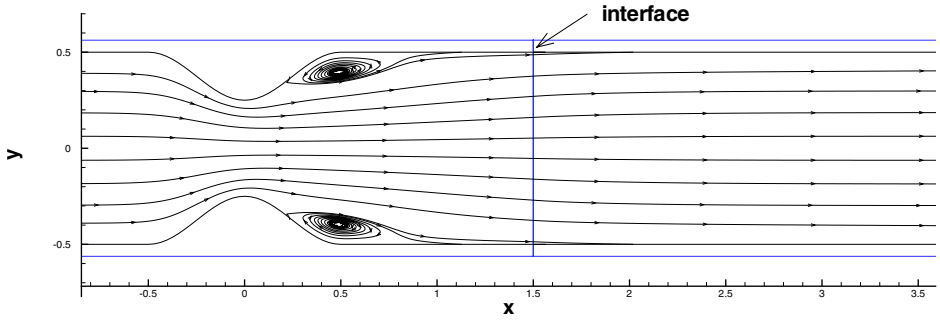

Figure 4.39 Exemplary particle paths of the steady solution at Re = 50.

Chapter 5 Blood Flow through Constricted Tubes

In this chapter[3], the steady and unsteady blood flows through axisymmetric and 3D asymmetric stenosed vascular tubes were studied. The viscous flows in large distensible blood vessels were also investigated.

5.1 Steady and Pulsatile Flows in Axisymmetric Constricted Tubes

5.1.1 Steady Flows in Constricted Tubes

Firstly, the steady flows through a single constriction with different geometries were studied. In this study, geometry of the constriction is described by Cosine curve (i.e., Eq. (4.3)) and illustrated by Figure 4.1. For cases with severe constricted stenosis or higher Reynolds number, to improve the numerical stability of LBM and save CPU time, the multi-block strategy is used.

Three cases of $S_0=D$, $Re=50$ with $\beta=40\%$, $\beta=50\%$, $\beta=60\%$ were simulated. The area constriction of the three cases is 64%, 75% and 84%, respectively. Figure 5.1 shows the streamlines of the above cases. When $Re=50$, streamlines of the case with 64% stenosis is smooth and no flow separation occurs in the downstream of the stenosis. For the case with 75% stenosis, there is a very small eddy behind the stenosis. For more severe constricted stenosis, there is a larger eddy behind the stenosis. The wall vorticity of the above cases normalized by $\rho U^2/Re$ is illustrated in Figure 5.2. It is clear that for the same Reynolds number,

[3] Part of this work has been published as a conference paper:
Huang, H., Lee, T.S., Shu, C., Simulation pulsatile flow in constricted tubes by Lattice Boltzmann method, Asian Joint Conference on Propulsion and Power 2006, Apr.20-23, Beijing, China

when the constriction is more severe, the maximum wall vorticity is larger. It is also clear that for case of 75% and 84% stenosis, the wall vorticity reverses to negative value behind the stenosis due to the flow separation.

Two cases with higher Reynolds number were simulated. In the two cases, $S_0=D$, β=50% and Reynolds number is 200 and 400, respectively. The axial and radial velocity profiles of the two cases are shown in Figures 5.3 and 5.4. For high *Re* cases, the axial velocity profiles behind the stenosis are very different from the parabolic shape and there is an eddy behind the stenosis. To recover the initial parabolic shape, representing Poiseuille flow again, the distance downstream from the stenosis would be longer for higher Reynolds number.

In the following, we would like to discuss the effect of distance between two adjacent stenoses on streamlines, shear stress, vorticity and velocity distribution as blood pass through them.

The geometry of two stenoses and mesh are shown in Figure 5.5. If r_0 is the radius of the nonstenotic part of the pipe, radius of the stenoses $r(x)$ is given as following,

$$r(x) = r_0 - \beta r_0\{1+\cos[\pi(x-x_0)/ S_0]\}/2 \quad (-S_0< x-x_0 <S_0), \tag{5.1}$$

where $r_0=D/2$, β=50% is severity of stenoses and the axial length of each stenosis is $2S_0$. The distance between two stenoses is defined as L. In Eq. (5.1), for the first and second stenosis, $x_0=0$ and $x_0=L$, respectively. In our simulations, $S_0= D/2$. The tube extends -3.5D and 17D upstream and downstream of the centre of the constriction, respectively.

A group of results for L/D=1,2,3 with Reynolds number 10, 50 and 300 are illustrated in Figures 5.6, 5.7, 5.8, respectively.

In the three figures, the flow streamlines are illustrated above the axis and the

shear stress contours are below the axis. The shear stress values labelled in the figures are normalized by $\rho U^2/Re$, where U is the characteristic velocity. The maximum normalized shear stress value for Re=10, 50 and 300 case are about 40.40, 54.58 and 102.34 respectively. From Figure 5.6, we can see that when Re=10, the streamlines and shear stress contours for L/D= 1,2,3 are similar. The flow around each constriction almost has no interference with other.

In Figure 5.7, three cases of Re=50 are illustrated. The streamlines and shear stress contours for L/D=2 and 3 are similar. The shear stress contours demonstrated that for case L/D=1, there are weak interference. The streamlines in cases of Re=50 clearly demonstrate flow separation and small eddies formed behind the stenoses.

In Figure 5.8, we can see that when Re=300, between the two constrictions, there is a circulation zone which fills most part of the valley region. The shear stress fields are altered and the recirculatory eddy from the upstream constriction is spread downstream and affects the flow passing through the downstream constriction. In these cases, there are a separation streamline that divides the flows into two parts: the recirculating flow field between two constrictions and the main flow field near the center of the tube with relatively straight and parallel streamlines.

The variations of the axial velocity and wall vorticity due to the influence of the constriction spacing ratios and Reynolds number are shown in Figure 5.9 and 5.10 respectively. In Figure 5.9, it is obvious that the maximum axial velocity on axis does not occur at the throat because at that point, the fluid is still in acceleration and actually the maximum axial velocity occurs slightly downstream of each of the constrictions. For all cases with Re=300 and case of Re=50, L/D=1,

the maximum velocity value near the second constriction is slightly higher than the maximum value at the first constriction because the flow interference between the double constrictions exists. For the other cases with lower Reynolds number or large constriction spacing, the flow interference is very weak and the maximum velocity values near the two constrictions are almost same.

For the wall vorticity, the magnitude of the wall vorticity value increases rapidly when the flow approaches the constriction and reaches a peak value slightly before the throat position. At a location downstream of the peak value the wall vorticity decreases rapidly and reverses to a negative value when the separation begins at the wall of the tube. It is also obvious that the peak wall vorticity value increases with increasing Reynolds number. For all cases of Re=300 and case of Re=50, L/D=1, the flow interference exists. In those cases, the second peak wall vorticity values are always lower than the first ones. However, for other cases, the flow interference is very weak and the two peak values are almost the same.

5.1.2 Pulsatile Flows in Constricted Tubes

In this part, the pulsatile flows in constricted tubes were simulated. The geometry of constricted tubes is also described by Eq. (4.3) and illustrated by Figure 4.1.

The pulsatile flow is achieved by introducing a volumetric flow rate Q, which plotted in Figure 5.11. The flow rate Q is varied in a sinusoidal manner as $Q(t) = (Q_{max}/2)[1-\cos(2\pi t/T)]$, where Q_{max} is the maximum flow rate and T is the time period of the pulsatile flow. Although the physiological waveforms are not sinusoidal, the sinusoidal waveform has been considered a simple prototype of

physiological waveforms in a number of past experimental studies (e.g., Young and Tsai, 1973a) and is also adopted in our study.

The Reynolds number defined as $Re=U_{max}D/\nu$. The characteristic velocity was defined as $U_{max}=4Q_{max}/(\pi D^2)$. As we know, when applying the lattice BGK model, the maximum velocity in flow field usually should not exceed 0.15 when $c_s=1/\sqrt{3}$. In present cases, the U_{max} was chosen as 0.02. The Womersley number is defined as $\alpha = R\sqrt{\omega/\nu}$. The Strouhal number is defined as $St = 2\pi D/(U_{\max}T)$.

In some previous computational study, a sinusoidally varying parabolic velocity profile was employed at the inlet (Liao et al., 2004, Mittal et al. 2003). That is valid when the upstream of constrictions (i.e., inlet segment) is long enough. However, if the inlet segment is short, the fully developed pulsatile flow profile should be employed since the pulsatile flow profile in a tube is significantly different from a parabolic profile when Womersley numbers greater than about one. As we know, in the physiological flow study, the Womersley numbers are all much greater than one. Hence, in our study, the profile of laminar fully developed pulsatile flow in a tube is employed as the inflow condition. This inflow is obtained from the following equation

$$\frac{\partial u}{\partial t} - \nu\left(\frac{\partial^2 u}{\partial r^2} + \frac{1}{r}\frac{\partial u}{\partial r}\right) = \frac{1}{\rho}\left(\chi_0 + \chi_{cn}\cos(\omega t + \delta_1)\right), \tag{5.2}$$

where χ_0 and χ_{cn} are the steady and oscillatory pressure gradients, respectively. χ_{cn} and δ_1 are chosen to satisfy the required minimum and maximum bulk velocity in Eq. (5.3).

$$\frac{u_b}{U_{\max}} = \frac{1}{2}\left(1 + \frac{\chi_{cn}}{\chi_0}\sigma_u\cos(\omega t + \delta_1 - \delta_2)\right) = \frac{1}{2}\left(1 - \cos(\omega t)\right) \tag{5.3}$$

The value of δ_2 , σ_u was defined in the study of Uchida (1956). The final solution

of Eq. (5.2) is (Uchida, 1956)

$$\frac{u(r,t)}{U_{\max}}=\left(1-\frac{r^2}{R^2}\right)+Real\left\{\frac{\chi_{cn}}{i\omega\rho}\left[1-\frac{J_0\left[\frac{1}{\sqrt{2}}(\alpha+i\alpha)\frac{r}{R}\right]}{J_0\left[\frac{1}{\sqrt{2}}(\alpha+i\alpha)\right]}\right]e^{i(\omega t+\delta_1)}\right\} \tag{5.4}$$

It is noticed that in Eq. (5.4), different χ_{cn} should be chosen for different α to satisfy the Eq. (5.3). Form Eq. (5.4), we can see that the normalized inlet velocity profile only depends on the Womersley number. The profile shapes for α=4 and 8 are shown in Figure 5.11 (b) and (c) respectively for four different phases in the pulsation.

As we known, Reynolds number is defined as

$$\mathrm{Re}=\frac{U_{\max}D}{\nu}=\frac{U_{\max}(D/\delta_x)}{c(\tau-0.5)/3} \tag{5.5}$$

In the following discussion, for convenience, c is equal to 1. Form Eq. (5.5) we can see that for a certain Re and D/δ_x (i.e., a certain uniform grid), if $U_{\max}$ decreases, τ would be closer to 0.5. As a result, for a certain Re and grid, to ensure the numerical stability, $U_{\max}$ should not be too small. On the other hand, L_x/c_sT should be very small to eliminate the compressible effect due to the time variation of pressure field. The above requirements mean Strouhal number may not exceed a certain number. For example, if $U_{\max}>0.02c$, $L_x=14D$, $L_x/c_sT<10^{-2}$, then

$$St=2\pi D/(U_{\max}T)<0.129. \tag{5.6}$$

From Eq. (5.5) and Eq. (5.6), it is found that increasing the numerical stability, which makes τ closer to 0.5, can decrease the characteristic velocity $U_{\max}$ so as to simulate high St cases. If the numerical stability is not improved, it is no way to simulate cases of higher Re and high St.

The technique of increasing the mesh size is usually used to increase

numerical stability, which also means computational time increasing dramatically. Here multi-block strategy was used to increase numerical stability and save CPU time. As the study in Chapter 4, a fine mesh was used for the constricted part of the tube (there are 40 lattice nodes in a non-occluded radius).

In the following part, some results are presented. The pulsatile flow in the constricted tube with Re=200, St=0.32, α=4.0 case was simulated. In the case, U_{max} = 0.02 and T=78500δt_f, so as to ensure $L_x/c_sT \approx 2.4\times10^{-2}$.

In our simulations, the zero velocities are initialized everywhere. At the inlet boundary, pulsatile flow velocity profiles were specified. In the outlet boundary, the outlet pressure was specified and $\partial \mathbf{u}/\partial x = 0$ was also imposed.

The pulsatile flow pattern at different time is illustrated in Figure 5.12. At beginning, the inlet velocity is very small and the vorticity in the tube is very small. The streamlines were almost parallel to the geometry of the tube. When the inlet velocity becomes larger, an eddy behind the constriction is formed and the magnitude of the wall vorticity value increases rapidly when the flow approaches the constriction and reaches a peak value slightly before the throat position. After t=0.5T, the flow inlet velocity decreasing and the vortex becomes weaker. After t=0.9T, the inlet velocity further decreases and the pressure gradient in tube is negative and reverse the flow. A long weak vortex formed in the right hand of the constriction.

The same pulsatile flow simulation using finite volume method (FVM) was also performed. The wall vorticity obtained by LBM and FVM at time t=0.1T, 0.2T, 0.3T, 0.4T, 0.5T are compared in Figure 5.13. The wall vorticity at time t=0.6T, 0.7T, 0.8T, 0.9T, T are illustrated in Figure 5.14. The wall vorticities is normalized by $U_{\max}/D$. As illustrated in Figure 5.13 and Figure 5.14, the wall

vorticity obtained by LBM agree well with that of the FVM. Due to the uniform square mesh used in LBM, the wall vorticity was obtained by extrapolation. The highest wall vorticity predicted by LBM is slightly larger than that of FVM. The position of highest local wall vorticity predicted by LBM is slightly behind that predicted by FVM although all wall vorticity curve reach their highest value slightly upstream of the constriction.

5.2 3D Steady Viscous Flow through an Asymmetric Stenosed Tube

As we known, the constrictions of stenosed vascular tube can be roughly grouped into two basic types: approximately axisymmetric stenosis and stenosis formed by an isolated surface protuberance from one wall. (Young and Tsai**,** 1973a**)** In this study, the second type of constriction was considered and steady flows through three-dimensional asymmetric stenosis were simulated.

Figure 5.15 depicts the model used in our study. The model basically consists of straight rigid tube having a circular cross section with a protuberance from one wall. We call this side “Side A” and the opposite unstenosed side “Side B”. In longitudinal section, the stenosis shape in our model follows a circular shape. Figure 5.15(a) shows the longitudinal section of the model, and Figure 5.15(b) shows a typical cross section across the stenotic region. In Figure 5.15(a), ζ is the height of the stenosis and S_0 is a half of the stenotic length, r_0 is the radius of the unobstructed part of the tube and R_{m} is the radius of the circular stenosis.

With the origin situated as shown in Figure 5.15(a), the equation for the wall boundary is described using Cartesian coordinates (x, y, z) by the following

$$\begin{cases} x^2+y^2+z^2=r_0^2 & for \quad |x|>s_0 \\ y=d & for \quad |x|\le s_0, |z|\le \sqrt{r_0^2-(r_0-d)^2} \\ x^2+y^2+z^2=r_0^2 & for \quad |x|\le s_0, y>d \end{cases}, \tag{5.7}$$

where d is a function of x which can be obtained through solving the Eq. (5.8).

$$[d+(R_m-\zeta)]^2+x^2=R_m^2 \quad |x|\le s_0 \tag{5.8}$$

The model solved here is of 53% area occlusion and S_0=1.5r_0 . The center of the stenosis is at the origin (see Figure 5.15(a)). The cases of Reynolds number 100,200, 500 were simulated.

The streamline for case *Re*=100, 200 and 500 is illustrated in Figure 5.16 (a), (b) and (c) respectively. In each case, the velocity profile in z=0 plane is not symmetrical at the stenosis and in the downstream vicinity of the stenosis. It is also clear that the vorticity magnitude of the eddy behind the stenosis increases with Reynolds number.

As our model is not symmetric about the centreline, it is interesting to compare the shear stresses on the opposite sides of the tube. We have labeled "Side A" as the side with the stenosis, and 'Side B" is the side with no protuberance. Figure 5.17 (a), (b), (c) shows the variation of shear stresses along the walls on Sides A and B for the case of *Re*=100,200,500, respectively. The wall shear stress is normalized by the $\rho U^2/Re$. It is observed that shear stresses on both Side A and Side B reach their maximum value just before the throat of the stenosis (at x=0). There are distinct differences in the shear stresses exerted on Side A and B. On Side B, there is no negative shear stress. Hence, no flow separation or backflow occurs on this side of the wall. On Side A, there is a region of negative shear stress since flow separation occurs. It is also observed that the maximum shear stress on Side A and Side B increases with the Reynolds number.

In all cases, the peak shear stress on Side A is higher than that on Side B. For *Re*=100,200,500 considered in our study, the peak shear stress ratio on Side A and Side B is 1.45, 1.69, 2.11 respectively.

5.3 Steady and Unsteady Flows in an Elastic Tube

For simulations of flow in elastic tubes, moving boundary treatment would be encountered. As we know, for the stationary curved wall boundary, extrapolation scheme (Guo et al. 2002a) and improved bounce-back scheme (Bouzidi et al. 2001) are available. In this study the extrapolation scheme (Guo et al. 2002a) was used to handle the curved wall boundary. When we extend this boundary conditions for a moving boundary illustrated in Figure 5.18, we should ensure the velocity of the moving wall $u_w << c_s$. When lattice node changes from wall node into fluid node as indicated by filled square in Figure 5.18, one must specify the unknown distribution functions (e.g., f_3, f_4, f_7, f_8 for lattice node A).

Here, a second order extrapolation is used to compute the unknown distribution functions along the direction of a chosen discrete velocity $\boldsymbol{e}_i$ which maximizes the quantity $\mathrm{n}\cdot\boldsymbol{e}_i$, where n is the out-normal vector of the wall at the point A in Figure 5.18 through which the node moves to fluid region (Lallemand and Luo, 2003). For example, the unknown distribution functions $f_i(\mathbf{x}_A)$ (i=3,4,7,8) at node x_A can be determined by the following extrapolation formula

$$f_i(\mathbf{x}_A) = 3f_i(\mathbf{x}_B) - 3f_i(\mathbf{x}_C) + f_i(\mathbf{x}_C + \mathbf{e}_4). \tag{5.9}$$

Other methods to obtain values of these unknown distribution functions are also suggested in the study of Lallemand and Luo (2003). Since those possible schemes produce similar results as the above scheme (Lallemand and Luo, 2003), only the above treatment was used in present study.

In this section, we performed simulation of a long and thin axisymmetric elastic pipe with length L. We assume a linear relationship between pressure $p(x)$ and radius $R(x)$ as following

$$p(x) - p_o = \beta(R(x) - R_o), \tag{5.10}$$

where p_o is the pressure outside the tube, R_o is the radius for zero transmural pressure (i.e., the pressure difference between the inside and outside of tube) and β is a compliance constant. Eq. (5.10) is a good representation of the pulmonary blood vessels (Fung, 1997). We assume the pipe is long and thin (i.e., $L>>R_o$), the pipe is smooth under deformation and the entry and exit effects are neglected. Hence, the local flow field can be assumed to be the parabolic Poiseuille profile (Fung, 1997). The longitudinal velocity $u(x,r)$ in the tube at (x,r) is

$$u(x,r) = u_c(x)\left[1 - \frac{r^2}{R^2(x)}\right], \tag{5.11}$$

where r is the distance from the axis. $u_c(x,r)$ is the velocity at axis which can be written as

$$u_c(x) = -\frac{\partial p(x)}{\partial x}\frac{R^2(x)}{4\rho\nu}. \tag{5.12}$$

The volume-flow rate at x is

$$Q(x) = \int_0^R \rho u(x,r) 2\pi r dr = \frac{\rho u_c(x)}{2}\pi R^2(x) = -\frac{\pi R^4(x)}{8\nu}\frac{\partial p(x)}{\partial x}. \tag{5.13}$$

From Eq. (5.10), we obtain

$$\frac{\partial p(x)}{\partial x} = \beta\frac{d[R(x)]}{dx}. \tag{5.14}$$

Consequently, with Eq. (5.13) and Eq. (5.14), the volume-flow rate can be written as

$$Q(x) = -\beta \frac{\pi R^4(x)}{8\nu} \frac{d[R(x)]}{dx} \tag{5.15}$$

In a stationary, non-permeable axisymmetric tube, Q is a constant through the length of the tube. Integrating Eq. (5.15), we obtain, for steady flow, an explicit expression for $R(x)$ in terms of the inlet and outlet radius is

$$R(x) = \left\{ \left(R(L)^5 - R(0)^5 \right) \frac{x}{L} + R(0)^5 \right\}^{1/5}. \tag{5.16}$$

Substituting Eq. (5.16) into the Eq. (5.10), we can obtain the theoretical formula for pressure $p(x)$.

In our simulation, the Reynolds number was defined as

$$\mathrm{Re} = \frac{4Q}{\pi R \nu} = \beta \frac{[R(0)]^4 - [R(L)]^4}{10 L \nu^2}. \tag{5.17}$$

Firstly we simulate a steady case with p_{in} = 1.00294, p_{out} = 0.99762, p_0=1.0, $\beta = 0.002$, $\tau = 1$, Re=43.4 and the pipe is 100 lattice units in length. The initial equilibrium radius of the tube is R_0=9.5 for p_0 =1.0 and the computational grid is 100×13. At beginning, zero velocities were initialized in the whole flow field with the fixed wall. After the flow field reached a steady state, the wall was released. The pressure at each segment of the physical boundary is obtained by linear extrapolation and the fluid and the radius can be instantaneously determined by Eq. (5.10). Then the new geometry of the tube was adapted and 10 LBGK iterations are performed, the pressure is again measured, etc. This cycle is iterated until the following convergence criterion reached,

$$\varepsilon = \frac{\sum_i \left| R^{n+1}(x_i) - R^n(x_i) \right|}{\sum_i \left| R^n(x_i) \right|} < 10^{-4}, \tag{5.18}$$

where the superscript is the time level and the summation is over the all lattice units in length.

Figure 5.19 shows the resulting diameter and pressure as a function of position in the elastic tube. The theoretical curves (Eq. (5.16)) are shown as well. Our numerical results agree well with analytical solutions. It is also noticed that the curve or the expression for $R(x)$ and $p(x)$ of a 2D case with same parameters (Fang et al. 2002) are significantly different from the present study because the 2D case only consider the flow in elastic channel (Fang et al. 2002). If we change the parameter of τ and keep the other parameter in the case constant, when $\tau = 0.63$ which means Re=641, numerical simulation is still stable. For higher Re, numerical instability appears.

The unsteady periodic flow with $p_{\text{in}} = 0.9985+0.003\sin(2\pi t/T)$, $p_{\text{out}} = 0.9985$, p_0=1.0, $\beta = 0.002$, $\tau = 0.7$ and Womersley number $\alpha = 2.06$ was also simulated. The initial equilibrium radius of the tube is R_0=9.5 for p_0 =1.0 and the computational grid is 100×13. The simulation procedure is similar as that of steady flow. Figure 5.20 shows an example of this settling of the tube wall for both the above steady and periodic flows after the walls are released at t=1000. Figure 5.21 shows the curve of $R(x)$ at different times during one period.

In our simulations, it is found difficult to simulate the higher Womersley case due to numerical instability. For example, if L_x>$10R_0$ (to ensure our assumption $L>>R_o$), L_x/c_sT<0.05, then

$$\alpha = R_0\sqrt{2\pi/T\nu} < R_0\sqrt{2\pi\times 0.05c_s/(10R_0\nu)} = \sqrt{2\pi\times 0.005c_sR_0/\nu}\,. \quad (5.19)$$

As v is determined by τ , which cannot be very close to 0.5, the larger is the grid size, the higher Womersley number can be achieved. However, due to limitation of grid size, case of very high Womersley number cannot be simulated.

5.4 Summary

In this Chapter, firstly, the steady flows through a single constriction with different geometries were studied. It is clear that for the same Reynolds number, when the constriction is more severe, the maximum wall vorticity is larger. If there is a flow separation, the wall vorticity reverses to negative value behind the stenosis. We also discussed the effect of distance between two adjacent stenoses on streamlines, shear stress, vorticity and velocity distribution as blood pass through them. In those cases, if flow interference exists, the second peak wall vorticity values are always lower than the first ones and the maximum velocity value near the second constriction is slightly higher than that at the first constriction.

The unsteady flow through constricted tube was also simulated. The sinusoidal waveform was considered as a simple prototype of physiological waveforms. The case Re=200, St=0.32, α=4.0 was simulated and the LBM result agree well with that of FVM. It is also found that if the numerical stability is not improved, it is no way to simulate cases of higher Re and high St.

To consider more complex 3D stenosed model, the steady flow through a 3D asymmetric model was also simulated. It is observed that there is a distinct and significant difference in the wall shear stresses between the stenosed side and the side with no protuberance. The peak shear stress ratio of the two sides may be useful for study of the atherosclerotic process.

The steady and pulsatile flows in an elastic tube were simulated using a tube law. We improved the study of Fang et al. (2002) by applying our axisymmetric D2Q9 model since Fang et al. (2002) only consider the 2D elastic channel that is significantly different from the real tube.

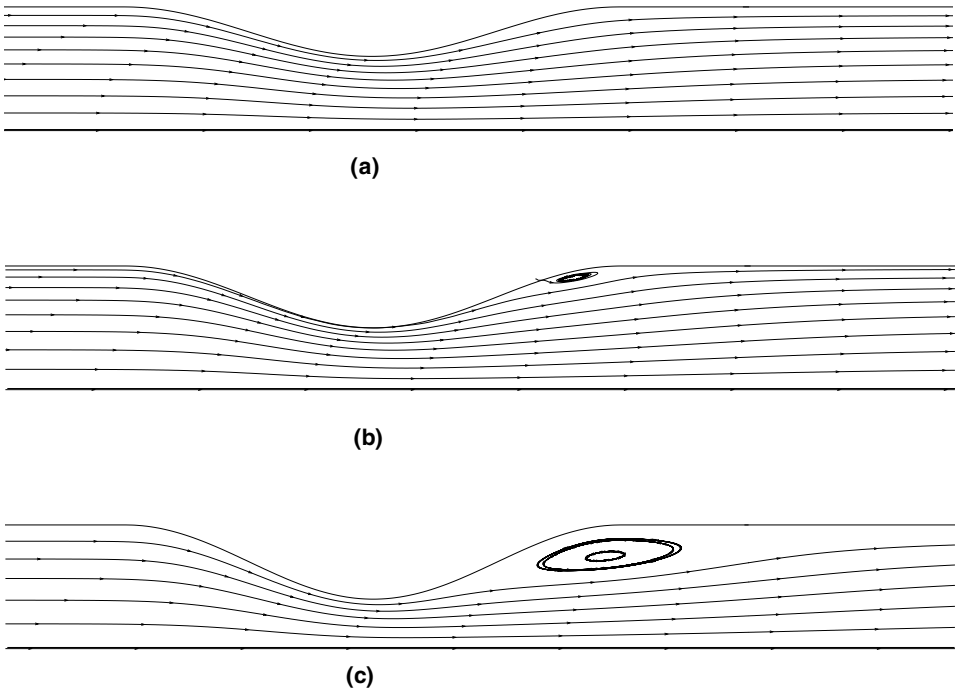

Figure 5.1 Blood flow through (a) 64%, (b) 75%, (c) 84% stenosis (S_0=D, Re=50)

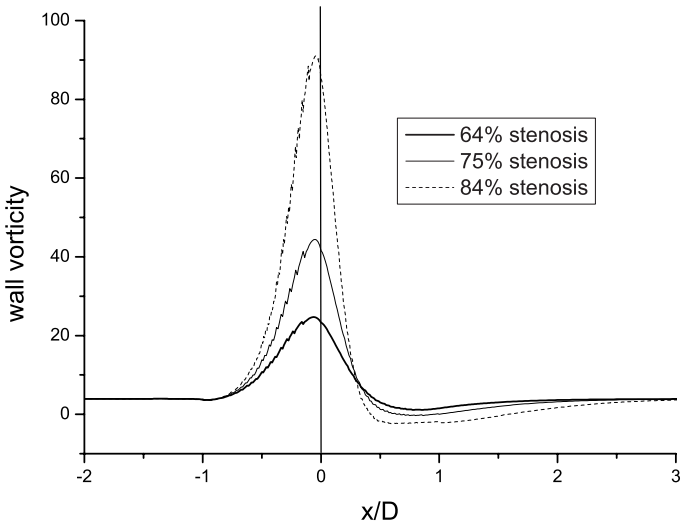

Figure 5.2 Wall vorticity along the constricted tubes

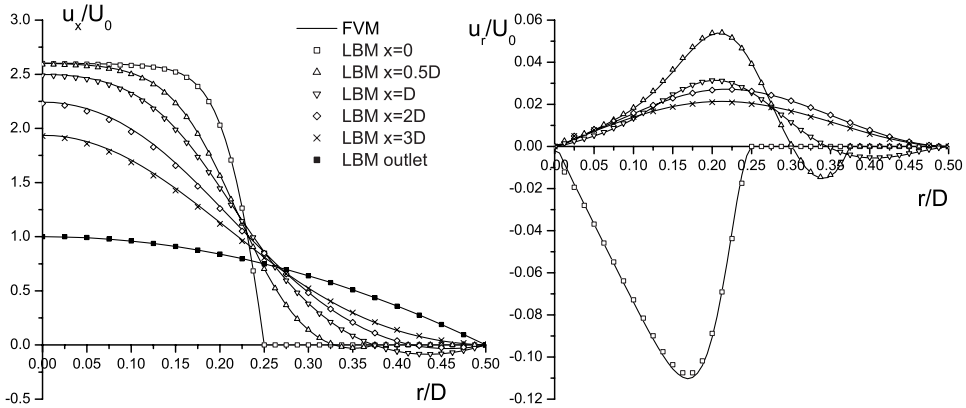

Figure 5.3 Velocity profiles in different position in case of S_0=D, Re=200

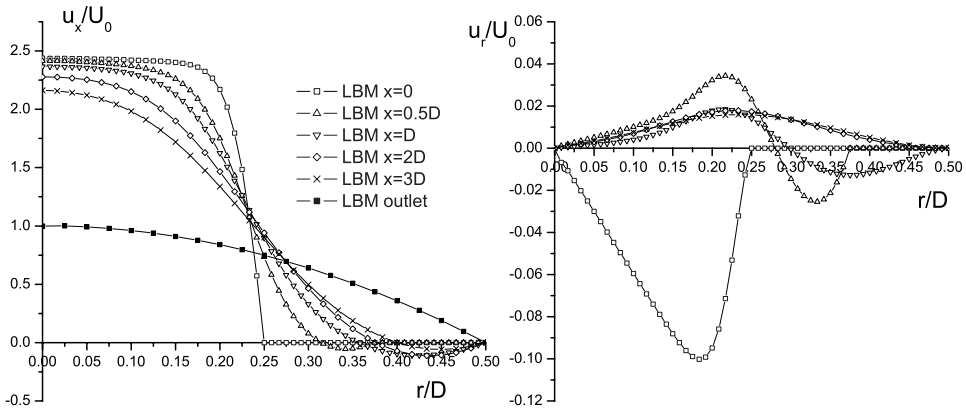

Figure 5.4 Velocity profiles in different position in case of S_0=D, Re=400

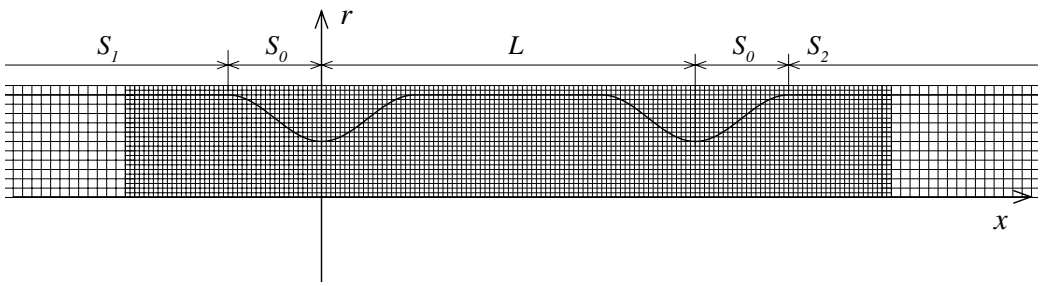

Figure 5.5 Geometry and mesh of constricted tubes

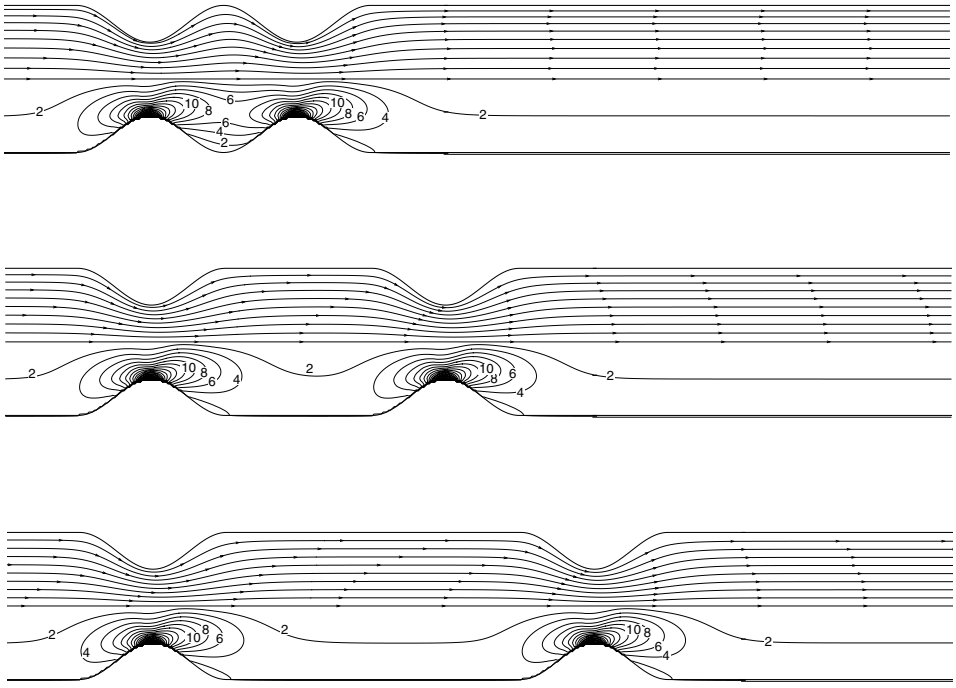

Figure 5.6 Streamlines and shear tress contours for constriction spacings *L/D*=1,2,3 (*Re*=10)

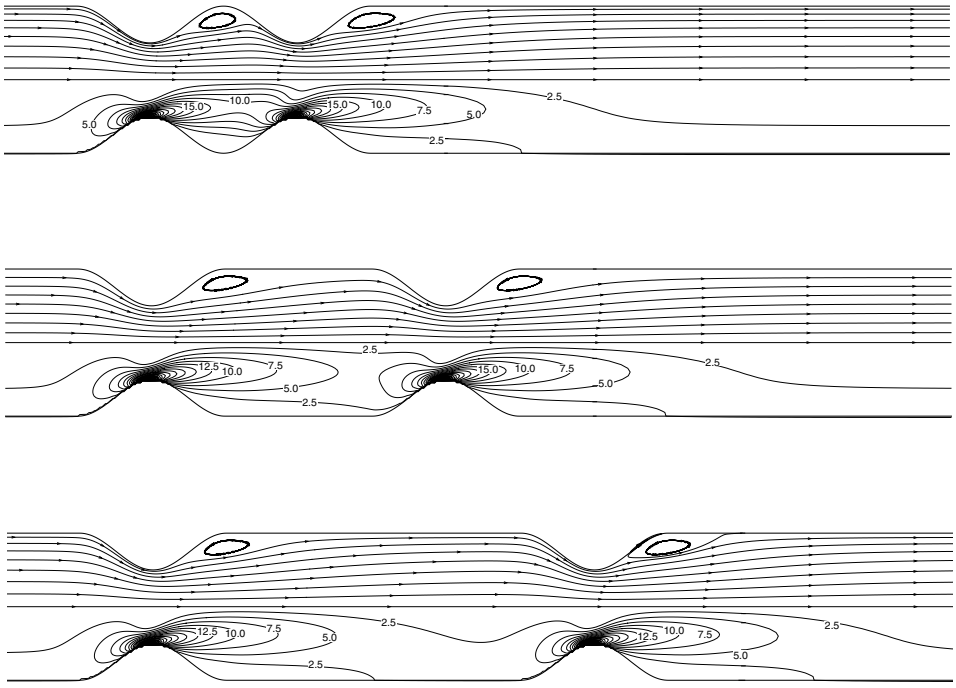

Figure 5.7 Streamlines and shear stress contours for constriction spacings *L/D*=1,2,3 (*Re*=50)

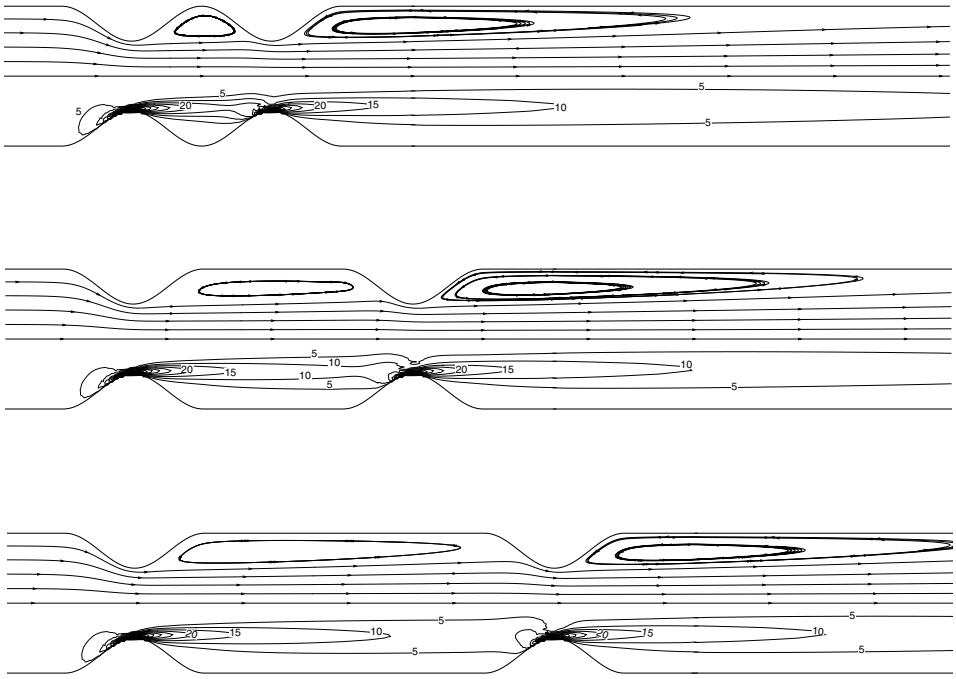

Figure 5.8 Streamlines and shear stress contours for constriction spacings *L/D*=1,2,3 (*Re*=300)

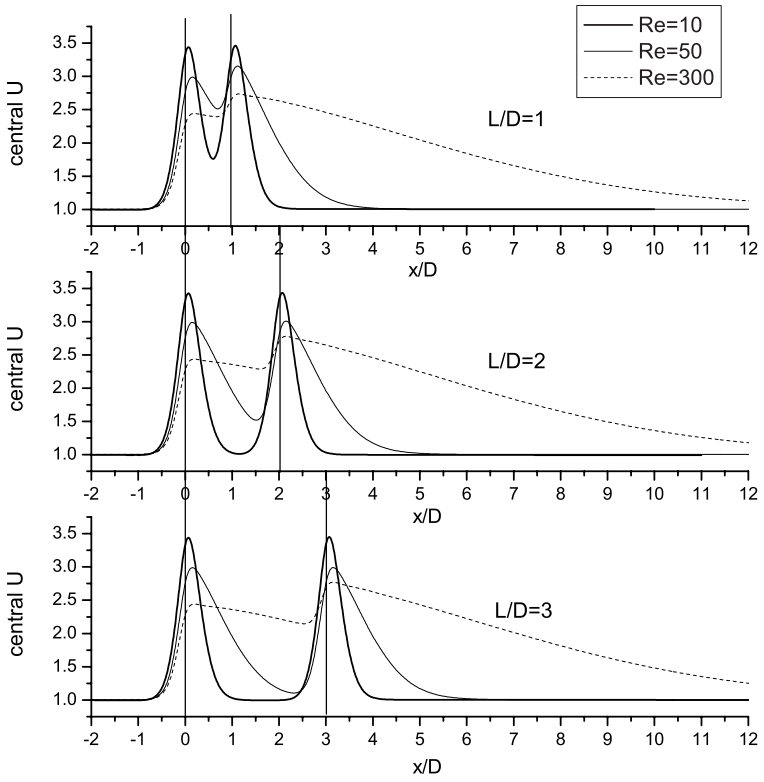

Figure 5.9 Variation of axial velocity on axis for different constriction spacings

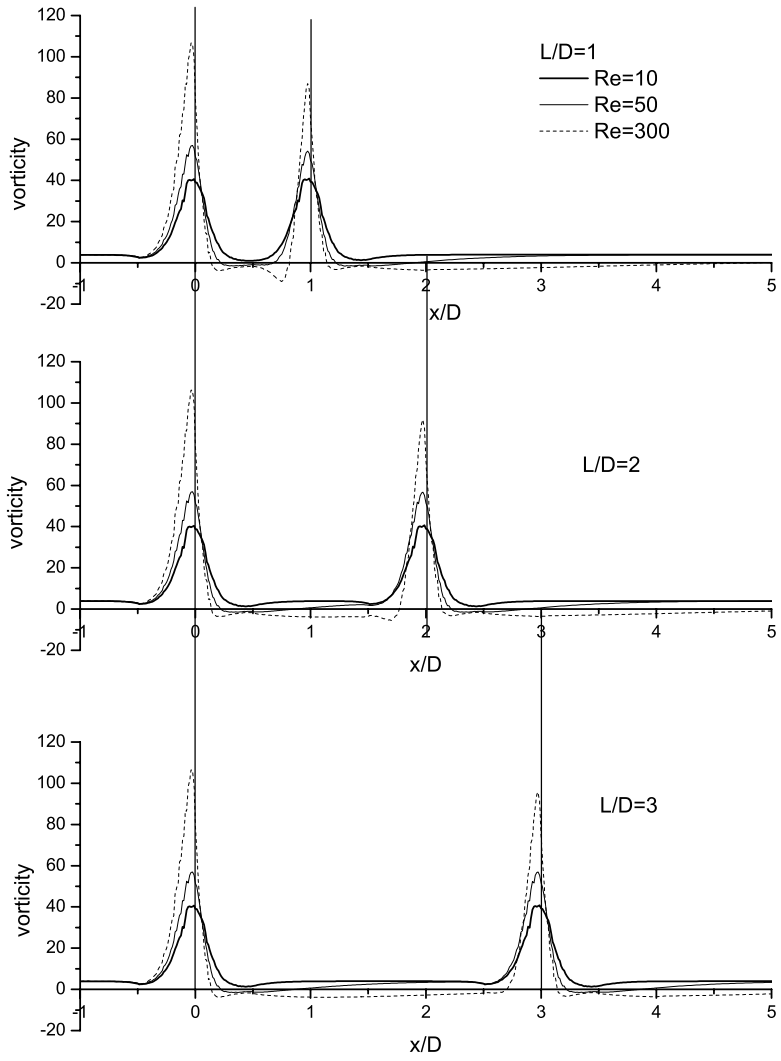

Figure 5.10 Variation of wall vorticity for different constriction spacings

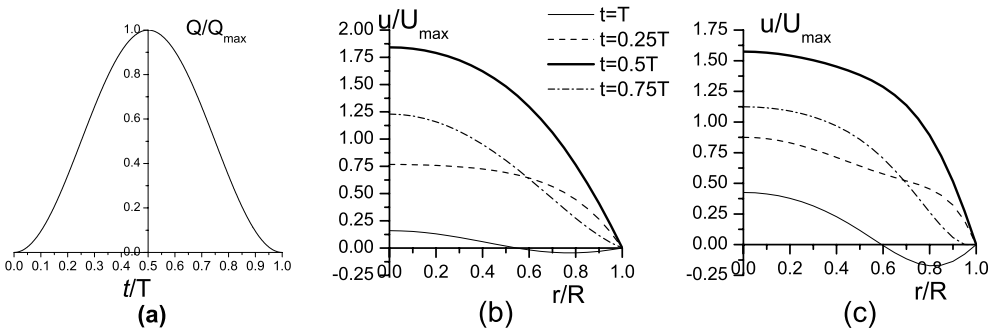

Figure 5.11 Inlet velocity profiles based on the Womersley solution. (a) Temporal variation of inlet volume flux. (b) Velocity profiles for α=4. (c) Velocity profiles for α=8.

Figure 5.12 The streamlines (above the axis) and vorticity contours (under the axis area) in the constricted tube for *Re*=200, *St*=0.32 at *t*=*nT*/10, *n*= 1,3,5,7,9

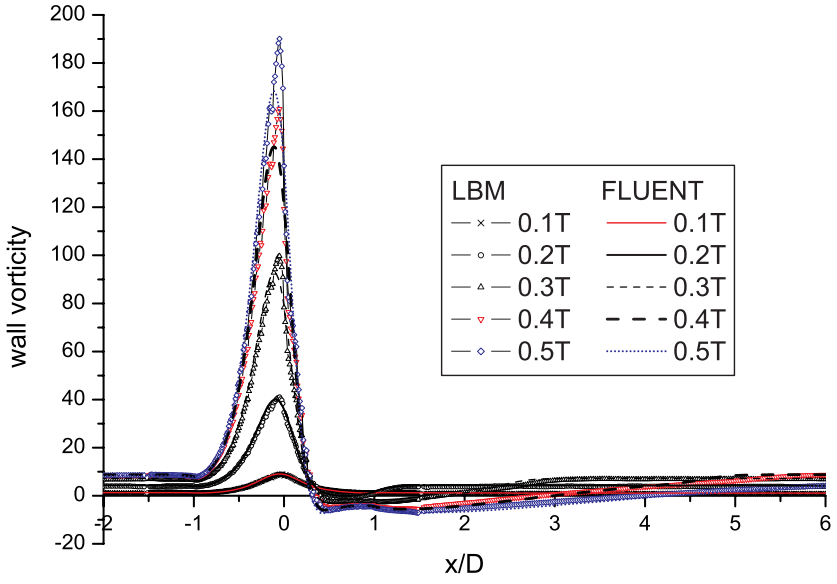

Figure 5.13 Wall vorticity obtained by LBM and FVM at *t*=*nT*/10, *n*= 1,2,3,4,5 for pulsatile flow through a constricted tube

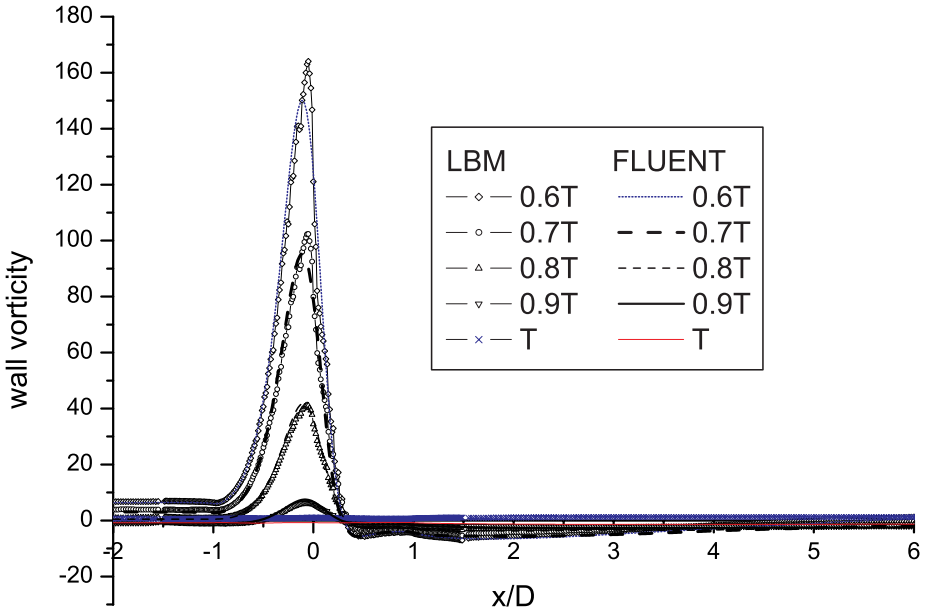

Figure 5.14 Wall vorticity obtained by LBM and FVM at $t=nT/10$, n= 6,7,8,9,10 for pulsatile flow through a constricted tube

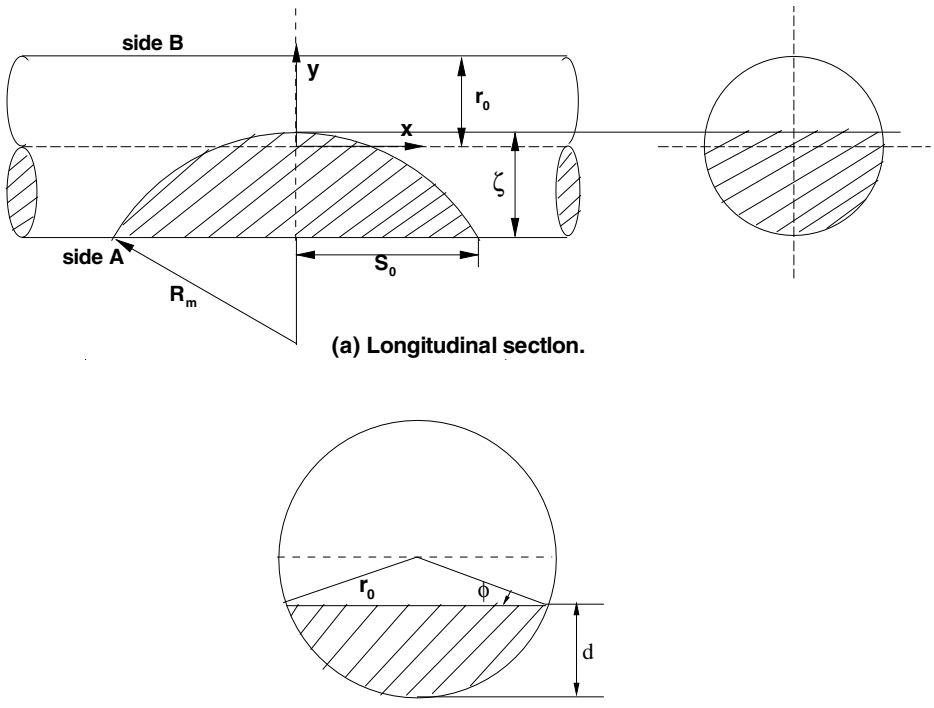

Figure 5.15 Geometry of the stenosis model

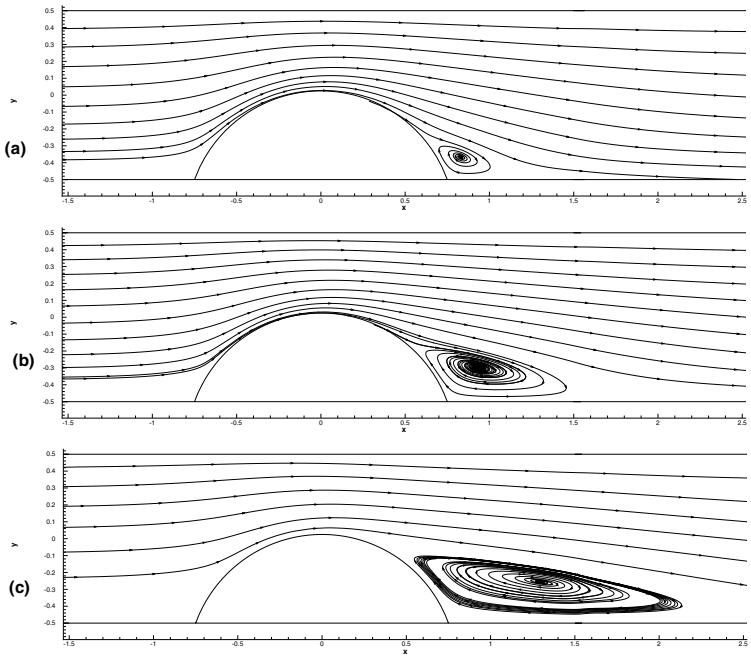

Figure 5.16 Streamline of flows though 3D asymmetric stenosis (a) *Re*=100, (b) *Re*=200, (c) *Re*=500

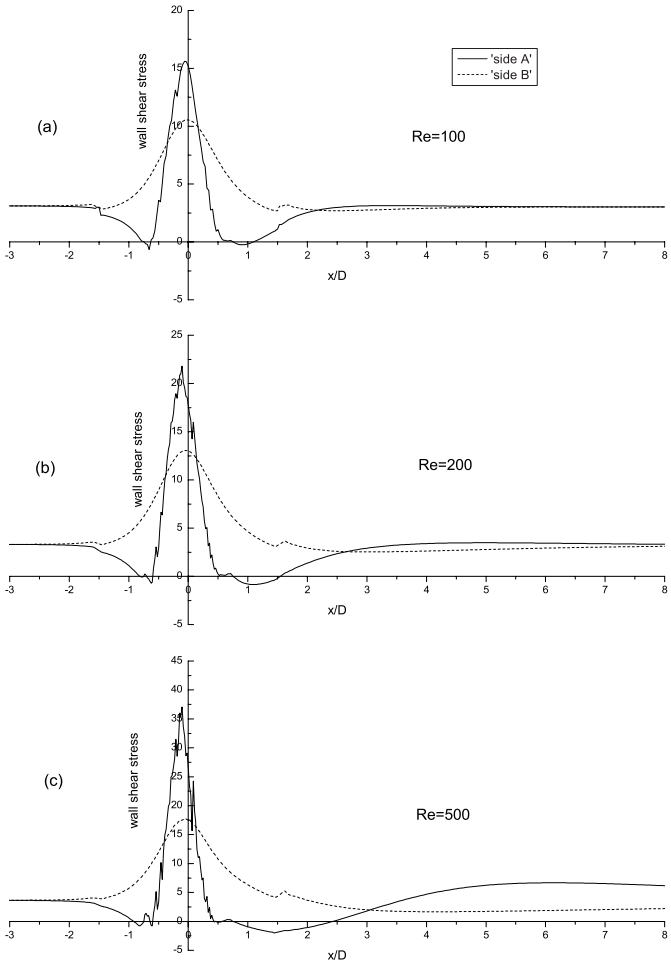

Figure 5.17 Wall shear stress along axial position (53% 3D asymmetric stenosis) (a) *Re*=100, (b) *Re*=200, (c) *Re*=500

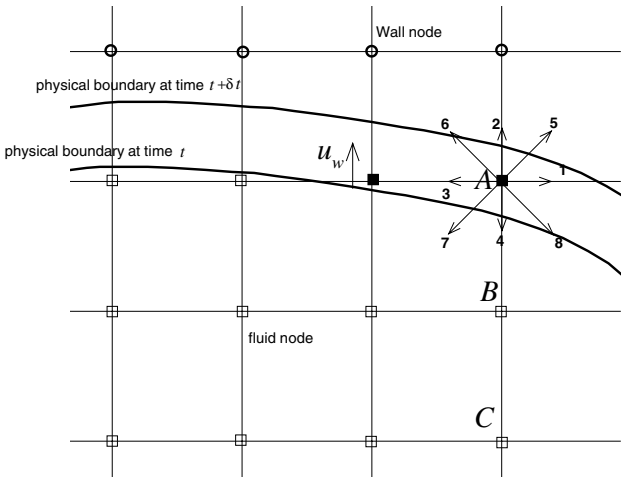

Figure 5.18 Illustration of a moving boundary with velocity u_w. The open circles (○) and square (□) denote the non-fluid and fluid nodes, respectively. The filled squares denote the nodes becoming fluid nodes from the non-fluid nodes after one time step

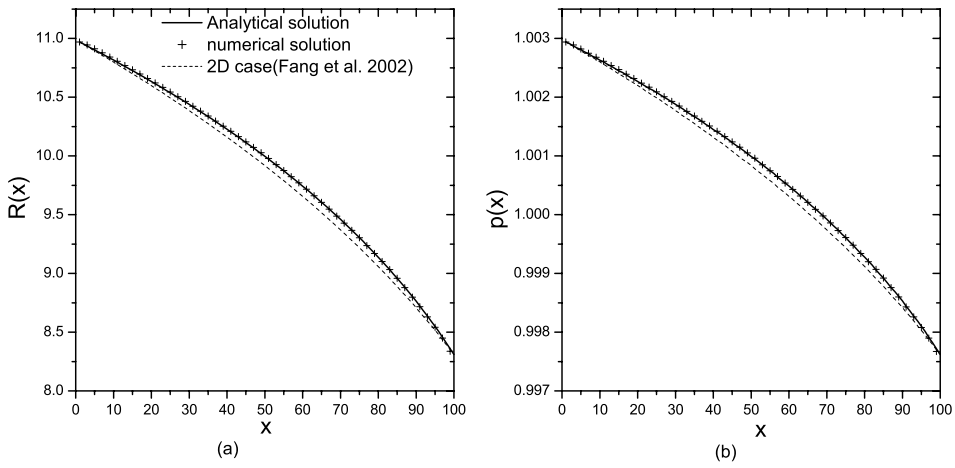

Figure 5.19 Numerical and analytical solution for (a) radius in an elastic tube, (b) pressure on inner elastic tube

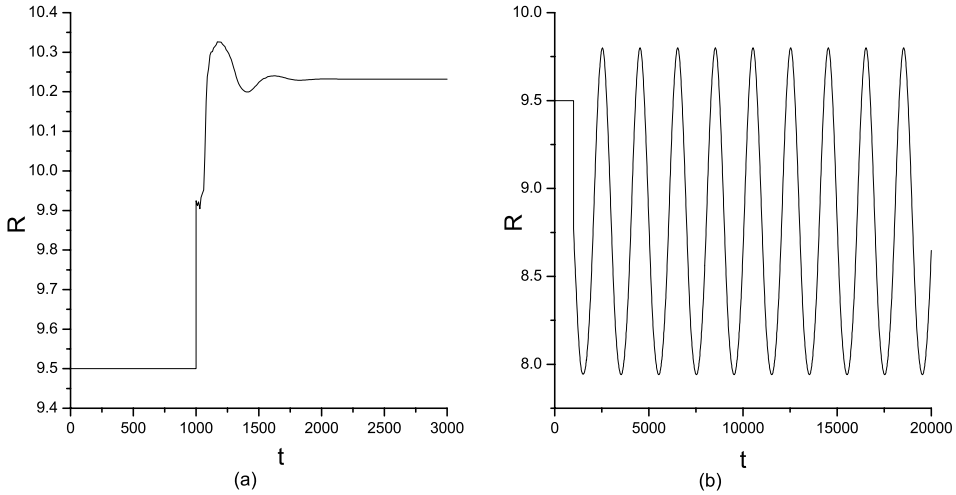

Figure 5.20 Variation of the radius at $x = 40$ after the walls are released at t=1000 . (a) steady flow on a 100×13 lattice (Re = 43.4); (b) pulsatile flow on a 100×13 lattice with T = 2000 (α=2.06)

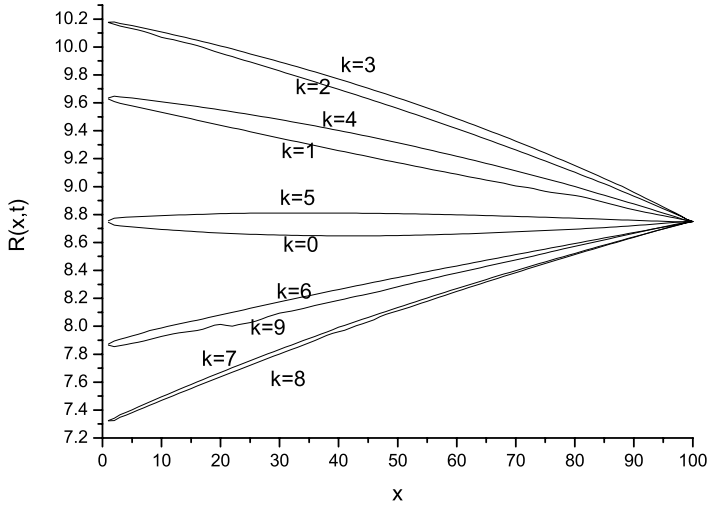

Figure 5.21 Variation of radius in an elastic tube at t=nT+(k/10)T during a period (pulsatile flow on a 100×13 lattice with T = 2000, α=2.06)

Chapter 6 LBM for Simulation of Axisymmetric Flows with Swirl

In this Chapter[4], the axisymmetric swirling flows would be solved by a hybrid scheme. The axial and radial velocities were solved by axisymmetric LBM and swirl velocity and temperature were solved by finite difference method. This hybrid scheme was firstly validated by simulation of Taylor-Couette flows between two concentric cylinders. Then the four benchmark problems for numerical simulation of the melt flows in Czochralski (CZ) crystal growth (Wheeler et al., 1990) were studied in detail.

6.1 Hybrid Axisymmetric LBM and Finite Difference Method

We consider the problems of the laminar axisymmetric swirling flow of an incompressible liquid. The continuity equation (6.1) and Navier-Stokes momentum equations (6.2) in the pseudo-Cartesian coordinates (x,r) are used to describe the flow in axial (x direction) and radial directions.

$$\frac{\partial u_\beta}{\partial x_\beta} = -\frac{u_r}{r} \tag{6.1}$$

$$\begin{aligned} &\partial_t u_\alpha + \partial_\beta (u_\beta u_\alpha) + \frac{1}{\rho_0}\partial_\alpha p - \nu\partial_\beta^2 u_\alpha \\ &= -\frac{u_\alpha u_r}{r} + \frac{\nu}{r}\left(\partial_r u_\alpha - \frac{u_r}{r}\delta_{\alpha r}\right) + \frac{u_z^2}{r}\delta_{\alpha r} + E \end{aligned} \tag{6.2}$$

Where u_β (β=x,r) is the two components of velocity and u_α is the velocity u_x

[4] This work has been published as:
Huang, H., Lee, T.S., Shu, C., Hybrid lattice-Boltzmann finite-difference simulation of axisymmetric swirling and rotating flows, *Int. J. Numer. Meth. Fluids,* 53(11), pp.1707-1726. (2007)

or u_r. In the above equation, u_z is the swirl velocity. E is the additional source term, which may appear in melt flows in CZ crystal growth. The Einstein summation convention is adopted.

Here for simplicity, the axisymmetric model B in Chapter 3 was used to simulate axial and radial velocities. In the model B, $A^{(1)}$, $A^{(2)}$ and $F_\alpha^{(1)}$ are all the same as that in Chapter 3 part 3.2.3 except here, the $F_\alpha^{(2)}$ is

$$F_\alpha^{(2)} = \rho_0\left[-\frac{u_\alpha u_r}{r} + \delta_t(\tau-1)c_s^2\partial_\alpha\left(\frac{u_r}{r}\right) + \frac{\nu}{r}\left(\partial_r u_\alpha - \frac{u_r}{r}\delta_{\alpha r}\right) + \frac{u_z^2}{r}\delta_{\alpha r} + E\right] \tag{6.3}$$

For the axisymmetric swirling flow, there are no circumferential gradients but there may still be non-zero swirl velocity u_z. The momentum equation for azimuthal velocity is

$$\frac{\partial u_z}{\partial t} + u_x\frac{\partial u_z}{\partial x} + u_r\frac{\partial u_z}{\partial r} = \nu\left(\frac{\partial^2 u_z}{\partial x^2} + \frac{\partial^2 u_z}{\partial r^2}\right) + \frac{\nu}{r}\left(\frac{\partial u_z}{\partial r} - \frac{u_z}{r}\right) - \frac{u_r u_z}{r} \tag{6.4}$$

The above momentum equation for azimuthal velocity can be solved by finite difference method. In this Chapter, Eq. (6.4) was solved explicitly by using first-order forward difference scheme in time and the second-order central difference scheme (e.g., Eq. (6.6) and (6.7)) for space discretization as Eq. (6.5).

$$\begin{aligned} u_z^{n+1} &= u_z^n + \\ &\delta_t\left[-\left(u_x^n\frac{\partial u_z^n}{\partial x} + u_r^n\frac{\partial u_z^n}{\partial r}\right) + \nu\left(\frac{\partial^2 u_z^n}{\partial x^2} + \frac{\partial^2 u_z^n}{\partial r^2}\right) + \frac{\nu}{r}\left(\frac{\partial u_z^n}{\partial r} - \frac{u_z^n}{r}\right) - \frac{u_r^n u_z^n}{r}\right] \end{aligned} \tag{6.5}$$

$$\frac{\partial u_z^n}{\partial x} = \frac{\left(u_z^n\right)_{i+1,j} - \left(u_z^n\right)_{i-1,j}}{2\delta_x} \tag{6.6}$$

$$\frac{\partial^2 u_z^n}{\partial x^2} = \frac{\left(u_z^n\right)_{i+1,j} + \left(u_z^n\right)_{i-1,j} - 2\left(u_z^n\right)_{i,j}}{\delta_x^2} \tag{6.7}$$

6.1.1 Boundary Conditions

In our simulations in this Chapter, when using LBM to solve the axial and radial velocities, the specular reflection scheme was used for axisymmetric boundary. As we know, specular reflection scheme can be applied to free-slip boundary condition where no momentum is to be exchanged with the boundary along the tangential component. Hence, for the free surface (e.g., $x=H$, $R_x<r<R_c$ in Figure 6.4) in our simulated case, the specular boundary condition is also applied.

For non-slip wall boundary, the bounce-back scheme was used.

When using the finite difference method to solve the equation for swirl velocity or the heat equation, we may encounter the Neumann boundary condition. Here the Neumann boundary condition was transferred into the Dirichlet boundary condition. For example, if $\partial T/\partial x = 0$ was imposed at the boundary $x=0$ (i.e., the r-axis, refer to Figure 6.4), the T value in the boundary lattice node (1,j) can be determined by extrapolation from the inner lattice nodes as $(T)_{1,j} = \left(4(T)_{2,j} - (T)_{3,j}\right)/3$, where j is the lattice index in r coordinate.

6.2 Taylor-Couette flows

Figure 6.1 illustrates the geometry of Taylor-Couette flow. Our computational domain is a r-x plane. The governing equations for the axisymmetric swirl flow are equations (6.1), (6.2) and (6.4) with E=0 in Eq. (6.2). The boundary conditions used in our simulation are also illustrated in the Figure 6.1. The Reynolds number is defined as $\mathrm{Re} = WD/\nu$, where W is the azimuthal velocity of inner cylinder, D is the gap of the annulus and v is the fluid viscosity. The radius ratio of inner cylinder and out cylinder is set as 0.5. The aspect ratio is set as 3.8.

Firstly, the grid independence of the results was examined and it was found that with grid 20×76 uniform grid, present numerical method can give very accurate results. The maximum stream functions in *r-x* plane for cases of *Re*=85, 100 and 150 were listed in Table 6.1. It seems that even with grid 20×76, The results of our hybrid scheme agree well with those of Liu (1998), which were obtained by very fine grid. The contours of stream function, pressure and vorticity for case *Re*=150 were shown in Figure 6.2. From Figure 6.2, we can see the four cell secondary mode. These contours and flow pattern also agree well with the results of Liu (1998).

Secondly, the efficiencies of our hybrid scheme (LBM+FD) and explicit finite volume method (FVM) were compared. The efficiency is evaluated by comparing the respective computing times required. To minimize the influence of computers and convergence criterion, in this study, both our hybrid scheme solver and FVM solver (FLUENT) are executed on a super computer (Compaq ES40: total performance of 5300 Mflops) in the National University of Singapore. In our simulations, the zero velocities were initialized everywhere. The residual used to monitor the convergence is defined using the u_z-momentum equation for two solvers as below:

$$\text{LBM+FD:} \quad \sum \left| \frac{u_z^{n+1} - u_z^n}{\delta t} \right| \tag{6.8}$$

$$\text{FVM:} \quad \sum \left| \frac{\partial u_z^n}{\partial t} + u_x^n \frac{\partial u_z^n}{\partial x} + u_r^n \frac{\partial u_z^n}{\partial r} + \frac{u_r^n u_z^n}{r} - \nu \left(\frac{\partial^2 u_z^n}{\partial x^2} + \frac{\partial^2 u_z^n}{\partial r^2} \right) - \frac{\nu}{r} \left(\frac{\partial u_z^n}{\partial r} - \frac{u_z^n}{r} \right) \right| \tag{6.9}$$

Note that all the computations are carried out on a single-CPU of the computer Compaq ES40, which does not take parallel advantage of the LBM.

For comparison purpose, the case of Taylor-Couette flow for *Re*=100 using

grid 30×114 was simulated. In the explicit FVM solver (FLUENT), the Courant number was set as *CFL*=1. The convergence for the hybrid scheme and FVM solver is displayed in Figure 6.3 in terms of relative residual error (the residual expressions were normalized by the initial residual). The overall convergence trend of our hybrid scheme is similar to that of FVM solver.

The CPU times for hybrid scheme and FVM are also listed in Table 6.2. It seems that to reach the same convergence criterion, our LBM+FD solver (τ=0.59) takes almost the same CPU time as the explicit FVM solver. The calculation of LBM+FD solver with relax time constant τ=0.68 is faster than calculation with τ=0.59.

According to our experience, for a 2D flow case with same grid, usually the explicit FLUENT solver requires about 8 times larger CPU time per iteration than our 2D LBM solver. It is also observed that for axisymmetric cases without rotation, the FLUENT solver requires about 4 times larger CPU time per iteration than axisymmetric LBM.

From Table 6.2, it is found that for the axisymmetric flow with rotation, compared with LBM+FD solver, FLUENT requires about 3.35 times larger CPU time per iteration. It is also observed from our numerical experiment that the time spent for the solving of the Eq. (6.5) (i.e., FD) in our LBM+FD scheme is around 12% of total CPU time.

6.3 Flows in Czochralski Crystal Growth

After our hybrid scheme was validated by Taylor-Couette flow simulations, the hybrid scheme was used to study the melt flows in Czochralski crystal growth. In the CZ crystal growth, the melt flow is very complex because it is a

combination of natural convection due to thermal gradients and forced convection due to rotation of the crystal and the crucible. Here, the Wheeler benchmark problems (Wheeler, 1990) in numerical simulation of melt flows in CZ crystal growth were studied in detail. The configuration and the momentum and thermal boundary conditions are all illustrated in Figure 6.4. In the problem, a vertical cylindrical crucible filled with a melt to a height $H=R_c$ rotates with an angular velocity Ω_c . In the top of the melt, it is bounded by a coaxial crystal with radius $R_x=\beta R_c$ (β=0.4) which rotates with angular velocity Ω_x. There is a phase boundary between the crystal and melt. In the top right part of melt ($R>R_x$), there is a free surface. The u_x, u_r, u_z are the axial, radial and azimuthal velocity component, respectively.

The continuity and momentum equations for Czochralski crystal growth can also illustrated by Eq. (6.1), (6.2) and (6.4) with $E = g\beta_0(T - T_c)\delta_{\alpha x}$. For the buoyancy force term $E = g\beta_0(T - T_c)\delta_{\alpha x}$, the Boussinesq approximation is applied, where g is the gravity acceleration; β_0 is the thermal expansion coefficient; T_c is the temperature of crucible. The governing equation of temperature is

$$\frac{\partial T}{\partial t} + u_x \frac{\partial T}{\partial x} + u_r \frac{\partial T}{\partial r} = \frac{\nu}{\mathrm{Pr}}\left(\frac{\partial^2 T}{\partial x^2} + \frac{\partial^2 T}{\partial r^2} + \frac{1}{r}\frac{\partial T}{\partial r} \right). \tag{6.10}$$

This equation can be solved explicitly by finite-difference method as Eq. (6.5). However, in this part, to accelerate convergence rate, finite difference equations for Eq. (6.4) and (6.10) were solved by the tridiagonal matrix algorithm (TDMA) at each iteration.

The dimensionless parameters: Reynolds number Re_c, Re_x, Prandtl number Pr and Grashof number Gr are defined as

$$\mathrm{Re}_c = \frac{R_c^2 \Omega_c}{\nu}, \quad \mathrm{Re}_x = \frac{R_c^2 \Omega_x}{\nu}, \quad \mathrm{Pr} = \frac{\nu}{\alpha}, \quad Gr = \frac{g\beta_0 (T_c - T_x) R_c^3}{\nu^2}$$

where α is the thermal diffusivity. In our simulations, Pr =0.05. The value of characteristic velocity $U_t = \sqrt{\beta_0 g (T_c - T_x) R_c}$ is chosen 0.15 for Gr<=10^5 and 0.25 for Gr>10^5. When U_t is determined, the kinetic viscosity v can be determined by the dimensionless numbers Gr. Then, the relaxation times τ is determined by the equation $\nu = c_s^2 \delta_t (\tau - 0.5)$. Another characteristic velocity $U_h = R_c \Omega_x \beta$ is also used when Gr=0 in our simulation and it is usually set as 0.1.

For the results, R_c, and ν / R_c are used as the characteristic length, speed scales and the dimensionless temperature is defined as $T' = (T - T_x)/(T_c - T_x)$, where T_x is the temperature of the crystal.

In our simulations, the zero velocities and zero temperature were initialized everywhere and the convergence criterion in our simulation was set as:

$$\sum_{i,j} \frac{\left\| \mathbf{u}(x_i, r_j, t + \delta_t) - \mathbf{u}(x_i, r_j, t) \right\|}{\left\| \mathbf{u}(x_i, r_j, t + \delta_t) \right\|} < 10^{-6} \tag{6.11}$$

where i, j are the lattice nodes index.

To compare with available data of Raspo et al. (1996), Buckle et al. (1993) and Xu et al. (1997), all of the present numerical results are expressed as stream function. The stream function ψ is defined as

$$\frac{\partial \psi}{\partial r} = -r u_x, \qquad \frac{\partial \psi}{\partial x} = -r u_r \tag{6.12}$$

with ψ=0 on the all boundaries of computing plane. In the following, the minimum and maximum values of stream function denoted by $\psi_{\min}$ and $\psi_{\max}$ will be used to compare the results of our hybrid scheme with available data in the literature (Xu et al., 1997; Raspo et al., 1996).

Firstly, the grid independence of the results was examined. The case A2, with Gr=0, Re_x=10^3, Re_c=0, was calculated by 3 kind of grids. The ψ_{min} and ψ_{max} are compared with result of Raspo et al. (1996) in Table 6.3. In Table 6.3, we can see that an 100×100 grid is sufficient to obtain accurate results.

After the grid independence study, as many as 11 cases with different parameter sets were simulated. The 11 cases listed in Table 6.4 were classified into 4 groups. In group A, the crystal rotates with Re_x varyes from 10^2 to 10^4, while the crucible is at rest and Gr is set to zero. In group B, the crystal and crucible rotate in opposite directions. Groups A and B are all forced convection problems. The cases in group C are natural convection problems. Those in group D are closer to practical applications because these melt flows combined both the natural convection and forced convection.

Table 6.4 shows the comparison of computed minimum and maximum stream function for all above 11 cases. In the table, the number in the bracket followed the case type indicates the grid size used. If not specified, the grid used in our simulation is 100×100. For comparison, we also present the results of Xu et al. (1997) using the second-order difference scheme with a grid size of 80×80. In all cases, the maximum absolute values of stream function computed by the LBM agree very well with those of Xu et al. (1997). Some very small deviations between the computed minimum absolute values of stream function can be neglected since the minimum absolute values of stream function are so small compared with the maximum absolute values. Due to requirement of numerical stability, the simulation of cases A3, B3, C2 used fine grids. The issue of numerical stability will be discussed in detail in the following section 6.4.

Figure 6.5 shows the calculated streamlines and temperature contours of case

A2. That's a typical result for group A. There is a primary vortex induced by rotation of the crystal. For the cases of group A, when the Reynolds number of crystal rotation is increased from 10^2 to 10^4, the maximum absolute value of the stream function increases from 0.2272 to 40.47, which means the intensity of vortex increases. For higher Reynolds number cases in group A, the center of the vortex moves towards the side wall of the crucible and the highest velocity region moves from the upper left corner to the upper right corner. Hence, better quality crystal can be produced if Re_x is high.

Figure 6.6 illustrates the streamlines and temperature contours of case B2, which represent the flow pattern of group B. For cases in group B, the crystal and crucible rotate in opposite directions. As a result, there are two vortices with opposite directions appearing in the upper left corner just below the crystal and the lower right corner. With the increase of rotation speeds of the crystal and crucible, the upper left vortex produced moves towards right corner and the lower right primary vortex induced by the crucible rotation moves to the left and dominates the flow field. It is noticed that for cases of forced convection problems where Gr=0 (cases in group A and B), the contours of temperature are very similar.

Figure 6.7 shows the streamlines and temperature contours of case C2. In this natural convection flow case, the crucible and the crystal are all at rest. There is a primary vortex induced by the temperature difference between the crystal and crucible. Compared with temperature contours in Figure 6.5 and Figure 6.6, the temperature contours of case C2 in Figure 6.7 shows the effect of buoyancy force on the temperature field.

Figure 6.8 shows the streamlines and temperature contours of case D2. The

streamlines and contours illustrated the combined effects of the natural convective flow and forced convective flow. It is found that the streamlines and temperature contours of cases in group D are very similar to those of case C1 which Grashof number is also equal to 10^5. From Table 6.4, it is also found that the ψ_{max} of cases in group D are all very close to that of case C1. That means in cases of group D, if $Re_x<10^3$, the natural convective flow dominates the melt flow while the force convective flow induced by the crystal only has minor effect.

6.4 Numerical Stability Comparison for Axisymmetric lattice Boltzmann Models

The numerical stability of LBM depends on the relax time τ, the Mach number of the flow and the size of mesh. It is well known that in LBM if τ is very close to the 0.5, numerical instability would appear. τ_{min} is usually case-dependent. The Reynolds number is usually defined as $\mathrm{Re}=\frac{UD}{\nu}=\frac{Uc(D/\delta_x)}{c_s^2(\tau-0.5)}$, the Mach number in LBM is $M=U/c_s<<1$. To simulate cases of high Reynolds number, with limitation of τ_{min} and Mach number, we must increase the value of (D/δ_x) (i.e., enlarge the grid size).

Generally speaking, adding complex position and time dependent source terms into the lattice Boltzmann equation would decrease the numerical stability. As our analysis in Chapter 3 shown, the previous model of Peng et al. (2003) is only a specific case of our general model and it recovers the NS equations in axisymmetric coordinates with some error. Compared with the model of Peng et al. (2003), our present model is much simpler since $F_\alpha^{(1)}=0$ and u_z only appears in the term $F_\alpha^{(2)}$ and gradients of u_z are not included. Hence, the present model is

expected to be more stable.

To compare the numerical stability of our model and previous model (Peng et al. 2003), the benchmark case A1 of melt flow in CZ crystal growth was simulated by the two models with the same boundary condition treatment. As we know, the numerical stability can be demonstrated by the minimum τ value at which numerical instability does not appear. However, it is hard to find out the exact τ_{min}. Here the τ_{min} was found approximately by the following way. The τ_{min} is set as $\tau_{min} = 0.5 + 0.0125k$, where k >0 is a integer, the τ_{min} is found out by finding the minimum k value at which numerical instability does not appear. So the numerical experiment was carried out to find τ_{min}. The τ_{min} for the two models is listed in the Table 6.5. From Table 6.5, we can see that in all cases, τ_{min} of present model are all smaller than that of Peng et al. (2003). It seems our present model is more stable.

The numerical stability is very important for simulation of high Reynolds number or high Grashof number cases. For example, if the case of Gr=10^7 is to be simulated by our model, since $\nu = c_s^2\delta_t(\tau - 0.5) = U_t R_c / \sqrt{Gr}$, we have

$$\frac{R_c}{\delta_x} = \frac{c_s^2(\tau - 0.5)\sqrt{Gr}}{cU_t} \tag{6.13}$$

Substituting $U_t \le 0.25$ (i.e., M<<1 in LBM) and $\tau \ge 0.6125$ (numerical stability requirement) into the Eq. (6.13), it is found the mesh points in R_c should satisfy the Eq. (6.14)

$$\frac{R_c}{\delta_x} = \frac{c_s^2(\tau - 0.5)\sqrt{Gr}}{cU_t} \ge \frac{1/3 \times (0.6125 - 0.5) \times \sqrt{10^7}}{1 \times 0.25} \approx 474 \tag{6.14}$$

That means to simulate the case of Gr=10^7, the coarsest grid should be 474×474, otherwise, the numerical instability would encounter in the simulation. While for this case of Gr=10^7, if numerical stability of the Peng's model (2003) requires

$\tau \geq 0.7375$, grid as fine as 1000×1000 is required. Hence, our numerical method provides a significant advantage in simulation melt flow cases with high Reynolds number and high Grashof number.

6.5 Summary

As conventional CFD solvers, present hybrid scheme combining the lattice Boltzmann methods and finite difference method is able to solve the axisymmetric swirling flow as a quasi-three-dimensional problem. This hybrid scheme was successfully applied to simulate the Taylor-Couette flow between two concentric cylinders. It was found the residual convergence behavior of this hybrid scheme is similar to that of explicit FVM. It is found that compared with LBM+FD solver, FLUENT requires about 3.35 times larger CPU time per iteration. However, to reach the same convergence criterion, the CPU time taken by our LBM+FD solver and explicit FVM solver are of same order.

The hybrid scheme was also applied to simulate flows in Czochralski crystal growth. Compared with the results in other literature, the hybrid scheme is able to provide very accurate results for benchmark problems. Present axisymmetric D2Q9 model also seems more stable than that of Peng et al.(2003). As a result, this scheme can give accurate results for high Reynolds number and high Grashof number cases.

Table 6.1 The maximum stream function in *x-r* plane for Taylor-Couette flow (grid 20×76)

Re	ψ_{max}	ψ_{max}*
85	4.810×10^{-2}	4.854×10^{-2}
100	5.501×10^{-2}	5.542×10^{-2}
150	6.427×10^{-2}	6.439×10^{-2}

* Liu, 1998

Table 6.2 Comparison of CPU time for hybrid scheme and FVM simulation of Taylor-Couette flow (*Re*=100, grid 30×114)

	Steps	CPU time (s)	ψ_{max}
FLUENT	13200	1523	5.530×10^{-2}
LBM+FD (τ=0.59)	45300	1560	5.553×10^{-2}
LBM+FD (τ=0.68)	21800	742	5.612×10^{-2}
Liu,1998	-	-	5.542×10^{-2}

Table 6.3 Grid independence test for Case A2, *Gr*=0, $Re_x=10^3$, $Re_c=0$

Grid	ψ_{min}	ψ_{max}
50×50	-4.73	1.80×10^{-4}
100×100	-4.98	7.31×10^{-5}
150×150	-5.046	6.52×10^{-5}
Raspo et al.1996	-5.074	7.89×10^{-5}

Table 6.4 Some results for the test cases by the hybrid scheme and QUICK*

Case	Gr	Re_x	Re_c	ψ_{min}	ψ_{max}	ψ_{min}*	ψ_{max}*
A1	0	10^2	0	-2.272×10^{-1}	7.921×10^{-6}	-2.172×10^{-1}	4.063×10^{-6}
A2	0	10^3	0	-4.979×10^{0}	7.311×10^{-5}	-4.994×10^{0}	1.826×10^{-5}
A3 (200)	0	10^4	0	-4.047×10^{1}	2.413×10^{-1}	-4.117×10^{1}	1.044×10^{-1}
B1	0	10^2	-25	-4.785×10^{-2}	1.140×10^{-1}	-4.433×10^{-2}	1.177×10^{-1}
B2	0	10^3	-250	-1.491×10^{0}	1.084×10^{0}	-1.478×10^{0}	1.148×10^{0}
B3 (250)	0	10^4	-2500	-8.226×10^{0}	5.075×10^{0}	-8.725×10^{0}	5.388×10^{0}
C1	10^5	0	0	-1.213×10^{-3}	2.863×10^{1}	-5.798×10^{-4}	2.841×10^{1}
C2 (150)	10^6	0	0	-3.805×10^{-1}	9.320×10^{1}	-1.200×10^{-1}	9.251×10^{1}
D1	10^5	10^1	0	-1.178×10^{-3}	2.863×10^{1}	-5.785×10^{-4}	2.841×10^{1}
D2	10^5	10^2	0	-1.564×10^{-4}	2.860×10^{1}	-4.517×10^{-4}	2.838×10^{1}
D3	10^5	10^3	0	-5.562×10^{-1}	2.528×10^{1}	-5.677×10^{-1}	2.517×10^{1}

* Xu et al. 1997

Table 6.5 Numerical stability comparison for case A1

Grid	τ_{min} (Present model)	τ_{min} (Peng et.al, 2003)
20×20	0.6125	0.6875
40×40	0.625	0.725
60×60	0.625	0.7375
80×80	0.625	0.7375
100×100	0.625	0.7375

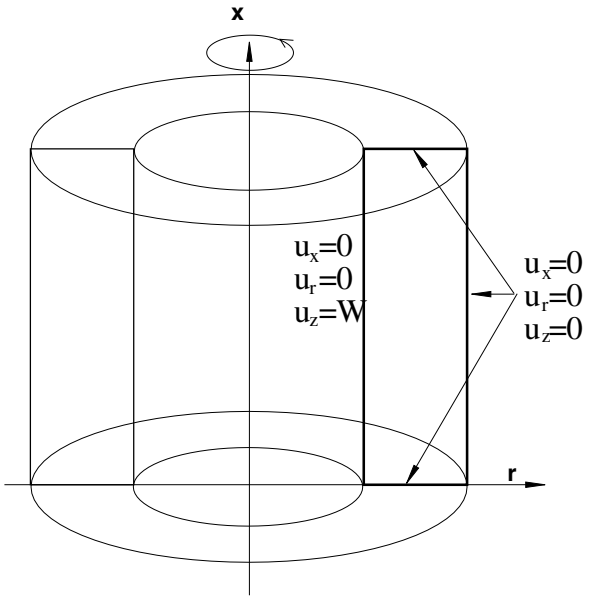

Figure 6.1 Geometry of Taylor-Couette flow and boundary conditions

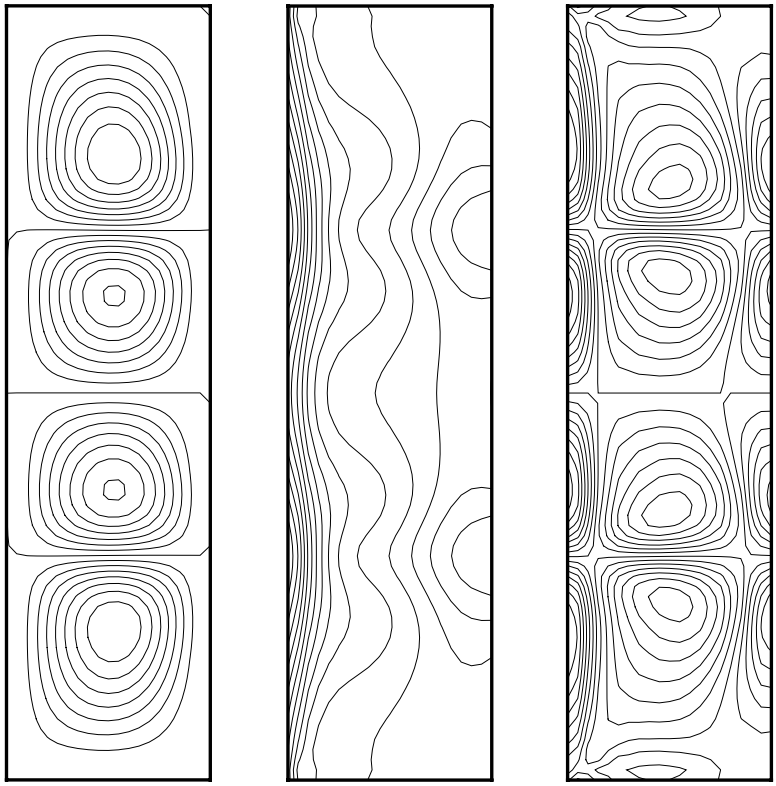

Figure 6.2 The contour of stream function, pressure and vorticity for case *Re*=150 with grid 20×76

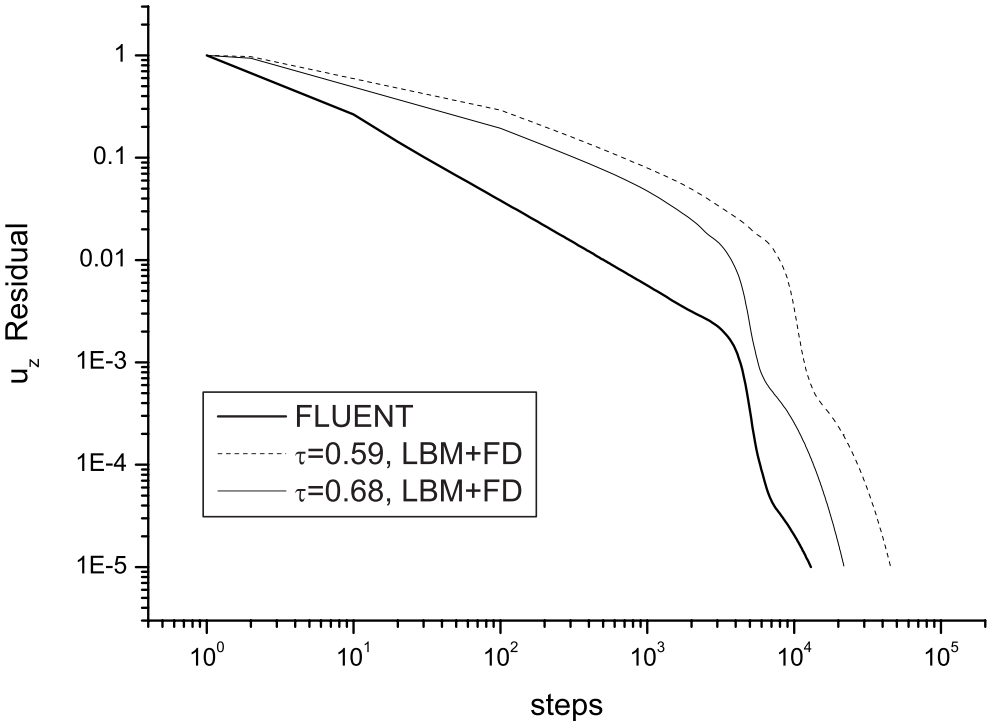

Figure 6.3 Convergence history for FLUENT and the hybrid scheme (LBM+FD)

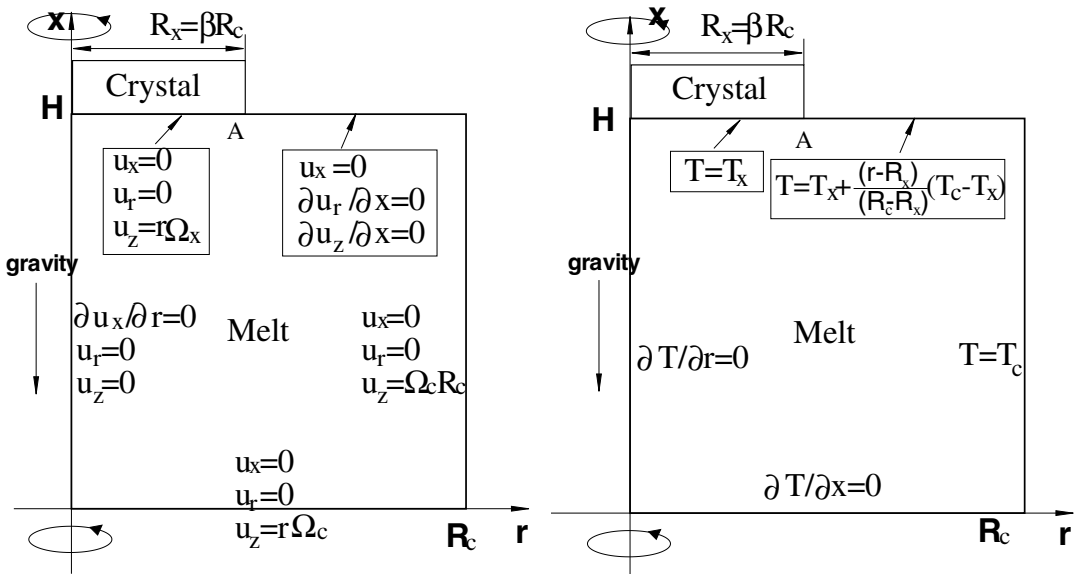

Figure 6.4 The momentum and thermal boundary conditions of melt flow in Czochralski crystal growth

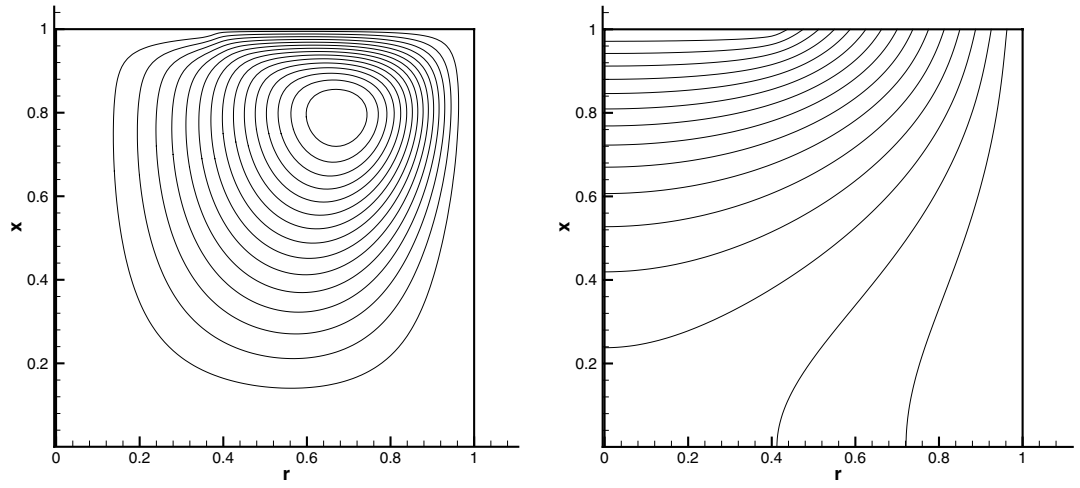

Figure 6.5 Streamlines and temperature contours of case A2, Gr=0, $Re_x=10^3$, Re_c=0

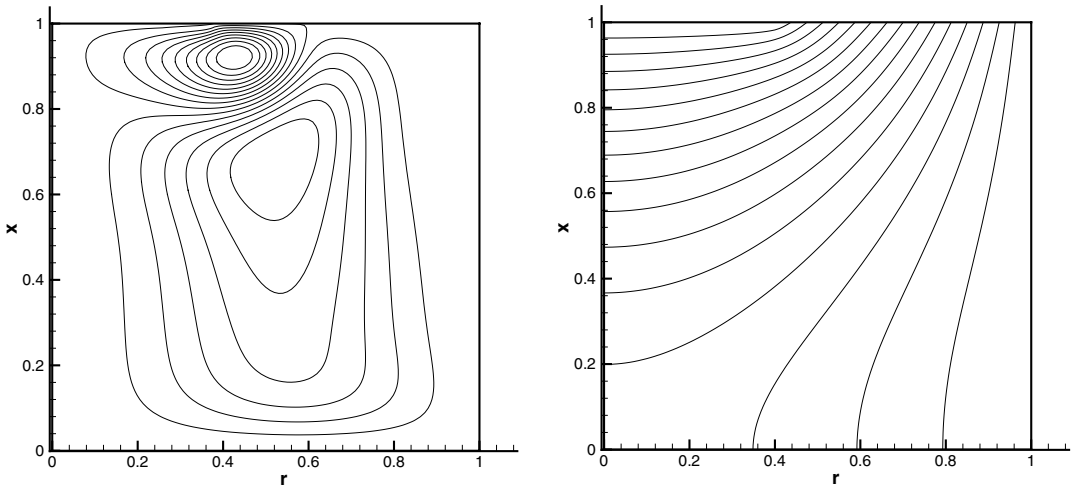

Figure 6.6 Streamlines and temperature contours of case B2, Gr=0, Re_x=10^3, Re_c=-250

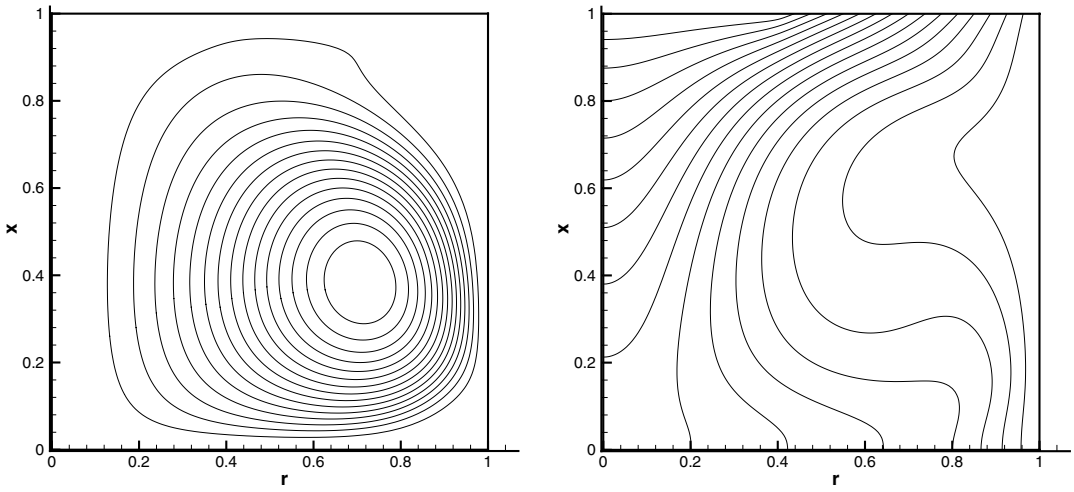

Figure 6.7 Streamlines and temperature contours of case C2, Gr=10^6, Re_x=0, Re_c=0

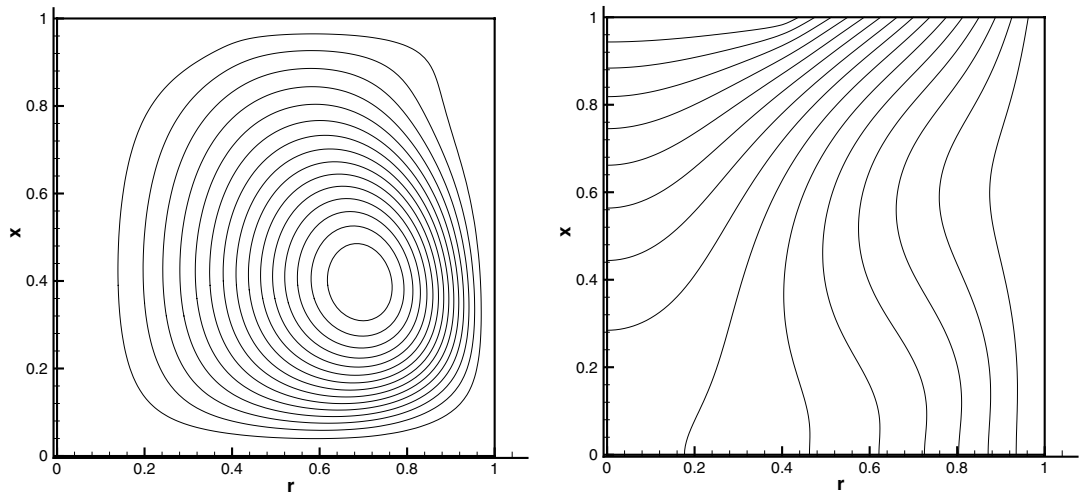

Figure 6.8 Streamlines and temperature contours of case D2, Gr=10^5, Re_x=10^2, Re_c=0

Chapter 7 Gas Slip Flow in Long Micro-tubes

In this Chapter[5], firstly, a slightly revised axisymmetric LBM is proposed to mimic the weakly compressible NS equations at macroscopic level and boundary condition is discussed. Then the LBM is applied to simulate the slip flow in microtubes for cases $0.01<Kn<0.1$ with different inlet/outlet pressure ratio. The results are compared with analytical solution or the available experimental data. Finally, the efficiency and accuracy comparisons between DSMC and LBM are carried out.

7.1 Compressible NS Equation and Axisymmetric LBM

Gas slip flow in a long micro-tube (the radius of the microtube is small compared with its length) with $0.01<Kn<0.1$ can be regarded as a internal weakly compressible, isothermal flow. The microtube flow is assumed to be axisymmetric. Hence, the time-invariant constant viscosity Navier-Stokes equations for such a compressible fluid, ignoring body force, are (Weng et al. 1999)

$$\rho\left(U\partial_x U+V\partial_r U\right)=-\partial_x p+\mu\left[\partial_x^2 U+(1/r)\partial_r U+\partial_r^2 U+(1/3)\partial_x\left(\nabla\cdot\mathbf{u}\right)\right], \quad (7.1)$$

$$\rho\left(U\partial_x V+V\partial_r V\right)=-\partial_r p+\mu\left[\partial_x^2 V+(1/r)\partial_r V+\partial_r^2 V-\left(V/r^2\right)+(1/3)\partial_r\left(\nabla\cdot\mathbf{u}\right)\right], \quad (7.2)$$

where $\nabla\cdot\mathbf{u}=\partial_x U+\partial_r V+V/r$.

The continuity equation is given by

$$\partial_x\rho U+\partial_r\rho V+\rho V/r=0 \quad (7.3)$$

The equation of state for an ideal gas is given by

[5] This work has been published as:
Huang, H., Lee, T.S., Shu, C., Lattice Boltzmann Simulation Gas Slip Flow in Long Microtubes, *Int. J. Numer. Meth. for Heat & Fluid Flow*, (in press, 17(6), 2007)

$$p = \rho RT\,. \tag{7.4}$$

In the above equations, U and V are the axial and radial components of velocity **u**, μ is the molecular viscosity, ρ is the density, p is the pressure and R is the specific gas constant. In Eqs. (7.1) and (7.2), we have assumed a Stokes continuum hypothesis for the second coefficient of viscosity.

To simulate the microtube flow, here, our axisymmetric model is derived from standard D2Q9 model with including more compressibility effect. Following the scheme B in Chapter 3, the source term added into the LBE is

$$S_i = \omega_i\left\{A^{(1)}\right\} + \omega_i\left\{A^{(2)} + \frac{e_{i\alpha} n F_\alpha^{(2)}}{c_s^2}\right\} \quad (i=0,1,2\ldots,8), \tag{7.5}$$

where $n = (1 - 1/2\tau)$. $A^{(1)}$ and $A^{(2)}$ are chosen as following

$$A^{(1)} = -\rho u_r / r\,, \tag{7.6}$$

$$\text{and} \quad A^{(2)} = -\left(\delta_t \partial_{1t} \rho u_r\right)/2r = \delta_t \partial_\beta \left(p\delta_{r\beta} + \rho u_\beta u_r\right)/2r\,. \tag{7.7}$$

The $F_\alpha^{(2)}$ is chosen as

$$F_\alpha^{(2)} = -\frac{\rho u_\alpha u_r}{r} + \delta_t(\tau - 1)c_s^2 \partial_\alpha\left(\frac{\rho u_r}{r}\right) + \frac{\rho\nu}{r}\left(\partial_r u_\alpha - \frac{u_r}{r}\delta_{\alpha r}\right) - \frac{2}{3}\partial_\alpha(\rho\nabla\cdot\mathbf{u}). \tag{7.8}$$

It should notice that in our present model, the density and velocities u_α (α=x,r) are defined as

$$\rho = \sum_i f_i \quad , \quad \rho u_\alpha = \sum_i e_{i\alpha} f_i + \delta_t F_\alpha^{(2)}/2\,. \tag{7.9}$$

At macroscopic level, the following continuity and momentum equations can be recovered.

$$\partial_t \rho + \partial_\beta\left(\rho u_\beta\right) = -\frac{\rho u_r}{r}\,, \tag{7.10}$$

$$\begin{aligned}&\partial_t \rho u_\alpha + \partial_\beta\left(\rho u_\beta u_\alpha\right) + \frac{\rho u_\alpha u_r}{r} + \partial_\alpha p - \nu\left[\partial_\beta\left(\rho\partial_\beta u_\alpha\right) + \frac{1}{3}\partial_\alpha\left(\rho\nabla\cdot\mathbf{u}\right)\right] \\ &= \frac{\mu}{r}\left(\partial_r u_\alpha - \frac{\delta_{\alpha r} u_r}{r}\right)\end{aligned} . \quad (7.11)$$

For steady flow (i.e., $\partial_t \rho = 0$ and $\partial_t \rho u_\alpha = 0$) and when the density variation is very small in the flow with small Mach number, the Eqs. (7.10) and (7.11) is almost identical as compressible NS equations (i.e. Eq. (7.3), Eq. (7.1) and Eq. (7.2)) .

7.1.1 Knudsen Number and Boundary Condition

Correlating the parameter τ with Kn is important for LBM application in simulation micro-flows (Nie *et al.*, 2002; Tang *et al.*, 2004). Here an expression between Kn and τ which based on the gas kinematics (Tang *et al.*, 2004) is used but we derived it in a simpler way as follows.

From the kinetic theory of gases, the density can be determined by

$$\rho = mp/k_B T , \quad (7.12)$$

where m represents the molecular mass and k_B is the Boltzmann constant. On the other hand, in LBM, we know that $p = c_s^2 \rho$. Hence, we have

$$k_B T/m = c_s^2 . \quad (7.13)$$

For an ideal gas modeled as rigid spheres, the mean free path λ is related to the viscosity ν as

$$\nu = 0.5 v_m \lambda , \quad (7.14)$$

where the mean velocity of the molecular $v_m = \sqrt{8k_B T/\pi m}$. Hence, we have

$$Kn = \frac{\lambda}{D} = \frac{2\nu}{v_m D} = \sqrt{\frac{\pi}{6}}\frac{(\tau - 0.5)}{N_D} \quad \text{or} \quad \tau = \frac{KnN_D}{\sqrt{\pi/6}} + 0.5 , \quad (7.15)$$

where D is the diameter of a microtube, N_D is the lattice number in the tube diameter, Kn is local Knudsen number. Since the mean free path is inversely proportional to the pressure, the local Kn can be calculated by

$$Kn = \frac{Kn_o p_o}{p(x,r)}, \tag{7.16}$$

where Kn_o and p_o are the Kn and the pressure at the outlet. So, in Eq. (7.15), τ is variable along the microtube and the corresponding v can be obtained from $v=c_s^2\delta_t(\tau\text{-}0.5)$.

Another important issue about using LBM to simulate the micro flows is the wall boundary condition. For this condition, the bounce-back scheme is usually used to realize non-slip boundary condition when simulating continuum flow. On the other hand, the specular reflection scheme (Lim *et al*., 2002) can be applied to the free-slip boundary condition where no momentum is to be exchanged with the wall along the tangential component. For real gas flow in microtubes, a combination of the two schemes is considered here. To describe boundary condition treatment, a wall $\partial\Omega$ is completely specified. For a point $\mathbf{x}$ ($\mathbf{x}\in\partial\Omega$), $\mathbf{n}$ is the inward unit normal vector of the wall. After streaming step implemented, the unknown distribution functions of $f_i(\mathbf{x},t)$, $\mathbf{e}_i\cdot\mathbf{n}>0$ can be evaluated by (Succi, 2002)

$$f_i(\mathbf{x},t) = bf_j(\mathbf{x},t) + (1-b)f_k(\mathbf{x},t), \tag{7.17}$$

where $f_j(\mathbf{x},t)$ is the distribution function in $\mathbf{e}_j$ direction, where $\mathbf{e}_i-\mathbf{e}_j=2\mathbf{e}_i$, and $f_k(\mathbf{x},t)$ is the distribution function in $\mathbf{e}_k$ direction, where $\mathbf{e}_i-\mathbf{e}_k=2\mathbf{n}$. b is the bounce-back probability chosen as 0.7 (Tang *et al.,* 2004).

For the inlet/outlet boundary conditions, the extrapolation scheme (Guo et al. 2002c) was applied. The axisymmetric extrapolation boundary condition we

proposed in Chapter 3 is applied for axisymmetric boundary condition.

7.2 Analytical Solutions for Micro-tube Flow

The streamwise velocity profile (first-order slip-flow model) in a long microtube with rarefaction effect is given by Weng, *et al*. (1999) as

$$U(x,r) = -\frac{r_0^2}{4\mu}\frac{\partial p}{\partial x}\left[1-\left(\frac{r}{r_0}\right)^2+\frac{2\lambda}{r_0}\right], \tag{7.18}$$

where λ is the molecular mean free path, r_0 is the radius of the microtube. Since $r_0 = D/2$ and local $Kn = \lambda/D$, using Eqs. (7.16) and (7.18), we have

$$U(x,r) = -\frac{D^2}{16\mu}\frac{dp}{dx}\left(1-4\left(\frac{r}{D}\right)^2+\frac{4Kn_o}{\tilde{p}}\right), \tag{7.19}$$

where $\tilde{p} = p(x,r)/p_o$.

The pressure distribution in a long microtube is given by Weng, *et al*. (1999) as

$$S = -\frac{8}{\sqrt{\pi}}+\left\{\frac{64}{\pi}+S_{in}^2+\frac{16}{\sqrt{\pi}}S_{in}+\left[\left(S_{out}^2-S_{in}^2\right)+\frac{16}{\sqrt{\pi}}\left(S_{out}-S_{in}\right)\right]\tilde{x}\right\}^{\frac{1}{2}}, \tag{7.20}$$

where $S = \left(Kn_o\sqrt{\pi}\right)^{-1}\tilde{p}$, $S_{in} = \left(Kn_o\sqrt{\pi}\right)^{-1}\mathrm{Pr}$, $S_{out} = \left(Kn_o\sqrt{\pi}\right)^{-1}$, $\mathrm{Pr} = p_{in}/p_o$ and $\tilde{x} = x/L$. L is the tube length. Hence, Eq. (7.20) can also be rewritten as,

$$\tilde{p}(\tilde{x}) = -8Kn_o+\sqrt{(8Kn_o)^2+(1+16Kn_o)\tilde{x}+\left(\mathrm{Pr}^2+16Kn_o\,\mathrm{Pr}\right)(1-\tilde{x})}. \tag{7.21}$$

From Eq. (7.21) we can see that gas flowing in a long microtube with a significant pressure drop will also exhibit compressibility effects.

The mass flow rate is computed by multiplying Eq. (7.18) by the density and integrating across the tube. The dimensional mass flow rate is given by Weng, *et al*. (1999) as

$$\dot{q} = -\frac{\pi\rho r_0^4}{2\mu}\frac{\partial p}{\partial x}\left[\frac{1}{4} + 2Kn\right] \quad . \tag{7.22}$$

Hence, the dimensional mass flow rate at outlet of microtube is

$$\dot{q} = -\frac{\pi\rho_o D^4 p_o}{16\mu L}\left(\frac{\partial \tilde{p}}{\partial \tilde{x}}\right)_o\left[\frac{1}{8} + Kn_o\right] \quad . \tag{7.23}$$

The non-dimensional pressure gradient along the tube can be calculated from Eq. (7.21) as,

$$d\tilde{p}/d\tilde{x} = \frac{1 - \mathrm{Pr}^2 + 16Kn_o(1-\mathrm{Pr})}{2\sqrt{(8Kn_o)^2 + (1+16Kn_o)\tilde{x} + (\mathrm{Pr}^2 + 16Kn_o\,\mathrm{Pr})(1-\tilde{x})}} . \tag{7.24}$$

With Eq. (7.24), the Eq. (7.23) can also be written as

$$\dot{q} = \frac{\pi D^4 p_o^2}{256\mu LRT}\left[(\mathrm{Pr}^2 - 1) + 16Kn_o(\mathrm{Pr} - 1)\right] \quad . \tag{7.25}$$

In addition, the mass flow rate for the continuum gas (without the rarefaction effect) is

$$(\dot{q})_{continuum} = -\frac{\pi D^4}{256\mu RT}\frac{\partial(p^2)}{\partial x} = \frac{\pi D^4 p_o^2}{256\mu RT}\frac{(\mathrm{Pr}^2 - 1)}{L} \quad . \tag{7.26}$$

7.3 Numerical Results of Micro-tube Flow

7.3.1 Distributions of Pressure and Velocity

In our simulation, the radius is represented by 11 lattice nodes (10 lattice space) and the length of the tube is 20 times of the diameter except for specially noted cases. In all of the cases, the Mach number in tube is very low. Even for case of Pr=3.0, maximum Mach number in tube is M=0.15/c_s <<1, which satisfy the requirement of our axisymmetric D2Q9 model. The streamwise momentum accommodation coefficient σ=1 has been used for almost all engineering calculations (Weng *et al.*, 1999). Therefore we take σ =1 throughout this Chapter.

Figures 7.1 and 7.2 show the axial and radial velocity distribution along the tube (Pr=2, Kn_o=0.1) respectively. The U, V velocity contours are also illustrated in Figures 7.1 and 7.2 respectively. From Figure 7.1, we can see that the axial velocity profile is parabolic type and the slip velocity at the wall and the central velocity increase toward the exit. Due to the pressure decreasing, the density of gas also decreases along the tube. To satisfy mass conservation, the average velocity must increase toward the exit. In Figure 7.2, the magnitude of the radial velocity is much smaller than that of axial velocity. These results are consistent with previous studies on microchannels (Arkilic *et al*., 1997 and Lim *et al*., 2002).

The pressure distribution along the tube predicted from the first slip boundary condition is illustrated in Eq. (7.27), which is originally given by Weng *et al.* (1999) (i.e., Eq. (7.21)).

$$\tilde{p}(\tilde{x}) = -8Kn_o + \sqrt{(8Kn_o)^2 + (1+16Kn_o)\tilde{x} + (\mathrm{Pr}^2 + 16Kn_o\,\mathrm{Pr})(1-\tilde{x})}\,. \quad (7.27)$$

In Eq. (7.27), $\tilde{p}$ is the pressure normalized by outlet pressure, $\tilde{x} = x/L$, L is the tube length. Pr is the ratio of the inlet and outlet pressure.

The pressure drop along the tube which deviate from linear pressure drop for different Pr with the outlet Knudsen number Kn_o=0.1 are shown in Figure 7.3. When Pr increase, the compressibility effect within the tube is also increase, results in a larger deviation from the linear pressure distribution. In Figure 7.3, it is also found that our results agree well with Eq. (7.27).

The pressure drops along the tube for different outlet Kn_o are shown in Figure 7.4. Compared with the analytical solution Eq. (7.27), the results of LBM is quite good. Figure 7.4 demonstrates that the larger Kn_o, the smaller the deviation from the linear pressure distribution. It seems that the rarefaction effect (indicate by Kn_o) can decrease the curvature in the pressure distribution which caused by the

compressibility effect. Maybe that means the compressibility effect and the rarefaction effect on the pressure distribution are contradictory.

The Knudsen numbers along the streamwise direction are shown in Figure 7.5. *Kn* is a function of the local pressure. With the decreasing pressure along the tube, the Knudsen number increases and reaches its maximum value at the outlet. For different outlet Kn_o , the slope of *Kn* curve along the tube is different. For smaller Kn_o, the slope of *Kn* curve is larger although *Pr* is same.

In Figure 7.6, the variation of slip velocity along the microtube wall is presented. The analytical solution of slip velocity (i.e., Eq. (7.19)) can be normalized by the central velocity at outlet U_{oc} ,

$$\frac{U(x,r)}{U_{oc}} = \frac{d\tilde{p}/d\tilde{x}}{(d\tilde{p}/d\tilde{x})_o} \frac{\left(0.25 + Kn - r^2/D^2\right)}{(0.25 + Kn_o)}, \tag{7.28}$$

where $d\tilde{p}/d\tilde{x}$ is the non-dimensional pressure gradient and the $(d\tilde{p}/d\tilde{x})_o$ means the pressure gradient at exit.

Hence, the analytical solution for slip velocity on the wall and average velocity in microtube are Eq. (7.29) and Eq. (7.30) respectively:

$$\frac{U_{slip}(x)}{U_{oc}} = \frac{d\tilde{p}/d\tilde{x}}{(d\tilde{p}/d\tilde{x})_o} \frac{Kn}{(0.25 + Kn_o)}, \tag{7.29}$$

$$\frac{U_{av}(x)}{U_{oc}} = \frac{d\tilde{p}/d\tilde{x}}{(d\tilde{p}/d\tilde{x})_o} \frac{(1/8 + Kn)}{(1/4 + Kn_o)}. \tag{7.30}$$

Form Eq. (7.29) we can see that since the local Knudsen number increases and the slope of pressure drop also increases along the tube, the slip velocity on the wall would increase along the microtube. Figure 7.7 illustrates the average velocity variations along the streamwise direction. The average velocity increases as the flow proceeds down the tube since density decrease along the microtube. In Figures 7.6 and 7.7, both the slip velocity on wall and local bulk velocity along

the microtube agree well with that of the analytical solution.

7.3.2 Mass Flow Rate and Normalized Friction Constant

The effect of rarefaction on mass flow rate is investigated by comparison of the LBE result with analytical predictions. The nondimensional mass flow rate $\widetilde{Q}$ can be expressed as a function of pressure ratio (obtained from Eq. (7.25) and Eq. (7.26))

$$\widetilde{Q} = \frac{\dot{q}}{(\dot{q})_{continuum}} = 1 + \frac{16Kn_o}{\Pr + 1} \tag{7.31}$$

In Figure 7.8, the nondimensional mass flow rate computed by the LBE method for Kn_o=0.1 is compared with the first order analytical prediction Eq. (7.31). For all cases, slip effects become less pronounced with increasing pressure ratio. The LBE results agree well with analytical results and the deviation is less than 4%.

Then in Figure 7.9, the friction factors predicted by present LBM simulations are compared with experimental results of Kim *et al.* (2000). The theoretical friction constant (C_0=f*Re=64) for fully developed incompressible flow is used to normalize friction constant C=f*Re. The microtubes used in the experiment are also illustrated in Figure 7.9. Here our numerical data were taken from results of cases Kn_o=0.013 with different inlet/outlet pressure ration. In these cases, for Kn=λ/D=0.013, the corresponding simulated diameters D of microtubes for Nitrogen, Argon and Helium are listed in Table 7.1. The diameters of our simulation are all close to that of corresponding experimental facility. Hence our numerical results are valid to compare with the experimental data. In Figure 7.9, the normalized friction constant C^* obtained by LBM ranges from 0.80 to 0.86, which agree well with the experiment data.

Besides the experiments of Kim *et al.* (2000), Chio *et al*. (1991) also found that for nitrogen flow in microtube with diameters smaller than 10 micrometers, $C=f^*Re=53$. Another experiment conducted by Yu *et al*. (1995) concluded that $C=f^*Re=50.13$ for laminar nitrogen flow in microtubes with diameter 19 micrometers. In Figure 7.9, it was observed that our numerical data are also in consistent with their experimental results (Choi *et al.*, 1991; Yu *et al*., 1995).

7.3.3 Comparison with DSMC

To demonstrate the efficiency of the LBM, we compared the accuracy and efficiency of the LBM and DSMC. It is well known that DSMC is the most popular model for simulation of micro flows. DSMC is a particle-based method proposed by Bird (1994). Unlike the molecular dynamics (MD) method which takes each individual molecule into consideration, DSMC method assumes that a group of molecules have the same properties such as velocity and temperature which can be obtained by statistical analysis. In this way, the computational effort can be greatly reduced compared with the MD method (Bird, 1976; Bird 1994). Here, the developed DSMC code (Mao *et al.*, 2003) was used to simulate the slip flow in microtubes.

In the DSMC simulation, the working gas is nitrogen. The physical geometry is 200μm long and radius of the tube is 2.5μm. The computational region is an axisymmetric plane divided into 400×30 sampling cells and each cell contains 4 subcells. The total number of simulated particles is about 4.8×10^5. That means nearly 40 particles in a sampling cell (Mao *et al.*, 2003). In this part, the case of $Kn_o=0.0134$ and $Pr=2.5$ was simulated.

In the LBM simulation, the uniform square lattices 801×21 is used to simulate

the same microtube flow. For this case, if the computational domain is an axisymmetric plane and the axisymmetric boundary condition is applied, the calculation is unstable. However, when the computational domain is bounded by upper and lower straight walls and the aixs is placed in the center of domain, the calculation is stable. Hence, here the diameter is represented by 21 lattice nodes.

The present DSMC and LBM calculations were performed on a single-CPU of the computer Compaq ES40 supercomputer. For the efficiency comparison, the same convergence criterion was set as:

$$\sum_i \frac{\left\|\mathbf{u}(\mathbf{x}_i,t)-\mathbf{u}(\mathbf{x}_i,t-1)\right\|}{\left\|\mathbf{u}(\mathbf{x}_i,t)\right\|} < 10^{-6} \tag{7.32}$$

The velocity field error is measured by θ which is defined as:

$$\theta = \sum_i \left(u(r_i)-u_a(r_i)\right)^2 \Big/ \sum_i u_a{}^2(r_i) \tag{7.33}$$

where $u_a(r_i)$ is the analytical solution obtained by Weng *et al.* (1999) and r_i is the mesh point at intersection x/L=0.375 where the microflow is supposed to be in fully developed region.

The efficiency and accuracy comparison is listed in Table 7.2. The mesh or cell number is comparable for LBM and DSMC simulations. However, since DSMC still has to simulate 4.8×10^5 particles, it used much larger memory than LBM in the simulation. To obtain the well converged results, DSMC takes much more CPU time than LBM.

The velocity profiles at intersection x/L=0.375 obtained by analytical solution (Weng *et al.*, 1999), LBM and DSMC are illustrated in Figure 7.10. The velocity U is normalized by outlet U_{oc}. r is normalized by the diameter. Compared with the analytical solution, the result of LBM seems more accurate than that of DSMC.

7.4 Summary

In this chapter, a revised axisymmetric D2Q9 model was applied to investigate gaseous slip flow with slight rarefaction through long microtubes. With assumption of small Mach number, this axisymmetric LBGK model can successfully recovered the weakly compressible Navier-Stokes equation in the cylindrical coordinates through Chapman Enskog expansion. For the slip wall boundary condition, the wall boundary condition combined the bounce-back and specular reflection scheme was applied for microtube flows with Kn_o in range (0.01, 0.1).

In the simulations of microtube flows with Kn_o in range (0.01, 0.1), the distributions of pressure, the slip velocity and the average velocity along the microtube all agree well with the analytical results. The friction factors are compared with experimental results and good agreements are also observed.

Through comparison, it was found that our LBM is more accurate and efficient than DSMC when simulating the slip flow in microtube. Although the present LBM is only applied to the slip flow simulation ($0.01<Kn_0<0.1$) in microtubes, the LBM may be extended to study the transition flow or higher Knudsen number cases in the future.

Table 7.1 Simulated diameter of microtubes for different gas flow (Kn_o=0.013)

Gas (10^5 *Pa*)	Nitrogen	Argon	Helium
Mean free path (*nm*)	67	72	196
Diameter of tube (μm)	5.2	5.5	15.0

Table 7.2 Efficiency and accuracy comparison (LBM and DSMC) (Kn_o=0.0134, Pr=2.5)

Method	CPU time (*s*)	Mesh or Cells	Memory (M)	θ
LBM	4.52×10^{2}	1.6×10^{4}	9.2	4.31×10^{-4}
DSMC	3.22×10^{4}	1.2×10^{4}	31.4	3.3×10^{-3}

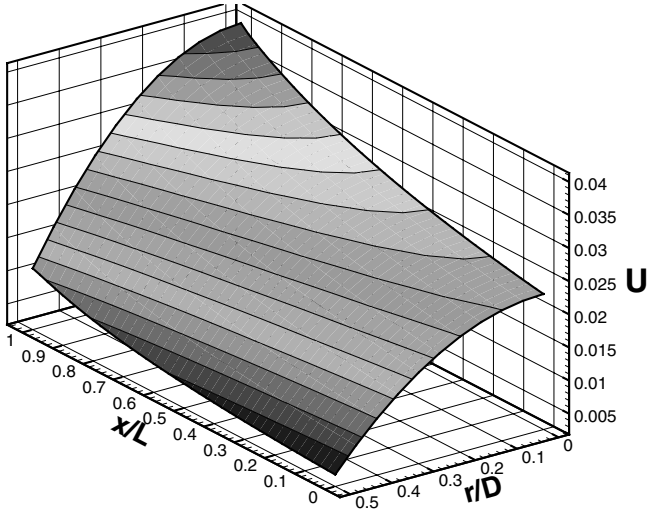

Figure 7.1 Axial-velocity distributions in the tube

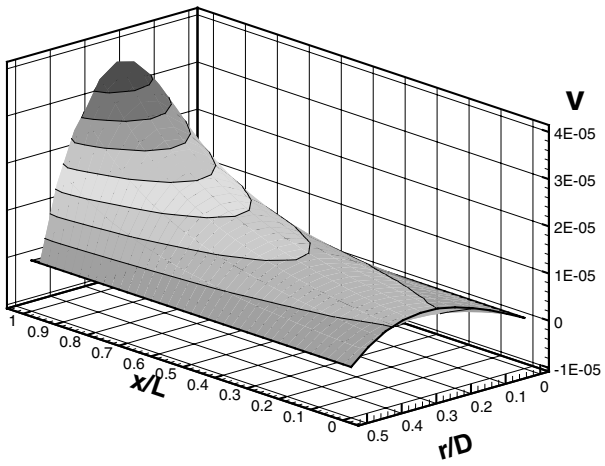

Figure 7.2 Radial-velocity distributions along the tube

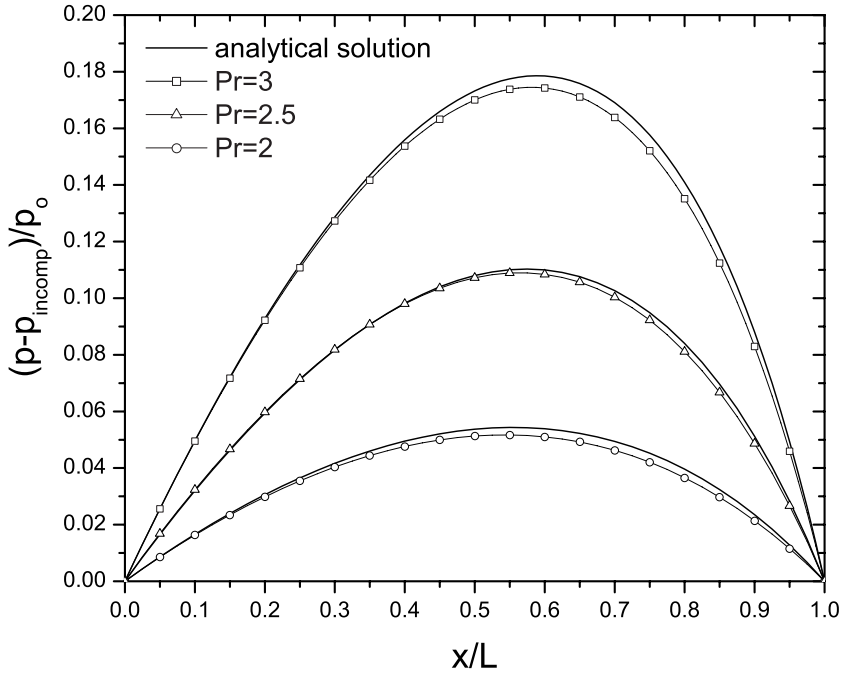

Figure 7.3 Pressure distribution along the tube for different *Pr* (Kn_o=0.1)

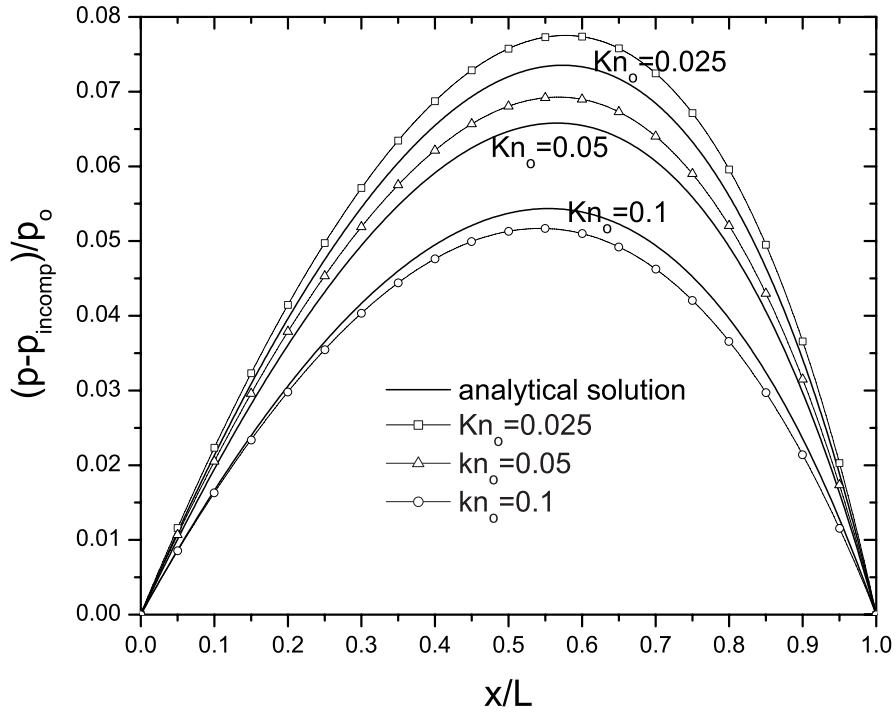

Figure 7.4 Pressure distribution along the tube for different Knudsen number (*Pr*=2)

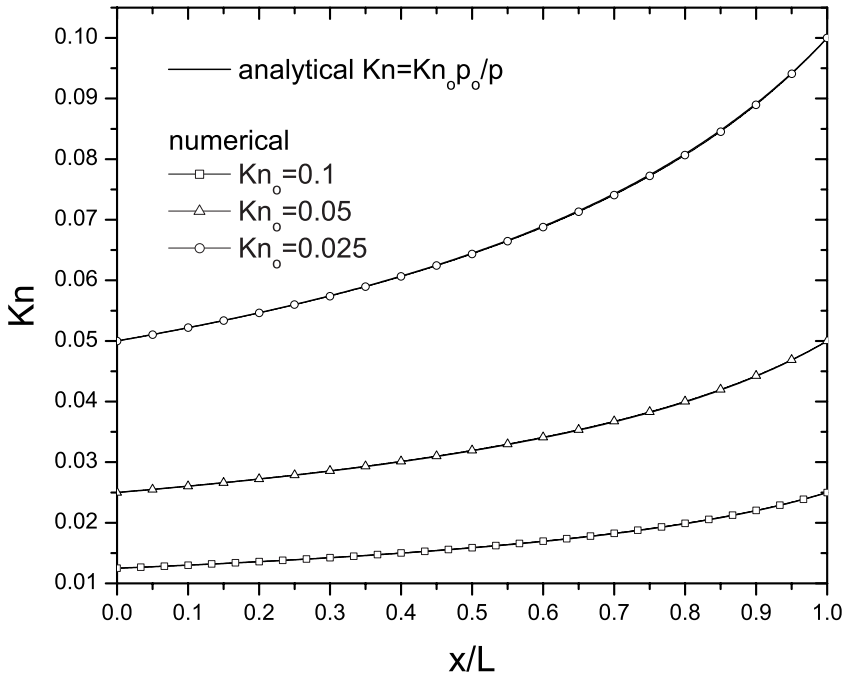

Figure 7.5 Local *Kn* distribution along the tube for different Kn_o (*Pr*=2)

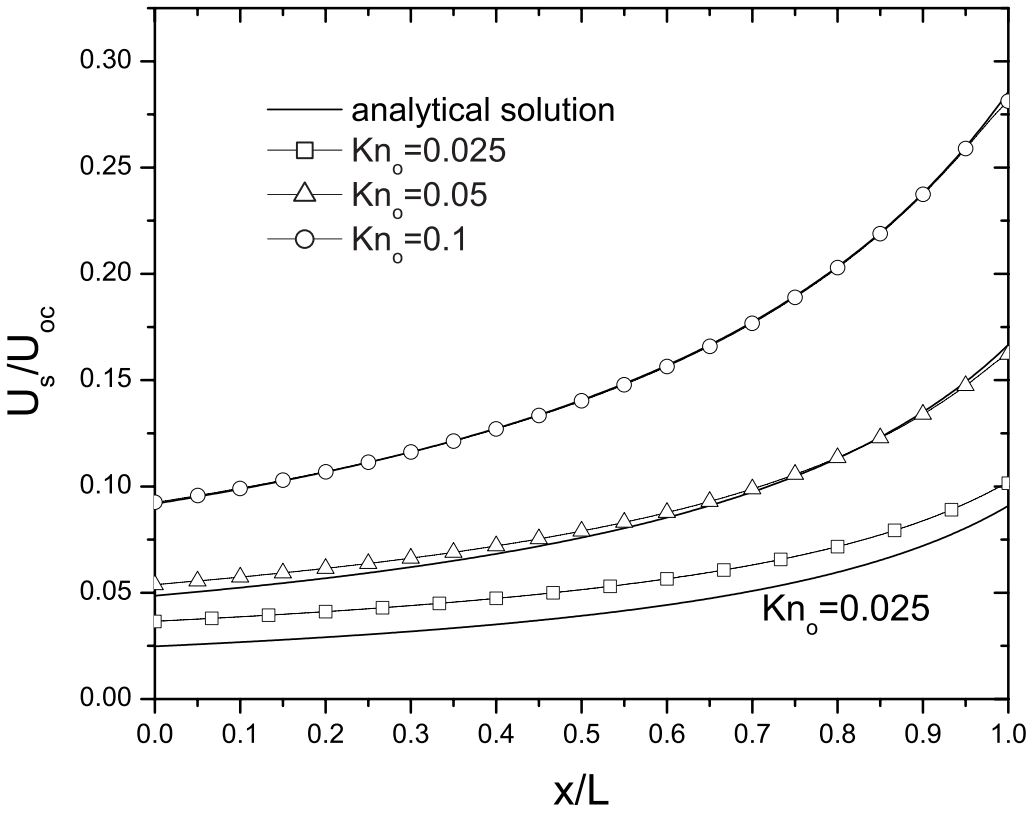

Figure 7.6 Slip velocity in wall along the tube for different Kn_o (*Pr*=2)

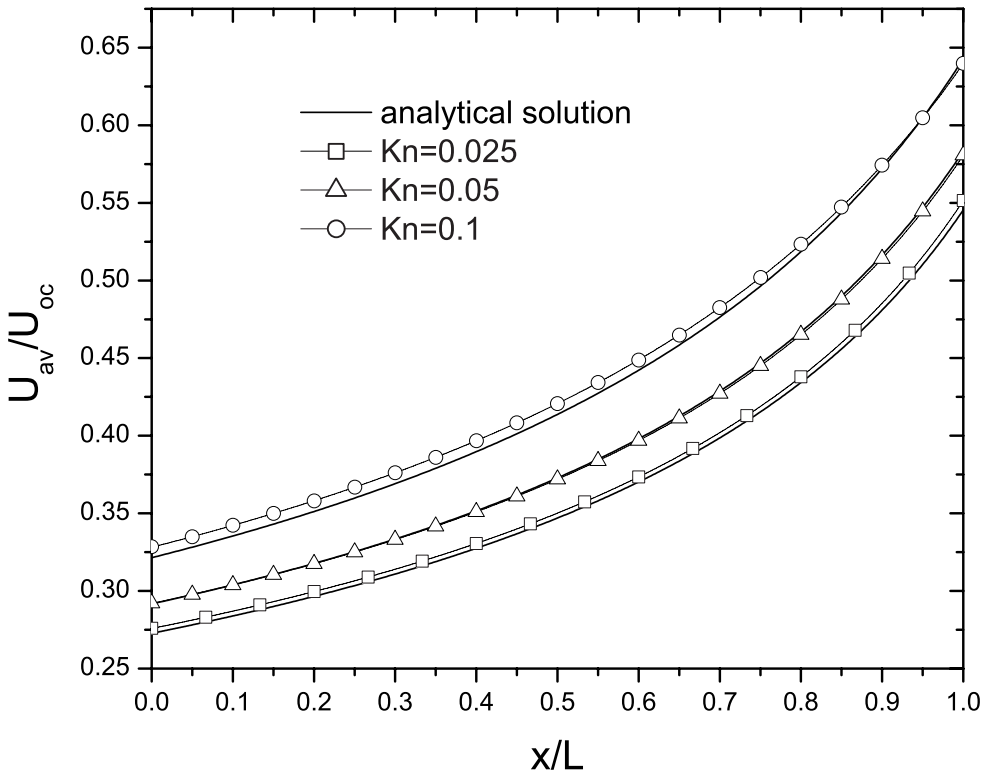

Figure 7.7 Average axial velocity U_{av} along the tube for different Kn_o (Pr=2)

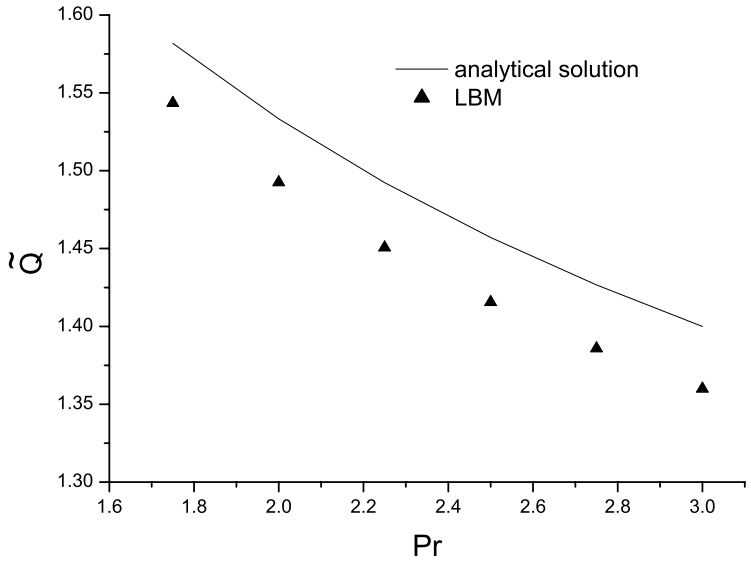

Figure 7.8 Mass flow rate normalized to non-slip mass flow rate as a function of Pr at Kn_o=0.1

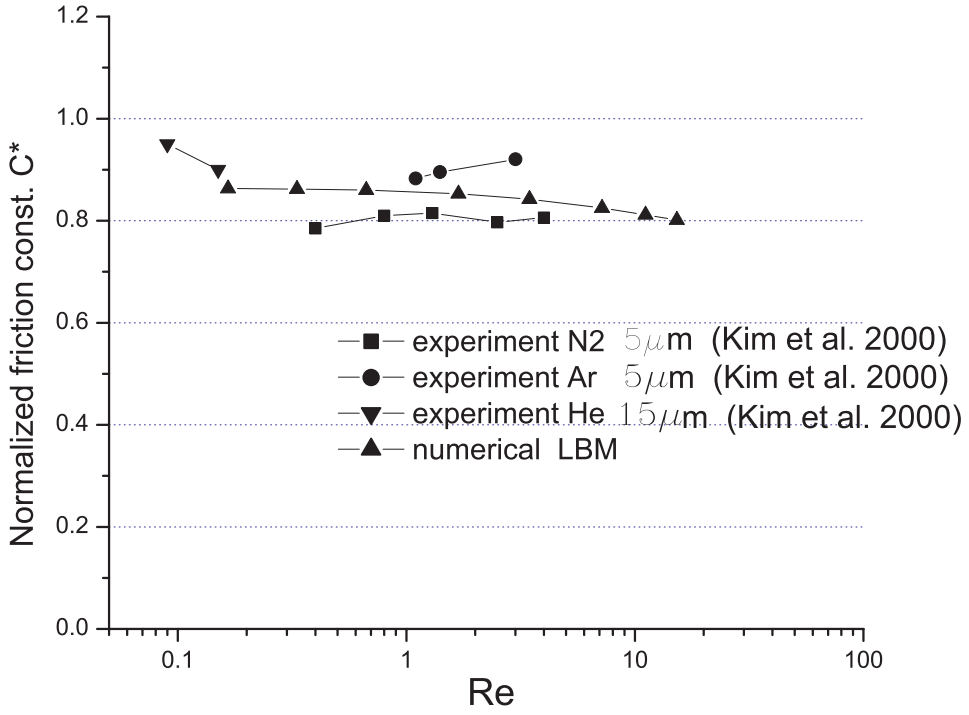

Figure 7.9 Normalized friction constant C^* of gas flow in microtube as a function of Re (Kn_o=0.013)

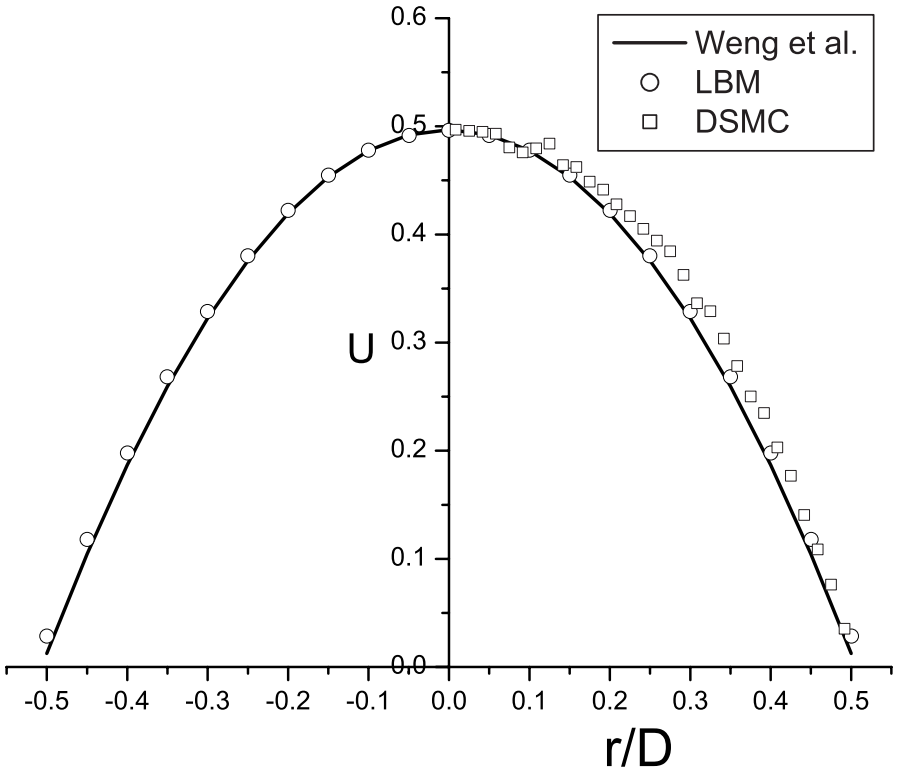

Figure 7.10 Velocity profiles at x/L=0.375 obtained by analytical solution, LBM and DSMC

Chapter 8 Extended Application of LBM

In this Chapter[6], a double-population thermal lattice Boltzmann model was applied to study the heat and fluid flow. A recent curved non-slip wall boundary treatment for isothermal lattice Boltzmann equation (Guo et al. 2002a) is extended to handle the thermal curved wall boundary. Firstly, the numerical simulations of Couette flow between two circular cylinders were used to validate the thermal boundary condition treatment. Then the natural convection in a 2D square cavity, and the natural convection in a concentric annulus between an outer square cylinder and an inner circular cylinder were studied. Complex 3D heat and fluid flows were also studied using this thermal boundary condition.

8.1 Thermal Curved Wall Boundary Condition

The double-population thermal lattice Boltzmann equation (TLBE) is introduced in Chapter 2. An accurate and simple curved wall boundary condition is important for application of the thermal lattice Boltzmann model.

As we know, basically, to evaluate internal energy density distribution functions, the two main steps of TLBE model are collision and streaming. In the collision step, the post-collision distribution function obtained by

$$\overline{g_i}^{+}(\mathbf{x},t)=(1-\omega_g)\overline{g_i}(\mathbf{x},t)+\omega_g g_i^{eq}(\mathbf{x},t)-\omega_g\tau_g f_i q_i, \tag{8.1}$$

where $\omega_g=\delta t/(\tau_g+0.5\delta t)$. In the streaming step, the distribution functions of new time level is

[6] Part of this work has been published as:
Huang, H., Lee, T.S., Shu, C., Thermal curved boundary treatment for the thermal lattice Boltzmann equation, *Int. J. Mod. Phys. C.* , 17(5), pp. 631-643 (2006)

$$\overline{g_i}(\mathbf{x}+\mathbf{e}_i\delta t, t+\delta t)=\overline{g_i}^{+}(\mathbf{x},t) \tag{8.2}$$

However, to fulfill the streaming step, some unknown internal energy density distribution functions on near-wall lattices should be determined. For example, in Figure 8.1, it is obvious that to fulfill the streaming step, some unknown $\overline{g_i}^{+}(\mathbf{x}_w,t)$ (i=3,7) in wall nodes $\mathbf{x}_w$ need to be specified. To specify $\overline{g_i}^{+}(\mathbf{x}_w,t)$, in Eq. (8.1) the term $\overline{g_i}(\mathbf{x}_w,t)$ can be decomposed into two parts (Guo et al. 2002a),

$$\overline{g_i}(\mathbf{x}_w,t)=g_i^{eq}(\mathbf{x}_w,t)+g_i^{ne}(\mathbf{x}_w,t), \tag{8.3}$$

where $g_i^{eq}(\mathbf{x}_w,t)$ and $g_i^{ne}(\mathbf{x}_w,t)$ are the equilibrium and nonequilibrium part of $\overline{g_i}(\mathbf{x}_w,t)$.

Firstly, we discuss how to determine the equilibrium part $g_i^{eq}(\mathbf{x}_w,t)$. Eq. (2.58), (2.59) and (2.60) illustrated that once $\rho(\mathbf{x}_w)$, $T(\mathbf{x}_w)$, $\mathbf{u}(\mathbf{x}_w)$ is known, then $g_i^{eq}(\mathbf{x}_w,t)$ can be determined. Here, for simplicity, ρ_w, T_w, $\mathbf{u}_w$ are used to denote $\rho(\mathbf{x}_w)$, $T(\mathbf{x}_w)$, $\mathbf{u}(\mathbf{x}_w)$, the macro variables in other lattice nodes are written in this way. Here, ρ_w is specified as $\rho_w=\rho(\mathbf{x}_w+\mathbf{e}_i)=\rho_f$. T_w is determined by linear extrapolation using either $T_{w1}=(T_b+(\Delta-1)T_f)/\Delta$ or $T_{w2}=(2T_b+(\Delta-1)T_{ff})/(1+\Delta)$. Where Δ is the fraction of the intersected link in the fluid region $\Delta=|\mathbf{x}_f-\mathbf{x}_b|/|\mathbf{x}_f-\mathbf{x}_w|$, which is illustrated in Figure 8.1. Usually, T_{w1} can be used as a good approximation for T_w for $\Delta>0.75$, However, if Δ is small, using T_{w1} to evaluate T_w may cause instability. Alternative, for $\Delta<0.75$ we used $T_w=\Delta T_{w1}+(1-\Delta)T_{w2}$. The extrapolation scheme is the same as that of Guo et al. (2002a).

Next, to determine the $g_i^{ne}(\mathbf{x}_w,t)$, extrapolation method is also used. $g_i^{ne}(\mathbf{x}_w,t)$ is evaluated as $g_i^{ne}(\mathbf{x}_w,t)=\Delta g_i^{ne}(\mathbf{x}_f,t)+(1-\Delta)g_i^{ne}(\mathbf{x}_{ff},t)$. From the Chapman-Enskog analysis (He et al. 1998), we know that $g_i^{ne}(\mathbf{x}_w,t)$ can be

expressed as $g_i^{ne} = g_i^{(1)}\delta_x$, where $g_i^{(1)}$ is of the same order as g_i^{eq} . Since $g_i^{(1)}(\mathbf{x}_w,t) - g_i^{(1)}(\mathbf{x}_f,t) = O(\delta_x)$, $g_i^{ne}(\mathbf{x}_w,t) - g_i^{ne}(\mathbf{x}_f,t) = O(\delta_x{}^2)$. For lattice node $\mathbf{x}_{ff}$, the accuracy analysis is the same as above. That means the approximation $g_i^{ne}(\mathbf{x}_w,t)$ is of second order in space which is in consistent with TLBE.

Finally, the thermal curved boundary treatment to specify $\overline{g_i}^{+}(\mathbf{x}_w,t)$ is

$$\overline{g_i}^{+}(\mathbf{x}_w,t) = g_i^{eq}(\mathbf{x}_w,t) + (1-\omega_g)g_i^{ne}(\mathbf{x}_w,t) - \omega_g\tau_g f_i q_i . \tag{8.4}$$

Since the Neumann curved wall boundary can be transferred into Dirichlet boundary condition, then the above Dirichlet curved wall boundary treatment can also be applied to Neumann curved wall boundary. As an example, we consider the same wall node "w" in Figure 8.1. Once the heat flux (temperature gradient $\partial T/\partial n$) at "b" is given, **n** is the unit vector normal to the local wall and pointing to fluid region. $(\partial T/\partial n)_i$ is used to represent the temperature gradient in $\mathbf{e}_i$ direction. That is $(\partial T/\partial n)_i = (\partial T/\partial n)\mathbf{e}_i\mathbf{n}/|\mathbf{e}_i|$. Using Taylor series expansion, with second order accuracy in space, the temperature on node "w" can be approximated by

$$T_w = \left(4T_f - T_{ff} - 2(\partial T/\partial n)_i |e_i|\delta_t\right)/3 . \tag{8.5}$$

Hence, after the equilibrium part is evaluated according to Dirichlet and Neumann boundary constraints, and the non-equilibrium part is obtained using a first-order extrapolation from fluid lattices, $\overline{g_i}^{+}(\mathbf{x}_w,t)$ is obtained to fulfill the streaming step.

8.2 Validation of the Thermal Curved Wall Boundary Condition

To demonstrate the capability of the present thermal curved wall boundary treatment and investigate its spatial accuracy, the Couette flow between two circular cylinders is simulated. In this flow, the inner cylinder with radius r_1 rotates with a constant tangent velocity u_0 ($u_0=\omega r_1$, ω is the angular velocity) and the outer cylinder with radius r_2 is kept stationary. The temperature of inner cylinder is kept as T_1 and that of outer cylinder is kept T_2. This Couette flow has the following analytical solution,

$$u_\theta(r) = C\left(\frac{r_2}{r_1} - \frac{r}{r_2}\right), \tag{8.6}$$

$$T_\theta(r) = \frac{\Pr C^2 r_2^2}{r^2} + \frac{\Pr C^2\left(1/\eta^2 - 1\right) + \left(T_1 - T_2\right)}{\ln \eta} \ln\left(\frac{r}{r_2}\right) + T_2 + \Pr C^2, \tag{8.7}$$

where $C = u_0\eta/\left(1-\eta^2\right)$, $\eta=r_1/r_2$, the Prandtl number $Pr=\nu/\alpha$, ν is the kinetic viscosity and α is the thermal diffusivity.

In simulations, a uniform square mesh is used to cover the flow domain. The present thermal boundary treatment is applied to the surfaces of the outer and inner cylinders. Firstly, cases of $Re=(r_2-r_1)u_0/\nu$ =10 with different values of η are conducted. In these cases τ_f=0.1, τ_g=0.1, r_2=40, and r_1 changes according to r_2 and η. The temperature profiles are plotted together with the analytical ones in Figure 8.2. The excellent agreement between the TLBM and the analytical solutions demonstrates the reliability of the present boundary treatment.

Spatial accuracy of the treatment is also tested for cases of Re=10 and 30. In these cases, τ_f=0.1, τ_g=0.1 and η=0.5. r_1 changes from 8 to 64, and r_2 changes according to η and r_1. The relative global L_2 norm errors in the temperature field

E_2 are measured and shown in Figure 8.3. In Figure 8.3, the slopes of the linear fitting lines for Re=10 and 30 are -1.98 and -2.00 respectively. The slopes are all very close to -2, which confirmed the thermal curved wall treatment is second-order accuracy.

8.3 Natural Convection in a Square Cavity

In order to further validate the thermal boundary treatment, a natural convection in a two-dimensional square cavity is investigated. The temperature difference between the left and right walls introduces a temperature gradient in the fluid, which induces the natural convection in the cavity. The top and bottom walls are adiabatic. The definition of Δ and the boundary conditions are illustrated in Figure 8.4. Here to test the thermal boundary treatment, Δ=0.25, 0.5, 0.75 were studied. The actual size of the cavity is $L\times L=(N\text{-}3+2\Delta)\times(N\text{-}3+2\Delta)$. N is the total lattice nodes in each spatial direction.

The Boussinesq approximation is applied to the buoyancy force term. This means that the properties β and ν are considered as constants, and the buoyancy term is assumed to depend linearly on the temperature, $\rho\mathbf{G}=\rho\beta g_0(T-T_0)\mathbf{j}$, where β is the thermal expansion coefficient, g_0 is the acceleration due to gravity, T_0 is the average temperature, here it is 1.0, and $\mathbf{j}$ is the vertical direction opposite to that of gravity.

The dynamical similarity depends on two dimensionless parameters: the Prandtl number Pr and the Rayleigh number Ra defined as

$$\mathrm{Pr}=\nu/\alpha, \tag{8.8}$$

$$Ra=\beta g_0(T_1-T_2)L^3/\nu\alpha. \tag{8.9}$$

In our simulations, Pr=0.7. The value of characteristic velocity

$U_c = \sqrt{\beta g_0 (T_1 - T_2) L}$ was chosen 0.1 for $Ra<=10^5$ and 0.15 for $Ra>10^5$. When U_c is determined, the kinetic viscosity v and the thermal diffusivity α can be determined by the two dimensionless numbers Pr and Ra through Eqs. (8.8) and (8.9). The two relaxation times τ_f, τ_g, are determined by Eq. (2.64). Another characteristic velocity $U_\infty = \alpha / L$ is also used to normalize velocity and stream functions.

The Nusselt number is one of the most important dimensionless parameters in describing the convective heat transport. The average Nusselt number in the whole flow domain is defined by

$$Nu_a = \frac{L}{\alpha (T_1 - T_2)} \int_0^L \int_0^L q_x(x, y) dx dy , \tag{8.10}$$

where q_x is the heat flux in x direction.

Firstly, the grid-dependence study is listed in Table 8.1, the data were taken from cases of $\Delta=0$, $Ra=10^4$. The grid size is taken as $N \times N$, where N is the total lattice nodes in each spatial direction. Table 8.1 shows the numerical results of normalized $u_{\max}$ on the vertical midplane of the cavity and corresponding position y, normalized $v_{\max}$ on the horizontal midplane and corresponding position x, and Nu_a. When grid size becomes larger, our results are closer to the benchmark solutions of Shu and Xue (1998). Grid size 103×103 is fine enough to obtain accurate results. Hence in the studies of other cases, the grid size used is 103×103.

Table 8.2 shows the numerical results of cases with $\Delta=0.5$ (actual size of the cavity is 101 ×101) for a wide range of Rayleigh numbers. The benchmark numerical solutions using the differential quadrature (DQ) method (Shu and Xue, 1998) are also listed for comparison. It can be seen from Table 8.2 that, our numerical results agree very well with those of Shu and Xue (1998). With the

increase of the Rayleigh number, due to the enhancement of natural convection, normalized $u_{\max}$, normalized $v_{\max}$, Nu_a are increased greatly, and the position of maximum vertical velocity on the horizontal midplane moves closer to the wall. Figure 8.5 and 8.6 show the contour of normalized stream function and isotherms of Ra=10^3, 10^4, 10^5, 10^6. These plots all agree well with those of Shu and Xue (1998).

To investigate the effect of different Δ, cases with Δ=0, 0.25, 0.5, 0.75 for Ra=10^4 were simulated. The results are illustrated in Table 8.3. It can be seen from Table 8.3 that for different Δ, TLBE with present thermal boundary treatments is able to give very accurate results.

8.4 Natural Convection in a Concentric Annulus between an Outer Square Cylinder and an Inner Circular Cylinder

The natural convection in a concentric annulus between an outer square cylinder and an inner circular cylinder were investigated for Rayleigh numbers 10^4, 5×10^4 and 10^5. The geometry ratio between the square cylinder and circular cylinder is defined as $\eta=2r_i/L$ and is fixed at 0.4 in our simulation. The temperatures of inner cylinder and outer square are fix as 2.5, 1.5 respectively. Here in our simulations the grid size is 103×103. The Prandtl number Pr = 0.71 and $U_c = \sqrt{\beta g_0 (T_1 - T_2) L} = 0.1$. Eq. (8.8) and (8.9) are also used to determine the kinetic viscosity v and the thermal diffusivity α.

The non-dimensional stream function is defined as $\psi = \psi^* / LU_\infty$, ψ^* is dimensional stream function and $U_\infty = \alpha / L$, The contours of non-dimensional stream functions in the annulus at Ra=10^4,5×10^4,10^5 are shown in Figure 8.7. The streamline of $\psi=0$ is almost in the vertical midplane and the contours are

symmetric with respect to vertical midplane. The isotherms in the annulus are shown in Figure 8.8, the contours are also symmetric with respect to the vertical midplane. Figure 8.7 and Figure 8.8. are all in good agreement with those plots of Shu and Zhu (2002) and Peng et al. (2004).

Since in the steady state, the Nusselt numbers along the inner and outer walls are the same, there is no need to pay separate attentions to the average Nusselt numbers for the outer and inner boundaries. The average Nusselt number on the inner cylinder or outer square can be computed by below definition,

$$Nu_a = \frac{\oint_\Omega \alpha \partial T/\partial n \big/ 2S}{\alpha(T_1 - T_2)/S}, \tag{8.11}$$

where T is the dimensional temperature, $\partial T/\partial n$ is the temperature gradient in the direction normal to the boundary. Ω is the boundary of inner or outer surface. S is the half length of corresponding boundary Ω. T_1, T_2 are the dimensional temperatures on the inner and outer walls respectively, α is the thermal conductivity. Here to avoid the difficulty of obtaining $\partial T/\partial n$ in the inner circular boundary, we calculated the Nu_a from the outer square boundary.

The numerical results of the maximum stream function $\psi_{\max}$ and the average Nusselt number Nu_a are shown in Table 8.4. The benchmark results using the DQ method (Shu and Zhu, 2002) are also included for comparison. Good agreement between present results and the benchmark results further validates the thermal curved wall boundary treatment.

8.5 Natural Convection in a 3D Cubical Cavity

In order to verify our thermal curved wall boundary treatment, we carried out the computation for a 3D fluid flow and heat transfer problems using the 3D

incompressible thermal LBM introduced in Chapter 3. The first problem considered is a natural convection in a 3D cubical cavity with two vertical side walls maintained at different temperatures. The remaining walls are adiabatic. The problem definition and the boundary conditions are displayed in Figure 8.9. In this figure, the temperature of left vertical side wall is set as T_1=1.5 and the right one is T_2=2.5.

The Boussinesq approximation is applied to the buoyancy force term. This means that the properties β and ν are considered as constants, and the buoyancy term is assumed to depend linearly on the temperature, $\rho\mathbf{G} = \rho\beta g_0 (T - T_0)\mathbf{k}$, where β is the thermal expansion coefficient, g_0 is the acceleration due to gravity, $T_0 = (T_1 + T_2)/2$ is the average temperature, here it is 2.0, and **k** is the vertical direction opposite to that of gravity.

The dynamical similarity depends on two dimensionless parameters: the Prandtl number *Pr* and the Rayleigh number *Ra* which are already defined in Eq.(8.8) and Eq.(8.9) respectively.

In our simulations, *Pr*=0.71. The value of characteristic velocity $U_c = \sqrt{\beta g_0 (T_1 - T_2) L}$ was chosen 0.1 for $Ra<10^5$ and 0.2 for $Ra>=10^5$. When U_c is determined, the kinetic viscosity ν and the thermal diffusivity α can be determined by the two dimensionless numbers *Pr* and *Ra* through Eqs. (8.8) and (8.9). And then by equations $\nu = \delta t(\tau_f - 0.5)c_s^2$ and $\alpha = 5(\tau_g - 0.5)/9$, two relaxation times τ_f, τ_g, are determined.

Nusselt number *Nu* is an important dimensionless parameter in describing the convective heat transport. The local Nusselt numbers at the isothermal wall x=0 are defined as

$$Nu(y,z)=\frac{L}{(T_1-T_2)}\left.\frac{\partial T(y,z)}{\partial x}\right|_{x=0}, \tag{8.12}$$

and the mean Nusselt number and overall Nusselt number are defined as

$$Nu_{mean}(y)=\frac{L}{(T_1-T_2)}\int_0^L\left.\frac{\partial T(y,z)}{\partial x}\right|_{x=0}dz, \tag{8.13}$$

$$Nu_{overall}=\frac{1}{L}\int_0^L Nu_{mean}(y)dy. \tag{8.14}$$

Numerical simulations of the natural convection in a cubic cavity at Rayleigh numbers of 10^3–10^5 are carried out using the particle velocity model of D3Q19. Table 8.5 shows representative quantities of the flow field and the heat transfer rates in the symmetry plane y=0.5L. In this symmetry plane, the following quantities of the flow field are included: the maximum horizontal velocity $u_{\max}$ on the vertical mid-line in this plane and its location z, the maximum vertical velocity $v_{\max}$ on the horizontal mid-line and its location x. The Nusselt numbers defined in this symmetric plane at the vertical boundary x=0 (refer to the vertical thick boundary line in Figure 8.9) are also included in Table 8.5. They are the maximum value of the local maximum and minimum Nusselt number $Nu_{\max}$ and $Nu_{\min}$ and their locations z and the average Nusselt number Nu_{mean}. The numerical results of a NS solver (Fusegi et al., 1991) are also included for comparison.

In Table 8.5, it seems that our simulation results generally compare well with those obtained from NS solver. The discrepancies are usually within 4% for case Ra=10^3 and Ra=10^4. For case Ra=10^5, the discrepency is around 7% which may due to small grid size in our simulation.

The 3D isothermal contours in the cavity for Ra=10^4 and 10^5 are shown in Figure 8.10. The three contours are T=1.75, 2, 2.25, respectively. To know the global behavior of the 3D natural convection, 3D streamlines passing through the

planes y=0.5L and y=0.85L for Ra=10^4 and 10^5 are plotted in Figure 8.11.

8.6 Natural Convection from a Sphere Placed in the Center of a Cubical Enclosure

The natural convection from a sphere placed in the center of a cubical enclosure is also simulated using 3D incompressible TLBE. The inner sphere and outer cubic walls maintained at different temperatures. The temperatures of sphere and cubic are set as T_1=1.5 and T_2=2.5, respectively.

The Boussinesq approximation is also applied to the buoyancy force term which is assumed as $\rho\mathbf{G} = \rho\beta g_0 (T - T_0)\mathbf{k}$, where $T_0 = (T_1 + T_2)/2$ is the average temperature, here it is 2.0.

In our simulations, Pr=0.71. The value of characteristic velocity $U_c = \sqrt{\beta g_0 (T_1 - T_2) L}$ was chosen 0.1 for Ra<10^5 and 0.2 for Ra>=10^5.

The 3D isothermal contours in this concentric cavity for Ra=10^4 and 10^5 are shown in Figure 8.12. The three isothermal contours illustrated in the figures are T=2.25, 2, 1.75, respectively. To know the global behavior of the 3D natural convection, 3D streamlines passing through the line y=0.5L, z=0.5L for Ra=10^4 and 10^5 are plotted in Figure 8.13.

8.7 Summary

In this Chapter, the thermal curved wall boundary was successfully handled by introducing the non-equilibrium extrapolation method. The unknown distribution population at a wall node which is necessary to fulfill streaming step is decomposed into its equilibrium and non-equilibrium parts. The equilibrium part is evaluated according to Dirichlet and Neumann boundary constraints, and

the non-equilibrium part is obtained using a first-order extrapolation from fluid lattices.

The numerical simulation of Couette flow between two circular cylinders confirmed the thermal curved wall treatment is second-order accuracy. The results of natural convection in a square cavity, and the natural convection in a concentric annulus between an outer square cylinder and an inner circular cylinder all agree very well with available data in the literature. That further validated the present thermal curved wall boundary treatment. Using this thermal curved wall boundary treatment, we also carried out the simulations for the natural convection in a cubical cavity and the natural convection from a sphere placed in the center of a cubical enclosure. Our numerical results demonstrated that this thermal curved wall boundary treatment can be applied to 3D thermal flow problems with complex geometry easily.

Table 8.1 Grid-dependence study for the natural convection in a square cavity at $Ra=10^4$, $\Delta=0$

Mesh	53×53	103×103	153×153	DQ*
u_{max}	15.980	16.133	16.133	16.190
y	0.818	0.819	0.823	0.825
v_{max}	19.390	19.580	19.580	19.638
x	0.121	0.120	0.120	0.120
Nu_a	2.225	2.241	2.244	2.245

* Shu and Xue 1998

Table 8.2 Numerical results for cases with $\Delta=0.5$, $Ra=10^3$-10^6

Ra	10^3		10^4		10^5		10^6	
	TLBE	DQ*	TLBE	DQ*	TLBE	DQ*	TLBE	DQ*
u_{max}	3.652	3.649	16.197	16.190	34.844	34.736	64.872	64.775
y	0.817	0.815	0.827	0.825	0.856	0.855	0.847	0.850
v_{max}	3.705	3.698	19.613	19.638	68.582	68.640	219.18	220.64
x	0.173	0.180	0.124	0.120	0.064	0.065	0.035	0.035
Nu_a	1.118	1.118	2.243	2.245	4.512	4.523	8.729	8.762

* Shu and Xue 1998

Table 8.3 Numerical results for $Ra=10^4$ with mesh size 103×103 and different Δ

	$\Delta=0$	$\Delta=0.25$	$\Delta=0.5$	$\Delta=0.75$	DQ*
u_{max}	16.133	16.218	16.197	16.173	16.190
y	0.819	0.828	0.827	0.825	0.825
v_{max}	19.580	19.652	19.613	19.600	19.638
x	0.120	0.122	0.124	0.116	0.120
Nu_a	2.241	2.240	2.243	2.239	2.245

* Shu and Xue 1998

Table 8.4 The maximum stream function ψ_{max} and the average Nusselt number Nu_a

	ψ_{max}		Nu_a	
Ra	TLBE	DQ#	TLBE	DQ#
10^4	0.99	0.97	3.22	3.24
5×10^4	4.96	4.82	4.01	4.02
10^5	8.27	8.10	4.79	4.86

Shu and Zhu 2002

Table 8.5 Representative field values in the symmetric plane (y=0.5L) for 3D nature convection in cubical cavity with Δ=0.0, Ra=10^3-10^5

Ra	10^3		10^4		10^5	
	TLBE	NS solver*	TLBE	NS solver*	TLBE	NS solver*
Meshes in x,y and z	32	32	32	62	42	62
u_{max}	0.1306	0.1314	0.1957	0.2013	0.1354	0.1468
z/L (x/L=0.5)	0.2000	0.2000	0.1667	0.1833	0.1500	0.1453
v_{max}	0.1309	0.1320	0.2131	0.2252	0.2248	0.2471
x/L (z/L=0.5)	0.8333	0.8333	0.8667	0.8833	0.925	0.9353
Nu_{max}	1.441	1.420	3.441	3.652	7.106	7.795
Nu_{max} position z/L	0.033	0.08333	0.2333	0.1623	0.200	0.08256
Nu_{min}	0.7124	0.7639	0.5792	0.6110	0.7568	0.7867
Nu_{min} position z/L	1.0	1.0	1.0	1.0	1.0	1.0
Nu_{mean}	1.132	1.105	2.372	2.302	4.841	4.646

* Fusegi et al., 1991

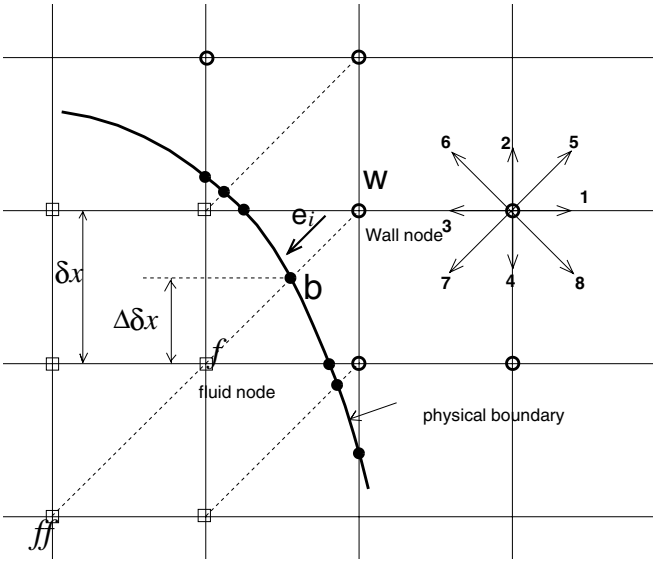

Figure 8.1 Curved boundary and lattice nodes (open circle is wall nodes, open square is fluid nodes, filled circle is the physical boundary nodes in the link of fluid node and wall node)

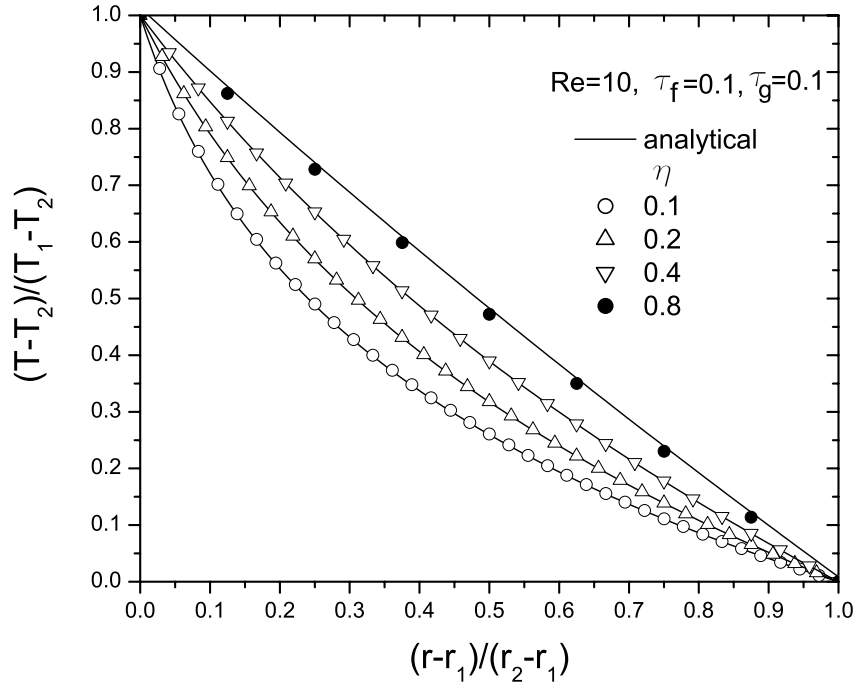

Figure 8.2 Temperature profiles of the Couette flow at *Re*=10 with difference value of the radius ratio

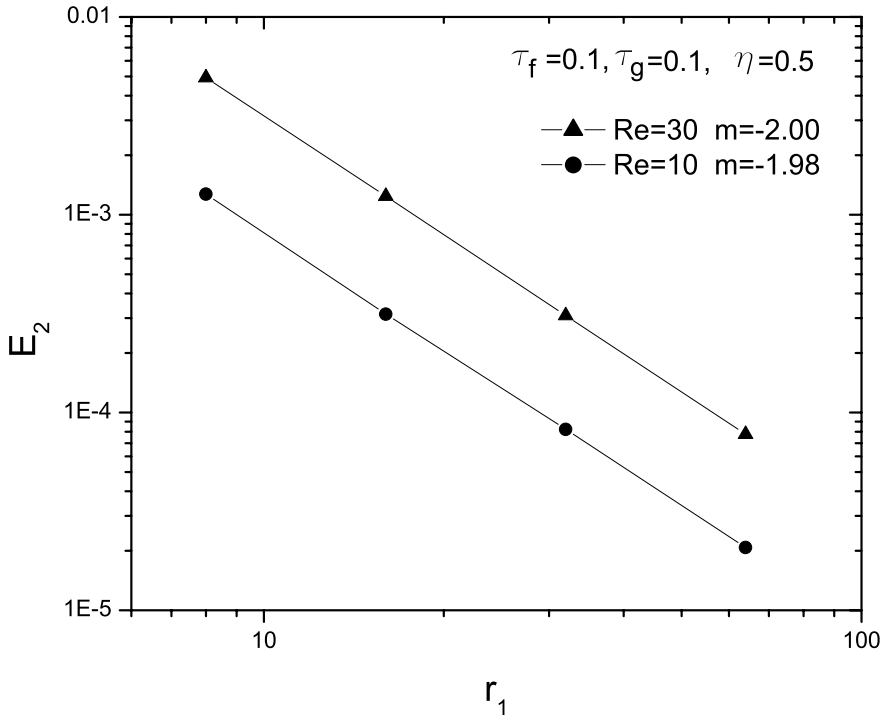

Figure 8.3 Temperature relative global errors versus the radius of the inner cylinder in the Couette flow. (*m* is the slope of linear fitting line)

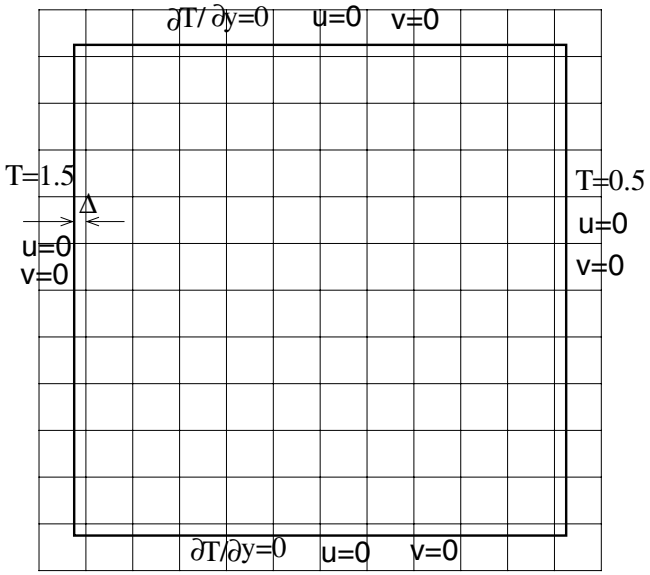

Figure 8.4 Boundary condition and geometry of natural convection in a square cavity (N=13)

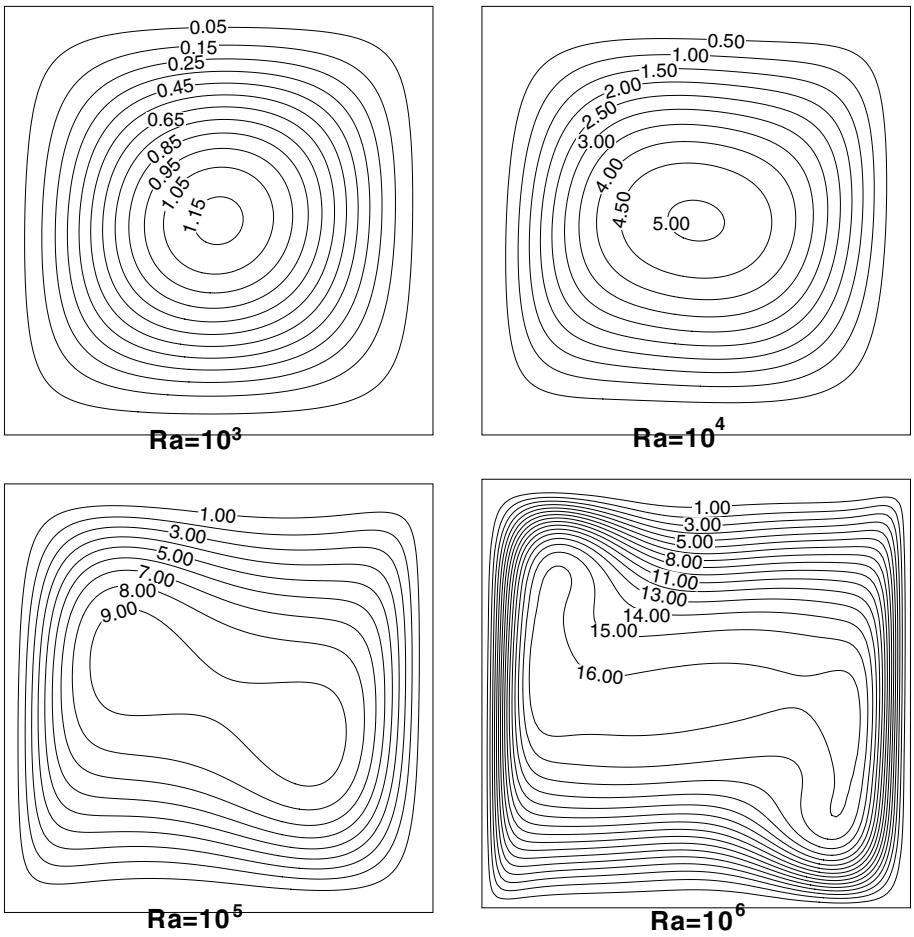

Figure 8.5 Streamlines of natural convection at Ra=10^3,10^4,10^5,10^6 for cases Δ=0.5

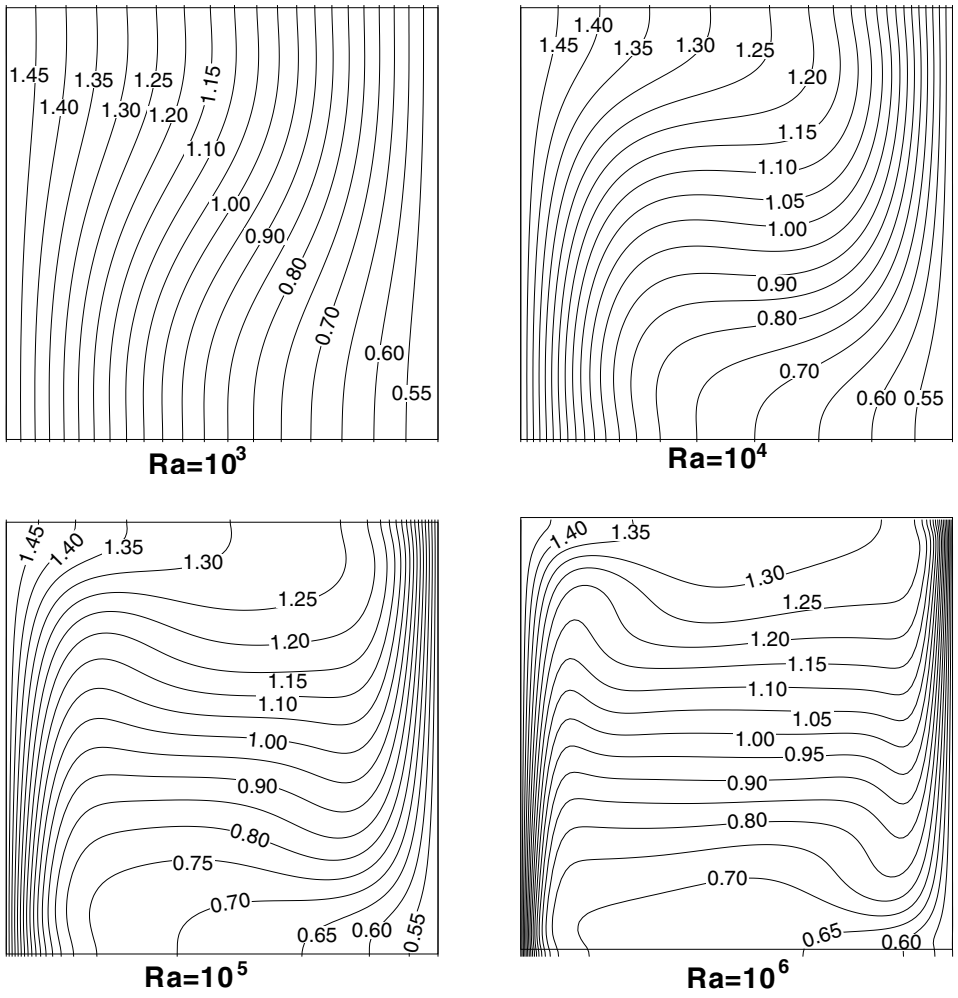

Figure 8.6 Isotherms of natural convection at Ra=10^3,10^4,10^5,10^6 for cases Δ=0.5

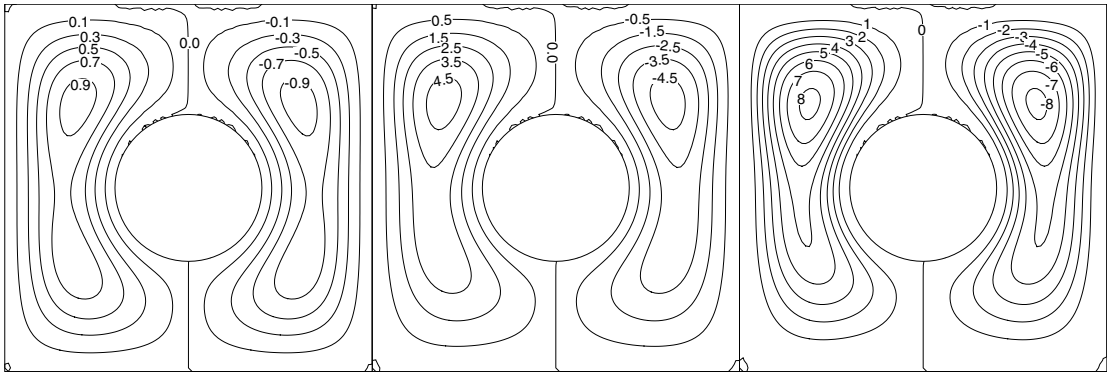

Figure 8.7 Streamlines of nature convection in a concentric annulus at Ra=10^4,5×10^4,10^5.

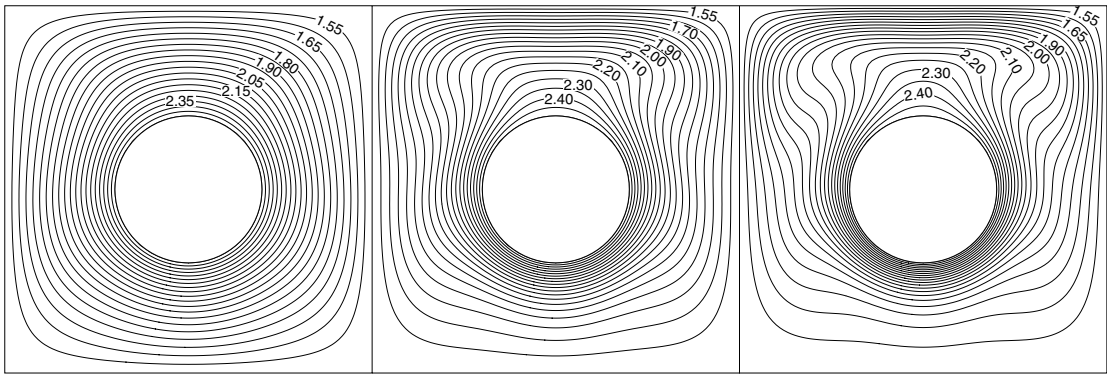

Figure 8.8 Isotherms of nature convection in a concentric annulus at Ra=10^4,5×10^4,10^5, the temperatures of inner cylinder and outer square are fix as 2.5, 1.5 respectively.

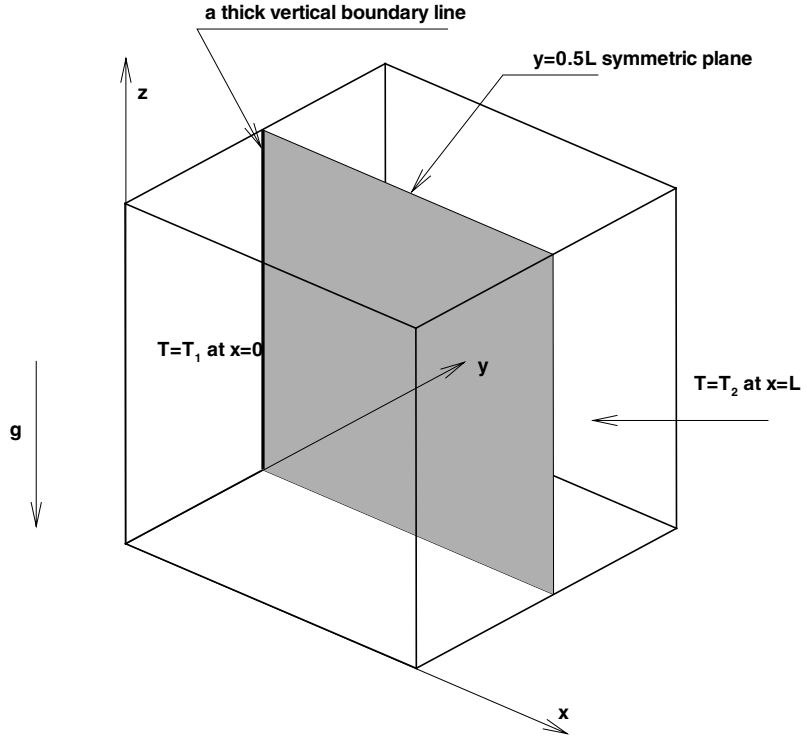

Figure 8.9 Configuration of natural convection in a 3D cubical cavity.

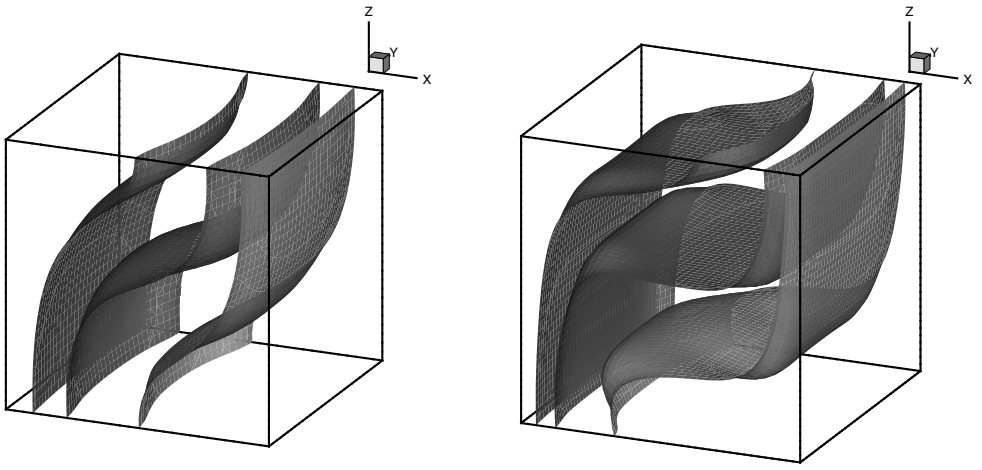

Figure 8.10 3D isotherms for the natural convection in a cubical cavity at Ra=10^4 (left) and10^5 (right).

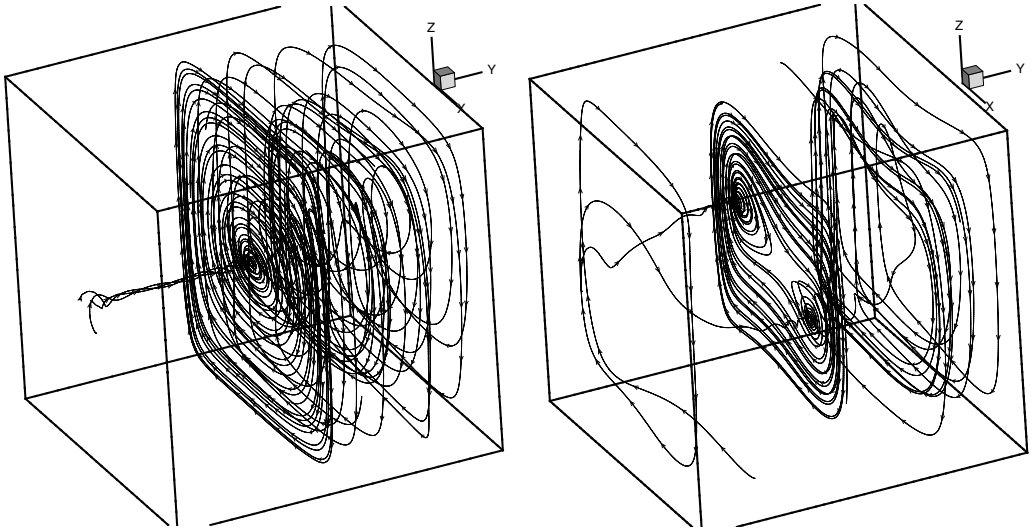

Figure 8.11 3D streamlines for the natural convection in a cubical cavity at Ra=10^4 (left) and 10^5 (right).

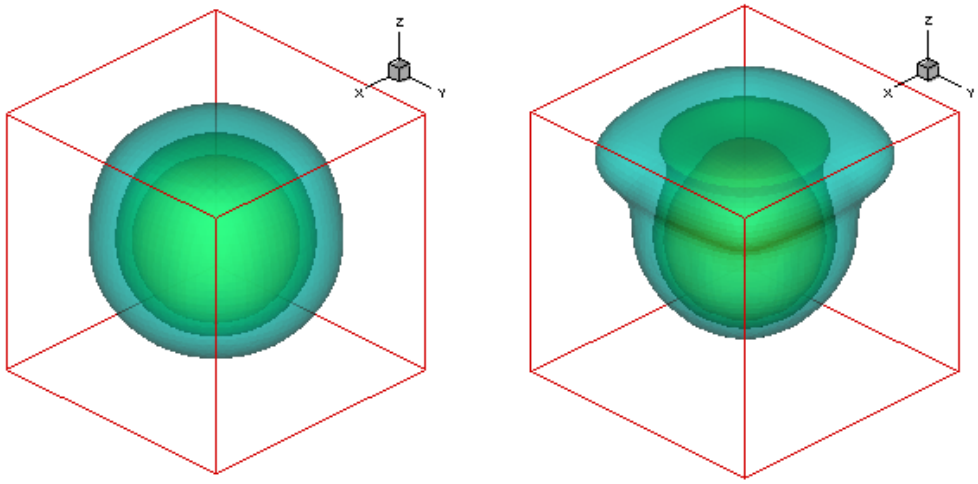

Figure 8.12 3D isotherms for the natural convection from a sphere placed in the center of a cubical enclosure at Ra=10^4 (left) and 10^5 (right)

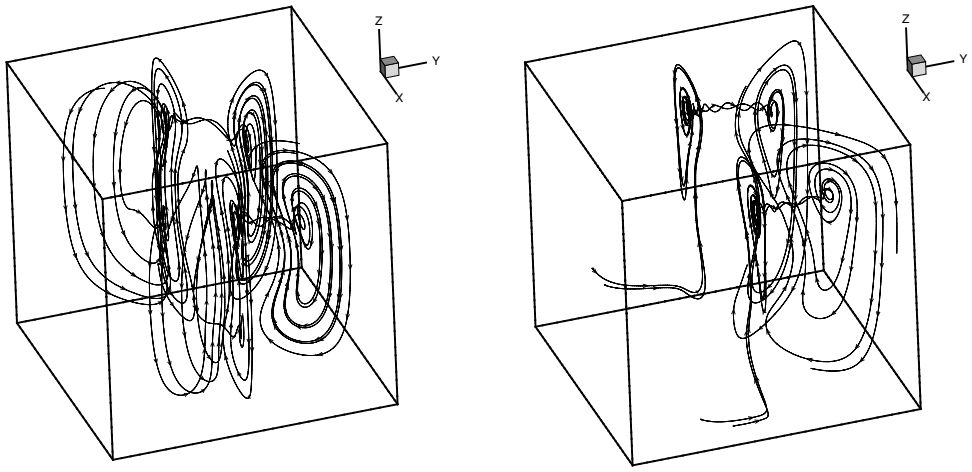

Figure 8.13 3D streamlines for the natural convection from a sphere placed in the center of a cubical enclosure at Ra=10^4 (left) and 10^5 (right).

Chapter 9 Conclusions and Future Work

In this study, we suggest a general method to derive axisymmetric lattice Boltzmann D2Q9 models in 2D coordinates. Using the general method, three different axisymmetric lattice Boltzmann D2Q9 models A, B and C were derived through inserting different source terms into the 2D LBE. Through fully considering the lattice effects in our derivation, all these models can mimic the 2D Navier-Stokes equation in the cylindrical coordinates at microscopic level. In addition, to avoid the singularity problem in simulations of Halliday et al. (2001), axisymmetric boundary models were proposed.

Compared with FVM solution, our axisymmetric model A, B and C can all provide accurate results. The 3D Womersley flow simulations with different Reynolds number and Womersley number further validated our axisymmetric model B. This model B is subsequently used mainly in all our applications. The LBM incorporating the extrapolation wall boundary condition (Guo et al., 2002a) and specular scheme for axisymmetric boundary is second-order in space. While the spatial convergence ratio of Bouzidi's wall boundary condition is about 1.6.

Using the axisymmetric model and the multi-block strategy, the steady and unsteady blood flows through constricted tubes and elastic vascular tubes were simulated. The flow patterns through tubes with different constriction ratio, Reynolds number are consistent with those given by other CFD method.

Direct 3D simulations are necessary in studies of the blood flow through asymmetric tubes. Our 3D LBM solver approximately has second-order accuracy in space (i.e., spatial convergence rate is 1.89) for flow in constricted tubes. It is found that there is a distinct and significant difference in the wall shear stresses between the stenosed side and the side with no protuberance.

A hybrid scheme combining the axisymmetric LB model and finite difference method was applied to solve the axisymmetric flows with rotation as a quasi-three-dimensional problem. The Taylor-Couette flows between two concentric cylinders and melt flows in Czochralski crystal growth were simulated. Compared with results in other literature, the hybrid scheme can provide very accurate results for benchmark problems. The present axisymmetric D2Q9 model also seems more stable than that of Peng et al. (2003). As a result, this scheme provides accurate results for high Reynolds number and high Grashof number cases with smaller grid size.

A revised axisymmetric D2Q9 model was also applied to investigate gaseous slip flow with slight rarefaction through long microtubes. In the simulations of microtube flows with Kn_o in range (0.01, 0.1), our LBM results agree well with analytical and experimental results. Our LBM is also found to be more accurate and efficient than DSMC when simulating the slip flow in microtube.

To simulate heat and fluid flow problem, a curved non-slip wall boundary treatment for isothermal Lattice Boltzmann equation (LBE) was successfully extended to handle the thermal curved wall boundary for a double-population thermal LBE. The method proved to be of second-order accuracy.

As far as I know, no one has proposed a general method to derive axisymmetric 2D LB models and no one has applied the models to simulate the blood flow in tubes or slip flow in micro-tubes. Our study suggests that LBM can also be a useful tool to study the blood flows and micro-tube flows. Our study also demonstrates that LBM can be use to study complex 3D heat and fluid flows.

As one of the novel CFD methods, LBM has not been explored comprehensively. The compressibility effect still exists in our axisymmetric

model and can be eliminated only if $L_x/c_sT<<1$ and Mach number $M<<1$ are satisfied. In our study, due to limitation of mesh size and numerical instability, it is still difficult to simulate the cases with higher *Re* and large Womersley number α.

Future research on the area of 3D and axisymmetric LBM should be carried out in the following three aspects.

1) For the LBM itself, the numerical stability should be further improved to simulate steady cases with higher *Re* number and pulsatile flow cases with high Womersley number α. That means the further improvements of wall boundary conditions and inlet/outlet boundary condition are needed because the calculation stability is mainly affected by these boundary conditions. Moving boundary condition in LBM also should be further improved.

2) Further study on incompressible LBM is needed to improve the results of unsteady flows since the compressibility of LBM model still affects the accuracy of our results especially for the unsteady flow cases.

3) Although present LBM is only applied to the slip flow simulation ($0.01<Kn_0<0.1$) in microtube, the LBM may be extended to study the transition flow or higher Knudsen number cases in the future.

References

Ahmed, S.A. and Giddens, D.P., Velocity measurement in steady flow through axisymmetric stenoses at moderate Reynolds numbers, *J. Biomech.*,16, pp.505-516. (1983)

Alexander, F.J., Chen, H., Chen, S., et al., lattice Boltzmann model for compressible fluids, *Phys. Rev. A*, 46(4): pp.1967-1970. (1992)

Arkilic, E. B., Schmidt, M. A. and Breuer, K. S., Gaseous slip flow in long micro-channels, *J. MEMS*, 6(2), pp.167-178. (1997)

Artoli, A.M., Hoekstra, A.G., Sloot, .PM.A., Accuracy of 2D Pulsatile flow in the lattice Boltzmann BGK method , *Lecture notes in computer science*, 2329, pp. 361-370. (2002a)

Artoli, A.M., Hoekstra, A.G., Sloot, P.M.A., 3D pulsatile flow with the lattice Boltzmann BGK method, *Int. J. of Modern Physics C*, 13(8), pp.1119-1134. (2002b)

Artoli, A.M., Kandhai, D., Hoefsloot, H.C.J., et al. Lattice BGK simulations of flow in a symmetric bifurcation, *future generation computer systems*, 20(6), pp.909-916. (2004)

Benzi, R. and Succi, S., 2-dimensional turbulence with the lattice Boltzmann equation, *J. of Phys. A*, 23 (1), L1-L5. (1990)

Beskok, A. and Karniadakis, G., Simulation of heat and momentum transfer in micro-geometries, *AIAA* Paper 93-3269. (1993)

Bhatnagar, P. L., Gross, E. P. and Krook, M., A Model for Collision Processes in Gases. I. Small Amplitude Processes in Charged and Neutral One-Component Systems, *Phys. Rev.*, 94**,** pp.511. (1954)

Bird, G.A., Molecular Gas Dynamics, Oxford. (1976)

Bird, G.A., Molecular Gas Dynamics and the Direct Simulation of Gas Dynamics, Oxford. (1994)

Bouzidi, M., Firdaouss, M. and Lallemand, P., Momentum transfer of a Boltzmann-lattice fluids with boundaries, *Phys. Fluids*, 13(11), pp.3452-3459. (2001)

Buckle, U., Schafer, M., Benchmark results for the numerical simulation of flow in Czochralski crystal growth, *J. Crystal Growth*, 126(4), pp.682-694. (1993)

Buick, J.M. and Greated, C.A., Gravity in a lattice Boltzmann model, *Phys. Rev. E,* 61, pp.5307-5320. (2000).

Cavalcanti, S., Bolelli, P. and Belardinelli, E., Pressure drops through arterial stenosis models in steady flow condition, *ASME J. Biomech. Eng.*, 114, pp.416-418. (1992)

Cercignani, C., The Boltzmann equation and its application: Springer, New York. (1988)

Chen, S.Y., Diemer, K, Doolen, D, et al., Lattice Gas Automata for flow through porous-media, *Physica D.*, 47 (1-2), pp.72-84. (1991)

Chen, S., Martinez, D. and Mei, R., On boundary conditions in lattice Boltzmann methods, *Phys. Fluids*, 8(9), pp. 2527-2536. (1996)

Chen, S. and Doolen, G., Lattice Boltzmann method for fluid flows, *Annu. Rev. Fluid Mech.* 30, pp.329-364. (1998)

Chen, H., Chen, S., and Matthaeus, W.H., Recovery of the Navier Stokes equations using a lattice-gas Boltzmann methods,*Phys. Rev. A*, 45(8), pp.5339-5342. (1992)

Choi, S.B., Barron, R. and Warrington, R., Fluid Flow and heat transfer in microtubes, *DSC*-Vol.32, *Micromechanical sensors, Actuator and Systems*, ASME, pp123-134. (1991)

Chopard, B. and Droz, M., Cellular Automata Modeling of Physical Systems. Cambridge University Press. (1998)

Cosgrove, JA, Buick, JM, Tonge, SJ, et al., Application of the lattice boltzmann method to transition of oscillatory channel flow, *J. Phys. A: Math. Gen.*, 36, pp.2609-2620. (2003)

D'Orazio, A., Succi, S., and Arrighetti, C., Lattice Boltzmann simulation of open flows with heat transfer , *Phys. Fluids,* 15(9), pp.2778-2781. (2003)

Fang, H.P., Wang, Z.W., Lin, Z.F., and Liu, M.R., Lattice Boltzmann method for simulating the viscous flow in large distensible blood vessels, *Physical Review E*, 65**,** Art.No.051925. (2002)

Ferziger, J.H. and Peric, M., *Computational Methods for Fluid Dynamics*, Springer, New York. (1999)

Filippova, O. and Hanel, D., Grid refinement for lattice-BGK methods, *J. Comp. Phys.*, 147 (1), pp.219-228. (1998)

Filippova, O. and Hanel, D., Acceleration of Lattice-BGK Schemes with Grid Refinement, *J. Comput. Phys.*, 165, pp.407-427. (2000)

Forrester, J.H. and Young, D.F., Flow through a converging-diverging tube and its implications in occlusive vascular disease, *J. Biomech.*, 3, pp.307-316. (1970)

Frisch, U., Hasslacher B. and Pomeau Y., Lattice-Gas Automata for the Navier-Stokes equation, *Phys. Rev. Lett.,* 56(14), pp.1505-1508. (1986)

Fusegi, T., Hyun, J.M., Kuwahara, K., Farouk, B., A numerical study of three-dimensional natural convection in a differentially heated cubical enclosure, *Int. J. Heat Mass Transfer*, 34(6), pp.1543–1557. (1991)

Fung, Y.C., Biomechanics Circulation (Springer-Verlag, Berlin). (1997)

Gad-el-Hak, M., The fluid mechanics of microdevices-The Freeman Scholar Lecture, *J. Fluids Eng.,* 121 (1), pp.5-33. (1999)

Grunau, D., Chen, S., and Eggert, K., A lattice Boltzmann model for multiphase fluid flows, *Phys. Fluids A*, 5(10), pp.2557-2562, (1993).

Ghia, U., Ghia, K. N. and Shin, C. T., High-Re solutions for incompressible flow using the Navier-Stokes equations and a multigrid method, *J. Comp. Phys.*, 48(3), pp.387-411. (1982)

Gunstensen, A. K. and Rothman, D. H., Zaleski, S, et al., lattice Boltamann model of immiscible fluids, *Phys. Rew. A*, 43(8), pp.4320-4327. (1991)

Guo, Z., Shi, B. and Wang, N., Lattice boltzmann Model for Incompressible Navier-stokes Equation, *J. Comp. Phys*, 165, pp.288-306. (2000)

Guo, Z., Zheng, C., and Shi, B., An extrapolation method for boundary conditions in lattice Boltzmann method, *Phys. Fluids,* 14 , pp.2007-2010. (2002a)

Guo, Z., Zheng, C. and Shi, B., Discrete lattice effects on the forcing term in the lattice Boltzmann method, *Phys. Rev. E*, 65, Art.No.046308. (2002b)

Guo, Z., Zheng, C., and Shi, B., Non-equilibrium extrapolation method for velocity and pressure boundary conditions in the lattice Boltzmann method, *Chinese Physics*, 11(4). (2002c)

Halliday, I., Hammond, L.A., Care, C. M., Good, K., and Stevens, A., Lattice Boltzmann equation hydrodynamics, *Phys. Rev. E*, 64, 011208. (2001)

Hardy, J., Pomeau, Y., and de Pazzis, O., Time evolution of a two-dimensional model system. I. Invariant states and time correlation functions, *J. Math. Phys*., 14, pp.1746. (1973)

He, X., Luo, L.S. and Dembo, M., Some progress in lattice Boltzmann method: Part I. NonuniformMesh Grids, *J. Comp. Phys.*, 129(2), pp. 357-363. (1996)

He, X.Y. and Luo, L.S., Lattice Boltzmann Model for the incompressible Navier-Stokes Equation, *J. Stat. Phys*, 88(3/4), pp.927-944. (1997a)

He, X.Y., Luo, L.S., A priori derivation of the lattice Boltzmann equation, *Phys. Rev. E*, 55(6), R6333-R6336 Part A (1997b)

He, X.Y., Luo, L.S., Theory of the lattice Boltzmann method: From the Boltzmann equation to the lattice Boltzmann equation, *Phys. Rev. E*, 56(6), pp.6811-6817. (1997c)

He, X. and Doolen, G., Lattice Boltzmann method on curvilinear coordinates system: Flow around a circular cylinder, *J. Comput. Phys.,* 134, pp.306-315. (1997a)

He, X. and Doolen, G., Lattice Boltzmann method on a curvilinear coordinate system: Vortex shedding behind a circular cylinder, *Phys. Rev. E,* 56(1), pp.434-440. (1997b)

He, X., Zou, Q., Luo, L.S. and Dembo, M., Analytical solutions of simple flows and analysis of non-slip boundary conditions for the Lattice Boltzmann BGK model, *J. Stat. Phys.,* 87, pp.115-136. (1997)

He, X., Chen, S., and Doolen, G. D., A novel thermal model for the Lattice Boltzmann method in incompressible limit, *J. Comput. Phys.* 146, pp.282-300. (1998)

Higuera, F. and Jimenez, J., Boltzmann approach to lattice gas simulations, *Europhys. Lett.*, 9(7), pp.663-668. (1989)

Hoekstra, A.G., Hoff Jos van't, Artoli, A.M., Sloot, P.M.A., Unsteady flow in a 2D elastic tube with the LBGK method, *Future Generation Computer Systems,* 20, pp.917–924. (2004)

Hou, S., Zou, Q., et al., Simulation of cavity flow by the lattice boltzmann method, *J. of Comp. Phys.*, 118, pp.329-347. (1995)

Huang, H., Lee, T.S., Shu, C., Lattice-BGK simulation of steady flow through vascular tubes with double constrictions, *Int. J. Numer. Methods Heat Fluid Flow*,16(2), pp. 185-203. (2006)

Huang, H., Lee, T.S., Shu, C., Thermal curved boundary treatment for the thermal lattice Boltzmann equation, *Int. J. Mod. Phys. C.* , 17(5), pp. 631-643 (2006)

Huang, H., Lee, T.S., Shu, C., Lattice Boltzmann Simulation Gas Slip Flow in Long Microtubes, *Int. J. Numer. Meth. for Heat & Fluid Flow*, (in press, 17(6), 2007)

Huang, H., Lee, T.S., Shu, C., Hybrid lattice-Boltzmann finite-difference simulation of axisymmetric swirling and rotating flows, *Int. J. Numer. Meth. Fluids,* 53(11), pp.1707-1726. (2007)

Huang, H., Lee, T.S., Shu, C., Computations of the Laminar Flow through Tubes with Double Constrictions Based on Two Different Methods: Lattice-Boltzmann and Finite-Volume, *2nd International Conference on Scientific and Engineering Computation IC-SEC 2004, Singapore*

Huang, H., Lee, T.S., Shu, C., Simulation pulsatile flow in constricted tubes by Lattice Boltzmann method, Asian Joint Conference on Propulsion and Power 2006, Apr.20-23, Beijing, China

Huang, H., Lee, T.S., Shu, C., A multi-block Lattice-BGK method for 3D viscous fluid flows, Asian Joint Conference on Propulsion and Power 2006, Apr.20-23, Beijing, China

Iwatsu, R., Ishii, K., Kawamura, T., Kuwahara, K., Hyun, J.M., Numerical-simulation of 3-Dimensional flow structure in a driven cavity, *Fluid Dynamics Research*, 5 (3), pp.173-189. (1989)

Jeffreys, H., Cartesian Tensors. Cambridge University Press, (1965).

Kim, M.S., Araki, T., Inaoka, K. and Suzuki, K., Gas flow characteristic in microtubes, *JSME international journal Series B, Fluid and Thermal engineering*, 43(4), pp. 634-639. (2000)

Ku, D. N., Blood flow in arteries, *Annu. Rev. Fluid Mech.*, 29, pp.399-434. (1997).

Ladd, AJC, and Verberg, R. Lattice Boltzmann simulations of particle-fluid suspensions. *J Stat Phys*, 104, pp.1191-1251. (2001)

Lai, Y., Lin, C. and Huang, J., Accuracy and efficiency study of Lattice Boltamann Method for Steady-State Flow Simulation, *Numer. Heat Tr. B-Fund*, 39 (1), pp. 21-43. (2001)

Lallemand, P. and Luo, L.S., Lattice Boltzmann methods for moving boundaries, *J. Comp. Phys.*, 184, pp.406-421. (2003)

Lee, T.S., Huang, H., Shu, C., An axisymmetric incompressible Lattice-BGK model for simulation of the pulsatile flow in a circular pipe, *Int. J. Numer. Meth. Fluids*, 49(1), pp.99-116. (2005)

Lee, T.S., Huang, H., Shu, C., An axisymmetric incompressible lattice Boltzmann model for pipe flow, *Int. J. Mod. Phys. C.*, 17 (5), pp.645-661. (2006)

Liao, W., Lee, T.S., Low H.T., Numerical studies of physiological pulsatile flow through constricted tube, *Int. J. Num. Meth. Heat & Fluid Flow,* 14(5-6), pp. 689-713. (2004)

Liu, Y., Numerical simulation of flows in Czochralski crystal growth and Taylor vortices, M. Eng. thesis, National University of Singapore. (1998)

Lim, C.Y., Shu, C., Niu, X.D. and Chew, Y.T., Application of lattice Boltzmann method to simulate microchannel flows, *Phys. Fluids,* 14(7), pp.2299-2308 (2002)

Luo, L.S., Symmetry breaking of flow in 2D symmetric channels: simulations by lattice-Boltzmann method, *Int. J. Mod. Phys. C.*, 8(4), pp.859-867 (1997)

Luo, L.S., Unified theory of lattice boltzmann models for nonideal gases, *Phys. Rev. Lett.,* 81(8), pp.1618-1621. (1998)

Luo, L.S., Theory of the lattice Boltzmann method: lattice Boltzmann models for nonideal gases, *Phys. Rev. E*, 62(4), pp.4982-4996. (2000)

Mao, X.H., Shu, C., Chew, Y.T., Numerical and theoretical study of a micro tube flow, *Int. J. Nonlinear Sciences and Numer. Simulation*, 4(2), pp.187-200. (2003)

McNamara, G. and Zanetti, G., Use of the Boltzmann equation to simulate Lattice-gas automata, *Phys. Rev. Lett.,* 61(20), pp.2332-2335. (1988)

McNamara, G. and Alder, B., Analysis of the lattice Boltzmann treatment of hydrodynamics, *Physica A,* 194, pp.218-228. (1993)

Mei, R., Luo, L.S., and Shyy, W., An accurate curved boundary treatment in the lattice Boltzmann method, *J. Comput. Phys.*, 155, pp.307-330. (1999).

Mei, R., Shyy, W., Yu, D. and Luo L.S., Lattice Boltzmann methods for 3-D flows with curved boundary, *J. Comp. Phys.*, 161(2), pp. 680-699. (2000)

Mei, R., Yu, D. and Shyy, W., Force evaluation in the lattice Boltamann method involving curved geometry, *Phys. Rev. E.*, 56(4), Art. No. 041203 Part 1. (2002)

Mittal, R., Simmone, S.P. and Najjar, F., Numerical Study of pulsatile flow in a constricted channel, *J. Fluid Mech.*, 485, pp.337-378. (2003)

Nannelli, F. and Succi, S., The lattice Boltzmann equation on irregular lattices, *J. Stat. Phys.,* 68 (3/4), pp.401-407. (1992)

Nie, X., Doolen, G.D. and Chen, S.Y., Lattice Boltzmann simulation of fluid flows in MEMS, *J. Stat. Phys.,* 107, pp.279-289. (2002)

Peng, Y., Shu, C., Chew, Y.T., Qiu J., Numerical investigation of flows in Czochralski crystal growth by an axisymmetric lattice Boltzmann method, *J. Comp. Phys.*, 186(1), pp. 295-307. (2003)

Peng, Y., Shu, C., Chew, Y.T., A 3D incompressible thermal lattice Boltzmann model and its application to simulate natural convection in a cubic cavity, *J. Comp. Phys.*, 193, pp. 260-274. (2003b)

Peng, Y, Shu, C, Chew, Y.T., et al. Lattice kinetic scheme for the incompressible viscous thermal flows on arbitrary meshes , *Phys. Rev. E*, 69(1): Art. No. 016703 Part 2. (2004)

Prud'homme, R., Chapman, T. and Bowen, J., Laminar compressible flow in a tube, *Appl. Sci. Res.,* 43, pp.67–74. (1986)

Qian, Y. H., d'Humières, D., and Lallemand, P., Lattice BGK models for Navier–Stokes equation, *Europhys. Lett*. 17, pp.479-484. (1992).

Raspo, I., Ouazzani, J., Peyret, R., A spectral multidomain technique for the computation of the czochralski melt configuration, *Int. J. Numer. Methods Heat Fluid Flow*, 6(1), pp.31-58. (1996)

Salom, J., Numerical Simulation of Convection Phenomena Based on Domain Decomposition Techniques and Experimental Validation, Ph.D. dissertation, Universitat Politecnica de Catalunya, Spain (1999).

Shan, X.W. and Doolen, G., Multicomponent lattice-Boltzmann model with interparticle interaction, *J. Stat. Phys*., 81 (1-2), pp.379-393. (1995)

Shan, X., Solution of Rayleigh-Bénard convection using a lattice Boltzmann method, *Phys. Rev. E,* 55(3), pp.2780-2788. (1997)

Shu, C., Xue, H., Comparison of two approaches for implementing stream function boundary conditions in DQ simulation of natural convection in a square cavity, *Int. J. heat & Fluid Flow,* 19(1), pp.59-68. (1998)

Shu, C, Zhu, Y.D., Efficient computation of natural convection in a concentric annulus between an outer square cylinder and an inner circular cylinder, *Int. J. Numer. Meth. Fluids,* 38(5): pp.429-445. (2002)

Skordos, PA. Initial and boundary conditions for the lattice Boltzmann method, *Phys Rev E*, 48, pp.4823-4842. (1993)

Succi, S., Benzi, R., Higuera, F., The lattice Boltzmann equation- A new tool for computational fluid dynamics, *Physica D,* 47(1-2), pp.219-230. (1991)

Succi, S., Mesoscopic modeling of slip motion at fluid-solid interfaces with heterogeneous catalysis, *Phys. Rev. Lett.* 89(6), Art.No.064502. (2002)

Tang, G.H., Tao, W.Q. and He, Y.L., Lattice Boltzmann method for simulating gas flow in microchannels, *Int. J. Mod. Phys. C*, 15(2), pp.335-347. (2004)

Teixeira, CM, Incorporating turbulence models into the lattice-Boltzmann method, *Int. J. Mod. Phys. C*, 9(8), pp.1159-1175. (1998)

Uchida, S., The pulsating viscous flow superimposed on the steady laminar motion of incompressible flow in a circular pipe, *Z. Angew. Math. Phys*., 7, pp. 377–386. (1956)

Van den Berg, H., Tenseldam, C. and VanderGulik, P., Compressible laminar flow in a capillary, *J. Fluid Mech.,* 246, pp.1–20 (1993)

Vanka, S.P., Block-implicit multigrid solution of Navier-Stokes equations in primitive variables, *J. Comp. Phys.*, 65(1), pp.138-158, (1986)

Weng, C.I., Li, W.L. and Hwang, C.C., Gaseous flow in microtubes at arbitrary Knudsen numbers, *Nanotechnology*, 10, pp373-379. (1999)

Wheeler, A.A., 4 test problems for the numerical simulation of flow in Czochralski crystal growth, *J. Crystal Growth*, 102 (4): pp.691-695. (1990)

White, F. M., Viscous Fluid Flow, McGraw-Hill, Singapore, 2nd ed.. (1991).

Wolf-Gladrow, D.A.. Lattice-Gas Cellular Automata and Lattice Boltzmann Models, Springer-Verlag, *Lecture Notes in Mathematics*, 1725, pp.1-13. (2000)

Xu, D., Shu, C., Khoo, B.C., Numerical simulation of flows in Czochralski crystal growth by second-order upwind QUICK scheme, *J. Crystal Growth*, 173(1-2), pp.123-131. (1997)

Young, D.F. and Tsai, F.Y., Flow characteristics in models of arterial stenoses. I. Steady flow, *J. Biomech*., 6, pp.395-410. (1973a).

Young, D.F. and Tsai, F.Y., Flow characteristics in models of arterial stenoses. II.Unsteady flow, *J. Biomech.*, 6, pp.547-559. (1973b).

Yu, D., Warrington, R., Barron, R. and Ameel, T., An experimental and Theoretical investigation of Fluid flow and heat transfer in Microtubes, *ASME/JSME Thermal Engineering Conference*, 1, pp.523-530. (1995)

Yu, D., Mei, R., Shyy, W., A multi-block lattice Boltzmann method for viscous fluid flows, *Int. J. Numer. Meth. Fluids*, 39, pp.99-120. (2002)

Ziegler, D.P., Boundary conditions for lattice Boltzmann simulations. *J. Stat. Phys.*, 71(5/6), pp.1171-1177, (1993).

Zou, Q. and He, X., On pressure and velocity boundary conditions for the lattice Boltzmann BGK model, *Phys. Fluids*, 9(6), pp. 1591-1598. (1997)